UNIVERSITY OF CALIFORNIA

Los Angeles

Porous Electrospray Fluid Mechanics

A dissertation submitted in partial satisfaction

of the requirements for the degree

Doctor of Philosophy in Aerospace Engineering

by

Peter Lloyd Wright

2022

ABSTRACT OF THE DISSERTATION

Porous Electrospray Fluid Mechanics

by

Peter Lloyd Wright
Doctor of Philosophy in Aerospace Engineering
University of California, Los Angeles, 2022
Professor Richard E. Wirz, Chair

Although electrospray devices traditionally use a capillary for fluid flow and electric field concentration, a sharpened porous medium can be used instead for these purposes. In porous media electrospray emitters, a working fluid flows through the porous medium to an emission surface, where the local electric field and fluid pressure allow for electrostatic emission of droplets or ions. Long lifetime and high-performance operation of these devices requires understanding the flow through the porous medium to emission sites. To investigate the behavior of porous electrospray devices, two complementary models are proposed: a multiplexed emission model and a transient flow model. Multiple experiments were developed and utilized to inform and validate these models; these experiments also provided insight into other electrospray thruster phenomena. Computational analysis was performed where necessary as well: verification of transient flow solutions and electrostatic analysis. In this sense, the research presented in this manuscript combines analytical, experimental, and computational analysis of the porous electrospray emitter in order to thoroughly understand the various aspects of its behavior.

A wedge is a common shape of electrospray emitter which allows for many individual emission sites to form on its sharp end. A sharp edge creates a region where the electric field is strong and nearly uniform. Along this edge, emission sites form due to the combined effects of the subsurface flow and local electric field. An analytical model is developed to examine the behavior and spacing of these emission sites via the pressure variation in the porous fluid flow associated with the flow

focusing on each emission site, which is coupled with the local electric field. The solution for site spacing and current is informed by empirical results with support from electric field modeling and investigation of porous media parameters. Emission site currents of up to 500 nA and site spacings of roughly 50 to 300 micron are predicted. Experimental measurements at UCLA of site spacing on a porous wedge confirm analytically predicted trends.

In all applications of electrospray propulsion, dynamic events are unavoidable. Transient flow to an emission site is described through the 'sucking-in' of the meniscus at the emitter surfaces where emission does not occur. Pressure in the porous medium is enforced using the Young-Laplace equation and Darcy's law. Even though the flow through porous electrospray emitters is generally low Reynolds number, which is typically associated with instantaneous reaction to pressure changes, the pressure-dependent fluid accumulation at free surface pores can cause transient flow conditions. A diffusion equation for pressure in a porous medium is presented along with flow solutions for the three common emitter geometries of pillars, cones, and wedges. Flow solutions predict that flow to the emission surface initially peaks and decays to a constant value, which corroborates published transient electrospray current traces. Experimental measurement of the transient response of a pillar-shaped electrospray emitter shows qualitative agreement with the diffusion model. Experimental investigation of a porous wedge electrospray emitter requires a more nuanced model to take into account the significant volume required to form the many Taylor cones on the surface of the emitter.

A porous tungsten electrospray thruster (PoWEE) was developed to validate porous flow and electrostatic models. Up to 130 µA of emitted current was demonstrated in vacuum at 4.8 kV emitter potential. The wire probe diagnostic has revealed that tens of emission sites exist per millimeter of emitter length, both on and off the centerplane of the wedge. Transient wire probe measurements confirm that individual sites exhibit delay-overshoot-decay behavior that conforms to published electrospray experimental results, despite the total wedge response differing from typical published data. The porous wedge electrospray was operated with a variety of target voltages in order to understand thruster facility effects. Current measurements, in situ photography, and a novel wet and dry thruster experiment have show that glow and secondary species collection at the

emitter can be simultaneously suppressed through adequate target biasing.

An electrospray emission model was developed using the first principles of fluid flow and electrospray emission. The model assumes that emission sites form on the surface of the electrospray emitter due to a distribution of electric fields on the surface of the emitter. Emitted current varies between sites due to the variation in driving pressure to each emission site. The current-voltage response of the porous wedge electrospray device is replicated, albeit at a reduced current throughput. The transient response is predicted by adding the steady response and transient homogeneous response of each emission site, while accounting for the fluid volume required for onset of emission. The experimental and model transient response match following cone volume iteration within a range of physically allowable sizes. The model shows that onset delay, rather than transient flow in the porous emitter, is the dominant mechanism for causing the transient response of porous wedge electrosprays. The corroboration of experimental results and modeling predictions shows that the transient ramp observed with porous wedge emitters is due to the distribution of onset delays of numerous emission sites, which is a direct result of nonuniform electric field on the emission surface. Furthermore, the nonuniform electric field is due to the sharp features present on the emission surface due to the emitter manufacturing process. As a result, this investigation highlights the effect that manufacturing uniformity has on both the transient and steady response of porous wedge electrospray emitters.

The dissertation of Peter Lloyd Wright is approved.

John Ziemer

Artur R. Davoyan

Kunihiko Taira

Dino Di Carlo

Richard E. Wirz, Committee Chair

University of California, Los Angeles

2022

TABLE OF CONTENTS

LIST OF FIGURES

LIST OF TABLES

ACKNOWLEDGMENTS

Working towards a PhD over the last 5 years has been an incredibly rewarding and challenging experience. The rigor, technical challenge, and stress has been nearly as expected, but there have been no shortage of unforeseen challenges. The largest example of this has been that how and where research is performed has been transformed significantly by the pandemic. Just recently I calculated that about 47% of my time at UCLA has been during the COVID-19 pandemic, meaning I am in the last PhD cohort to have a majority of our research performed before the pandemic. I'm not sure if the pandemic has had a net negative or positive impact on the quality of my work, but it has certainly affected the type of work presented in this manuscript. For example, the transient flow diffusion equation was derived during the first few weeks when we were all at home worrying about toilet paper and sewing masks; the specific solutions for each geometry were derived after cancelling a flight home due to the Omicron variant. Its unlikely that I would have been able to perform this work without extended periods for focusing on math and neglecting experiments.

The research in for this effort would not have been possible without the opportunities and guidance from my previous mentors and supervisors. My first foray into the world of space component engineering and analysis with the late Prof. Ted Fritz and Nathan Darling at BUSAT gave me invaluable experience that gave others confidence in my ability to tackle aerospace challenges. Nate Demmons and Dr. Dan Courtney while at Busek taught me about how to research, operate, and design electrospray propulsion systems. I miss the friends I made at Busek but have been so happy to reconnect at the various aerospace conferences around the world. Finally, the funding and support that I have received as part of the NASA Space Technology Research Fellowship (NSTRF), recently rebranded as the NSTGRO fellowship, have made the research presented in this dissertation possible. Thanks to Dr. Rob Thomas for his guidance throughout the past 4 years.

Thank you to my advisor Prof. Richard Wirz. For challenging me to tackle the first principles of electrospray propulsion. For providing the resources and guidance to develop experiments for validating models. And for passionately explaining how experimental, computational, and analytical methods synergize into effective research. Also, thank you to the rest of my committee for

your patience and insight, both of which have been tremendously appreciated.

I am deeply grateful to have such great peers in the lab with which to develop ideas and enjoy time. In particular, I owe a substantial debt to my closest collaborators: Dr. Anirudh Thuppul, Dr. Nolan Uchizono, and Dr. Adam Collins. Some of the ideas and experiments presented in this manuscript would not have been possible without their help. In particular, development and testing of the wire probe diagnostic would have been impossible without Adam, and the hybrid emitter was a direct result of conversation with Ani while trying to understand electrospray emission modes. The countless current amplifiers, developed by Nolan, made porous electrospray testing possible in the lab, and the facility effects investigations would have been fruitless without Nolan's insight and guidance. The quality of my experience in the lab, and of this manuscript (if possible!), would have been drastically reduced in their absence.

Thanks to my family for your endless support. I have tried to emulate John's mathematical intelligence, my mother's creativity, and my father's diligence throughout the past 5 years and occasionally succeeded. Lastly, thanks to Kaitlyn for the continuous Pizza Port. And thanks to you for reading this dissertation!

CURRICULUM VITAE

Dec. 1990	World's Youngest Person
2009 – 2013	B.S. in Mechanical Engineering, Boston University, Boston MA.
2013 – 2017	Research Engineer at Busek Co. Inc., Natick, MA.
2017 – 2022	Ph.D. student in Aerospace Engineering, University of California, Los Angeles (UCLA).
2018 – 2022	NASA Space Technology Research Fellowship (NSTRF) Recipient

PUBLICATIONS

[1] Peter Wright, Anirudh Thuppul, and Richard E. Wirz, "Life-Limiting Emission Modes for Electrospray Thrusters," AIAA Joint Propulsion Conference (2018), doi.org/10.2514/6.2018-4726 .

[2] Anirudh Thuppul, Peter Wright, and Richard E. Wirz, "Lifetime Considerations and Estimation for Electrospray Thrusters," AIAA Joint Propulsion Conference (2018), doi.org/10.2514/6.2018-4652 .

[3] Richard E. Wirz, Adam Collins, Anirudh Thuppul, Peter Wright, Nolan Uchizono, Henry Huh, McKenna Breddan, John Ziemer, and Nathaniel Demmons, "Electrospray Thruster Performance and Lifetime Investigation for the LISA Mission," AIAA Propulsion and Energy Forum (2019), doi.org/10.2514/6.2019-3816 .

[4] Peter Wright, Henry Huh, Nolan Uchizono, Anirudh Thuppul, and Richard E. Wirz, "A Novel Variable Mode Emitter for Electrospray Thrusters," International Electric Propulsion Conference (2019), researchgate.net:336197533 .

[5] Adam Collins, Anirudh Thuppul, Peter Wright, Nolan Uchizono, Henry Huh, McKenna Breddan, John Ziemer, Nathaniel Demmons, and Richard E. Wirz, "Assessment of grid impingement for electrospray thruster lifetime," International Electric Propulsion Conference (2019), researchgate.net:340236136 .

[6] Anirudh Thuppul, Adam Collins, Peter Wright, Nolan Uchizono, and Richard E. Wirz, "Spatially-Resolved Mass Flux and Current Measurements of Electrospray Plumes," International Electric Propulsion Conference (2019), researchgate.net:336220674 .

[7] Nolan Uchizono, Adam Collins, Anirudh Thuppul, Peter Wright, Daniel Eckhardt, John Ziemer, and Richard E. Wirz, "Electrospray Steady-State and Transient Emission Behavior," International Electric Propulsion Conference (2019), researchgate.net:336262919 .

[8] Peter Wright, Stephen Samples, Nolan Uchizono, and Richard E. Wirz, "Comment on "Jet propulsion by microwave air plasma in the atmosphere" [AIP Adv. 10, 055002 (2020)]," AIP Advances (2020), doi.org/10.1063/5.0013575 .

[9] Anirudh Thuppul, Peter Wright, Adam Collins, John Ziemer, and Richard E. Wirz, "Lifetime Considerations for Electrospray Thrusters," MDPI Aerospace (2020), doi.org/10.3390/aerospace7080108 .

[10] Nolan Uchizono, Adam Collins, Anirudh Thuppul, Peter Wright, Daniel Eckhardt, John Ziemer, and Richard E. Wirz, "Emission Modes in Electrospray Thrusters Operating with High Conductivity Ionic Liquids," MDPI Aerospace (2020), doi.org/10.3390/aerospace7100141 .

[11] Peter Wright and Richard E. Wirz, "Multiplexed Electrospray Emission on a Porous Wedge," Physics of Fluids (2021), doi.org/10.1063/5.0030031 .

[12] Peter Wright and Richard E. Wirz, "Transient Flow in Porous Electrospray Emitters," AIAA Propulsion and Energy Forum (2021), doi.org/10.2514/6.2021-3437 .

[13] Anirudh Thuppul, Adam Collins, Peter Wright, Nolan Uchizono, and Richard E. Wirz, "Mass Flux and Current Density Distributions of Electrospray Plumes," Journal of Applied Physics (2021), doi.org/10.1063/5.0056761 .

[14] Nolan Uchizono, Peter Wright, Adam Collins, and Richard E. Wirz, "Facility Effects for Electrospray Thrusters," AIAA SCITECH Forum (2022), doi.org/10.2514/6.2022-1361 .

[15] Peter Wright, Nolan Uchizono, Adam Collins, and Richard E. Wirz, "Characterization of a Porous Tungsten Electrospray Emitter," International Electric Propulsion Conference (2022), researchgate.net:361779957 .

[16] Adam Collins, Peter Wright, Nolan Uchizono, and Richard E. Wirz, "High Angle Mass Flux of an Electrospray Plume," (2022), Journal of Electric Propulsion, under review doi.org/10.21203/rs.3.rs-1687358/v1 .

[17] Peter Wright and Richard E. Wirz, "Transient Flow in Porous Electrosprays," Transport in Porous Media, under review (2022) .

CHAPTER 1

Introduction

In this section, brief introductions to spacecraft propulsion and the electrospray field will be presented. Following these introductions is an explanation of the motivation, objective, hypothesis, and approach of this thesis. The section concludes with an outline of the manuscript.

1.1 Space Propulsion

While many spacecraft missions do not use propulsion, some of the most ambitious missions do. Propulsion generally allows for more mission capability and versatility. Arguably the simplest implementation of spacecraft propulsion is for attitude control[4], although this can be implemented in a sophisticated manner, such as in the disturbance reduction system for the upcoming LISA mission [5]. More impulse from a propulsion system may be required for orbital changes, including phase and altitude transfers. The recent constellations being developed by OneWeb, Amazon, and SpaceX are possible due to simultaneous launches of multiple satellites and using propulsion for distributing satellites along an orbital path [6]. Propulsion can be used for drag compensation when operating a low altitude orbit, such as in the spectactularly designed GOCE mission which measured the gravity field of Earth [7]. On the other hand, propulsion can be implemented to deorbit satellites to prevent the buildup of additional orbital debris, or 'space junk', around our planet [8]. Finally, highly capable propulsion systems enable travel through our solar system, such as with the Dawn mission, which used xenon gridded ion thrusters to reach the asteroids Vesta and Ceres [9].

All maneuvers in space can be distilled down to changes in momentum. Attitude control requires a change in angular momentum, while most other maneuvers require a change in translational momentum. In-space propulsion provides a change in momentum to the spacecraft by

imparting an impulse on the propellant used by the propulsion system. Calculating the total capability of a propulsion system is made more complicated by the fact that the spacecraft's mass is changing as it expells propellant. Thankfully, in 1903 Tsiolkovsky derived an equation for the total change in speed of a rocket propelled vehicle, ΔV, well before space travel was possible: [10]

$$\Delta V = g_0 I_{sp} \ln \frac{m_0}{m_f} \tag{1.1}$$

where I_{sp} is the specific impulse of the propulsion system, g_0 is standard gravitational acceleration on Earth's surface, i.e. $9.81\,\mathrm{m/s^2}$, m_0 is the initial spacecraft mass with propellant, and m_f is the final spacecraft mass after all propellant has been used. Specific impulse, I_{sp} or ISP, is the defacto metric of propellant mass utilization efficiency in the proplusion field, and is defined as:

$$I_{sp} = \frac{T}{g_0 \dot{m}} \tag{1.2}$$

where T is thrust and $\dot{m}$ is propellant flow rate. Typically the specific impulse is approximated as the propellant exit velocity, c, divided by standard gravity, g_0. The momentum change required for any maneuver in space depends on the spacecraft mass, so ΔV is typically used instead because it does not depend on spacecraft mass. In this way, ΔV can be thought of as a spacecraft mass specific change in momentum. The ΔV requirements for travelling to various bodies throughout our solar system are shown in Figure 1.1.

When planning a space mission and evaluating propulsion options, typically the ΔV for the mission and I_{sp} for the propulsion system are known. In this situation, a different form of Equation 1.1 is used:

$$\frac{m_{prop}}{m_f} = \exp\left(\frac{\Delta V}{g_0 I_{sp}}\right) - 1 \tag{1.3}$$

where m_{prop} is the total mass of propellant on the spacecraft. Together, the term on the left of Equation 1.3 is known as the propellant mass fraction. Typical spacecraft propellant mass fraction curves are shown in the top half of Figure 1.2 for a range of ΔV requirements. From this figure, it is clear that increasing specific impulse is beneficial to minimizing the required mass of propellant

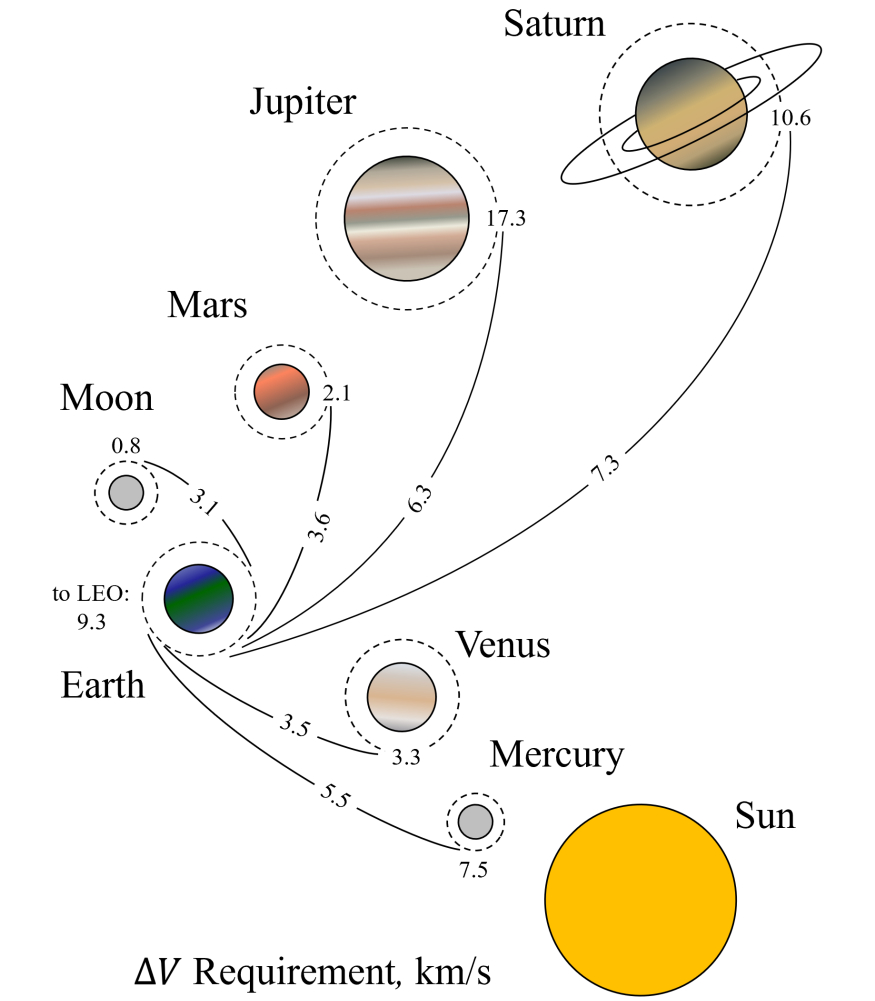

Figure 1.1: The propulsive requirements (i.e. ΔV) for transfers between Earth and various orbital bodies within the solar system.

in the spacecraft. Two important propulsion system metrics were overlooked in this analysis, however: subsystem power and firing time.

Electric propulsion systems use electric power to increase the exit velocity of expelled propellant. While chemical propulsion systems are limited to about 350 s I_{sp}, electric propulsion systems can exceed 10 000 s I_{sp} by using electrical power to accelerate propellant to higher velocities. The downside of electric propulsion is that increasing specific impulse comes at the cost of required electrical power. The required electrical power can be estimated from thruster metrics [11]:

$$P = \frac{T g_0 I_{sp}}{2\eta_T}, \tag{1.4}$$

where P is the propulsive power and η_T is the thruster efficiency. Additionally, if the thruster is operated at a constant setpoint, then the thruster firing time, t_{fire}, is by definition:

$$t_{fire} = \frac{m_{prop}}{\dot{m}}, \tag{1.5}$$

Equations 1.2, 1.3, 1.4, and 1.5 can be combined to determine the firing time as a function of mission requirements and propulsion system metrics:

$$t_{fire} = \frac{m_{sc}(g_0 I_{sp})^2}{2P\eta_T}\left[\exp\left(\frac{\Delta V}{g_0 I_{sp}}\right) - 1\right]. \tag{1.6}$$

The required firing time from Equation 1.6 is shown in the bottom of Figure 1.2 for a range of ΔV requirements. The propulsion subsystem power, thrust efficiency, and spacecraft mass were assumed to be 50 W, 50 %, and 10 kg respectively. While it initially appeared that increasing specific impulse was the answer to large ΔV requirements, increasing the specific impulse also increases the required thruster operational time. Achieving long thruster lifetime is crucial for all space missions as a result, due to how costly both mass and power are in space. The cost of launching a payload to low earth orbit (LEO) has only recently dropped below $10,000 per kg thanks to recent innovations by SpaceX [12]. The cost of power on the ISS is roughly $2,000 per kWh, [13] contrasted with the price of electricity in California being orders of magnitude lower at 18 cents per kWh in 2021 [14].

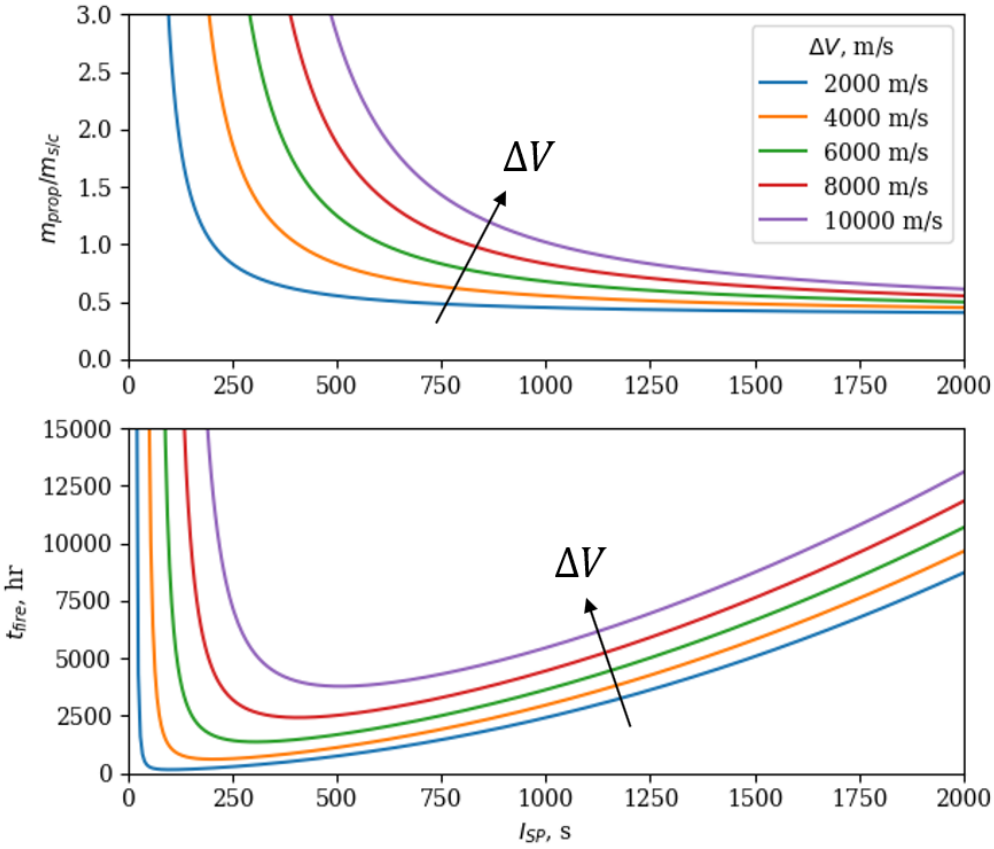

Figure 1.2: Top: the propellant mass fraction required as a function of the specific impulse of the propulsion system and required ΔV for the mission. Bottom: the thruster lifetime required to meet the mission ΔV requirement as a function of thruster specific impulse and ΔV requirement.

1.2 Electrospray

In this section, a very brief review of research contributing to the electrospray field is presented. This history spans from early experimental evidence of electrospraying cones in the 17th century to the standardization of the configuration of the porous electrospray emitter within the past few years.

The earliest known experimental evidence of the electrospray phenomenon dates back to 1600 in Gilbert's *De Magnete*. Gilbert experimented with the effect that a piece of amber, when rubbed, has on nearby materials. He observed a droplet of water deforming into a cone when charged amber was placed nearby, as translated by S.P. Thompson [15]:

> *Indeed it plainly does draw the body itself in the case of a spherical drop of water standing on a dry surface; for a piece of amber applied to it at a suitable distance pulls the nearest parts out of their position and draws it up into a cone; otherwise, if it were drawn by means of the air rushing along, the whole drop would have moved.*

Lord Rayliegh was also concerned with the behavior of water droplets in the presence of an electric field. In 1882, he developed an expression for the maximum charge that a liquid droplet can sustain before it disintegrates [16]. The expression can be understood quite simply by equilizing the outward-pointing electric pressure from a point charge at the center of the droplet with the inward-pointing capillary pressure, or Young-Laplace pressure:

$$P_E = P_\gamma, \tag{1.7}$$

$$P_E = \frac{1}{2}\varepsilon_0 E^2 = \frac{1}{2}\varepsilon_0 \left(\frac{Q}{4\pi\varepsilon_0 R^2}\right), \tag{1.8}$$

$$P_\gamma = \frac{2\gamma}{R}, \tag{1.9}$$

where P_E is electric or Maxwell pressure, P_γ is capillary or Young-Laplace pressure, ε_0 is the permittivity of free space, Q is the charge of the droplet, R is the radius of the droplet, and γ is the surface tension coefficient of the liquid. Simplification of this equality reveals the charge limit of a droplet:

$$Q^2 = 64\pi^2\gamma R^3\varepsilon_0. \tag{1.10}$$

This limit is now known as the Rayligh limit. Rayliegh predicted that a charged droplet would produce fine jets at opposite ends of the droplet before reaching this limit. This is essentially the same as the electrospray process and reveals the simple analytical methods that can be used to understand the electrospray phenomenon.

In 1914, Zeleny used a glass capillary to flow liquid into a region with a strong electric field and described the behavior of the liquid [17]. He described, in detail, the operating modes of electrospray devices as a function of flow rate and electric field. 50 years later, Taylor derived the angle of the characteristic cone shape that forms when a meniscus deforms under the influence of an electric field [18]. Taylor derived the cone shape by treating it as an isopotential surface, but similarly to Rayliegh's analysis of charged droplets in 1882, the result can be understood easily by equilization of capillary and electric pressures along the surface of the meniscus.

$$E_\theta \approx Ar^{\nu-1}\sin\theta P'_\nu(\cos\theta), \tag{1.11}$$

where E_θ is the electric field perpendicular to the surface of a cone from Jackson [19]. As the capillary pressure scales with $r^{-1/2}$ for a cone, the electric pressure must also scale with $r^{-1/2}$. To enforce this r-dependency, the half angle of the cone must be 49.3°, which is now known as the Taylor cone angle. Experimental measurements by Taylor in his 1964 paper show incredible agreement with his analytical prediction. Further validation of the Taylor angle are shown in this manuscript [20, 21].

Various researchers developed electrospray emitters for use as space propulsion devices in the 1960s and early 1970s using doped glycerol as a propellant [22, 23, 24, 25, 26]. Unfortunately, the electrospray thruster (or colloid thruster, a term many researchers preferred) were largely abandoned in the early 1970s [27]. By this time, relatively mature electrospray thrusters seem to have been produced, but the viability of the technology was hindered by the performance of glycerol-based propellants.

The development of room-temperature ionic liquids (RTILs or ILs) led to a resurgence in the popularity of electrospray thrusters a few decades later. Research in ILs increased rapidly in the late 1980s and early 1990s and scientists and engineers considered how they could be used in a variety of fields [28]. Notably, the development of water-stable ILs in 1992 using the 1-ethyl-3-methylimidazolium (EMI) cation piqued the interest of electric propulsion researchers [29]. Ionic liquids were advantageous to doped glycerol propellants because of their negligible vapor pressure and high conductivity. Their high conductivity enabled stable operation at lower flow rates, leading to higher specific charge of emitted particles; in turn, operating voltage could be significantly reduced in order to achieve high specific impulse operation. Gamero and Hruby, at Busek, used the ionic liquid EMI-Im to develop a capillary electrospray thruster in 2001 [30]. Lozano and Martinez-Sanchez shortly afterwards, at MIT, developed a ionic liquid ion source (ILIS) thruster using the ionic liquid EMI-BF4 which emitted pure ions from the charged meniscus, maximizing the specific charge of emitted species from the thruster [31, 32]. Since then, in 2015 the Busek-JPL developed capillary electrospray thruster operated in space for over 4000 hours as part of the LISA-Pathfinder mission, establishing electrospray thrusters as a flight-qualified technology [5]. Porous electrospray thrusters have emerged as the configuration of choice for achieving ion emission or generally high specific charge emission, due to the flow restriction they provide, ease of manufacture, and natural multiplexing that can occur at emission surfaces. The configuration of porous electrospray thrusters has converged to an emitter-interface-reservoir design, as investigated by Courtney and Shea in 2015 [2]. This configuration has since been used across the globe for developing porous electrospray thrusters [33, 34, 35, 36].

1.3 This Dissertation

As described in the previous sections, much of the electrospray propulsion industry focuses on porous emitters to achieve high specific impulse operation. Most of the academic and industry research is focused on emission (e.g. droplet vs ion mode) and plume (e.g. ion fragmentation) physics. There is a significant gap in understanding how porous flow in electrospray thrusters influences their operation. In particular, little is known about the self assembly of emission sites

on a porous emitter, or the transient flow supporting emission sites. These questions are important both in the context of predicting and understanding emitter performance, as well as in the context of extending device lifetime. As discussed in this chapter, device lifetime becomes increasingly important as specific impulse increases.

The objective of this research is to determine the dominant mechanisms of porous flow for high-ISP thruster performance, operation, and lifetime. Three key features of porous flow that are necessary to understand for porous electrospray emitters are the steady flow, multiplexing flow, and transient flow. My hypothesis is that porous flow and emission site electrohydrodynamics can be used to describe porous electrospray emission for the aspects described above. My approach for investigating this hypothesis is to develop and validate models to describe porous flow as relevant to electrospray emission. Specifically these models are being developed to describe transient flow in electrospray devices and emission site multiplexing. Finally, development of a porous wedge electrospray emitter provides the opportunity to validate models with experimental results for the aspects described.

The outline of the dissertation is as follows. In chapter 1, the basics of space propulsion were introduced, followed by a brief history of electrospray thruster research up to the present day. This chapter concludes with the goals of this research. Chapter 2 describes the model for multiplexed electrospray emission on a porous wedge. This chapter describes how flow in a porous medium separates as it approaches each emission site and how the electric field from each emission site causes this flow. This chapter was adapted from Wright and Wirz, 2021 [1]. Chapter 3 introduces a model for transient flow in porous emitters. This model shows how small changes in the stored propellant in exposed pores may lead to the transient response of porous eletrospray thrusters due to the radius of a meniscus changing with pressure. This chapter has been adapted from a manuscript under consideration with *Transport in Porous Media* [37]. Chapters 4 and 5 describe the effort to develop a porous tungsten electrospray thruster. A pillar-style electrospray emitter was developed and the porous material was characterized for presentation at the AIAA Power and Energy Forum [38]; chapter 4 is a modified version of the manuscript from this presentation. As described in chapter 5, a wedge-shaped electrospray was subsequently developed and characterized; results

from this effort were presented at the International Electric Propulsion Conference (IEPC) [39]. Significant further development and characterization of the wedge electrospray emitter are shown in this chapter, beyond what was presented at the IEPC. Chapter 6 uses the models, experiments, and results from Chapters 2 through 5 to develop and analytical model to describe steady and transient fluid flow and emission from the porous wedge electrospray emitter. The model combines steady and transient flow models, an understanding of the emission surface morphology, and established electrospray emission models to describe porous electrospray emission behavior. Experimental results from the porous tungsten wedge electrospray are used as validation for the model. Finally, chapter 7 summarizes the major conclusions of the research and shows avenues for future work to build on the research presented in this dissertation.

CHAPTER 2

Multiplexed Electrospray Emission

Although electrospray devices traditionally use a capillary for fluid flow and electric field concentration, a sharpened porous medium can be used instead for these purposes. In porous media electrospray emitters, a working fluid flows through the porous medium to an emission surface, where the local electric field and fluid pressure allow for electrostatic emission of droplets or ions. Porous emitters have been used for aerosol generation,[40] mass spectrometry, [41] and electric space propulsion in both pointed tip[42, 43] (including cones [44, 45] and pyramids[46, 47, 34]) and wedge configurations. [2, 48, 49, 50, 51, 52] A typical porous electrospray apparatus consists of an emitter substrate with a small characteristic pore size, coupled with a porous reservoir with a larger characteristic pore size. The small pore size of the emitter, compared to that of the reservoir, ensures that the emitter substrate stays wetted as liquid is sprayed from the system; liquid depletes from the reservoir to replace liquid in the emitter. An extractor electrode in close proximity to the emitter provides a strong electric field at the emitter when the emitter is charged, producing droplet and/or ion emission from the charged meniscus. [33]

A common approach to increasing the output of an electrospray device is to create many emission sites in parallel, a concept known as multiplexing. A straightforward approach to multiplexing is through manufacturing many individual features which will produce emission sites. Such a device requires high manufacturing consistency to produce uniform emission among sites. On the other hand, a wedge configuration for porous electrospray emitters allows for hundreds or thousands of discrete emission sites on a single emitter feature.[2, 50] A sharp edge creates a region where the electric field is strong and nearly uniform. Along this edge, emission sites form due to the combined effects of the subsurface flow and local electric field. Rather than manufacturing individual features for each emission site, the wedge configuration allows for natural electrospray

multiplexing through the interactions between emission sites. Due to these site to site interactions, the total output from a porous wedge electrospray emitter is reflective of both the emission site characteristics and site spacing. Experimental results from cone-shaped porous emitters have shown that multiple emission sites can form in a single high electric field region as voltage is increased.[53] Experimental observations of wedge-shaped emitters confirm emission from discrete sites along the sharp edge of the wedge. [54, 55] Understanding the behavior of individual emission sites is critical to accurate estimation of device performance and lifetime.[56]

Multiple approaches exist for reducing the detrimental effects associated with the emission at the ends of the wedge, or 'edge effects.'[48] The increased sharpness at the end of the wedge increases the electric field in this region. One approach for mitigating edge effects is replacing the linear wedge with an annular wedge to eliminate the ends of the wedge segment;[48] another approach is to widen the extractor aperture at the ends in order to reduce the electric field in these regions.[52] A properly designed emitter using any of these approaches will mitigate off-nominal emission at wedge endpoints such that the majority of emission is characterized by emission in the uniform field region. Understanding the emission behavior in this uniform field region is crucial to understanding the behavior of the porous wedge electrospray device.

To investigate behavior and properties related to emission site spacing, this study develops a simplified model by considering the porous flow to each emission site. The applied electric field creates a pressure minimum at each emission site. The transition of the uniform upstream flow to individual flow cells at the emission surface causes a saddle point in the pressure at the stagnation points between emission sites. The coupling of the local electric field produced by each emission site with the fluid pressure at the surface of the porous medium causes the emission site spacing to change with applied electric field and reservoir pressure. A diagram of emission sites on the wedge is shown in Fig. 2.1c, based on figurative diagrams[50] and experimental results.[55, 54, 53] Emission sites are assumed to lie on the midplane of the emitter throughout; plume measurements indicate that emission sites

The objective of this research is to investigate the electric field and subsurface flow phenomena responsible for emission site current and spacing on the surface of a linear edge porous electro-

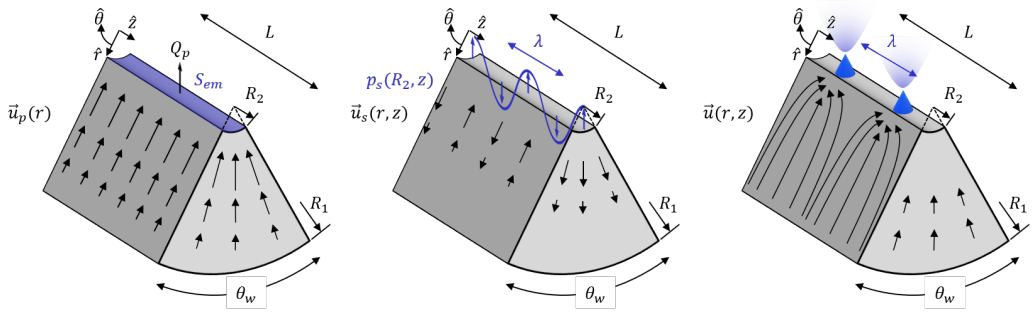

(a) (b) (c)

Figure 2.1: The wedge emitter geometry, with the a) primary flow, b) secondary flow, and c) combined flow.

spray emitter. The uniform region of the wedge emitter, i.e. away from the ends, is considered for this investigation. The analysis is performed for low Reynolds number porous flow of superposed primary and secondary flows. The electric field caused by neighboring sites is simplified to produce analytical relations for the effect of these sites on fluid pressure in the porous medium. Experimental results from Courtney and Shea[2] are used to validate analytical results.

2.1 Porous Flow

For flow in porous media, both Darcy's law, $\vec{u} = -\frac{k}{\mu}\nabla P$, and continuity, $\nabla \cdot \vec{u} = 0$, are applicable. $\vec{u}$ is the fluid velocity, P is pressure, k is the porous permeability, and μ is the fluid viscosity. This form of Darcy's law is valid for low Reynolds number, i.e. $Re < 1$, where inertial effects can be neglected.[57] The Reynolds number is described as $Re = \rho u d/\mu$, where ρ is the fluid density, and d is the particle size in the porous medium. [57] Darcy's law and continuity are combined to show that the Laplacian of pressure is zero for low Re porous flows: $\nabla^2 P = 0$. As such, the flow can be decomposed into a primary and secondary flow for ease of solving and the solutions can be superposed into a new solution. I consider a primary flow that describes the net flow from the base of the emitter and a secondary flow that describes the local flow variation into discrete flow cells at each emission site, as shown in Fig. 2.1. For clarity in describing each flow, fluid velocity and pressure are denoted by a p-subscript for the primary flow and by an s-subscript for the secondary

flow.

The geometry for the flow is a porous wedge of a specified angle, θ_w, with an upstream radius, R_1, and a downstream radius, R_2. The upstream radius is defined by the normal distance from the base of the wedge to the virtual apex of the wedge. The downstream radius is assumed as the distance from the virtual apex of the wedge to the midplane surface of the emission surface, as shown in Fig. 2.2. Assuming the downstream boundary condition in this way pulls the low pressure boundary condition closer to the virtual apex of the wedge and spreads the condition over a larger area. As a result, the fluid flow of the modelled emitter departs from that of a physical device near the emission site. The exposed surface of the physical device intersects with the assumed fluid flow domain for $R_2 < r < R_{2+}$, where R_{2+} is the distance from the virtual apex of the wedge to where the convex emission surface intersects with the sides of the wedge at $\theta = \pm\theta_w/2$. In this region of a physical device, the flow is not necessarily axisymmetric. While assuming a convex surface at R_2 approximates the flow to the emission surface, it is likely an underestimate of the hydraulic resistance to the emission site for the above reasons. For an emitter wedge half-angle of 30°, R_2 is equal to the radius of curvature of the emission surface, R_{emit}, and R_{2+} is twice R_2. The porous medium is assumed to be isotropic and uniformly characterized by its permeability.

The electric field is also decomposed into both primary and secondary electric fields, using the same subscript notation as previously described for the flow field. The primary electric field is produced by the extraction electrode on the surface of the emitter when no emission sites are present. The secondary electric field is produced by the charge concentration near each emission site. The medium for the electrostatic region is vacuum and the space charge is neglected outside of the plume and cone at each emission site, so the electric potential, ϕ, in the region is described by $\nabla^2\phi = 0$. Because the electric potential is described by Laplace's equation, superposition of solutions in this region is valid.

The pressure boundary conditions for flow through the emitter are the emission pressure at the emission sites on the tip of the wedge and the Laplace pressure provided by the meniscus in the reservoir. Both of these pressure conditions are below the ambient pressure, causing the fluid throughout the porous medium to be below ambient pressure. For the working fluid to leave the

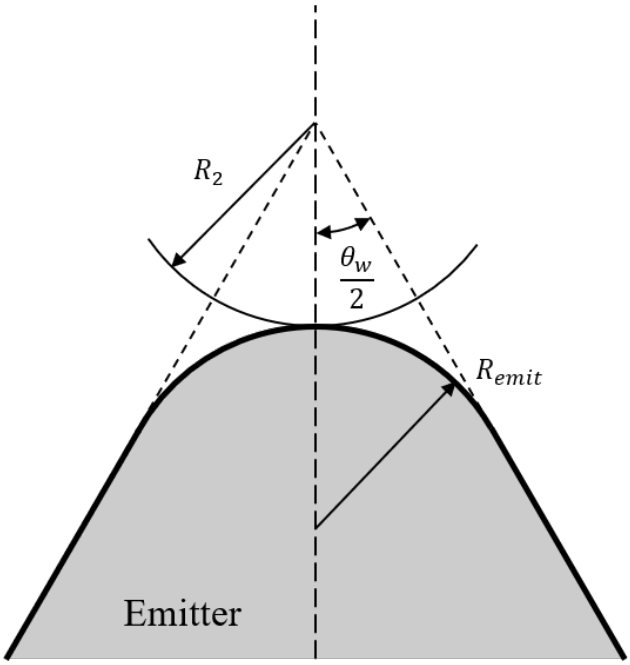

Figure 2.2: The convex emission surface with a radius of R_{emit} is assumed as a concave surface with radius R_2 to maintain axisymmetry in the porous flow domain.

porous medium, the electric pressure at the surface must exceed the Laplace pressure provided by the reservoir. The emission surface represents the highest electric field region of the emitter, so it is expected that the electric field is insufficient to cause the working fluid from escaping the porous emitter away from the emission surface. As a result, there is no fluid velocity in the normal direction to exposed porous surfaces, such as the limits of the wedge at $\theta = \pm\theta_w/2$ where $u_\theta = 0$. Also, because there is a free meniscus at $\theta = \pm\theta_w/2$, the interface is considered to be a free-slip boundary condition. The result from these two conditions is that there is no flow in the θ-direction and no dependence on θ for flow in the r- and z-directions, so the dependence on the flow on θ can be ignored.

The primary flow describes the net flow from the porous reservoir to the emission site. The flow rate through the emitter, Q_p, is defined by the single emission site flow rate, Q_{site}, the spacing between sites, λ, and the emitter length, L, as follows:

$$Q_p = \frac{LQ_{site}}{\lambda}. \tag{2.1}$$

There is no pressure gradient in the z- or θ-directions for the primary flow, so $u_{p,z} = u_{p,\theta} = 0$ and the flow velocity in the r-direction is described by the flow rate and cross-sectional area, $A(r)$:

$$u_{p,r} = -\frac{Q_p}{A(r)} = -\frac{Q_{site}}{\theta_w r \lambda}. \tag{2.2}$$

Applying Darcy's law to flow in the radial direction determines the pressure field for the primary flow:

$$P_p(r) = \frac{\mu Q_{site}}{k\theta_w \lambda} \ln(r) + C_1, \tag{2.3}$$

where C_1 is a constant.

The secondary flow describes the spatially periodic separation of the net flow into individual emission sites, assuming a regular variation of the pressure in the z-direction. This condition causes flow in the r- and z-directions localized to the emission surface while assuming uniformity in the θ-direction. Pressure in the secondary flow is solved for by assuming a separation of variables solution with components $M(r)$ and $N(z)$ for the axisymmetric form of $\nabla^2 P = 0$. The equation is solved by finding the solution to the eigenvalue problem:

$$\frac{\frac{1}{r}\frac{\partial}{\partial r}\left(r\frac{\partial M}{\partial r}\right)}{M} = -\frac{\frac{\partial^2 N}{\partial z^2}}{N} = \alpha^2, \tag{2.4}$$

where α is the eigenvalue. The solutions to these equations are the zeroth-order modified Bessel functions of the first and second kind for $M(r)$ and an oscillatory solution for $N(z)$:

$$P_s(r,z) = \left[C_2 K_0(\alpha r) + C_3 I_0(\alpha r)\right] e^{i\alpha z}, \tag{2.5}$$

where I_0 and K_0 are the modified Bessel Functions of the first and second kind, respectively, and C_2 and C_3 are constant coefficients. The wavelength for the pressure oscillation is defined by the emission site separation distance, $\lambda = 2\pi/\alpha$. To simplify Eq. 2.5, the emission site spacing is assumed to be small compared to the base of the wedge, i.e. $\lambda \ll 2\pi R_1$, such that the pressure variation within the wedge due to the I_0 term is negligible. With these assumptions, the secondary flow pressure solution can be alternatively expressed as:

$$P_s(r,z) = C_2 K_0\left(\frac{2\pi r}{\lambda}\right) e^{\frac{2\pi i z}{\lambda}}. \tag{2.6}$$

For cases where a small λ assumption cannot be made, the pressure due to the secondary flow is derived in the Appendix.

As shown in Fig. 2.1, the primary and secondary flows are coupled such that stagnation points exists at the midpoint between each emission site. At these points the primary and secondary flows are equal and opposite. At the stagnation point, $(r,z) = (R_2, n\lambda)$ where n is an integer, the pressure gradients in the r-direction for the primary and secondary flows are equal and opposite:

$$\frac{\mathrm{d}}{\mathrm{d}r}P_p(R_2) = -\frac{\partial}{\partial r}P_s(R_2, n\lambda). \tag{2.7}$$

Substituting Eqs. 2.3 and 2.6 into Eq. 2.7 and simplifying yields:

$$\frac{\mu Q_{site}}{k\theta_w R_2 \lambda} = \frac{2\pi C_2}{\lambda} K_1\left(\frac{2\pi R_2}{\lambda}\right). \tag{2.8}$$

C_2 is used to enforce the stagnation point when superposing the primary and secondary flows:

$$C_2 = \frac{\mu Q_{site}}{2\pi k\theta_w R_2} \frac{1}{K_1\left(\frac{2\pi R_2}{\lambda}\right)}. \tag{2.9}$$

The combined pressure solution is simply a superposition of the primary and secondary flows:

$$P(r,z) = \frac{\mu Q_{site}}{k\theta_w}\left(\frac{1}{\lambda}\ln(r) + \frac{1}{2\pi R_2}\frac{K_0\left(\frac{2\pi r}{\lambda}\right)}{K_1\left(\frac{2\pi R_2}{\lambda}\right)} e^{\frac{2\pi i z}{\lambda}}\right) + C_1. \tag{2.10}$$

2.2 Applying Boundary Conditions

The total current output of the emitter is obtained by equating the applied pressure difference to the decrease in pressure associated with the flow through porous medium. The applied pressure difference, from the base of the wedge to the emission surface, is from $r = R_1$ to $(r,z) = (R_2, (2n+1)\lambda/2)$.

The effect of the secondary flow is negligible for $r >> R_2$, so the pressure at the wedge base is uniform in the z-direction and approximated as the reservoir pressure. The pressure drop due to flow through the porous medium, ΔP_{por}, is solved as:

$$\Delta P_{por} = \frac{\mu Q_{site}}{k\theta_w}\left(\frac{1}{\lambda}\ln\left(\frac{R_2}{R_1}\right) - \frac{1}{2\pi R_2}\frac{K_0\left(\frac{2\pi R_2}{\lambda}\right)}{K_1\left(\frac{2\pi R_2}{\lambda}\right)}\right). \tag{2.11}$$

The right side of Eq. 2.11 represents the single flow cell hydraulic resistance multiplied by the single flow cell flow rate.

The reservoir pressure is approximated by the Laplace pressure, or capillary pressure, from a meniscus at a fully-wetted pore upstream in the reservoir[57, 58] and the emission surface pressure is approximated by the Maxwell pressure supplied by the magnitude of the local primary extraction electric field, E_p.[59, 60, 44] The applied pressure difference from the fluid reservoir to emission site, ΔP_{app}, is:

$$\Delta P_{app} = \frac{4\gamma}{D_{res}} - \frac{1}{2}\varepsilon_0 E_p^2, \tag{2.12}$$

where γ is the fluid surface tension coefficient, D_{res} is the characteristic reservoir pore size, and ε_0 is the permittivity of free space. Furthermore, the individual emission site flow rate is replaced by the individual emission site current, I_{site}, the fluid density, ρ, and the mean specific charge of emission products, q/m:

$$Q_{site} = \frac{I_{site}}{\rho}\frac{m}{q}. \tag{2.13}$$

Applying these conditions and setting the porous flow pressure drop to be equal to the applied pressure difference, an expression for the pressure balance for a linear edge electrospray emitter is developed:

$$\frac{\mu I_{site}}{k\rho\theta_w}\frac{m}{q}\left(\frac{1}{\lambda}\ln\left(\frac{R_2}{R_1}\right) - \frac{1}{2\pi R_2}\frac{K_0\left(\frac{2\pi R_2}{\lambda}\right)}{K_1\left(\frac{2\pi R_2}{\lambda}\right)}\right) = \frac{4\gamma}{D_{res}} - \frac{1}{2}\varepsilon_0 E_p^2. \tag{2.14}$$

To simplify Eq. 2.14, all λ-dependent terms are combined into a single function, F:

$$F(\lambda, R_1, R_2) = \frac{1}{\lambda}\ln\left(\frac{R_2}{R_1}\right) + \frac{1}{2\pi R_2}\frac{K_0\left(\frac{2\pi R_2}{\lambda}\right)}{K_1\left(\frac{2\pi R_2}{\lambda}\right)}. \tag{2.15}$$

F can be expressed as the sum of its terms:

$$F = F_1 + F_2 : \tag{2.16}$$

$$F_1 = \frac{1}{\lambda}\ln\left(\frac{R_2}{R_1}\right), \tag{2.17}$$

$$F_2 = \frac{1}{2\pi R_2} \frac{K_0\left(\frac{2\pi R_2}{\lambda}\right)}{K_1\left(\frac{2\pi R_2}{\lambda}\right)}. \tag{2.18}$$

F, F_1, and F_2 are plotted with respect to the site spacing, λ, in Fig. 2.3. For the geometry from Courtney and Shea,[2] F_1 and F_2 are equal for $\lambda = 2.56\,\text{mm}$. For $\lambda \ll 2.56\,\text{mm}$, F_1 dominates F, so F_2 can be ignored. For the case where many emission sites exist over the length of the emitter, L, i.e. $\lambda \ll L$, F can be approximated as F_1, and Eq. 2.14 can be simplified as:

$$\frac{\mu I_{site}}{k\rho\theta_w\lambda}\frac{m}{q}\ln\left(\frac{R_2}{R_1}\right) \approx \frac{4\gamma}{D_{res}} - \frac{1}{2}\varepsilon_0 E_p^2. \tag{2.19}$$

The small site spacing approximation is possible due to the argument of the Bessel terms in Eq. 2.18 being below 1, i.e. for the condition $\lambda \leq 2\pi R_2 \approx 125\,\mu\text{m}$.

The ratio of total emitter current, I_{total}, to the emitter length, L, is equal to the ratio of the single emission site current to the emission site spacing:

$$\frac{I_{total}}{L} = \frac{I_{site}}{\lambda}. \tag{2.20}$$

Equation 2.20 allows Eq. 2.14 to be solved for the total current from the electrospray device:

$$I_{total} \approx \frac{\rho k\theta_w L}{\mu \ln\left(\frac{R_2}{R_1}\right)}\frac{q}{m}\left(\frac{4\gamma}{D_{res}} - \frac{1}{2}\varepsilon_0 E_p^2\right). \tag{2.21}$$

For a given working fluid and emitter, all parameters contributing to I_{total} in Eq. 2.21 are effectively constant except for specific charge and electric field.

2.3 Electrostatic Region

Similarly to the porous flow solutions, the electric field is separated into primary and secondary electric fields. The primary electric field represents the electric field due to the voltage difference between emitter and extractor electrodes, while the secondary field describes the effect of charge accumulation due to each emission site.

The electric field applied to the emitter reduces the pressure at the emission surface, driving flow through the porous medium. In this effort, I use the electric field in the absence of Taylor

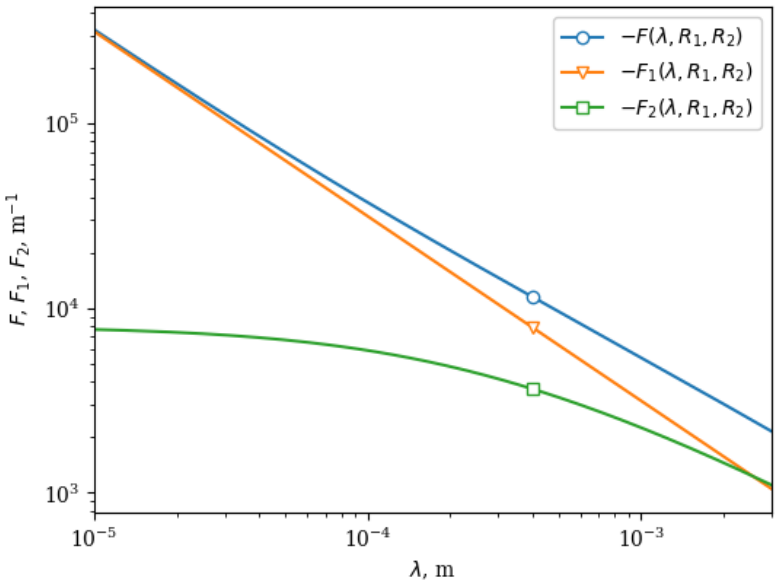

Figure 2.3: F and its terms as a function of emission site spacing for $R_1 = 465\,\mu\text{m}$ and $R_2 = 20\,\mu\text{m}$.

cones to estimate the pressure at the emission surface. Even though the electric field on the cone increases drastically towards the apex, the curvature of the meniscus increases in response.[18, 61] Because the electrostatic and surface tensions effects are in equilibrium, I expect that the pressure difference due to varying electric field along the meniscus can be neglected. Thus, the applied electric field provides a reasonable basis for estimating the pressure at the emission site.[60]

Recombining the primary and secondary solutions for the electric field introduces challenges with regard to how boundary conditions should be maintained. Addition of the two electric field solutions superposes the electric potential from each solution throughout the electrostatic region. Near to the emission sites, the electric field from the cone causes the isopotential surface at the extraction voltage to extend past the emission surface.

Because the emission site is of the same order as the emission site to extractor electrode distance (175 µm) over the operating conditions of the emitter, adding the secondary electric field to the primary field overestimates the voltage on the emitter surface and extractor electrode to approximately the same margin. Results for the emission site spacing as a function of voltage and reservoir pores size are shown in Fig. 2.9. Although approximating the electric fields in the man-

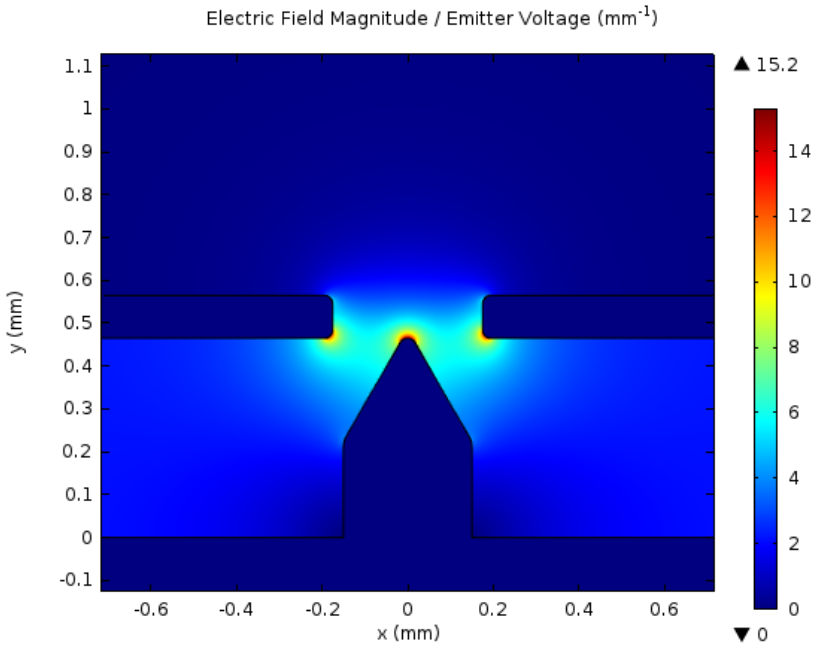

Figure 2.4: Simulation of the normalized electric field produced by the wedge emitter used to estimate the primary electric field.

ner described may not maintain the correct potential at each electrode, the important quality to maintain is the voltage difference between the emitter and extractor electrodes. By maintaining the extraction voltage in this way, the superposition of primary and secondary electric fields serves as a useful way to estimate the electric field from emission sites while maintaining the electric field produced by the extractor electrode.

The primary electric field is linearly related to the emitter voltage by a parameter C_E, which is a function of the emitter and extractor electrode geometry:[44]

$$E_p = C_E V_{emit}. \tag{2.22}$$

C_E has been determined with an electrostatic solver for the geometry defined in Courtney and Shea,[2] as shown in Fig. 2.4, yielding a value of $15.3\,\mathrm{mm}^{-1}$ for a uniform emitter tip radius of $20\,\mu\mathrm{m}$.

The startup voltage condition, V_{start}, can be found by setting $\Delta P_{app} = 0$, and solving Eqs. 2.12

and 2.22 for emitter voltage:

$$V_{start} = \frac{1}{C_E}\sqrt{\frac{8\gamma}{\varepsilon_0 D_{res}}}. \tag{2.23}$$

To find the emission site spacing and single emission site current, the coupled effects of the secondary electric field and secondary flow solution must be considered. To ensure a valid secondary solution, there must be no pressure difference across the meniscus, i.e. the Maxwell pressure and static pressure must be in equilibrium at the interface. For ease of calculation, the pressures are equalized at the stagnation point between adjacent emission sites. The secondary electric field is approximated by a point charge representing the charge within each Taylor cone and a semi-infinite line of charge representing each plume of charged particles emitted from the Taylor cone at each emission site. At each stagnation point, only the two nearest-neighbor emission sites are considered when estimating the electric field.

The linear charge density of the simplified plume, σ_l, is equal to the ratio of the emitted current to particle exit velocity, c. The exit velocity can be estimated through conservation of energy:

$$\sigma_l = \frac{I_{site}}{c} = I_{site}\sqrt{\frac{m}{2V_{emit}q}}, \tag{2.24}$$

where V_{emit} is the emitter voltage. The electric field imposed by two plumes on the stagnation point between two emission sites, $E_{s,1}$, is twice the electric field imposed in the upstream direction by a single semi-infinite line of charge:

$$E_{s,1}(R_2, n\lambda) = \frac{2\sigma_l}{4\pi\varepsilon_0\left(\frac{\lambda}{2}\right)} = \frac{I_{site}}{\pi\varepsilon_0\lambda}\sqrt{\frac{m}{2V_{emit}q}}. \tag{2.25}$$

The electric field produced by each Taylor cone is simplified to a point charge at its apex. I assume that the size of the Taylor cone scales with a characteristic length, which is assumed to be the radius of curvature of the meniscus required to compensate for the negative pressure applied by the primary electric field. Thus, the normal distance from the tip of the wedge to the assumed point charge is estimated to be equal to the characteristic length of the cone.

$$a = \frac{4\gamma}{\varepsilon_0 E_p^2}. \tag{2.26}$$

The meniscus formed by a Taylor cone with negative backpressure has been determined to have a concave cross-section[62, 63] that departs from the 49.3° half-angle cone determined by Taylor.[18]

The total charge and shape of a charged meniscus at a negative-pressure emission site are an ongoing research topic,[64] so for the sake of simplicity and the purpose of this investigation, the specific geometry of the emission site is ignored in favor of a simplified representation of the Taylor cone size.

The connection between fissioning charged droplets and Taylor cones has been previously noted.[65] The Taylor cone is approximated as half of a droplet with radius a undergoing Rayleigh fission. Thus, the charge contained in the Taylor cone, q_{TC}, is approximated as half of the charge required for a droplet to fission by the Rayleigh instability, [16, 66] which is simplified with Eq. 2.26 as:

$$q_{TC} = \frac{1}{2}\sqrt{64\pi^2\varepsilon_0\gamma a^3} = \frac{32\pi\gamma^2}{\varepsilon_0 E_p^3}. \tag{2.27}$$

Experimentally, droplet fission has been observed at 70 to 90% of the Rayleigh limit[67, 68] and the charge of a Taylor cone has been estimated as low as 57% of the Rayleigh limit;[69] for simplicity, emission below the Rayleigh limit is ignored as part of this investigation.

The electric field produced by 2 point charges at adjacent Taylor cones on the stagnation point is determined using Coulomb's law and Eqs. 2.26 and 2.27:

$$\begin{aligned} E_{s,2}(R_2, n\lambda) &= \frac{2aq_{TC}}{4\pi\varepsilon_0}\left(a^2 + \frac{\lambda^2}{4}\right)^{-\frac{3}{2}} \\ &= \frac{64\gamma^3}{\varepsilon_0^3 E_p^5}\left(\left(\frac{4\gamma}{\varepsilon_0 E_p^2}\right)^2 + \frac{\lambda^2}{4}\right)^{-\frac{3}{2}}. \end{aligned} \tag{2.28}$$

The electric field from the cone and from the plume are superposed to determine the Maxwell pressure on the meniscus at the midpoint between emission sites:

$$E_s(R_2, n\lambda) = E_{s,1}(R_2, n\lambda) + E_{s,2}(R_2, n\lambda): \tag{2.29}$$

$$\begin{aligned} E_s(R_2, n\lambda) &= \frac{I_{site}}{\pi\varepsilon_0\lambda}\sqrt{\frac{m}{2V_{emit}q}} \\ &+ \frac{64\gamma^3}{\varepsilon_0^3 E_p^5}\left(\left(\frac{4\gamma}{\varepsilon_0 E_p^2}\right)^2 + \frac{\lambda^2}{4}\right)^{-\frac{3}{2}}. \end{aligned} \tag{2.30}$$

If the height of the Taylor cone is assumed to be much smaller than the distance between neighboring emission sites, then the distance from the apex of the Taylor cone to the stagnation point can be approximated as half the emission site spacing. Results with this approximation are designated in Figs. 2.9 and 2.10 as using the small angle approximation for the secondary electric field. Additionally, the electric field from the plume is assumed to be negligible compared to that from the cone; when operating in vacuum, there is little resistance on emitted particles to cause high charge density in the plume compared to the meniscus of the cone. A quantitative comparison of the electric fields from the cone and plume is presented later in this chapter as further justification of this assumption. With these assumptions, Eq. 2.30 can be simplified as:

$$E_s(R_2, n\lambda) = \frac{64\gamma^3}{\varepsilon_0^3 E_p^5}\left(\frac{\lambda^2}{4}\right)^{-\frac{3}{2}} = \frac{2^9\gamma^3}{\varepsilon_0^3 E_p^5 \lambda^3}, \tag{2.31}$$

which results in a Maxwell pressure of:

$$\Delta P_{s,E} = \frac{1}{2}\varepsilon_0\left(\frac{2^9\gamma^3}{\varepsilon_0^3 E_p^5\lambda^3}\right)^2 = \frac{2^{17}\gamma^6}{\varepsilon_0^5 E_p^{10}\lambda^6}. \tag{2.32}$$

The pressure difference from the emission site to the midpoint between emission sites is determined from Eqs. 2.6 and 2.9 as:

$$\Delta P_{s,u} = \frac{\mu I_{site}}{\pi\rho k\theta_w R_2}\frac{m}{q}\frac{K_0\left(\frac{2\pi R_2}{\lambda}\right)}{K_1\left(\frac{2\pi R_2}{\lambda}\right)}. \tag{2.33}$$

The secondary flow pressure difference and the Maxwell pressure from the secondary electric field are equated to enforce the static equilibrium condition for the full secondary flow and electric field solution:

$$\frac{\mu I_{site}}{\pi\rho k\theta_w R_2}\frac{m}{q}\frac{K_0\left(\frac{2\pi R_2}{\lambda}\right)}{K_1\left(\frac{2\pi R_2}{\lambda}\right)} = \frac{2^{17}\gamma^6}{\varepsilon_0^5 E_p^{10}\lambda^6}, \tag{2.34}$$

which in turn is simplified for I_{site} as:

$$I_{site} = \frac{2^{17}\pi\gamma^6}{\varepsilon_0^5 E_p^{10}\lambda^6}\frac{\rho k\theta_w R_2}{\mu}\frac{q}{m}\frac{K_1\left(\frac{2\pi R_2}{\lambda}\right)}{K_0\left(\frac{2\pi R_2}{\lambda}\right)}. \tag{2.35}$$

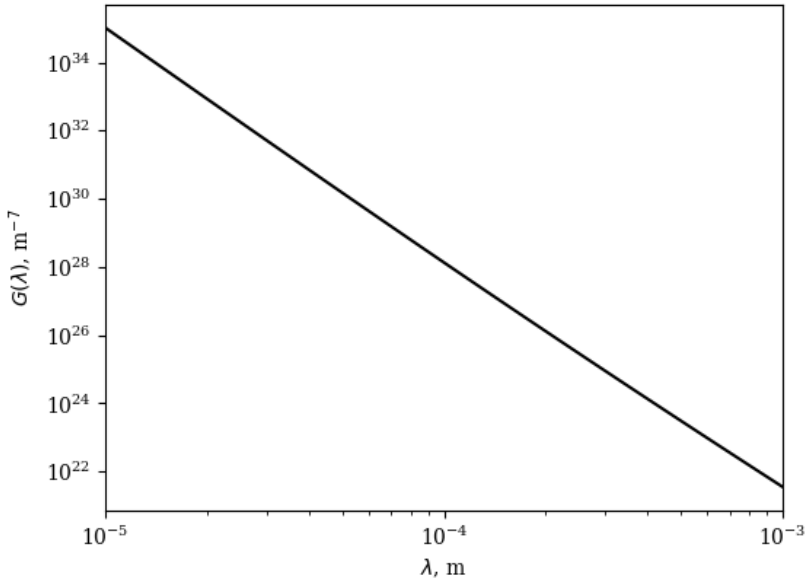

Figure 2.5: $G(\lambda)$, which represents the left side of Eq. 2.36, plotted over the relevant range of λ.

To solve for the emission site spacing as a function of applied electric field, Eq. 2.35 is substituted into Eq. 2.19 and simplified, yielding the following equation:

$$\frac{1}{\lambda^7}\frac{K_1\left(\frac{2\pi R_2}{\lambda}\right)}{K_0\left(\frac{2\pi R_2}{\lambda}\right)} = \frac{\varepsilon_0^5 E_p^{10}}{2^{17}\pi\gamma^6 R_2 \ln\left(\frac{R_2}{R_1}\right)}\left(\frac{4\gamma}{D_{res}} - \frac{1}{2}\varepsilon_0 E_p^2\right). \tag{2.36}$$

The left and right sides of Eq. 2.36 can be expressed as $G(\lambda)$ and $H(E_p, D_{res})$ respectively, with fluid properties and emitter geometry remaining constant. $G(\lambda)$ and $H(E_p, D_{res})$ are plotted in Figs. 2.5 and 2.6, where H is plotted for the pore sizes assumed to represent each reservoir porous media grade. Evaluating Eq. 2.36 over the operating range of the device investigated has shown that small changes to E_p are roughly magnified twofold at nominal operating conditions, although the emission site spacing becomes increasing sensitive to changes in E_p when operated close to the startup voltage.

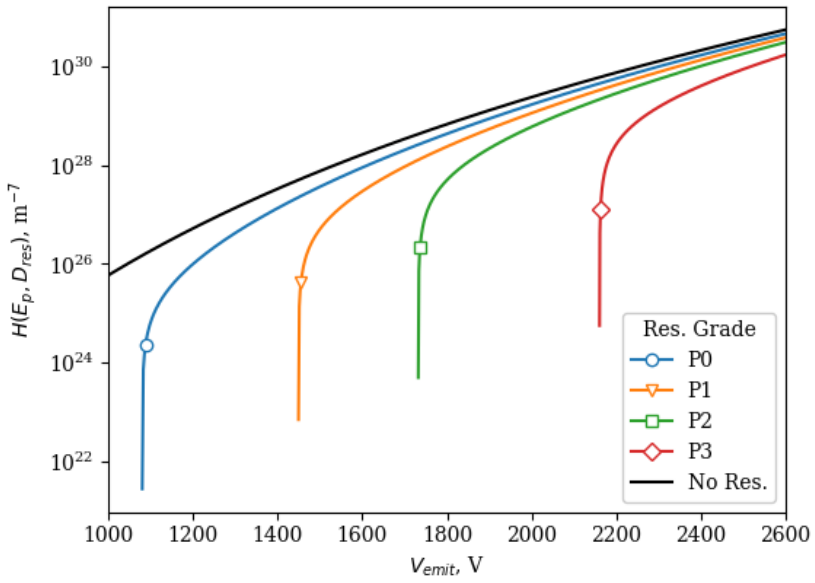

Figure 2.6: $H(E_p, D_{res})$, which represents the right side of Eq. 2.36, plotted over the relevant range of emitter voltage.

2.4 Operational Parameters

The mean specific charge of emitted species is assumed to scale with the specific charge of the Taylor cone from which they originate: [70]

$$\frac{q}{m} \propto \frac{q_{TC}}{\rho a^3} \rightarrow \frac{q}{m} \propto \frac{1}{\rho}\frac{\gamma^2}{E_p^3}\left(\frac{E_p^2}{\gamma}\right)^3 = \frac{E_p^3}{\rho\gamma}. \tag{2.37}$$

An empirical constant A, with units of $C^4s^4m^{-6}kg^{-2}$, is introduced to represent the effects of meniscus shape, relative permittivity, and all other relevant parameters. The specific charge of emitted species, q/m, is then treated as:

$$\frac{q}{m} = A\frac{E_p^3}{\rho\gamma}. \tag{2.38}$$

Courtney and Shea[2] show that the electrospray plume is dimer-dominated with little droplet emission when operating their emitter with a P5-grade reservoir at approximately 20 µA, or 312 C g^{-1} at an emitter voltage of approximately 2200 V. To match the specific charge of a dimer-dominated

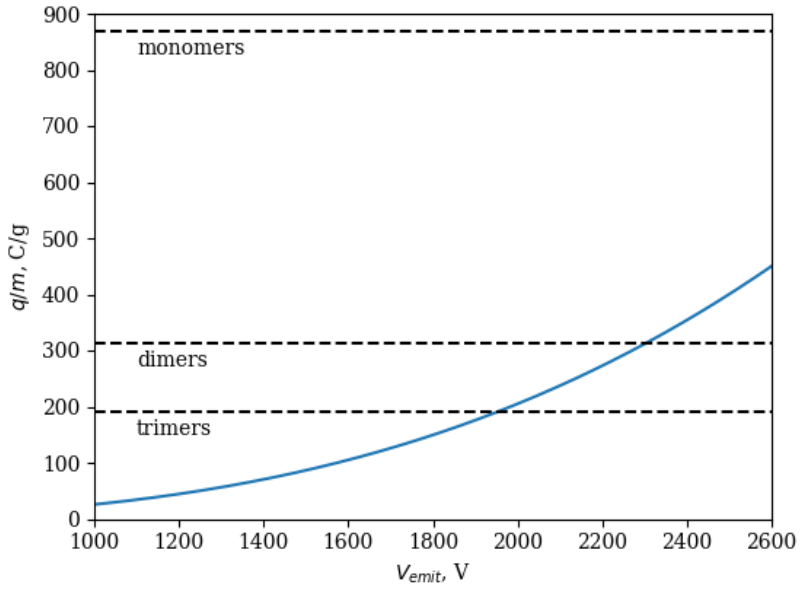

Figure 2.7: The specific charge of emitted species as a function of emitter voltage per Eq. 2.38 [1], with the positive monomer, dimer, and trimer q/m values for reference.

plume at high voltage, a value of $5 \times 10^{-16}\,\mathrm{C^4\,s^4\,m^{-6}\,kg^{-2}}$ is assumed for A. The resulting specific charge for the range of applied emitter voltages is shown in Fig. 2.7. The value assumed for A is likely specific to the emitter configuration and working fluid investigated here. Equation 2.38 is consistent with the conclusion from Courtney and Shea, that the specific charge increases with the negative Laplace pressure of the reservoir.[2] Decreasing the reservoir pore size increases the magnitude of the restorative pressure provided by the reservoir, raising the startup voltage of the device and decreasing the emitted flow rate through Eq. 2.21; the increased electric field required for emission significantly increases the charge concentration on the Taylor cones from which the species are emitted.

A porous reservoir provides a restorative force to the fluid upstream of the emitter. The Laplace pressure provided by the porous reservoir is characterized by the largest wetted pores in the medium. Porous materials designated P0 (160-250 µm), P1 (100-160 µm), P2 (40-100 µm), and P3 (16-40 µm) per ISO 4793 are considered for use as porous reservoirs. Porous materials of grades P0, P1, P2, and P3 are simplified as being characterized by uniform pore diameters of

180, 100, 70, and 45 µm respectively. Within the emitter substrate, formed from P5 (1.0-1.6 µm) porous material, the pressure is above the restorative pressure from the characteristic pore size (-136 kPa), so the pressure in the emitter is not limited by the emitter pore size. For the range of applied voltage in this study, the effect of emitter pore size is ignored.

Typically, porous permeability is determined by measuring the flow rate through a porous sample under an applied pressure difference. In lieu of experimental measurements or manufacturer specifications, the porous permeability of the P5-grade porous frit used as the emitter material is estimated to be 1×10^{-15} m^2 for the predicted total emitter current to match with experimental results. This value has order of magnitude agreement with the porous permeability inferred from manufacturer data for porous frits manufactured by Robu of the same porosity grade.[71] From the manufacturer data for driving pressure and flow rate, rearranging Darcy's law provides a porous permeability of $k = 6 \times 10^{-15}$ m^2 for P5-grade porous material from Robu.

2.5 Results and Discussion

The procedure for modeling the operation of the electrospray emitter is as follows. First, using Eq. 2.21 and the experimental properties of the device (i.e. emitter geometry[2] and propellant properties for EMI-BF4[72]), the total current from the device is determined and shown in Fig. 2.8. The specific charge is determined using Eq. 2.38. The emission site spacing is then obtained analytically with the small angle approximation using Eq. 2.36 and iteratively without the small angle approximation; these results are plotted in Fig. 2.9. Comparison of the exact and small angle approximation (used to determine Eq. 2.31) solutions for emission site spacing show that the two are in approximate agreement. This entire process is repeated for each porous reservoir of interest, using the associated characteristic pore size to determine the Laplace pressure supplied by the reservoir. The Laplace pressure of the reservoir is then ignored to determine the site spacing for the case of an open reservoir, indicated as *No Res.* in Figs. 2.9 and 2.10. Finally, the current of each emission site is determined using Eq. 2.20 and plotted in Fig. 2.10.

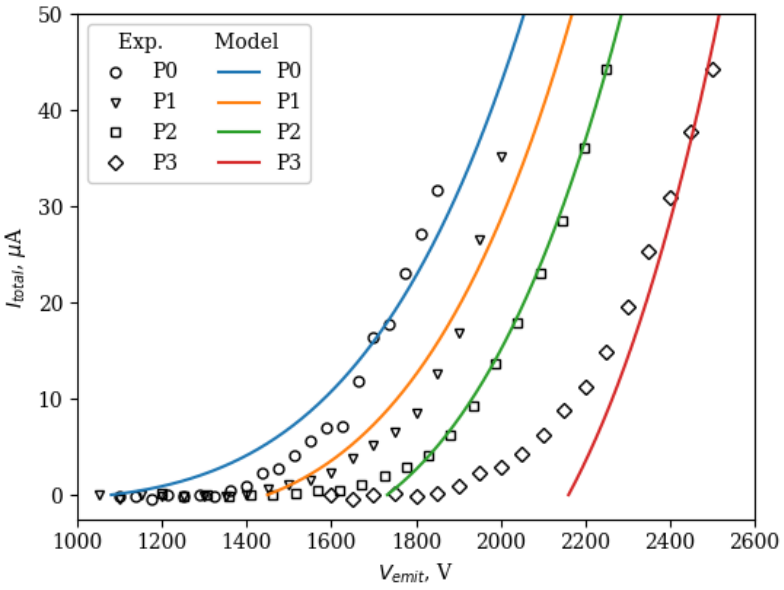

Figure 2.8: The total current produced by the device as a function of emitter voltage and reservoir grade. Results from the presented model are shown with experimental results from Courtney and Shea.[2] Experimental results reproduced from [Appl. Phys. Lett. 107, 103504 (2015); doi: 10.1063/1.4930231], with the permission of AIP Publishing.

While this effort assumes that the system is 2D and homogeneous, the physical device is not so. For example, the emission surface is assumed to be smooth and well-described by a 2D geometry, whereas the fabricated emitter has variation in the sharpness along the length of the emitter. Variations in sharpness will create electric field concentration points that will produce electrospray emission below the predicted startup voltage. Additionally, because porous permeability is a macroscopic property, any anisotropy or nonhomogeneity is ignored. The scale over which porous permeability is determined is much larger than the emission site spacing, so uncharacterized nonhomogeneity may have a strong effect on the fluid flow cells. It is expected that the divergence of predicted results from experimental data at voltages close to the startup voltage is due to simplifications such as these, i.e. the nonhomogeneity of the device that is ignored in the model.

Predicted results for emission site spacing match well with *ex situ* estimation from Courtney et al.[50] of "a few emission sites [...] per 100 µm of length." For total currents above a few µA,

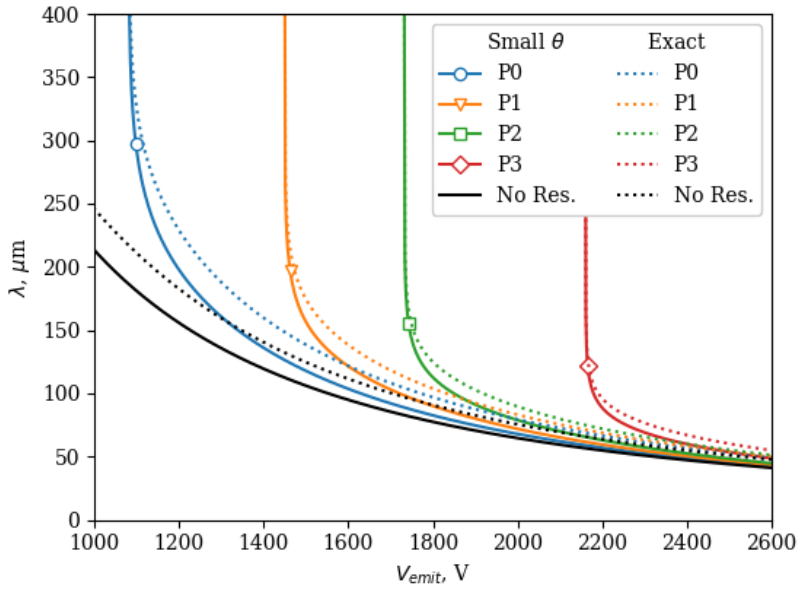

Figure 2.9: The distance between adjacent emission sites with varying reservoir grade and with no reservoir, with and without using the small angle approximation for the secondary electric field to determine Eq. 2.31.

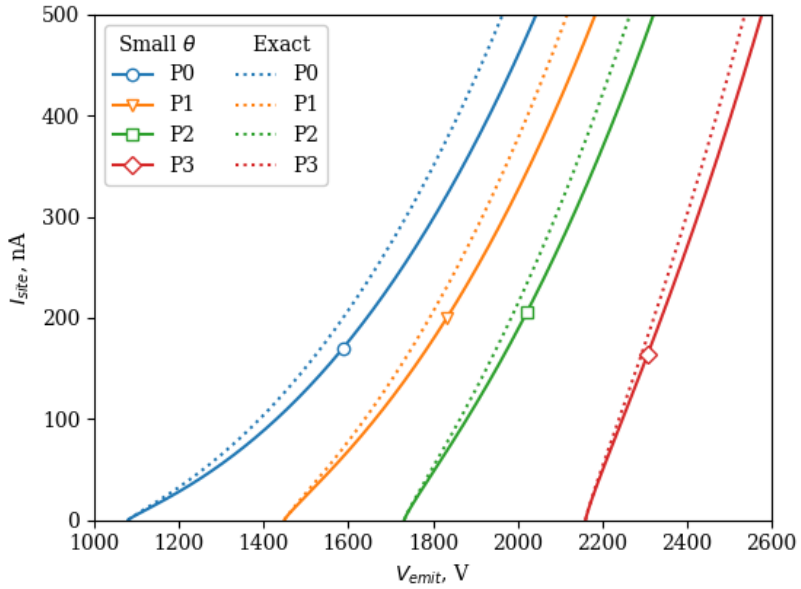

Figure 2.10: The current emitted by each emission site, with and without using the small angle approximation for the secondary electric field to determine Eq. 2.31.

the predicted emission site spacing is below 250 µm, showing that $\lambda \ll 2.56$ mm to neglect F_2 to simplify Eq. 2.14 is a valid assumption.

After determining the site spacing and individual emission site current, the contributions to the secondary electric field from the plume and cone were calculated and shown in Fig. 2.11. For all voltages and reservoir configurations, the contribution from the cone was over 500 times that of the contribution from the plume. As $E_{s,1}/E_{s,2} < 0.2\%$, neglecting the electric field from the plume to simplify Eq. 2.30 is valid. While the emitted particles were assumed to be ejected from the emission surface at their final velocity for this study, considering the acceleration of particles as they travel downstream would increase the contribution of the electric field from the plume. The electric field solution in Fig. 2.4 showed that the local electric potential decreases to 70% of the emitter potential within 25 µm of the emitter surface, which is less than half the smallest site spacings predicted for the modeled conditions. Through conservation of energy, it can be estimated that emitted particles reach roughly 55% of their final velocity within the first 25 µm downstream of the emitter. Because the linear charge density assumed to represent the plume scales with the inverse of particle velocity per Eq. 2.24, approximating the plume as a collection of particles at their final velocity only underestimated the electric field contribution of the plumes by a factor of 2 at most. Taking this factor into account raises the contribution of the electric field from the plume to less than 0.5% of that from the cones, so neglecting the electric field from the plume is valid.

Figure 2.12 shows the pressure and fluid velocity near the emission surface at the emitter. The effect of the secondary flow is generally limited to within the region of $r < \lambda$. In a physical device, small-scale spatial variation in porous permeability in this region may have a large effect on the secondary flow. The hydraulic pressure drop associated with the secondary flow was used in Eq. 2.33 to determine the emission site spacing; a spatially-varying porous permeability would violate the homogeneous assumption used to describe the porous flow in this effort. To account for heterogeneity in the medium on the order of the site spacing, the right side of Eq. 2.36 may be multiplied by $\hat{k}^{-1}$, where $\hat{k}$ represents the local porous permeability normalized by the mean porous permeability. In this way, localized variation in porous permeability near the emission surface may be the cause of spatially nonuniform emission that has been observed experimentally.[55, 54]

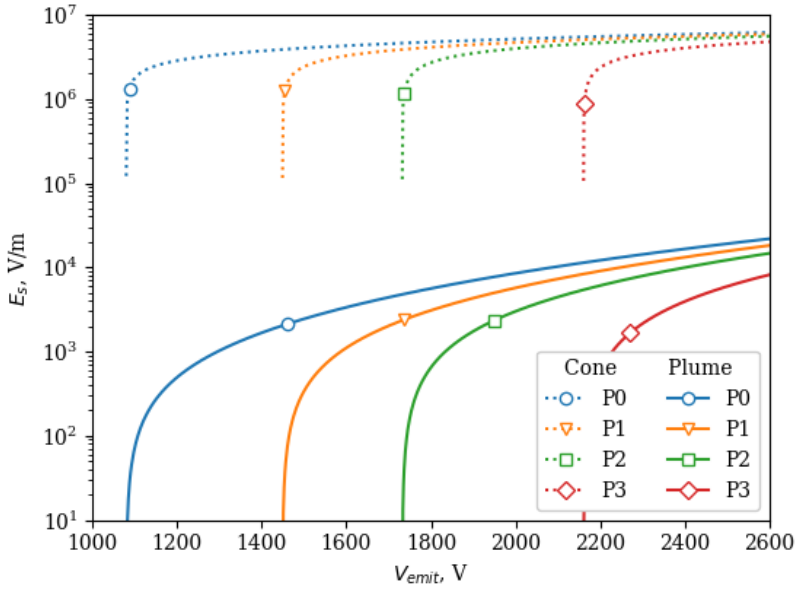

Figure 2.11: Comparison of the secondary electric field produced by cones and plumes at the midpoint between emission sites.

To investigate the low Reynolds number assumption for simplifying Darcy's law, the maximum flow velocity in the porous medium is determined. The maximum flow velocity always occurs at the pressure wells of the emission sites, where the primary and secondary flows are equal and additive; the fluid velocity here is twice the primary flow velocity at the emission surface from Eq. 2.2. The maximum Reynolds number in the porous medium is then solved as:

$$Re = \frac{2I_{site}}{\rho\theta_w R_2 \lambda}\frac{m}{q}\frac{\rho d}{\mu} = \frac{2I_{site}d}{\mu\theta_w R_2 \lambda}\frac{m}{q}, \tag{2.39}$$

where d is taken as the characteristic pore size for the emitter substrate: 1.0 to 1.6 µm; in lieu of information about the particle size in the porous medium, the particle size is assumed to be similar to the characteristic pore size. The Reynolds number for flow in the porous medium is below 10^{-6} for all the presented results, so the low Re assumption is valid.

By enforcing a stagnation point, the emission site spacing expands and contracts in response to changes in the primary flow rate. Emission site expansion is accompanied by a corresponding decrease in the secondary flow fluid velocity to account for the decreased primary flow rate. In lieu of a full stability analysis, the stagnation point condition between emission sites is sufficient.

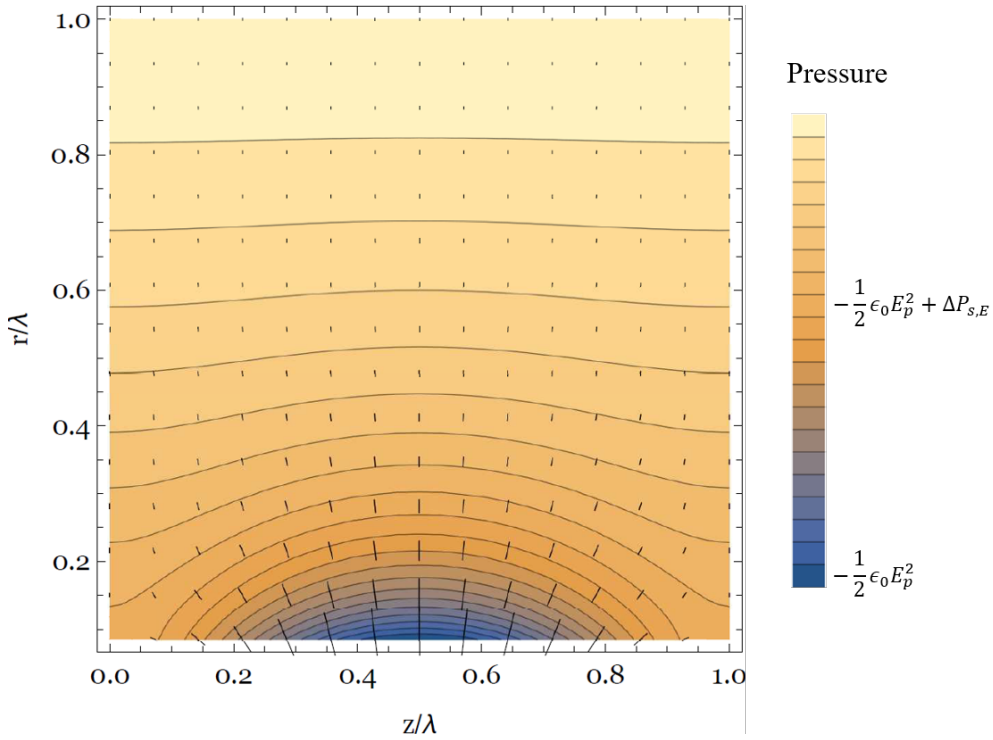

Figure 2.12: Generalized results for pressure in one emission cell, with the emission surface along the horizontal axis. Superposed line segments represent the flow direction and magnitude.

Results from this effort may inform experimental results for porous electrospray emitters of different geometries in the mass spectrometry community, for example where nonlinear increases in total current have been observed with increasing emitter voltage. [73, 74]

To further simplify Eq. 2.21, the specific charge can be substituted by Eq. 2.38 and a parameter S can be introduced to represent the hydraulic resistance for the primary flow to the emission surface:

$$I_{total} \approx \frac{AE_p^3 \Delta P_{app}}{S\gamma}; \qquad S = \frac{\mu \ln\left(\frac{R_2}{R_1}\right)}{k\theta_w L}. \tag{2.40}$$

From this relation it is clear that the total emission current, I_{total}, is inversely proportional to the primary flow hydraulic resistance, which I designate as the wedge hydraulic resistance S, with units of Pa s m^{-3}. The effects that fluid properties and geometry have on the specific charge coefficient A require further investigation. The effect that the wedge angle θ_w has on the electric field via the electric field to voltage coefficient C_E must be considered, even though Eq. 2.40 suggests that I_{total} is proportional to the wedge angle.

This model provides insight into how a porous emitter generally responds to operational and design changes; however, more accurate representation requires further investigation into the assumptions and approximations made in developing this model. For example, emission sites were assumed to lie on the midplane of the emitter, experimental evidence however suggests that emission sites may be oriented about 10° from midplane.[50] The secondary flow, in particular, would benefit from a 3-dimensional representation of the flow near each emission site. For a more accurate representation of the secondary electric field, charge in the plume and the shape and charge distribution at a porous electrospray site should be considered. A more general solution for $P(r,z)$ as derived in the Appendix will be more useful for cases where the emission site spacing is large. For example, in wedge geometries where the radius to the base of the wedge R_1 is small, the emission site spacing λ may be comparable to R_1 over the entire operating range of the device. In these cases, the assumption $\lambda \ll 2\pi R_1$ cannot be made.

2.6 Conclusion

This study develops an analytical model that provides intuitive and useful relationships for understanding the steady state response of a porous wedge electrospray emitters, specifically the total current and emission site spacing. By considering an equilibrium of the effects from Coulomb repulsion and the subsurface pressure variation, quantitative descriptions (i.e. through Eqs. 2.10 and 2.36) provide insight into the effects that fluid properties, emitter geometry, and porous media properties have on the behavior and performance of such devices. This analysis leads to the conclusion that the wedge hydraulic resistance, as defined in Eq. 2.40, is adequate for understanding the total output for the investigated geometry. An explanation for the variation in the specific charge of plume constituents is proposed through Eq. 2.38. Quantitative evaluation of the porous flow leads to Eq. 2.21 and the conclusion that the secondary flow can be ignored only to predict the total current for the considered geometry.

CHAPTER 3

Transient Porous Flow

3.1 Introduction

In all applications of electrospray propulsion, dynamic events are unavoidable. When used for precision control, electrospray thrusters are continuously varied to provide the required thrust on a spacecraft [48]. Electrospray thrusters have also been operated under pulse-width-modulated (PWM) control, in which changes in the operating condition of the device are rapid and drastic [4]. Alternating polarity of emission is often implemented to increase device lifetime, which in turn can create a brief decrease in the applied electric field on the emission surface [31]. Each of these schemes results in time-dependent flow through the electrospray emitter. If the charge to mass ratio of emitted species has any dependence on flow to the emission sites, then time dependent flow through the emitter can negatively affect the polydispersive efficiency, plume divergence, performance and lifetime [50, 20, 56]. For these reasons, understanding the transient flow response of porous electrospray emitters is imperative to developing high performance, long lifetime electrospray devices.

Mass flow in electrospray devices is exceptionally difficult to measure. Flow though capillary emitters can be estimated from reservoir pressure and hydraulic resistance [23, 75], however flow in porous electrospray devices is passively driven by electrostatic pressure and cannot be as easily determined. Direct measurements of mass loss in the Busek BET-300-P multiplexed wedge electrospray thruster measured a mass flow rate of up to $14\,\mu g/s$ [4]; with hundreds of emission sites, the flow to each emission site was likely $\sim 100\,ng/s$. Common analytical balances that have been used for mass and thrust measurements have resolutions as low as $100\,\mu g$ [76, 77]. An emitter with a single emission site on one of these thrust stands would have to be operated for $\sim 1000\,s$

before mass loss could be measured, and useful characterization would require hours of operation. Based on previously mentioned results from literature, the transient settling time is expected to be much shorter than these measurement times, so direct measurement of mass loss is infeasible for capturing transient mass flow rate in non-multiplexed electrospray emitters. For these reasons, characterization of the electrospray plume is a more promising avenue for capturing transient electrospray phenomena. By capturing emergent phenomena in the electrospray plume, the effect of flow settling can be determined.

The objective of this effort is to develop mathematical expressions to describe the transient response of porous electrospray devices. To this end, we have developed a fluid flow model for diffusion of pressure through a porous medium with exposed pores on non-emitting surfaces of the emitter. In Section 3.2 we will present the derivation of the governing equation for transient pressure diffusion in a porous medium from first principles. Then in Section 3.3 the governing equation will be applied to common porous electrospray emitter geometries. The presented theory is compared to the commonly used onset delay model in Section 3.5. Although published experimental results are limited, the presented analytical relations are applied to available experimental results in Section 3.6. Finally, the implications and challenges of the presented model are discussed in Section 3.7.

3.2 Theory

3.2.1 Steady-State Flow

In a porous electrospray emitter, propellant flows through the emitter substrate to the emission surface. The viscous loss associated with flow through a porous medium is described by Darcy's law:

$$\vec{u} = -\frac{k}{\mu}\nabla P, \tag{3.1}$$

where $\vec{u}$ is the fluid velocity, P is pressure, k is the porous permeability, and μ is the fluid dynamic viscosity. This form of Darcy's law is valid for Reynolds number $Re < 1$, where inertial effects can

be neglected [57]. The Reynolds number is described as $Re = \rho u d/\mu$, where ρ is the fluid density, and d is the particle size in the porous medium.

For boundary conditions, the reservoir pressure is the capillary pressure produced by a meniscus at a fully-wetted pore upstream in the reservoir [57, 58] and the emission surface pressure is approximated by the Maxwell pressure supplied by the magnitude of the local primary extraction electric field, E_p [59, 60]. The applied pressure difference from the fluid reservoir to emission site, ΔP_{app}, is described by Equation 2.12 and repeated for clarity:

$$\Delta P_{app} = \frac{4\gamma}{D_{res}} - \frac{1}{2}\varepsilon_0 E_p^2, \tag{3.2}$$

where γ is the fluid surface tension coefficient, D_{res} is the characteristic reservoir pore size, and ε_0 is the permittivity of free space. The electric field on the emitter surface has a linear relation to extraction voltage, which can be determined by computational simulation of the extraction geometry [78, 1] or through analytical evaluation of the extraction geometry [59, 79].

3.2.2 Transient Flow

In this section, the stored volume of fluid in each exposed pore will be combined with Darcy's law to develop a diffusion equation for pressure in a porous medium with exposed pores. As previously described, the flow within porous electrosprays is the result of decrease in pressure from the reservoir to the emission surface. Conservation of momentum in the streamwise direction shows how pressure gradient causes flow through the emitter. Perpendicular to the flow, pressure enforces the meniscus shape in exposed pores. As the meniscus changes, the amount of storable liquid in the pore changes as well. This phenomenon has been described diagramatically by Lozano and Martinez-Sanchez [80] for flow through grooves of externally-wetted emitters and by Courtney and Shea [2] for porous emitters. The fluid volume associated with the change in storable liquid at each pore must eventually pass through the emission surface downstream.

The curvature of the meniscus is found using the Young-Laplace equation, where the pressure drop across a meniscus, ΔP_{men}, is equal to the surface tension coefficient, γ, multiplied by the mean curvature of the meniscus. We assume that the meniscus forms a spherical shape, so the

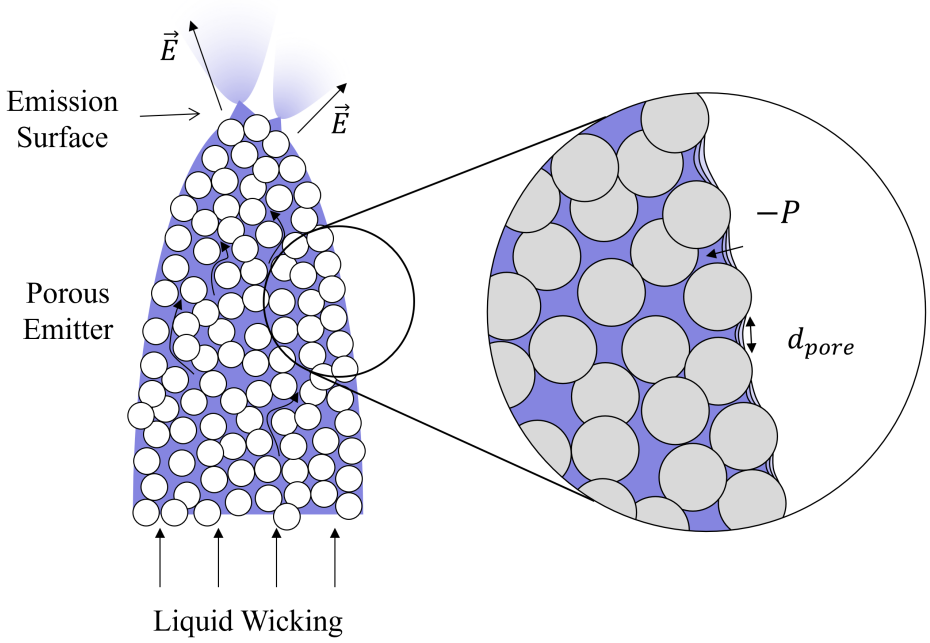

Figure 3.1: Flow in a porous electrospray emitter, with a magnified cross-section of a wetted porous surface. The meniscus of the liquid recedes into the porous medium as pressure decreases due to viscous dissipation.

mean curvature is twice the reciprocal of the radius of the meniscus, R_{men}:

$$\Delta P_{men} = \frac{2\gamma}{R_{men}}. \tag{3.3}$$

We assume the device is operating in vacuum, i.e. there is no ambient pressure; the pressure drop across the meniscus can be replaced with the local pressure, P. For the case where there is no pressure difference across the meniscus, a flat surface is formed. As pressure decreases, the meniscus recedes into the porous medium and increases in curvature, resulting in a decreased capacity for storing liquid in the porous medium. The lost storage capacity of surface pores is determined as a spherical cap formed by the meniscus. For a sufficiently smooth emitter surface, the bounds of the spherical meniscus are defined by the radius of a single surface pore, R_{pore}. The volume of this spherical cap, V, and the depth that the meniscus has receded into its pore, h, are defined as:

$$V = \frac{1}{6}\pi h^2(3R_{men} - h), \tag{3.4}$$

$$h = R_{men}\left(1 - \left(1 - \frac{R_{pore}^2}{R_{men}^2}\right)^{1/2}\right), \tag{3.5}$$

We simplify Equation 3.5 by performing a Taylor expansion and ignoring higher order terms:

$$h = R_{men}\left(1 - \left(1 - \frac{1}{2}\frac{R_{pore}^2}{R_{men}^2} + \ldots\right)\right) \approx \frac{R_{pore}^2}{2R_{men}}, \tag{3.6}$$

which in turn allows us to linearize Equation 3.4 and substitute into Equation 3.3 to determine the effect of local pressure on the pore's capacity for storing liquid, ΔV_{pore}:

$$\Delta V_{pore} = \frac{\pi R_{pore}^4 P}{16\gamma}. \tag{3.7}$$

The linearized relationship is 91% accurate within 50% of the characteristic pressure, and 98% accurate within 25% of the characteristic pressure for saturated pores in the emitter porous medium ($2\gamma/R_{pore}$) [38]. A common choice for porous medium is P5-grade porous glass, which has a pore radius of 0.5 to 0.8 µm [2, 36, 81]. As an example, the emitter from Courtney and Shea [2] is considered, for which the electric field at the emission surface has been estimated as the emitter voltage multiplied by 15.3 mm^{-1}. For EMI-BF4 in the emitter substrate, 5.7 kV is required to reach 25 % of the characteristic pressure of saturated porous in the emitter. The emitter was operated up to a maximum of 2.5 kV, which shows that the device was operated well within the range of validity for the linearization used to produce Equation 3.7. Even if the emitter was fabricated from P4-grade porous glass (as with Ma et al. [81]), which has a pore radius of 5 to 8 µm, the operational range still falls within the 91% accuracy threshold for the linearization. For these reasons, we consider the linearization to be generally applicable to the common implementation of porous electrospray emitters.

The equation for continuity can be adjusted to account for the changing capacity for stored liquid volume in a differential element, dV:

$$\nabla \cdot \vec{u} = -\frac{\partial}{\partial t}\frac{\Delta V}{\mathrm{d}V}. \tag{3.8}$$

where t is time. The negative sign is adopted due to the convention in Equation 3.7. Combined with Darcy's law, Equation 3.8 becomes:

$$\frac{k}{\mu}\nabla^2 P = \frac{\partial}{\partial t}\frac{\Delta V}{\mathrm{d}V}. \tag{3.9}$$

The change in liquid capacity in a differential element, $\Delta V / \mathrm{d}V$, can be expressed as a function of pressure through Equation 3.7, the surface pore density n_{pore}, and the exposed surface area to volume ratio of a differential element:

$$\frac{\Delta V}{\mathrm{d}V} = \Delta V_{pore} n_{pore}\frac{\mathrm{d}A}{\mathrm{d}V} = \frac{\pi R_{pore}^4 P}{16\gamma}\left(\frac{\varepsilon}{\pi R_{pore}^2}\right)\frac{\mathrm{d}A}{\mathrm{d}V}. \tag{3.10}$$

Equation 3.10 is used to convert Equation 3.9 into a diffusion equation for pressure in a porous medium with an exposed surface, where D is the diffusion coefficient for this flow:

$$\frac{\partial}{\partial t}P = D\nabla^2 P; \quad D = \frac{16\gamma k}{\varepsilon\mu R_{pore}^2}\frac{\mathrm{d}V}{\mathrm{d}A}. \tag{3.11}$$

To estimate the diffusion coefficient for a porous emitter where the pore size and permeability are unknown, permeability is approximated through the Carman-Kozeny equation [57] and pore size is approximated from particle size and porosity, ε. If the porous medium has roughly circular pores between spherical particles, then:

$$R_{pore} = \frac{D_p}{2}\left(\frac{\varepsilon}{1-\varepsilon}\right)^{1/2} \tag{3.12}$$

where D_p is the particle diameter. The diffusion coefficient can then be simplified as:

$$D = 0.356\frac{\Phi^2\gamma\varepsilon}{\mu(1-\varepsilon)}\frac{\mathrm{d}V}{\mathrm{d}A}. \tag{3.13}$$

The sphericity of particles is taken into account through Φ. Equation 3.13 shows that the diffusion coefficient can be reasonably estimated without performing pore size or permeability

tests on a porous sample. Porosity can be measured from the mass of a porous sample with a known volume. The term $\frac{dV}{dA}$ will depend on the geometry of the porous emitter. Regardless of geometry, pressure in the emitter domain settles over a time scale that is independent of change in pressure at the emission surface. As a result, the system response to a nondimensional pressure change at the emission surface can be characterized to understand the system response to any pressure change. An instantaneous pressure jump from $P = 0$ throughout the emitter domain to $P = 1$ at the emission surface at time $t = 0$ will be considered in the following section to determine the transient response, regardless of emitter geometry.

3.3 Modeling Common Electrospray Geometries

In this section, three common porous emitter geometries will be considered: pillar, cone, and wedge. For the cone and wedge geometries, example results are shown for the following conditions: $R_I = 0.1, R_1 = 1, D_0 = 2$.

3.3.1 Pillar Geometry

Pillar-shaped geometries are seldom used for porous electrospray emitters [82, 83, 38]; however, the simplicity of the flow solution warrants analysis. The pillar emitter can be approximated as a semi-infinite cylinder. To determine the pressure response within the porous substrate, it is assumed to be at a uniform pressure before a disturbance is introduced at the tip of the semi-infinite domain at $t = 0$. The assumed geometry of the body and the differential element are shown in Figure 3.2. Inside of the differential element, the fluid is assumed to be uniform pressure. The differential volume, dV, and differential surface area, dA, are determined from the thickness of the differential element, dy. The ratio of these two quantities is necessary for determining the diffusion coefficient.

$$\frac{dV}{dA} = \frac{R_{cyl}}{2}, \tag{3.14}$$

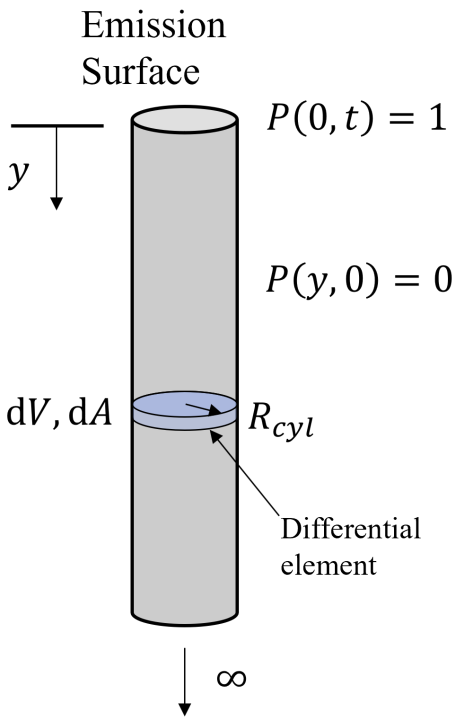

Figure 3.2: Geometry of a pillar emitter, with the differential element used in transient porous flow analysis specified.

where R_{cyl} is the radius of the cylinder. Thus the diffusion coefficient for a semi-infinite cylinder geometry per Equation 3.11 is solved as:

$$D_{cyl} = \frac{8\gamma k R_{cyl}}{\varepsilon \mu R_{pore}^2}. \tag{3.15}$$

Diffusion of a property such as pressure into a semi-infinite medium is often solved using a similarity solution [84]. For a nondimensionalized pressure disturbance upon the emission surface at at $t = 0$ such that $P(y, t = 0) = 0$ and $P(y = 0, t > 0) = 1$, the solution for pressure is

$$P = \left[1 - \text{erf}(\xi)\right]; \quad \xi = \frac{y}{2\sqrt{D_{cyl} t}}, \tag{3.16}$$

where ξ is a similarity variable. The pressure gradient at the tip is found by using the chain rule with Equation 3.16 and the definition of the similarity variable ξ:

$$\frac{\partial P}{\partial y}(0,t) = \frac{1}{\sqrt{2\pi D_{cyl} t}}. \tag{3.17}$$

Flow rate through the emission surface decreases with time in proportion to the pressure gradient through Equation 3.1. The similarity solution is no longer relevant when the pressure diffuses into the porous medium at a distance L from the emitter tip, thus forming the time constant, T_C, for this emitter geometry:

$$T_C = \frac{L^2}{4D} = \frac{L^2 \varepsilon \mu R_{pore}^2}{32 \gamma k R_{cyl}}. \tag{3.18}$$

For $t < T_C$, flow is best described by the transient solution, while for $t > T_C$, the flow is best described by the steady flow solution. The flow response for a pillar-shaped emitter sheds light onto the characteristics of flow solutions obtained through the presented diffusion equation: flow through the emission surface decays nonlinearly and approaches the steady solution predicted through Darcy's law. This response also matches with the physical interpretation of the pressure diffusion into the porous medium, where fluid must be exhausted from exposed pores on the emitter surface before reaching an equilibrium state. Fluid accumulation in exposed pores temporarily reduces the effective hydraulic resistance of the emitter until excess fluid is exhausted through the emission surface.

3.3.2 Cone Geometry

The cone geometry is the most widely adopted for use in porous electrospray emitters [44, 46, 47, 36, 34, 85]. A significant advantage of the cone shape compared to the wedge emitter is that the additional radius of curvature results in a sharper emitter tip, allowing for device operation at lower voltages. High emitter densities of 100s of emitters per cm^2 have been implemented to achieve high throughput density [43, 86]. When conventionally machined [36] or electric discharge machined [47], the resulting emitter can be pyramid-shaped rather than cone-shaped; these two emitter shapes are sufficiently similar such that the two can be analyzed using the same flow geometry.

The geometry for the cone emitter domain is shown in Figure 3.3 with the chosen differential

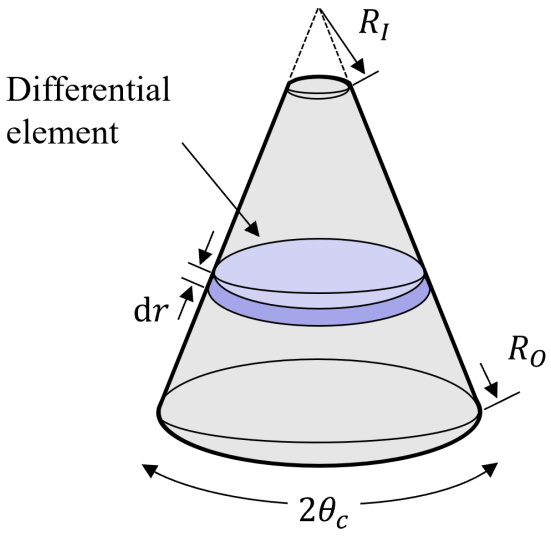

Figure 3.3: Left, geometry of a cone emitter, with the differential element used in transient porous flow analysis specified.

element. Flow is azimuthally uniform and in the radial direction. Differential elements for the cone geometry have the following property:

$$\frac{\mathrm{d}V}{\mathrm{d}A} = \big(1-\cos(\theta_c)\big)\cot(\theta_c), \tag{3.19}$$

where θ_c is the half angle of the cone. The diffusion coefficient for the cone geometry, D_c is evaluated through element geometry and Equation 3.11.

$$D_c = \frac{16\gamma k r}{\varepsilon\mu R_{pore}^2}\big(1-\cos(\theta_c)\big)\cot(\theta_c) = D_{0,c}r. \tag{3.20}$$

For the cone geometry, the diffusion coefficient is no longer uniform over the domain of the emitter. For brevity, the diffusion coefficient for a cone, D_c, is replaced by $D_{0,c}$, which has no spatial dependence. The governing equation for this domain is then:

$$\frac{\partial}{\partial t}P = \frac{D_{0,c}}{r}\frac{\partial}{\partial r}\left(r^2\frac{\partial}{\partial r}P\right). \tag{3.21}$$

To solve for the pressure response in the domain of the porous emitter, we consider a nondimensionalized pressure change at the emission surface at $t = 0$ such that $P(r,t=0) = 0$ and $P(R_I,t>0) = 1$. This transient heterogenous problem is simplified as the superposition of steady solution, P_s, and homogeneous transient solution, P_t [87]:

$$P(r,t) = P_s(r) + P_t(r,t). \tag{3.22}$$

P_s satisfies boundary conditions $P_s(R_O) = 0, P_s(R_I) = 1$ and P_t satisfies homogeneous boundary conditions $P_t(R_O,t) = P_t(R_I,t) = 0$. The steady and homogeneous transient solutions combine to form the solution for nonhomogeneous boundary conditions at R_O and R_I. The steady state solution for pressure in the cone, $P_{c,s}$, is found through Eq. 3.21, where time derivatives can be neglected:

$$P_{c,s}(r) = \frac{R_I}{R_O - R_I}\left(\frac{R_O}{r} - 1\right). \tag{3.23}$$

A separation of variables solution is assumed in order to solve for the homogeneous transient component, $P_{c,t}$. The boundary conditions are that the pressure has no time dependence at the upstream and downstream boundaries, i.e. $P_{c,t}(R_O,t) = P_{c,t}(R_I,t) = 0$. The homogeneous transient component of pressure in the domain is:

$$\begin{aligned} P_{c,t}(r,t) = \sum_{n=1}^{N} & 2C_n\sqrt{\frac{D_0}{\lambda_n r}}e^{-\lambda_n t} \\ & \times \left[Y_1\left(2\sqrt{\frac{\lambda_n r}{D_0}}\right) - \frac{Y_1\left(2\sqrt{\frac{\lambda_n R_I}{D_0}}\right)}{J_1\left(2\sqrt{\frac{\lambda_n R_I}{D_0}}\right)} J_1\left(2\sqrt{\frac{\lambda_n r}{D_0}}\right) \right], \end{aligned} \tag{3.24}$$

where J_1 and Y_1 are the Bessel functions of the first and second kind respectively, both of order 1, and n refers to the nth value of λ that satisfies the boundary conditions, and N is the number of modes considered. Valid values of λ_n satisfy the boundary conditions through the following equation.

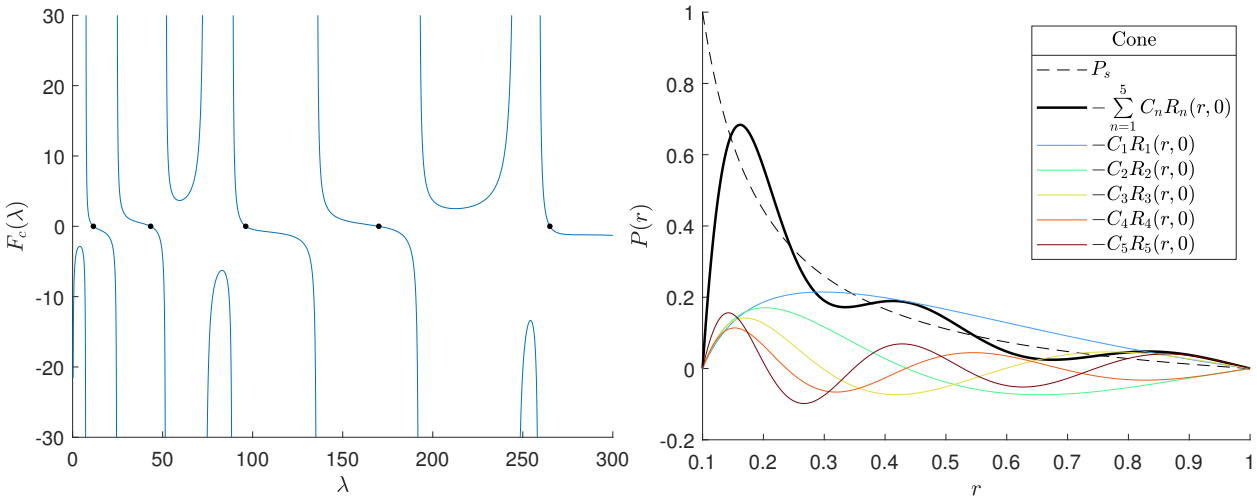

Figure 3.4: Left, the left hand side of Eq. 3.25, for $R_I = 0.1$, $R_O = 1$, and $D_{0,c} = 2$, with valid zeros indicated. Right, the first 5 modes of the transient solution for the primary flow, with magnitudes determined through the described optimization strategy. The analytical approximation of the steady flow through these transient bases and the steady analytical solution are shown as well.

$$\frac{Y_1\left(2\sqrt{\frac{\lambda R_I}{D_0}}\right)}{J_1\left(2\sqrt{\frac{\lambda R_I}{D_0}}\right)} - \frac{Y_1\left(2\sqrt{\frac{\lambda R_O}{D_0}}\right)}{J_1\left(2\sqrt{\frac{\lambda R_O}{D_0}}\right)} = 0. \tag{3.25}$$

The left hand side of Equation 3.25 is plotted in Figure 3.4 with valid zeros.

The r-dependent terms in Equation 3.24 are combined to find the bases for this equation $R(\lambda_n, r)$, shown in Figure 3.4. Numerical projection of these bases onto each other shows that they are non-orthogonal, complicating the process for determining the proper values of C_n for approximating the steady solution. Coefficient values are determined by satisfying the initial condition $P(r, t = 0) = 0$ through Eq. 3.22. Values of C_n were determined through numerical optimization of the following equation, using seed values obtained through projecting $P_{c,s}$ onto the basis functions:

$$P_{c,t}(r, t = 0) = -P_{c,s}(r) \tag{3.26}$$

The success of this numerical optimization can be seen in the good agreement with the equilibrium solution through the basis functions, as shown in Fig. 3.4. The transient homogeneous

solution captures the salient features of $P_{c,t}$ with some periodic oscilation.

To obtain the heterogeneous transient solution, the equilibrium solution (Equation 3.23) and homogeneous transient solution (Equation 3.24) are added per Equation 3.22. The solution can then be multiplied by the applied pressure difference, per Equation 3.2.

3.3.3 Wedge Geometry

In this section, the wedge geometry of emitters will be considered. This geometry is less popular than the cone geometry, but has seen implementation in both research groups [2, 52, 88] and industry [48]. In contrast to cone-shaped emitters, wedge-shaped emitters have a linear extraction surface where the applied electric field is strong and ideally uniform. Numerous emission sites form on the emitter in this region, caused by electric field and hydraulic interactions [54, 1]. In contrast to cone emitters, these emitters will operate at a higher voltage due to only having one radius of curvature at the emission surface. On the other hand, only having curvature in one direction results in a narrow plume in the ridgewise direction of the wedge [50, 89]. Additionally, the long emission surface results in a tight collection of emission sites along the wedge without the need for emitter parallelization. For the wedge emitter, we consider flow in a cylindrical coordinate system. Because the governing equation is linear for this flow, the flow can be described by the superposition of a primary and secondary flow. The primary flow describes the net flow in the radial direction to the emission surface, while the secondary flow describes the local flow concentration to each emission site on the surface.

3.3.3.1 Primary Flow

The analytical geometry for flow in the wedge emitter domain is shown in Figure 3.5. The differential element for this flow has properties of:

$$\frac{\mathrm{d}V}{\mathrm{d}A} = \frac{r\theta_w}{2}. \tag{3.27}$$

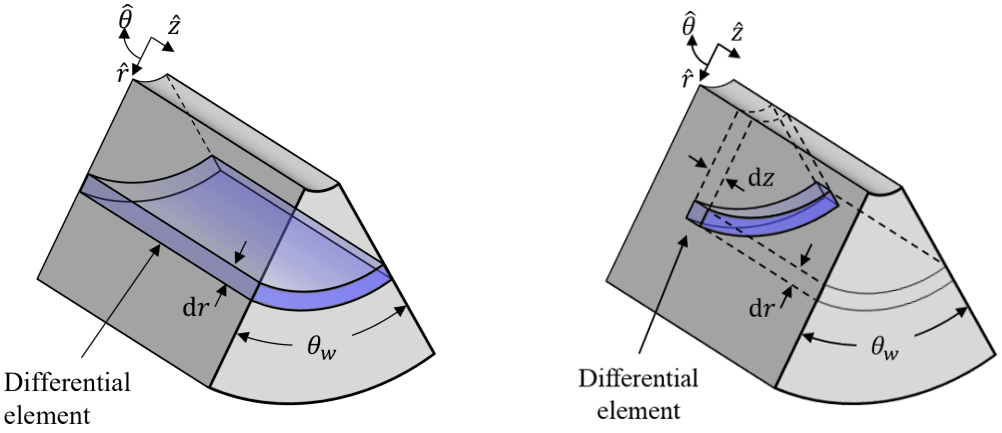

Figure 3.5: Geometry for flow in a wedge emitter. The differential elements used for analyzing the primary and secondary flows are shown in the subfigures at left and right respectively.

where θ_w is the full angle of the wedge. For the chosen differential element, the diffusion coefficient from Equation 3.11 is evaluated as:

$$D_w = \frac{8\gamma k r \theta}{\varepsilon \mu R_{pore}^2} = D_{0,w} r, \tag{3.28}$$

As was the case for the cone emitter flow, the diffusion coefficient has an r-dependence, so D_w is replaced by $D_{0,w}$ for brevity. The governing equation for flow in this domain is then:

$$\frac{\partial}{\partial t} P = \frac{D_{0,w}}{r} \frac{\partial}{\partial r} \left(r \frac{\partial}{\partial r} P \right). \tag{3.29}$$

Separation of variables is used to find the solution to the transient component of the flow after subtracting the equilibrium solution, as with the cone flow. The steady solution, $P_{w1,s}$, is found by solving Equation 3.29 for $P_{w1,s}(R_O) = 0$ and $P_{w1,s}(R_I) = 1$:

$$P_{w1,s}(r) = \frac{\ln\left(\frac{R_O}{r}\right)}{\ln\left(\frac{R_O}{R_I}\right)}. \tag{3.30}$$

As with the cone emitter geometry, a separation of variables solution is assumed for the transient homogeneous solution. The boundary conditions are that the pressure has no time dependence

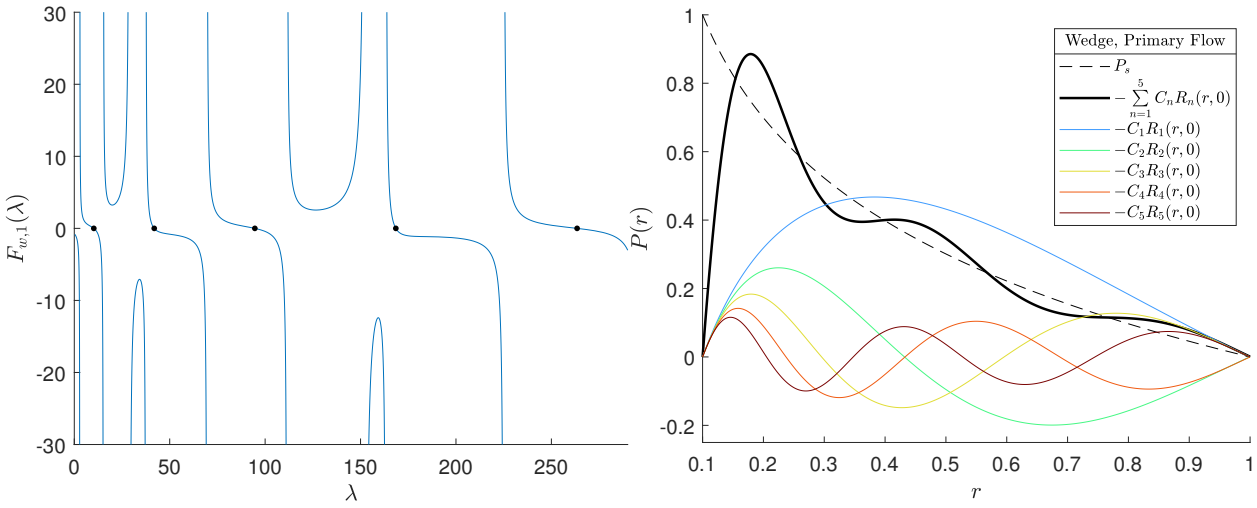

Figure 3.6: Left, the left hand side of Eq. 3.31, for $R_I = 0.1$, $R_O = 1$, and $D_{0,w} = 2$, with valid zeros indicated. Right, the first 5 modes of the transient solution for the primary flow, with magnitudes determined through projection of the steady flow solution. The analytical approximation of the steady flow through these transient bases and the steady analytical solution are shown as well.

at the upstream and downstream boundaries, i.e. $P(R_O,t) = 0$ and $P(R_I,t) = 0$. To prevent a trivial solution, C_1 is chosen such that $R(R_O) = R(R_I) = 0$. As with the cone flow, this yields a criterion for selecting values for λ that satisfy the boundary conditions of R:

$$\frac{Y_0\left(2\sqrt{\frac{\lambda_n R_I}{D_0}}\right)}{J_0\left(2\sqrt{\frac{\lambda_n R_I}{D_0}}\right)} - \frac{Y_0\left(2\sqrt{\frac{\lambda_n R_O}{D_0}}\right)}{J_0\left(2\sqrt{\frac{\lambda_n R_O}{D_0}}\right)} = 0. \tag{3.31}$$

For the wedge primary flow, the homogeneous transient solution has a form of:

$$P_{w1,t}(r,t) = \sum_{n=1}^{N} 2C_n \left[Y_0\left(2\sqrt{\frac{\lambda_n r}{D_0}}\right) - \frac{Y_0\left(2\sqrt{\frac{\lambda_n R_I}{D_0}}\right)}{J_0\left(2\sqrt{\frac{\lambda_n R_I}{D_0}}\right)} J_0\left(2\sqrt{\frac{\lambda_n r}{D_0}}\right) \right] e^{-\lambda_n t}. \tag{3.32}$$

As with the solution for flow in the cone, the full solution is obtained by adding the transient homogeneous and steady solutions from Equations 3.32 and 3.30 respectively. The left hand side of Equation 3.31 and the bases of Equation 3.32 are shown in Figure 3.6.

3.3.3.2 Secondary Flow

The flow to individual emission sites is considered as the secondary flow. The governing equations for transient and steady flow are linear, so solutions can be superposed to form valid solutions. For the case where the base of the wedge, R_O, is much greater than the emission surface radius, R_I, and the emission site spacing, d_{site}, Bessel I terms can be ignored in the steady solution [1]. A sinusoidal pressure oscillation in z with an amplitude of 1 is assumed in order to develop an analytical approximation of the flow concentration into individual emission sites. The secondary flow can later be added to a matching primary flow from the previous section to enforce stagnation points in between each emission site.

For the transient secondary flow, the diffusion coefficient is the same as for the transient primary flow. The governing equation for pressure, $P(r,z,t)$, is evaluated in axisymmetric coordinates as:

$$\frac{\partial}{\partial t}P = D_{0,w}\left(r\frac{\partial^2}{\partial r^2} + \frac{\partial}{\partial r} + r\frac{\partial^2}{\partial z^2}\right)P. \tag{3.33}$$

Assuming that the site spacing is smaller than R_O, the steady state pressure in the domain, $P_{w2,s}$, is [1]:

$$P_{w2,s}(r,z) = \frac{K_0(\alpha r)}{K_0(\alpha R_I)}e^{i\alpha z}, \tag{3.34}$$

where α is the wavenumber for the oscillating pressure condition at the emission surface and is equal to $2\pi/d_{site}$.

A separation of variables approach is taken and the homogeneous transient pressure solution, $P_{w2,t}$, is separated into R, Z, and T components for the $r-$, $z-$, and $t-$dependencies, respectively. For the transient secondary flow, the diffusion coefficient is the same as for the transient primary flow. Separation of variables is used to solve transient pressure response in this domain:

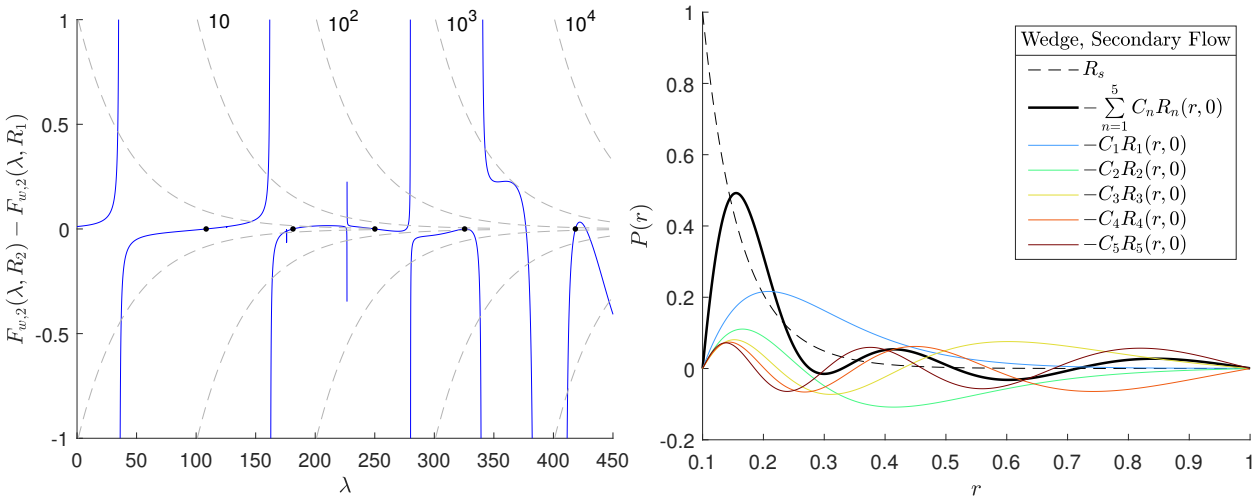

Figure 3.7: Left, the left hand side of Eq. 3.36, for $R_I = 0.1$, $R_O = 1$, $D_{0,w} = 2$, and $d_{site} = 0.5$, with valid zeros indicated. Note that a variable scale for the vertical axis is utilized to highlight interesting features of Eq. 3.36. Right, the first 5 modes of the transient solution for the secondary flow, with magnitudes determined through the described optimization strategy. The analytical approximation of the steady flow through these transient bases and the steady analytical solution are shown as well.

$$P_{w2,t}(r,t,z) = \sum_{n=1}^{N} C_n e^{-\lambda_n t + \alpha(r-iz)} \times \left[L_{\frac{1}{2}\left(\frac{\lambda_n}{D_0\alpha}-1\right)}(2\alpha r) - \frac{U\left(\frac{1}{2}-\frac{\lambda_n}{2D_0\alpha},1,2\alpha r\right)}{U\left(\frac{1}{2}-\frac{\lambda_n}{2D_0\alpha},1,2\alpha R_I\right)} L_{\frac{1}{2}\left(\frac{\lambda_n}{D_0\alpha}-1\right)}(2\alpha R_I) \right], \tag{3.35}$$

where U is the confluent hypergeometric function of the second kind [90] and L is the Laguerre polynomial [91]. Values of λ satisfy the following equation:

$$\frac{U\left(\frac{1}{2}-\frac{\lambda_n}{2D_0\alpha},1,2\alpha R_I\right)}{L_{\frac{1}{2}\left(\frac{\lambda_n}{D_0\alpha}-1\right)}(2\alpha R_I)} - \frac{U\left(\frac{1}{2}-\frac{\lambda_n}{2D_0\alpha},1,2\alpha R_O\right)}{L_{\frac{1}{2}\left(\frac{\lambda_n}{D_0\alpha}-1\right)}(2\alpha R_O)} = 0. \tag{3.36}$$

Satisfying Eq. 3.36 appears to be a necessary but not sufficient criterion; valid flow solutions with values for λ that satisfied Eq. 3.36 were determined through inspection. Valid solutions for λ are shown in Figure 3.7 with their associated bases from Equation 3.35.

The added complexity due to inclusion of an additional independent flow parameter motivates simplification of the transient behavior prediction. As with the other flows discussed previously, the long-term behavior of the flow is described by the first eigenvalue while higher eigenvalues describe successively shorter-term behavior. Understanding the first eigenvalue allows for understanding the envelope of transient settling for the flow. The secondary flow in a porous wedge is largely confined to the emission surface; as long as R_I and d_{site} are significantly smaller than the base of the wedge R_O, the base radius R_O has negligible effect on the secondary flow. Approximate values for the first eigenvalue can be found by neglecting the second term in Eq. 3.36 through the argument that the flow is confined to the emission surface. Dimensional analysis suggests a solution of the form:

$$\lambda_1 \propto \frac{D_{0,w} R_I^m}{d_{site}^{m+1}} \equiv \eta, \tag{3.37}$$

where η is a nondimensional parameter capturing the combined effect of d_{site} and R_I on λ. Least squares fitting over a range of input parameters suggests a proportionality coefficient of 69.2 and $m = 0.738$. The first eigenvalue of the wedge secondary flow for a variety of geometric parameters are shown in Figure 3.8.

Because the secondary flow is confined to the region of the emitter near the emission surface, the time required for this flow to settle will generally be much shorter than that of the primary flow. When considering large changes to the pressure condition at the emission surface of an electrospray, the secondary flow settling should be considered when a detailed understanding of the transient response is required. However, emission sites can be unsteady even at a constant operating condition [92]. For capillary emitters, oscillations in the cone are coupled with the unsteadiness of the jet on the order of single kHz frequencies [93]; in porous electrosprays, the porous medium may act as another mechanism for unsteady emission with lower frequencies possible as a function of emission site spacing. Equation 3.37 predicts that settling time increases with site spacing to the power -1.738. In other words, higher frequency pulsating emission sites are expected when emitting with high emission site densities.

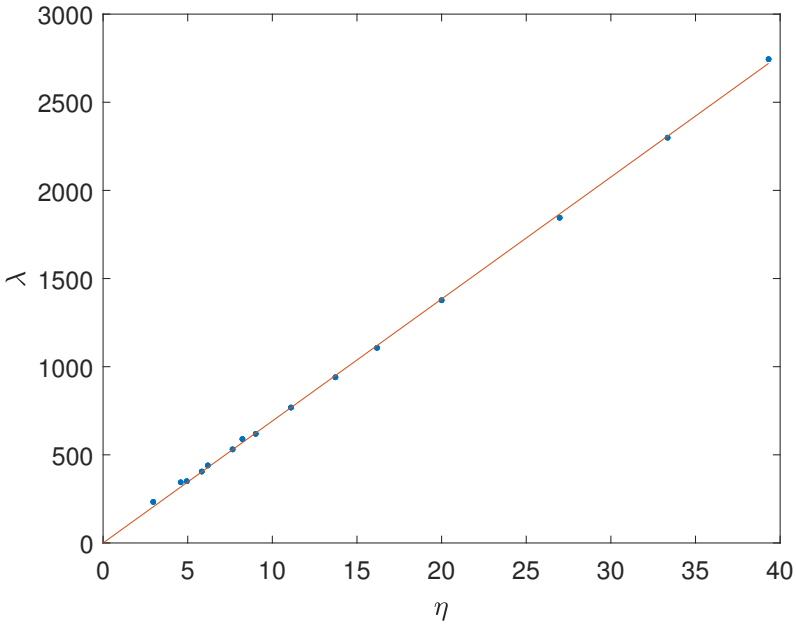

Figure 3.8: The first eigenvalue of the wedge secondary flow for $D_{0,w} = 2$ and values of R_I from 0.1 to 0.25, R_I from 5 to 10, and d_{site} from 0.1 to 0.3. Dimensional analysis and least squares fitting show good agreement with the numerically determined zeros with fit parameters of $A = 69.2$ and $m = 0.738$ per Eq. 3.37.

3.4 Error Estimation

The analytical results from Section 3.3 are supported by a numerical solver, which uses the finite difference method with an explicit time step to predict the temporal response of pressure in the medium. The time step was chosen to ensure a Von Neumann stability parameter of less than 0.2 throughout the domain [94]. The error of each analytical solution, σ, is estimated by comparing the analytical flow field to that which was produced by the numerical solver, normalized by the pressure integrated over the domain:

$$\sigma(t) = \frac{\sqrt{\sum_{x=1}^{X} \left(P_d(x,t) - P_a(x,t)\right)^2}}{\sum_{x=1}^{X} P_d(x,t)}, \tag{3.38}$$

where P_d is the pressure obtained by the discretized method, P_a is the pressure obtained by analytical the analytical solution for the specified emitter geometry, x is the location from the discretized solver, and X is the number of points used in the discretized solver. Equation 3.38 was used to evaluate the accuracy of the analytical expressions for the transient pressure response of the cone, primary wedge, and secondary wedge flows.

The error for the transient pressure response of the cone domain is shown in Figure 3.9. Error generally decreases over time and with an increase in the number of evaluated modes. Due to the nonorthogonality of modes, increasing the number of modes does not necessarily decrease error over the entire time domain.

The error for the transient pressure response of the primary flow in the wedge domain is shown in Figure 3.10. The modes for the primary flow in the wedge are orthogonal, so increasing the number of modes always has a favorable effect on decreasing error. Including higher order modes produces an analytical prediction with a more accurate short term response. When interested in the immediate response of a porous emitter, including more modes is important for this reason.

The error for the transient pressure response of the secondary flow in the wedge domain is shown in Figure 3.11. Error is initially high and decreases sharply around $1/\lambda_N$ where N is the

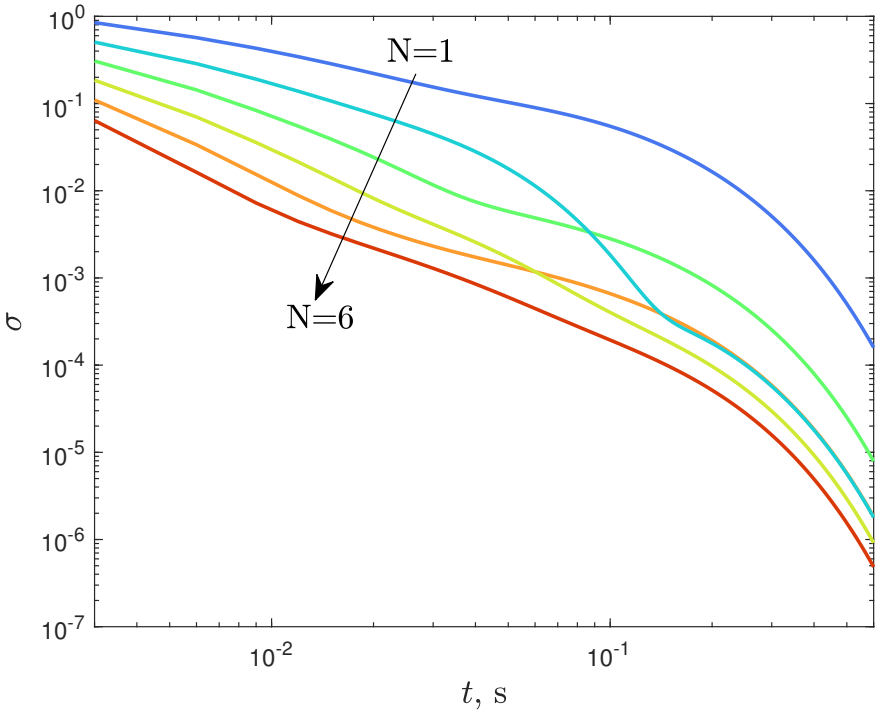

Figure 3.9: Error associated with analytical approximation of the transient flow in a porous cone, using up to the first 6 modes in Eq. 3.24.

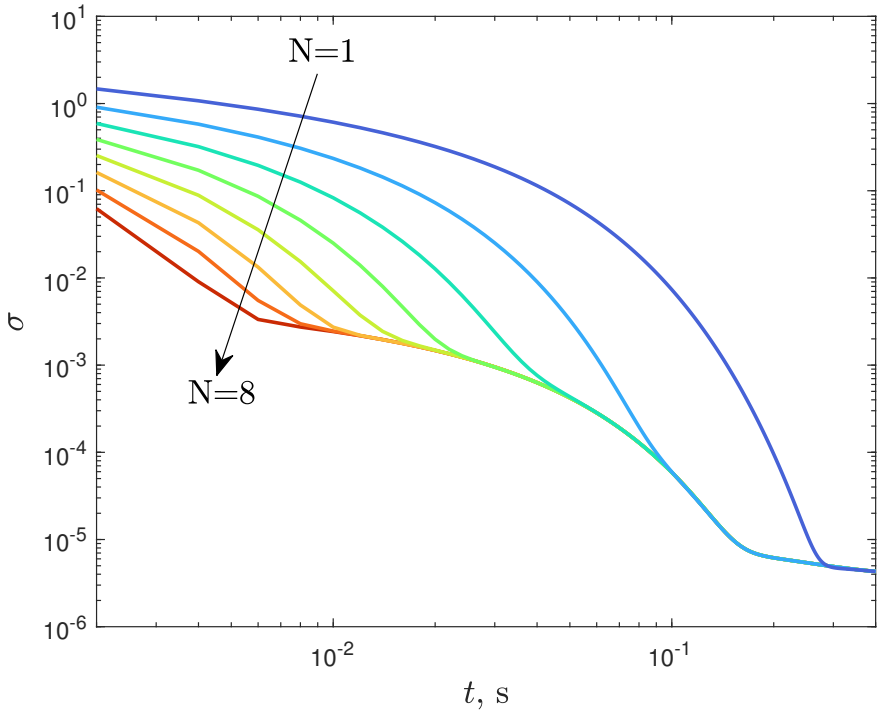

Figure 3.10: Error associated with analytical approximation of the transient primary flow in a porous wedge, using up to the first 8 modes in Eq. 3.32.

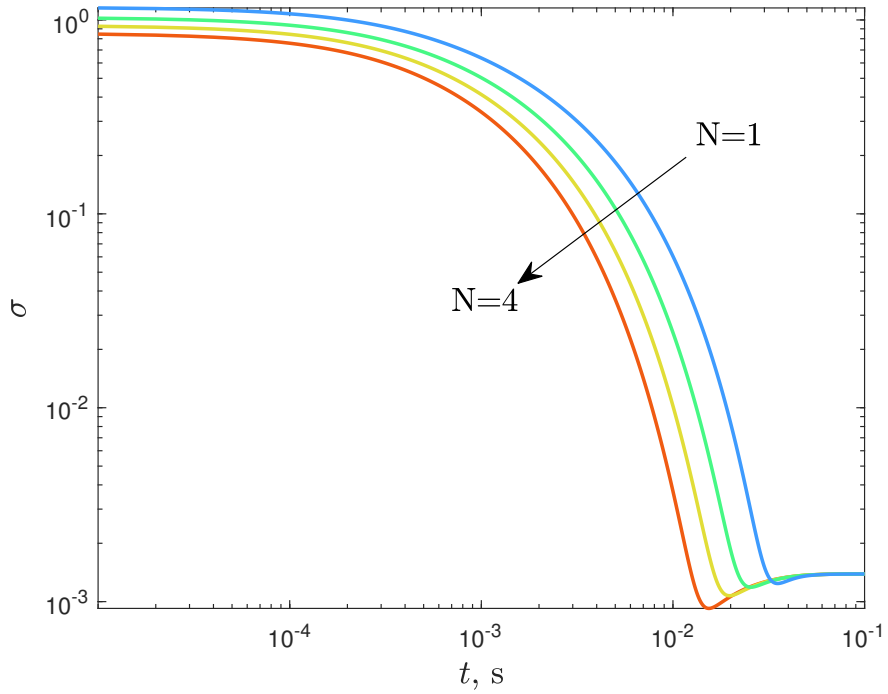

Figure 3.11: Error associated with analytical approximation of the transient secondary flow in a porous wedge, using up to the first 4 modes in Eq. 3.35.

number of modes considered. Increasing the number of modes decreases the time required for the solution to capture the transient response. The reason for the initial dwell at high error is that the analytical modes produce pressure oscillation throughout the spatial domain of the emitter while the physical response is mostly confined to within d_{site} from R_I. This effect is shown in Figure 3.7; the steady solution reaches $P = 0$ by $r = 0.5$ while oscillations persist throughout the domain. Unless the analytical domain is artificially reduced, the analytical solution may only provide useful information about the long-term transient response of the secondary flow and not the immediate response.

3.5 Comparison with Onset Delay Evaluation

A commonly used method of evaluating the time-response of an electrospray is through onset delay characterization. Thompson and Prowett developed the onset delay model by considering viscous effects and the volume associated with a Taylor cone during emission [95]. The theory has been

applied to experimental results from externally-wetted electrosprays [80] and porous electrosprays using Darcy's law to understand the effect of viscosity [96].

Onset delay and diffusion of pressure, as presented in this study, are complementary models because the first describes only up to the time of emission, while the latter is more suited to understanding the flow once emission is underway. On the other hand, they are similar models in that the flow can be considered settled once a sufficient volume of fluid has passed through the emitter. By comparing the propellant volume throughput required to reach steady state, the two models can be compared to see when each are relevant. For simplicity the presented pressure diffusion is evaluated for a cylindrical, or pillar style, emitter. The same analysis could be repeated for the cone or wedge analyses with the same conclusions, albeit different settling behavior.

To determine the onset delay, the volume of a Taylor cone at the emission surface must be evaluated. While an ideal Taylor cone takes an angle of 49.3° due to the balance of surface tension and electric pressure, fluid pressure can cause the shape to differ from this ideal geometry. When using a porous reservoir, fluid can be supplied to the emission sites at a strong negative pressure, causing a Taylor cone with a concave cross-section. This phenomenon is supported by empirical evidence [97] and analytical models [63, 62, 64]. At the base of a concave Taylor cone, the meniscus is influenced by the feeding pressure, surface tension, and electric stress. Towards the apex of the cone, electric pressure and surface tension effects dominate the behavior of the meniscus, causing the meniscus to trend towards the Taylor angle close to the apex. Furthermore, while the size of emission sites tends to grow to the limits of the emitter geometry when formed without a negative pressure, a negative pressure can limit the size of the base of an emission site on a porous medium.

The volume of a Taylor cone with a strong restorative pressure is considered by assuming an ideal Taylor shape, but reducing the radius of the base of the emission site in response to the negative fluid pressure in the porous medium. Because the meniscus at the base of the cone is influenced by the restorative pressure, electric pressure, and surface tension, the radius of base is taken to be the cone radius where these 3 effects are comparable. This assumption results in the onset cone volume shrinking with restorative pressure, which is consistent with experimental measurements of cone volume decreasing with voltage [96] and onset voltage increasing with restorative pressure

[2]. The surface tension pressure is assumed to be equal to that of the restorative pressure at the analytical approximation for the base of the cone:

$$P_{res} = \frac{\gamma}{R_\gamma} = \frac{4\gamma}{D_{res}}, \tag{3.39}$$

where D_{res} is the pore diameter of the porous reservoir and R_γ is a characteristic radius of the emission site at onset. Because the effect of surface tension is inversely proportional to radius of curvature, increasing the restorative pressure decreases the radius of the base of the cone. We assume that there is one emission site at startup, generally the number of emission sites at startup is of order 1 [98, 99]. The volume of a cone, V_{TC}, can be determined from its base radius, R_{TC}, and height, h_{TC}:

$$V_{TC} = \frac{1}{3}\pi R_{TC}^2 h_{TC} = \frac{1}{3}\pi \left(R_\gamma \cos(\theta_{TC})\right)^2 \frac{R_\gamma \cos^2(\theta_{TC})}{\sin(\theta_{TC})}, \tag{3.40}$$

$$V_{TC} = \frac{\pi D_{res}^3 \cos^4(\theta_{TC})}{192 \sin(\theta_{TC})} \approx 0.0039 D_{res}^3, \tag{3.41}$$

where θ_{TC} is the ideal Taylor cone half angle of 49.3°. For the effect of pressure diffusion through the porous emitter, the change in volume can be evaluated by comparing the change in propellant volume from the initial condition to the steady state emission condition. At startup, the pressure throughout the emitter is uniformly at the reservoir pressure. The stored liquid associated with diffusion of pressure, V_{diff}, is evaluated over the surface of the emitter:

$$V_{Diff} = \int \Delta V_{pore} n_{pore} \, \mathrm{d}S = \frac{\pi \varepsilon R_{pore}^2 RL}{16\gamma} \left(\frac{1}{2}\varepsilon_0 E^2 - \frac{4\gamma}{D_{res}}\right), \tag{3.42}$$

where the electric field imposed on the emission surface depends on the applied voltage difference and geometry of the porous emitter. To determine whether a given emitter is expected to operate in an onset delay dominated mode or a diffusion dominated mode, a ratio of the two propellant volumes, $\hat{V}$, is formed by dividing Equation 3.41 by Equation 3.42:

$$\hat{V} = \frac{V_{TC}}{V_{Diff}} = \frac{\gamma D_{res}^3 \cos^4(\theta_{TC})}{12 \varepsilon R_{pore}^2 RL \sin(\theta_{TC})} \left(\frac{1}{2}\varepsilon_0 E^2 - \frac{4\gamma}{D_{res}}\right)^{-1}. \tag{3.43}$$

Large values of $\hat{V}$ (i.e. $\hat{V} \gg 1$) indicate that much more propellant is stored in the Taylor cone at startup than will be wicked from surface pores away from the emission surface. More specifically, available propellant will be wicked away from surface pores before filling the Taylor cone volume required for startup. For this case, it is expected that onset delay will dominate the transient response of such an emitter. On the other hand, small values for $\hat{V}$ indicate that the volume of a Taylor cone at startup will be filled well before available propellant in emitter surface pores has been depleted. For this case, it is expected that pressure diffusion will dominate the transient response. The condition $\hat{V} = 1$ is expected to be the bifurcation between these two regimes as it indicates a similar volume of propellant is associated with each transient behavior. Equation 3.43 is plotted in Figure 3.12 for a pillar emitter with various porous reservoirs, EMI-Im as a working fluid, and emitter geometry and material properties per Wright and Wirz [38]: $\gamma = 0.038\,\mathrm{Nm}^{-1}$, $R = 0.5\,\mathrm{mm}$, $L = 5\,\mathrm{mm}$, $C_E = 7.8\,\mathrm{mm}^{-1}$, $\varepsilon = 0.23$, and $R_{pore} = 1.5\,\mu\mathrm{m}$. From this plot, three major observations are noted. Firstly, onset delay is expected to dominate the transient behavior of an emitter near its startup voltage. For electrospray devices operating at emission voltages, Eq. 3.41 predicts large Taylor cone size while the volume associated with porous diffusion is small. Secondly, increasing the applied voltage is expected to cause the transient behavior to be more dominated by diffusion. The volume throughput associated with diffusion of pressure increases with voltage while the volume in a Taylor cone decreases. Finally, increasing the restorative pressure, as shown by decreasing reservoir pore size from P0 to P3, causes diffusion to dominate the transient emitter response. The restorative pressure associated with small pore-size reservoirs is expected to have a strong effect on reducing the size of Taylor cones near startup. These observations are supported by empirical evidence of onset delay dominating the transient response for porous electrospray emitters used without a porous reservoir [96] and negligible onset delay for electrospray emitters using a porous reservoir [100].

This is not to say that this is a replacement for onset delay models when characterizing the transient response of porous electrospray emitters, but rather that there are regimes where one or the other dominate the transient response. Both perspectives are important for characterizing the transient response of electrospray emitters.

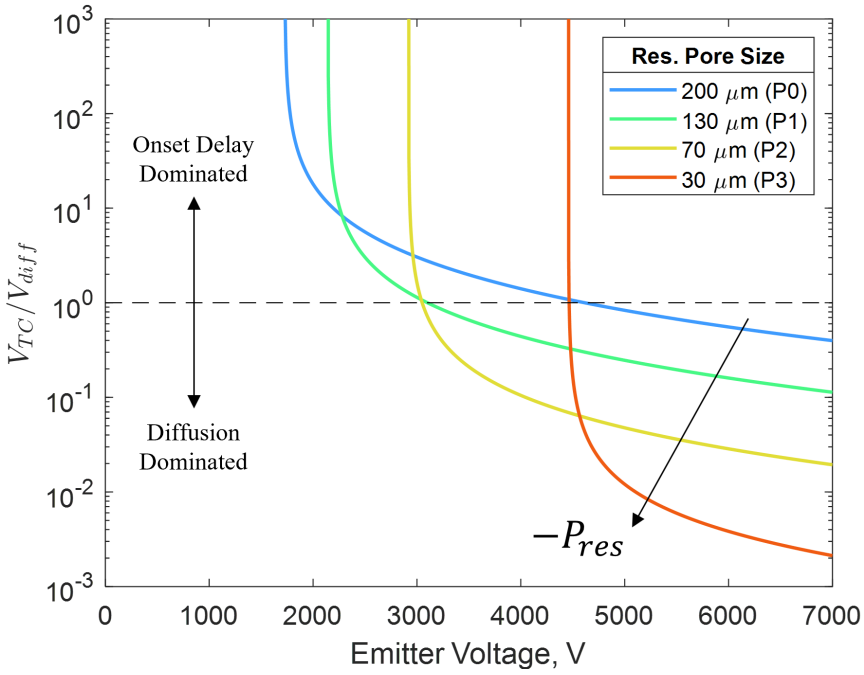

Figure 3.12: Comparing the volume required to fill a Taylor cone on the emission surface to the fluid volume stored in surface pores of the emitter as a function of emitter voltage and reservoir porosity grade. The transient response of a porous emitter is predicted to be dominated by onset delay if this volume ratio is large, or dominated by pressure diffusion if this volume is small.

3.6 Applications

In this section, we will apply the analytical flow within a pillar, cone, and wedge to available published results. To determine the settling time of a cone- or wedge-shaped porous electrospray emitter, the first eigenvalue must be determined through Equation 3.25 or 3.31. This first mode represents half-wavelength pressure oscilation, which dominates the long time-response in the domain. To apply the analytical flows, we evaluated published literature based on the inclusion of descriptions of 3 important characteristics: the porous medium, emitter geometry, and transient current response. The properties of the porous medium are necessary for determining the diffusion coefficient, the emitter geometry for determining the domain of the flow, and the transient current response for validation.

3.6.1 Cone Emitter

Recently published results from Natisin et al. [36] show a relatively detailed view of the emitter geometry and use an off-the-shelf porous medium for emitter manufacture.

Although the emitter has a pyramidal shape, the emitter is simplified as a cone where $R_O = 360\,\mu\text{m}$, $R_I = 40\,\mu\text{m}$, and $\theta_c = 16°$. The P5-grade porous material used for the emitter has 50 % porosity and 0.8 µm pore radius. The permeability is estimated as $5 \times 10^{-15}\,\text{m}^2$ from pressure to flow rate curves [101], which agrees well with an estimate for permeability of $7.1 \times 10^{-15}\,\text{m}^2$ using the Cozeny-Karman equation[57]. EMI-BF4 was used as a propellant [36, 72]. From these properties, we evaluate Eq. 3.25 numerically to find the first eigenvalue, $\lambda_1 = 808\,\text{s}^{-1}$. The inverse of the eigenvalue is the time constant for settling of the flow in the emitter, $t_c = 1.2\,\text{ms}$. Experimental evaluation indicated that the thruster reached "relatively stable emission rapidly over typical time-scales of a few milliseconds" [36]. Exponentially decaying systems nearly reach their equilibrium value after a few time constants, so the analytical prediction is in good agreement with the experimental behaviour.

3.6.2 Wedge Emitter I

In 2015, Courtney and Shea [2] used a porous wedge emitter to investigate the effect of reservoir conditions on emitted species. The material and emitter geometry were sufficiently described in order to predict the transient response using the approach described in this manuscript.

The emitter is interpretted as a wedge where $R_O = 465\,\mu\text{m}$, $R_I = 20\,\mu\text{m}$, and $\theta_w = 60°$. P5-grade porous material was used for the emitter. EMI-Im and EMI-BF4 were used as propellants separately. Through Eq. 3.31, the time constants for using EMI-Im and EMI-BF4 are predicted as 350 and 330 µs respectively. Despite its similar properties to the cone emitter from Natisin et al. [36], the emitter is expected to settle more quickly due to the reduced exposed surface area associated with the wedge domain compared to the cone domain.

Although the transient behavior was not described in the aforementioned study, Courtney later published detailed transient emission characterizations for a porous wedge emitter as part of a

different study [100]. Unfortunately the emitter dimensions and material are not publicly available, so the transient settling time cannot be predicted. However, the available data are indicative of the way that porous wedge electrospray emitters settle, albeit over a different time scale depending on the emitter material and geometry. As the device operation is settling, experimental data shows that the thrust is initially high but decreases to its steady value, while the device current increases to its equilibrium value. The trend of thrust agrees with the increased flow to the emission surface during settling as predicted by the presented theory. On the other hand, the initially low current from the device seems to disagree with the presented model, but the multiple emission sites that form on the emission surface complicate the ability to tie current measurements to mass flow rate estimates. The current may increase during settling due to a combination of onset delays, start-up emission behavior, and the sharing of flow through emission sites.

3.6.3 Wedge emitter II

Chen et al. recently constructed a wedge-shaped porous emitter capable of up to 500 µA [52]. The device uses EMI-BF4 as a working fluid, with properties as previously described. The emitter is described by half-angle, upstream radius, and downstream radius of 46°, 20 µm, and 326 µm respectively. A range of particles from 1 to 10 µm were used to produce the porous medium. If the sintered particles are assumed to be a homogeneous mixture with a porosity of 50 %, the Carman-Kozeny equation predicts a permeability range of 2.8×10^{-13} m^2 to 2.8×10^{-15} m^2 depending on the assumed particle size. However, pore size also scales with particle size, so the effect of particle size can be neglected through the assumptions used to develop Eq. 3.13. Through Eq 3.31, the emitter throughput is expected to settle with a time constant of 190 µs.

The configuration of the thruster varies from those previously discussed in this section in that it utilizes a pool reservoir instead of a porous reservoir. Additionally, a cutaway in the underside of the emitter restricts flow to the emission surface. Because of this added flow feature, it is unreasonable to assume that the flow has settled once the effect of emission site pressure has diffused to the base of the wedge. Additional time is required for the pressure to diffuse through the cutaway feature in the emitter. Experimental results show the emitter current settling over

several seconds, while a detailed view of the step response shows that the initial overshoot in current decays over a few milliseconds. To quantify the settling time constant, we fit the following function to the experimental data presented in Chen et al. [55]:

$$I = C_1 e^{-t/\tau} + C_2 t + C_3. \tag{3.44}$$

The first term in Eq. 3.44 represents the short time-scale settling associated with diffusion of pressure through the wedge, the second term approximates the long time-scale settling, and the third term describes the equilibrium state. Least squares optimization of this function to presented data yields a settling time constant of 300 µs, a 58 % overestimate of the analytically predicted time constant of 190 µs. The agreement of the experimental data and analytical prediction is quite good, given the uncertainty in emitter substrate properties. Altering the porosity to 39 % causes the estimated time constant to match the experimentally-determined time constant to 3 significant digits. We expect that the long-term settling is due to the additional diffusion distance required for pressure to penetrate through the cutaway feature in the emitter to the pool reservoir.

3.7 Discussion

In this section, we aim to discuss and review the behavior of electrospray devices as related to the transient flow model presented in this manuscript. Additionally, the model has limitations in its applicability and challenges that to its accuracy.

The five key conclusions regarding transient settling in porous emitters are as follows:

- Diffusion of pressure causes exponential decay in emission in response to voltage changes. Initially the response will be steeper-than-exponential decay due to the superposition of short and long wavelength modes. For the latter half of the emission response, short wavelength modes will have decayed and the half wavelength mode will dominate the emission response.
- Onset delay dominates the emitter response near the startup voltage. Operating at higher voltages increases the applied pressure difference on the emitter, increasing the flow through

the emitter. Because the diffusion of pressure is linear, the settling time is expected to be independent of emitter voltage. As a result, diffusion of pressure becomes more important at higher voltages.

- Onset delay becomes negligible with increasing restorative pressure. As reservoir pore size decreases, the Taylor cone volume is expected to decrease, with the settling time for diffusion of pressure again remaining constant. Diffusion becomes more important as smaller pore reservoirs are incorporated into the emitter assembly.

- Emission sites settle more quickly as they densify. As the site density increases, the region of the emitter influenced by the secondary flow to each emission site decreases, which in turn decreases the settling time. Pulsating emission sites are expected increase in frequency with proximity to adjacent emission sites.

- The settling time can be approximated even if the details of the porous medium are unknown. If the porous medium is formed from a homogeneous mixture of sintered spherical particles, the porous permeability can be estimated through the Carman-Kozeny equation. The permeability scales with the square of particle size while pore size is proportional to particle size, so the particle size has negligible effect on the diffusion coefficient.

This analysis describes the settling of flow in a porous medium, but does not investigate the flow within the Taylor cone. For a complete picture of the transient response of an electrospray emitter, it will be important to develop a deeper understanding of how the electric field manifests as a pressure well at each emission site. Coupling the emission site behavior with pressure and flow rate at the base of the Taylor cone is necessary to develop a complete understanding of the transient emission behavior. Furthermore, the quantitative comparison of pressure diffusion and onset delay models is hindered by the analytical representation of the volume required for an emission site at onset. An analytical or empirical model describing the onset volume as a function of operational conditions would be valuable for quantitative comparison of the two identified transient emission models.

The model is limited by how well the differential elements represent constant pressure surfaces. Although the analysis assumes that the isobaric surfaces are constant-y surfaces for the pillar emitter or constant-r surfaces for the cone emitter and wedge primary flow, in reality these surfaces will bulge upstream. The additional flow associated with transient settling originates from fluid volume stored in surface pores, so streamlines will be deflected towards the emitter centerline or centerplane while these pores deplete. Once the flow settles, flux from nonemitting surfaces associated with pore depletion vanishes and the constant potential surfaces match the differential elements for the transient flow. Because constant pressure surfaces approach the differential element geometry over time, the elements can be considered to reasonably approximate the flow. For a more accurate representation of transient settling, an additional direction of flow would need to be considered for each of the presented geometries (e.g. flow in the $r-$ and $\theta-$directions for the wedge primary flow) and the domain would need to be split into interior elements where Darcy's Law is enforced and exterior elements where Eq. 3.11 is enforced. Such an approach would lead to an improvement in the accuracy of analytical predictions of transient settling to the detriment of the simplicity of analytical relations produced by the effort, such as Eq. 3.31.

The menisci formed at the surface of the emitter are assumed to be contrained by single pores. However, if the manufacturing process results in a rough emitter surface, this assumption may not hold. For example, conventional machining of glass occasionally produces visible chips in the emitter between the scale of the emitter and sintered particle [43, 34]. If the roughness is of a scale less than the reservoir pore size, then menisci on the emitter surface may span multiple pores. In this case, the assumptions used to develop Eq. 3.4 may not hold, resulting in an underestimate of fluid stored in exposed pores and thus of transient settling time. Roughness over a wide range of characteristic lengths will affect the linearity of the diffusion equation, so the conclusion that flow settles over a time scale independent of pressure change would not hold. As a result, the presented diffusion equation presented in this manuscript is most applicable to emitters with smooth nonemitting surfaces.

3.8 Conclusion

In conclusion, a diffusion equation for pressure in porous electrospray devices has been developed from first principles for capillary action and porous flow. The diffusion equation explains the initial overshoot and transient decay that is commonly seen with porous electrospray emitters. Applying the diffusion equation to common emitter geometries yields predictable time constants for the flow to settle in pillar, wedge, and cone shaped emitters. Transient flow analysis complements the established onset delay model for electrospray emission; emitter design and operation affect which regime best describes the transient response of a porous emitter. As electrosprays are considered for more ambitious missions, the effects of transient flow on device lifetime, minimum impulse bit, and thrust noise spectra become more important to understand. Applying the diffusion equation to available literature has been reasonably successful where possible. We encourage future researchers to consider characterizing their porous materials and transient response in order to understand this feature of electrospray emitter operation.

CHAPTER 4

Porous Tungsten Electrospray Emitter (PoWEE) - Pillar

After finding that published transient electrospray results do not present sufficient information for validating the proposed theory for settling time, developing an electrospray thruster which allowed for full control of emitter geometry and material was necessary for investigating emitter operation. By characterizing the emitter material through ex situ experimentation and by inspecting the emitter after manufacture, the parameters contributing to the settling time could be explictily determined.

In this section, the emitter preparation and testing will be described. First, the emitter material characterization is described, including visual inspection and permeability and bubble point tests. Second, the fabrication of the emitter and assembly of the thruster is described. The *in situ* diagnostics used to investigate the thruster plume are described last. These include a high-angle beam dump, wire probe, Retarding Potential Analyzer (RPA), and long-exposure camera.

4.0.1 Steady-State Flow

In a porous electrospray emitter, propellant flows through the emitter substrate to the emission surface. The viscous loss associated with flow through a porous medium is described by Darcy's law, $\vec{u} = -\frac{k}{\mu}\nabla P$, where $\vec{u}$ is the fluid velocity, P is pressure, k is the porous permeability, and μ is the fluid viscosity. This form of Darcy's law is valid for low Reynolds number, i.e. $Re < 1$, where inertial effects can be neglected [57]. The Reynolds number is described as $Re = \rho u d/\mu$, where ρ is the fluid density, and d is the particle size in the porous medium. Applying Darcy's law to a sharpened cylinder emitter geometry used in this effortallows for us to derive a hydraulic resistance for the emitter, R_H. The emitter geometry is simplified as a cylinder and truncated cone

in series. The cone is truncated by two spheres concentric with the virtual apex of the cone; one to describe the emission surface and one to describe the base of the cone. The hydraulic resistance of the emitter is then the sum of the hydraulic resistances of the cylinder, $R_{H,cyl}$, and the cone, $R_{H,cone}$:

$$R_{H,cyl} = \frac{\mu L}{\pi R^2 k}, \tag{4.1}$$

$$R_{H,cone} = \frac{\mu}{2\pi k\left(1-\cos(\theta_c)\right)}\left(\frac{1}{R_I}-\frac{1}{R_O}\right), \tag{4.2}$$

where, L is the length of the cylinder, R is the radius of the cylinder, R_I and R_O are the inner and outer radii of the cone resepectively, and θ_c is the half-angle of the cone. Some of these geometric definitions are modified to use in the context of the described emitter geometry: R becomes R_{em}, L is replaced by $L_{em} - R_{em}/\tan(\theta_c)$, R_O becomes $R_{em}/\sin(\theta_c)$, and R_I becomes R_{tip}. Equations 4.1 and 4.2 are added to determine the emitter hydraulic resistance:

$$R_H = R_{H,cyl} + R_{H,cone} = \frac{\mu}{k}\left(\frac{1}{\pi R_{em}^2}\left(L_{em}-\frac{R_{em}}{\tan(\theta_c)}\right)+\frac{1}{2\pi\left(1-\cos(\theta_c)\right)}\left(\frac{1}{R_{tip}}-\frac{\sin\theta_c}{R_{em}}\right)\right), \tag{4.3}$$

For boundary conditions, the reservoir pressure is approximated by the Laplace pressure, or capillary pressure, from a meniscus at a fully-wetted pore upstream in the reservoir [57, 58] and the emission surface pressure is approximated by the Maxwell pressure supplied by the magnitude of the local primary extraction electric field, E_p [59, 60]. The applied pressure difference from the fluid reservoir to emission site, ΔP_{app}, is:

$$\Delta P_{app} = \frac{4\gamma}{D_{res}} - \frac{1}{2}\varepsilon_0 E_p^2, \tag{4.4}$$

where γ is the fluid surface tension coefficient, D_{res} is the characteristic reservoir pore size, and ε_0 is the permittivity of free space. The electric field on the emitter surface has a linear relation to extraction voltage and is determined by simulation of the extraction geometry. Flow through the

porous medium has been treated in this way recently to understand emission site multiplexing on a porous wedge [1].

4.0.2 Emitter Material Characterization

To test the validity of the presented models, the porous media used in supporting experiments must be adequately characterized and prepared. Both the permeability and pore size for the media for the emitter and reservoir must be characterized. The pore size is determined visually and through a hydrostatic pressure test. The permeability is determined with a driving pressure test and estimated through use of the Carman-Kozeny equation. Finally, the steps performed to prepare porous emitters after machining are described.

4.0.3 Pore Size

The simplest method of measuring pore size is through visual inspection. Due to the small size of pores in the porous tungsten material used for the emitter, a scanning electron microscope (SEM) was used to inspect the porous surface at the required magnification. Internal pores of the sample were exposed through brittle fracture of the sample. SEM images of the porous tungsten are shown in Figure 4.1. 25 pores on the exposed surface were measured by fitting an ellipse to the visible pore and finding the hydraulic diameter of the ellipse. The distribution of these pores are shown in Figure 4.1. From these measurements, the mean pore size is 1.97 µm, with a variance of 1.19 µm. This method of pore size measurement is valuable in that it provides a physical basis for other pore size measurement schemes. Unfortunately, this method is not physically relevant for the operation of an electrospray device because it does not fully capture how a fluid interacts with these pores.

To measure the pore size in a more physically accurate manner, the pores' ability to resist an applied pressure while wetted is required. A notionally identical sample to that which is shown in Figure 4.2 was immersed in a shallow ethanol bath with the open end of the porous sample facing upwards. The pressure was recorded while observing bubbles from the exposed porous surface. Localized bubbles were observed on the surface of the sample at 5 psig, with bubbles

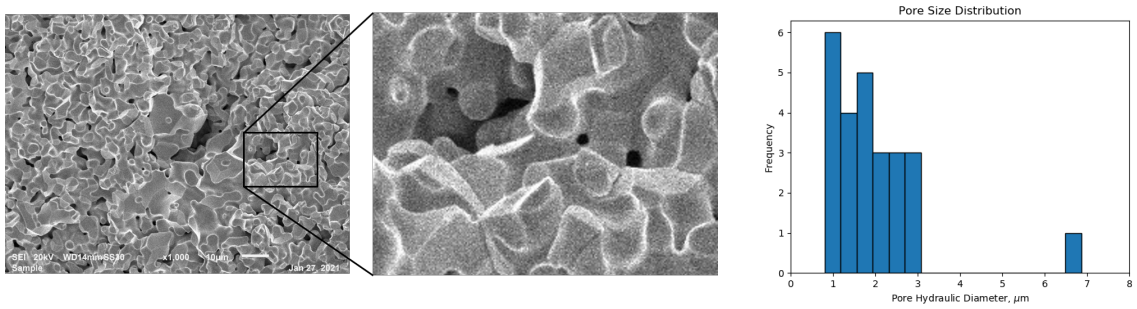

Figure 4.1: Left, scanning electron microscopy (SEM) images of the porous tungsten surface. The surface was exposed by brittle fracture. Four small pores through which fluid travels are seen in the center image, a zoomed-in view of left. Right, histogram of the hydraulic diameter of 25 visible pores on the exposed surface of the tungsten sample.

emerging across the surface at 6 psig. From these observations, I conclude that the pore size in the sample is 2 µm to 3 µm. [102] The sample porosity and particle size support the accuracy of this measurement.

4.0.4 Permeability

Permeability can be estimated using the Carman-Kozeny equation: [57]

$$k = \Phi_s \frac{\alpha^3 D_{part}^2}{180(1-\alpha)^2} \tag{4.5}$$

where Φ_s is the sphericity of particles, α is the material open volume fraction, and D_{part} is the particle diameter. For simplicity, the particles are assumed to be spherical, so $\Phi_s = 1$. The porosity of the porous tungsten is approximately 25%, and the particle size is estimated to be on the order of 10 µm from the SEM images of the porous material. From these properties, the porous permeability of the porous tungsten sample can be estimated as 1.5×10^{-14} m^2.This estimation is limited in its usefulness by the difficulty in accurately measuring partical diameter and the validity of the assumption of spherical particles, but provides a basis on which to judge the accuracy of permeability measurements.

The permeability of a sample can be measured through the pressure required to drive flow through a porous sample. A mass flow controller (MFC) is used to measure both the pressure and

flow rate of nitrogen into the porous sample simultaneously. A diagram of the flow and a picture of the experimental apparatus are shown in Figure 4.2.

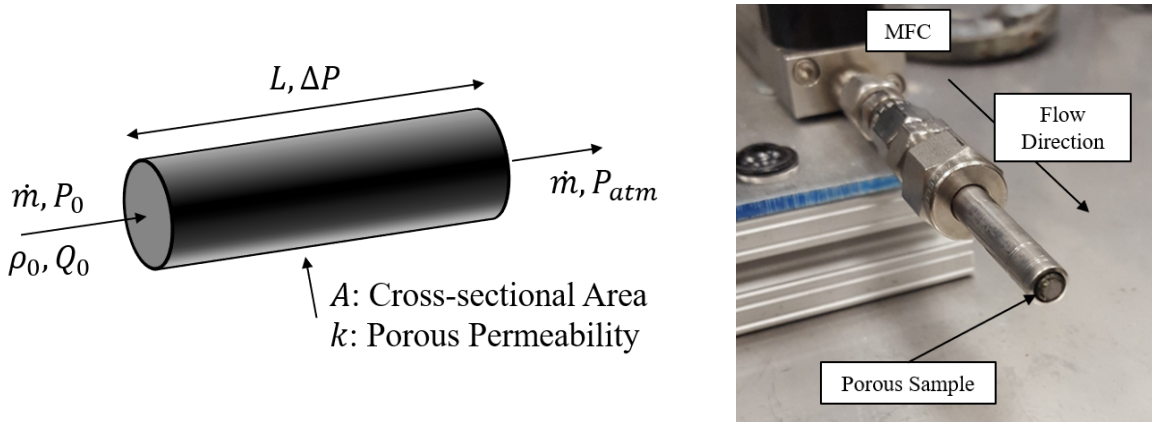

Figure 4.2: Left, the flow diagram for determining the permeability of a cylindrical sample from the pressurized flow rate response. Right, the experimental setup for the porous sample held in place downstream of a mass flow controller (MFC).

Pressure and flow rate are measured and recorded from the MFC during this process. Pressure in the upstream volume decreases as gas escapes from the system, producing a sweep of flow rate as a function of driving pressure. Pressure as a function of flow rate for a typical test is shown in Figure 4.3. Using the Ohm's law analogy for fluid flow, the slope at any point on the P-Q curve is the hydraulic resistance. The hydraulic resistance can then be substituded into Darcy's law to detemine the porous permeability:

$$\frac{\Delta P}{L} = R_{hyd} \rightarrow \frac{\mathrm{d}P}{\mathrm{d}x} = -\frac{\mu Q}{kA}, \tag{4.6}$$

where ΔP is the pressure drop across the porous sample, R_{hyd} is the hydraulic resistance of the sample, L and A are the length and cross-sectional area of the sample respectively, k is the porous permeability of the material, μ is the viscosity of the working fluid, and Q is the volumetric flow rate recorded by the MFC. Such a naive approach is valid for low driving pressures, however the working fluid's compressibility will cause the fluid to accelerate as it expands during decompression through for higher driving pressures. Although velocity and volumetric flow rate are not constant through the sample, mass flow rate is constant. To account for fluid compressibility, the

ideal gas law is used as an equation of state to describe changes in density due to fluid pressure. The sample is assumed to be isothermal. The pressure bounds of P_0 at the inlet to the sample and P_{atm} at the exit of the sample are applied. Bear shows how this approach yields the expected flow rate for a given pressure drop across a porous sample: [57]

$$Q_0 = \frac{kA}{2\mu P_0 L}\left(P_0^2 - P_{atm}^2\right). \tag{4.7}$$

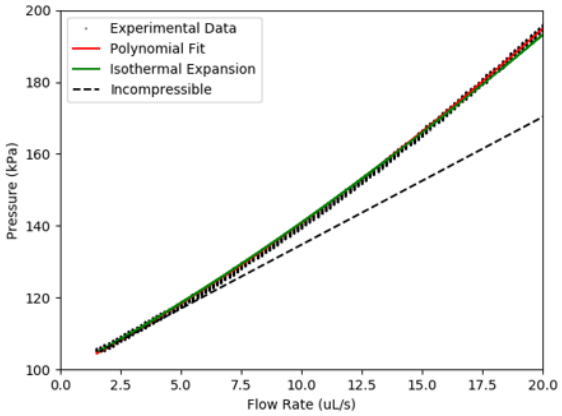

Figure 4.3: Pressure required to drive flow through the porous sample. The slope of the curve at any point is the hydraulic resistance of the sample.

To produce the plot shown in Figure 4.3, permeabilty was first determined by performing a polynomial fit on experimental data to determine the limit in hydraulic resistance as driving pressure aproaches 0. With this permeability, the nonlinear response of the system at higher driving pressures is predicted using Equation 4.7. As shown by the 'Isothermal Expansion' curve in Figure 4.3, assuming isothermal expansion of a compressible gas accurately describes the response of the system. The measurement of permeability obtained using this procedure is 7.83×10^{-15} m^2, or about half of what was predicted by the Carman-Kozeny equation. These two permeability values are within an order of magnitude, lending credence to the validity of the permeability measurement. The overestimation by the Carman-Kozeny equation is possibly due to the sphericity assumption to describe the particles of the medium. The particles shown in Figure 4.1 are clearly not spherical, so the increased tortuosity of the flow path due to this configuration may have decreased the porous permeability to the measured value.

4.0.5 Emitter Fabrication and Assembly

The emitter was manufactured from 3 mm diameter porous tungsten rod. The emitter shape consists of a 5 mm tall, 1 mm diameter pillar sharpened to a 30° half angle, on top of a base of 3 mm and 1.6 mm height. After conventionally machining the porous tungsten rod to rough dimensions on a lathe, surface pores were electrochemically etched open using the process described by Brady for sharpening tungsten wires. [103] The resulting tip of the emitter had a radius of roughly 100 µm. The emitter and a close up view of its emission surface can be seen in Figure 4.4.

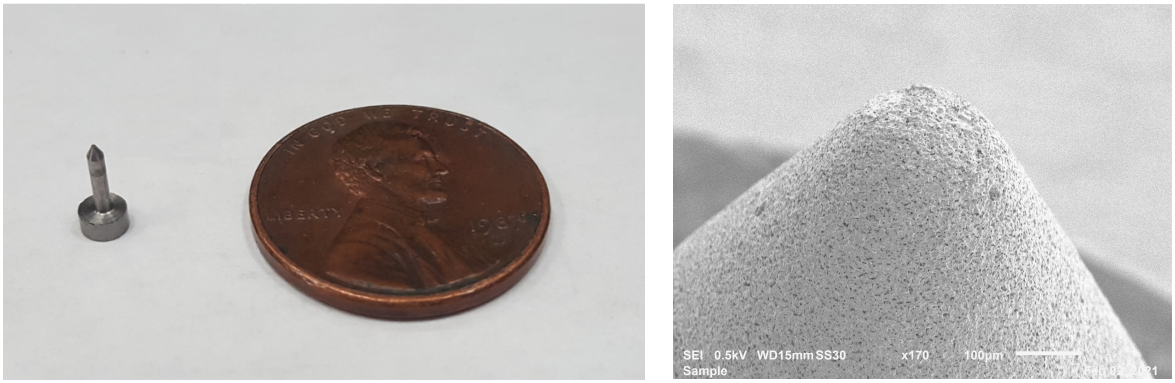

Figure 4.4: Left, conventionally machined porous tungsten emitter with US penny for scale. Right, SEM image of the emitter tip after electrochemical etching.

The electrospray thruster configuration used in this effort draws inspiration from recent porous electrospray development efforts around the globe. [2, 34, 36, 46] An emitter with a small pore size is used in combination with a relatively larger pore size reservoir. A P2-grade borosicate glass frit was used for the reservoir, and qualitative-grade filter paper was used as the interface between the emitter and reservoir. A thin filter paper acted as a means of hydraulically coupling the reservoir to the emitter. The fluid stack was clamped to the ultem housing by a stainless steel emitter holder, while a wave spring ensured adequate contract between the emitter, filter paper, and reservoir. An extractor with a circular aperture was then held in close proximity to the tip of the emitter and secured to the ultem housing. EMI-Im was used for the propellant, which was added through the emitter in atmosphere after assembly. A diagram and photo of the emitter are shown in Figure 4.5.

Based on the emitter geometry and propellant properties, Equation 3.18 can be applied to esti-

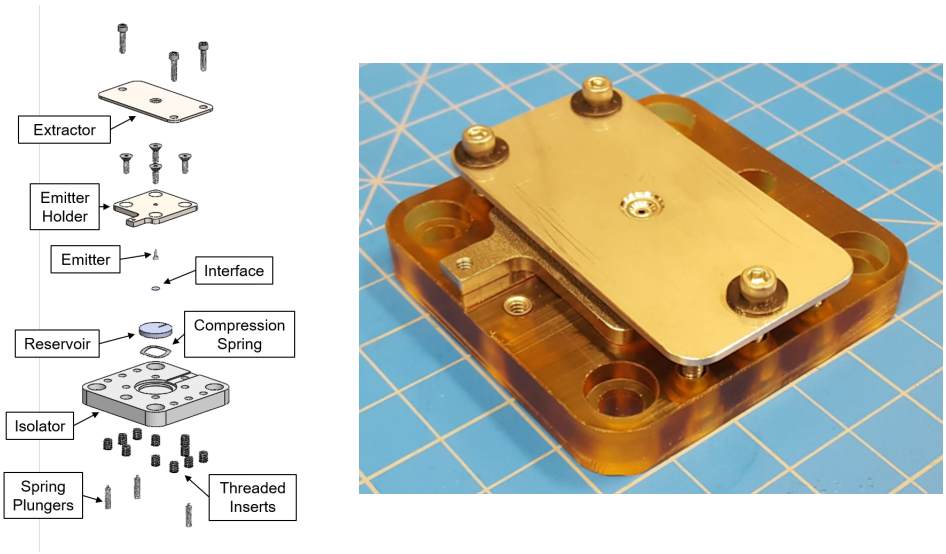

Figure 4.5: Left, an exploded view of the thruster design. Right, thruster as fabricated and assembled.

mate the thruster settling time. The surface tension and viscosity of EMI-Im at room temperature are 0.0381 N/m and 0.028 Pa s respectively [104, 105]. The emitter had a length and radius of 5 mm and 0.5 mm respectively. The porous material was determined to have a porous permeability of 7.8×10^{-15} m^2, a pore radius of roughly 1.5 µm, and a porosity of 23 %. Based on these properties, Equation 3.18 predicts a settling time of 80 ms.

4.0.6 Diagnostics

The thruster was tested in vacuum with multiple diagnostics downstream for analyzing the plume of the electrospray emitter. A linear stage is used to move the thruster between different positions where each of the diagnostics can be used. When positioned in the center of the linear stage, the plume of the electrospray emitter intercepts with a downstream beam dump for measuring the current from the electrospray emitter. The beam dump was constructed from a stainless steel sheet and formed into a half-cylinder of 60 cm diameter and 50 cm length. Moving the thruster to either end of the linear stage allows for plume characterization using a swept wire probe or RPA. A long-exposure camera is used to view emitter glow during operation. A diagram of the experimental setup in vacuum is shown in Figure 4.6.

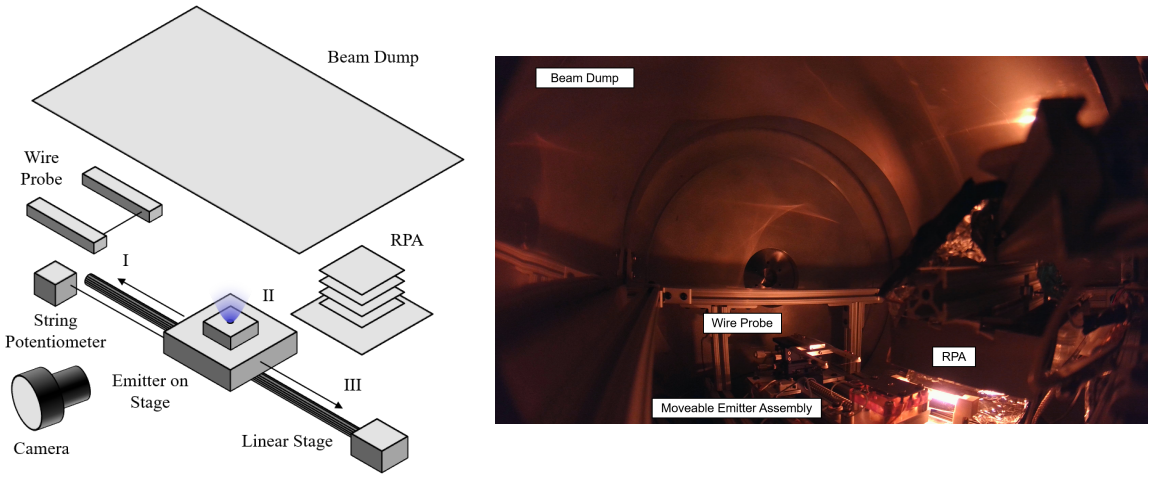

Figure 4.6: Left, experimental setup in vacuum, with a motorized stage for moving the thruster between multiple testing positions. Right, the experimental setup shown in vacuum during bakeout.

A retarding potential analyzer (RPA) was constructed to determine the potential drop from electrospray emission and to identify fragmented species in the plume. Stainless steel mesh with 73% transparency and 1.4 mm square openings was used for the grids. The thruster-facing grid was held at ground potential. The electron repelling and secondary suppression grids were controlled between 0 and -25 V. The current to the collector plate was measured while the retarding grid potential was varied from 0 to 5000 V. A diagram of the RPA is shown in Figure 4.7. For use in vacuum, the RPA shown in Figure 4.7 was housed in a stainless steel box with a 1.9 cm aperture. Each grid in the RPA was constructed with a larger grid diameter than the housing aperture.

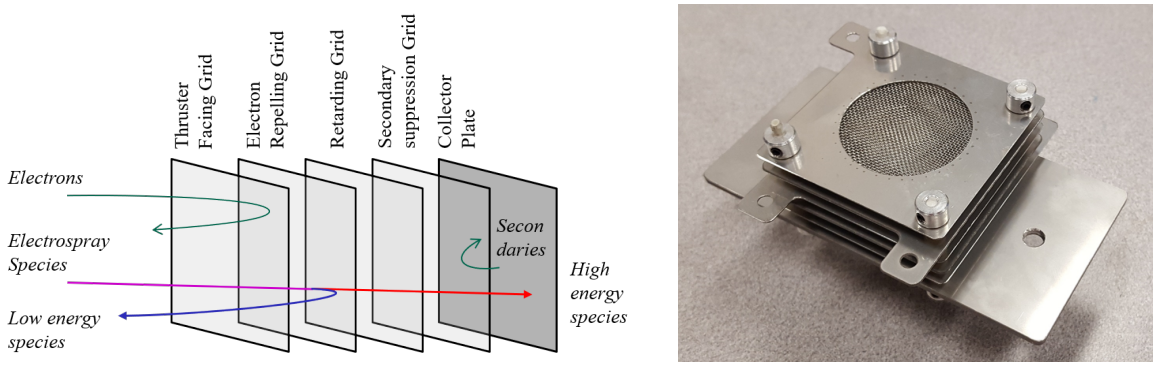

Figure 4.7: Left, simplified diagram of the working principle of the retarding potential analyzer. Right, the retarding potential as fabricated.

A wire probe is placed at the opposite end of the motorized stage from the RPA. By sweeping the thruster under a thin wire, the 1D shape of the plume can be measured quickly. A 0.127 mm diameter tungsten wire was held 4.3 mm downstream of the extractor so as to have negligible effect on the extraction electric field at the emitter surface.

4.1 Results and Discussion

While measuring current to the beam dump, *I-V* curves were obtained at slow ($\sim$10 s) and fast ($\sim$1 s) sweeping times. The emitter shows roughly the same *I-V* response in either case, although the fast *I-V* curves were much smoother. The abrupt increases in current when increasing voltage slowly were likely due to less stable emission sites turning on during the sweep. Experimental *I-V* curves are shown in the left side of Figure 4.8. The predicted mass flow rate as a function of applied voltage on the right side of Figure 4.8, using Equations 4.3 and 4.4. Experimental measurements of current indicate that startup occured at roughly 1000 V higher than expected, which may be due to inaccuracy estimating the emitter electric field. Decreasing the emitter electric field by 30 % brings the two startup voltage in line. Despite this disrepancy, predicted flow rate up of to 300 ng/s matches well with experimental measurements of a few emission sites on the emitter and rough estimates from literature of the flow to each emission site being $\sim$100 ng/s [4]. Comparing the predicted mass flow rate and emitter current, the average specific charge of emitted species was about 50 C/g, which would indicate that the emitter operated in a droplet emission mode or mixed droplet-ion emission mode.

The thruster response to abrupt voltage-on events was also measured. To capture the effects of porous flow onset, the thruster was not subjected to an extraction voltage for several minutes prior to testing. Monitoring the current response over a short period shows a current response in line with results from literature, [106] as shown in Figure 4.9. After an initial spike in current, emission settles over a time scale similar to the predicted settling time for the emitter. The current monitored over a longer period shows a more featured response, as shown in Figure 4.10. Current initially decreases until about 20 s after onset, but increases again after 100 s. Intermittent increases in

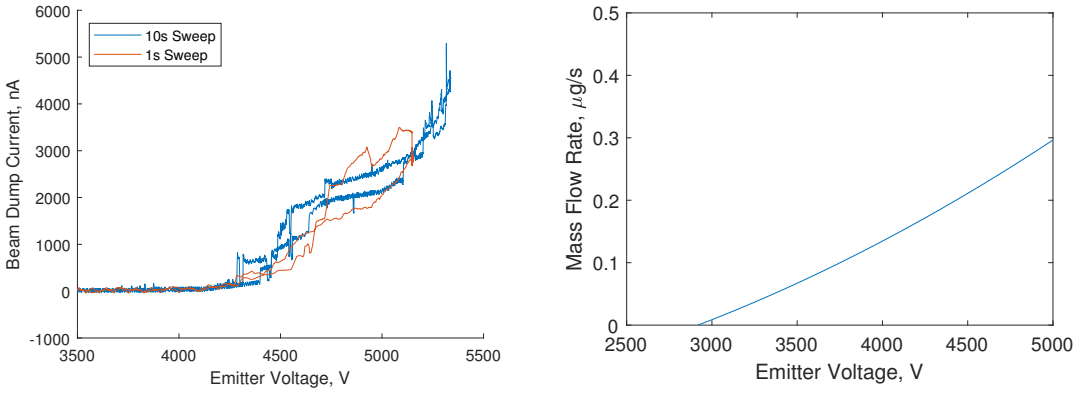

Figure 4.8: Left, simplified diagram of the working principle of the retarding potential analyzer. Right, the retarding potential as fabricated.

current are also observed after 100 s, likely due to additional emission sites initiating and settling.

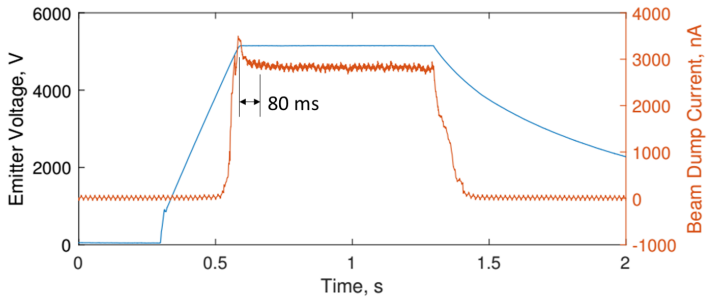

Figure 4.9: Current response of the thruster when abruptly subjected to an emitter voltage of 5.15 kV. The predicted settling time of 80 ms is shown from the current peak.

The motorized linear stage was used to sweep the thruster continuously back and forth under the wire probe after abruptly voltage initiation. This setup produced a plume sweep every 3.3 s in alternating directions. The current measured on the wire probe was correlated with thruster position via a string potentiometer to produce 1-D plume profiles. The time dependent wire probe current and plume profiles at two emitter voltages are shown in Figure 4.11. The location is provided with reference to the emitter centerline. These data suggest that the plume was produced by multiple emission sites on the tip of the emitter. At 5.08 kV emitter voltage, plumes from two emission sites are apparent, with an intermittent emission site along the centerline. A fourth emission

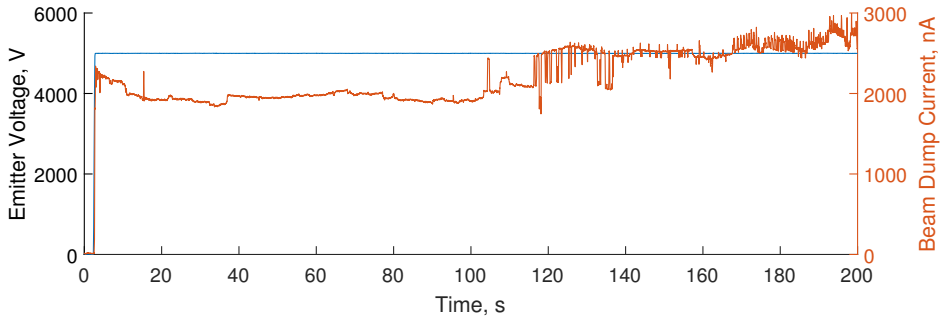

Figure 4.10: Current response of the thruster when abruptly subjected to an emitter voltage of 5.00 kV.

site may have been intermittently present between the two prominent emission sites, as indicated by occasional widening of the rightmost emission site. At 5.08 kV emitter voltage, many more emission sites are present. The plumes of each site are more overlapped than at lower voltage, indicating that emission sites have become more densely packed; emission site spacing decreasing with voltage is consistent with the predicted behavior of porous wedge electrospray devices[1] and with reported experimental results.[53] From the independent peaks that appear over the course of the 200 s measurement, it is likely that at least 6 emission sites existed on the emitter tip at this voltage setpoint.

Due to the uncertain nature of intermittent emission sites, it is difficult to make conclusions regarding intermittent emission sites from the wire probe data. intermitten emission would only be recorded with the wire probe if it was in the correct position during one of these events. Therefore it is unlikely that all intermittent emission events were captured by the wire probe. However, intermittent emission was recorded by the wireprobe along the centerline within the first 40 s after startup and after 130 s with the emitter at 5.08 kV (i.e. in the left plot of Figure 4.11. These measurements coincide with the periods when unsteady emission was measured by the beam dump, in Figure 4.10, supporting the claim that the unsteady current was due to intermittent emission sites.

Retarding potential curves were obtained with the thruster operating at 5.00 kV emitter voltage. The electron repelling grid and secondary suppression grids were held at the same voltage and operated from 0 to -25 V. The thruster was operated at a constant voltage for several minutes

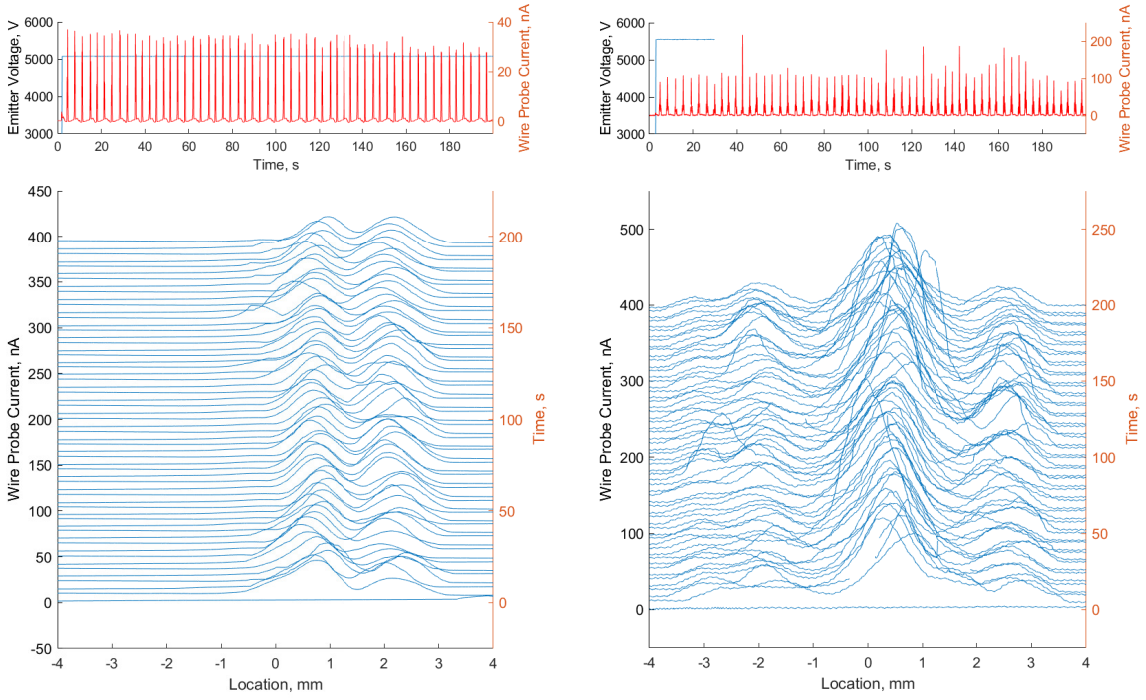

Figure 4.11: 1-D plume sweeps of the thruster after subjected to an abrupt voltage initiation. Plume sweeps are continuosly adjusted upwards with time in the lower plots to distinguish individual sweeps. The time of each sweep is indicated by the intercept with the right axis. Left, 5.08 kV emitter voltage and right, 5.55 kV emitter voltage.

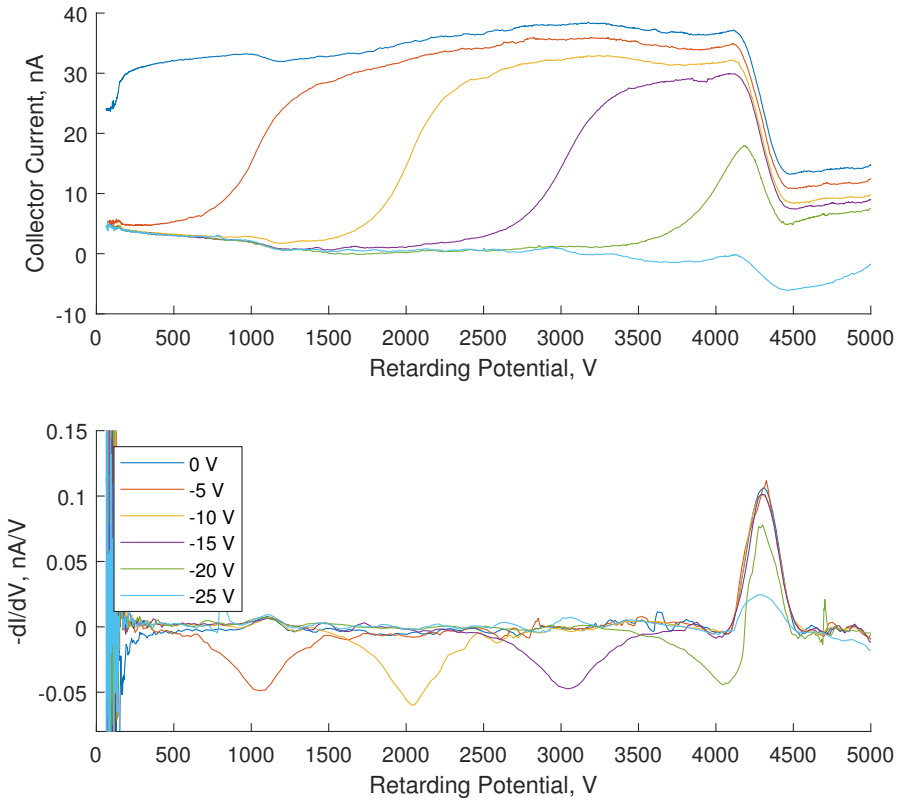

Figure 4.12: Results from the retarding potential analyzer with the thruster operating at 5.00 kV emitter voltage. Each curve represents a different electron suppression grid voltage, with the voltage indicated in the legend in the lower plot. Each top curve was differentiated to produce the energy distribution shown below.

before operating the RPA. An energy distribution function (EDF) was produced by numerically differentiating the collector current with respect to retarding potential. Current measured to the collector steeply dropped between 4.10 and 4.47 kV retarding potential voltage, indicating a plume potential of 4.3 kV. Thus, a potential drop of 700 V occurs during the emission process. Smaller peaks in the energy distribution function across all electron suppression grid voltages are visible at 1.1 kV and 3.5 kV.

Inspection of the emitter and extractor after several hours of emission show evidence of non-uniform emission from the emitter tip. Images of both the extractor and emitter are shown in

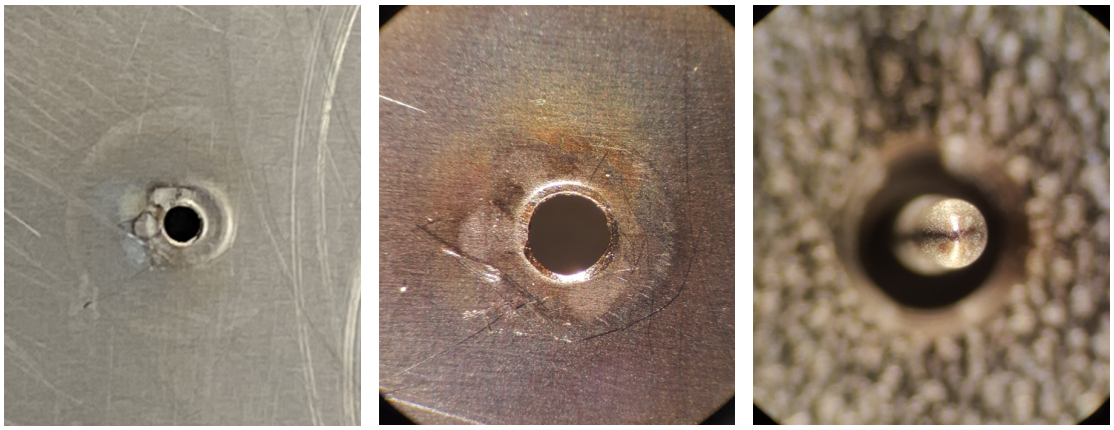

Figure 4.13: Images of the top of the emitter (right) and underside of the extractor (left and center) after testing. The extractor was flipped laterally for these pictures, so the left side of the extractor corresponds to the right side of the emitter, and vice versa. The center and right images were taken at the same magnification.

Figure 4.13. Both the extractor and emitter show similar flower petal-shaped patterns where bright areas that widen away from the centerline are surrounded by dark outlines. These patterns appear on the right side of the emitter and left side of the extractor, which would be aligned when assembled. These patterns are further evidence of multiple emission sites on the tip of the emitter. The patterns were likely caused by a combination of propellant decomposition and secondary emission due to propellant impingement. [107]

From the time-dependent current response shown in Figure 4.10, it is clear that the current from the emitter takes as least as long as 120 s to settle. Furthermore, the current response and 1-D plume sweeps shown in Figure 4.11 suggest that the increase in measured current from the emitter after about 120 was due to intermittent emission from new sites. Formation of multiple emission sites occurs on a porous surface due to the combined effects of the subsurface flow and local electric field. Because the emitter voltage was held constant, it is unlikely that formation of new emission sites was caused by a change in the local electric field. Thus, new emission sites starting up around 120 s after emitter voltage intiation were likely caused by a change in the subsurface flow to the emission sites, and change in subsurface flow after 120 s is consistent with the proposed model for the transient response of flow in a porous emitter. These results show that flow in the emitter may

develop over a longer period than predicted by Equation 3.18. Whether the flow may settle over this time scale is subject to future analytical investigation.

4.2 Conclusion

In conclusion, a diffusion equation for transient flow in a porous medium with exposed menisci has been proposed. To validate this model, a porous tungsten electrospray emitter has been developed and tested at the UCLA Plasma and Space Propulsion Lab. The pillar shape electrospray emitter is optimal for validating the proposed diffusion equation due to the ease of solving the equation analytically. Measurements of the current response from the emitter show that the short term response corroborates the predicted settling time of 80 ms. 1-D plume sweeps of the emitter suggest that the flow to the emitter may flow components that develop over time scales longer than predicted. Additionally, images taken after emission and the 1-D plume sweeps show evidence of emission site multiplexing on the tip of the emitter, which may complicate the flow analysis.

CHAPTER 5

Porous Tungsten Electrospray Emitter (PoWEE) - Wedge

5.1 Introduction

To understand the fluid effects responsible for emergent behavior from porous electrospray emitters, I have developed multiple complementary models from first principles of porous flow, electrostatics, and hydrodynamics as described in Chapters 2 and 3. The steady state flow through a porous electrospray device has been described by Darcy's law in the porous medium and the applied pressure difference across the device. A model to describe emission site multiplexing on a porous wedge has been developed. Additionally, the transient response of a porous emitter is affected by the volume required for onset of emission and diffusion of pressure through the porous medium. To capture transient device behavior, an analytical model has been developed to describe the role of fluid storage in transverse exposed pores on flow settling. The applicability of these models is limited by their lack of validation. As a result, the objective of this effort is to develop a porous wedge electrospray device to inform these proposed flow models.

5.2 Approach

The experimental investigation of porous electrospray emitters combines analytical models, experimental characterization, and computational methods to investigate the various effects contributing to device operation and performance. Both the experiments and analytical models focus on understanding emission from a sharpened wedge, with a porous reservoir to provide a restorative pressure. Supporting experiments include measuring the porous permeability and pore size of the porous material used for the emitter and reservoir. Computational modeling is used to evaluate the

electric field at the emission surface. These results aid the analytical models developed for steady and transient flow through the emitter by establishing the emission surface pressure boundary condition. Experimental results from emitter testing using characterized porous materials inform the flow models to provide insight into emission physics. A swept wire probe is used to determine the plume shape near the emission surface.

5.3 Analytical Models

The development of steady state, transient, and multiplexing flow models for electrospray emitters is discussed in this section.

5.3.1 Steady Flow Model

In a porous electrospray emitter, propellant flows through the emitter substrate to the emission surface. The viscous loss associated with flow through a porous medium is described by Darcy's law, $\vec{u} = -\frac{k}{\mu}\nabla P$, where $\vec{u}$ is the fluid velocity, P is pressure, k is the porous permeability, and μ is the fluid viscosity. This form of Darcy's law is valid for low Reynolds number, i.e. $\mathrm{Re} < 1$, where inertial effects can be neglected [57]. The Reynolds number is described as $\mathrm{Re} = \rho u d/\mu$, where ρ is the fluid density, and d is the particle size in the porous medium. Applying Darcy's law to a wedge emitter geometry allows for us to derive an analytical prediction for pressure in the emitter based on the emitter geometry:

$$P_s(r) = \frac{\ln\left(\frac{R_1}{r}\right)}{\ln\left(\frac{R_1}{R_2}\right)}\left(\frac{4\gamma}{D_{res}} - \frac{1}{2}\varepsilon_0 E_p^2\right) - \frac{4\gamma}{D_{res}}, \tag{5.1}$$

where R_1 is the base of the emitter, R_2 is the emission surface, γ is the surface tension coefficient of the propellant, D_{res} is the pore diameter in the reservoir, ε_0 is the free space permittivity, and E_p is the electric field at the emission surface. Equation 5.1 predicts that flow rate in a porous emitter has a quadratic dependence on emitter voltage once the startup voltage is exceeded.

5.3.2 Emission Site Multiplexing

Porous wedge electrospray emitters have a long and thin surface where a high electric field creates multiple emission sites from the emitter. In an analytical model, flow through the porous medium has been coupled with the electric field produced by the charge concentration at each emission site to understand emission site multiplexing [1]. The model produced the following relation for emission site spacing as a function of thruster operating parameters.

$$\frac{1}{\lambda^7}\frac{K_1\left(\frac{2\pi R_2}{\lambda}\right)}{K_0\left(\frac{2\pi R_2}{\lambda}\right)} = \frac{\varepsilon_0^5 E_p^{10}}{2^{17}\pi\gamma^6 R_2 \ln\left(\frac{R_2}{R_1}\right)}\left(\frac{4\gamma}{D_{res}} - \frac{1}{2}\varepsilon_0 E_p^2\right). \tag{5.2}$$

The relationship above serves as an analytical prediction for site spacing, as there is little data published for site density on a porous wedge electrospray emitter. Recent published data for the number of emission sites on a porous emitter match the trends of the number of emission sites with emitter voltage [52]. The model would benefit from validation with a characterized electrospray emitter.

5.3.3 Transient Diffusion of Pressure in Porous Electrosprays

Diffusion of pressure through a porous electrospray can be described through how the meniscus recedes at the emitter surfaces where emission does not occur. Surface tension causes the surface curvature to change with the local pressure, which is enforced through Darcy's law. Even though the flow through porous electrospray emitters is generally low Reynolds number, which is typically associated with instantaneous reaction to pressure changes, the pressure-dependent accumulation of propellant at the surface of the emitter can cause transient flow conditions. Evaluating the change in storable propellant at exposed pores due to the Young-Laplace equation yields a diffusion equation for pressure in a porous medium with an exposed surface, where D is the diffusion coefficient for this flow:

$$\frac{\partial}{\partial t}P = D\nabla^2 P; \quad D = \frac{16\gamma k}{\alpha\mu R_{pore}^2}\frac{\mathrm{d}V}{\mathrm{d}A}. \tag{5.3}$$

This diffusion equation has provided useful predictions for the transient response of a porous pillar style electrospray emitter [38]. In a wedge electrospray emitter, two time constants are expected to emerge based on the relevant length scales for the base flow (emitter size) and flow separation to each emission site (site spacing). A more detailed description of porous diffusion in electrospray emitters and analytical predictions for diffusion in cone, pillar, and wedge emitters have been developed for a manuscript in submission, as described earlier in this dissertation [37].

5.4 Experimentation

The previously discussed analytical models are supported by *in situ* and *ex situ* experimentation. In this section, the porous media characterization and *in vacuo* emission testing with a wire probe will be discussed.

5.4.1 Porous Media Characterization

I have developed experimental apparatus for testing porous permeability and pore size. Porous permeability is evaluated by flowing a pressurized gas through a porous sample of known size and measuring the flow rate. The pressure and flow rate are simultaneously measured using a Mass Flow Controller (MFC). This device and the results from material characterization have been previously discussed [38]. The porous material was determined to have a porous permeability of $7.83 \times 10^{-15}\,\mathrm{m}^2$ and a mean pore size of $2.0\,\mu\mathrm{m}$.

5.4.2 Porous Emitter Experimentation

A wedge-shaped electrospray emitter has been fabricated from 3 mm diameter porous tungsten rod. The wedge shape was formed by wire Electric Discharge Machining (EDM). The Wire-EDM manufacturing process is non-abrasive which should improve emitter tip quality but adds contaminants to the emitter and may seal surface pores. Contaminants were removed using ultrasonic agitation in a heated degreaser solution for 1 min. Surface pores were opened by electrochemically etching in 2M NaOH, borrowing from the procedure used by Brady et al. [103]. An alternating

voltage of 6 V was applied to the emitter for 15 s. These two etching and degreasing procedures were repeated alternatingly 3 times each. This procedure resulted in an emitter with open pores both at and away from the emission surface, as revealed by Scanning Electron Microscope (SEM) imagery of the emitter before assembly shown in Figure 5.2.

The emitter assembly utilizes a fluid stack that is comparable to porous electrospray thrusters using emitters manufactured from porous glass [2, 34, 35, 36]. A view of the emitter assembly is shown in Figure 5.1. As for the wedge geometry, the emitter has a total length of 17.8 mm, a full-angle of 60°, and a height of 2.54 mm. The etching process produced an emission surface radius of 30 to 50 µm. A stainless steel extractor is placed downstream of the emitter. The extractor aperture has a 1 mm width. The emitter to extractor distance varies between 0.15 mm and 0.19 mm over the length of the emitter. With these geometric constraints, cimulation of the extraction field suggests an electric field of 7 mm in propotion to extraction voltage. A P3-grade porous glass reservoir was used to provide a controlled backpressure in the emitter. The small piece of filter paper placed between the emitter and reservoir helps to ensure hydraulic coupling of the two, and a spring behind the reservoir provided a compression force between these components.

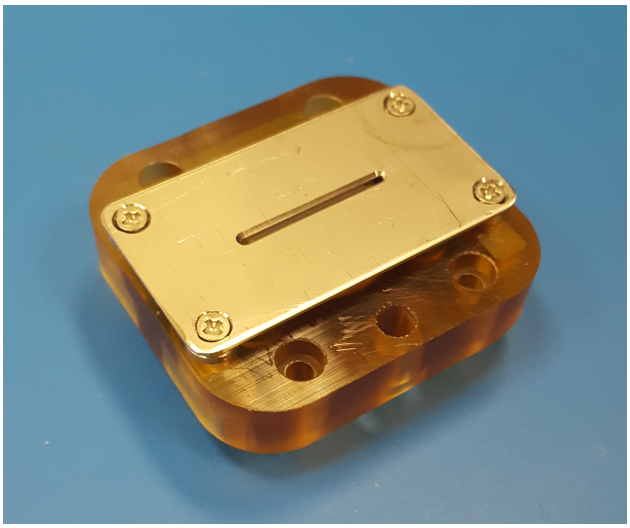

Figure 5.1: The porous tungsten electrospray emitter (PoWEE). The outer dimensions of the assembly are roughly 50 by 45 by 13 mm.

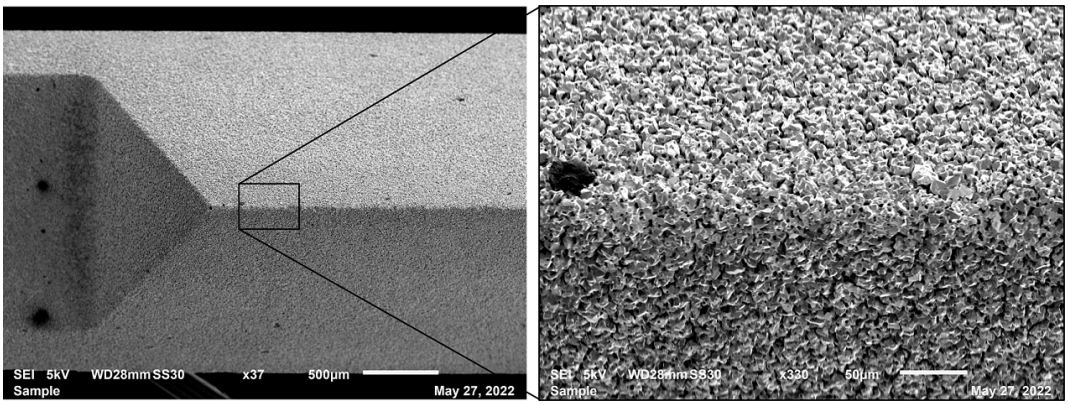

Figure 5.2: SEM of the porous wedge emitter after degreasing, etching, and cleaning.

5.4.3 Diagnostics

PoWEE was operated in a vacuum chamber with a 56 cm diameter stainless steel half-cylinder beam target downstream. The beam target was isolated from the chamber to allow for biasing on the order of 1 kV. A halogen lamp was used for heating the device before operation, to reduce propellant water content [108].

A number of diagnostics are used in vacuum to characterize the porous electrospray emitter. A wire probe was used to characterize the plume of the electrospray emitter. Wire probes have been used previously to understand spatial uniformity in a multiple wedge electrospray thruster [54, 109]. A wire probe assembly has been developed to sweep a grounded, 51 µm diameter tungsten wire 1.8 mm downstream of the emission surface of the PoWEE thruster. The wire measures incident current through a slice of the plume nominally oriented perpendicular to the emitter edge. Rotation of the thruster is included in the experimental setup for the ability to replicate the experimental setup used to create 2D tomographical maps of current flux using the BET-300-P thruster [54, 109]. With a single wedge present, emission sites notionally form in a straight line along the sharp edge; orienting the wire probe perpendicular to the ridgeline-direction allows for characterization of the plumes from individual emission sites on the emitter. The wire probe is mounted on a manual z-stage for fine adjustment ex situ and a motorized linear stage for sweeping across the emission surface in situ. The rotary stage can be actuated continuously in situ. On top of the rotary stage is a manual xy-stage onto which the thruster is mounted, for aligning the rotary axis with the

center of the emitter ex situ. The wire probe stage position was measured using a wire encoder. This assembly is shown in Figure 5.3. Stepper motors for actuating the linear and rotary stages were controlled by Arduino.

Two long exposure cameras (ZWO ASI178MC and ZWO ASI178MM, color and monochrome respectively) were used in situ for visualization of the emitter and experimental setup. Both cameras support very long exposure times of up to 2000 s for applications such as astronomical observations, although 60 s to 200 s exposures were generally adequate for photographing emitter illumination from a short distance. The monochrome camera was used for a close view of the emitter in operation while the color camera was used farther away for a wide view of the experimental setup.

High voltage was delivered to the emitter using an Ultravolt 6LE DC-DC converter. Two current amplifiers were developed in-house using high-side sensing configurations to measure currents to the emitter and the beam target. The extractor was grounded via an in-house developed low-side current-sensing amplifier. The wire probe current to ground was measured using a Keithley 6517B electrometer. Data were recorded using a National Instruments USB-6001 DAQ at a sample rate on the order of 5 kHz, depending on the experiment.

5.5 Results

PoWEE was operated in vacuum at the UCLA Plasma and Space Propulsion's HOAGIE facility [110, 38]. The emitter was loaded with EMI-Im in atmosphere during assembly. Prior to testing, the assembly was heated to 45°C at high vacuum for 12 h to remove water content [108]. All measurements were taken at a vacuum pressure of 3.2×10^{-5} torr or less.

The steady response of PoWEE was evaluated after operating at a nominal setpoint for a few minutes. Over such a period, extractor impingement could decrease by up to 50 % to its steady value. After this sort of conditioning, steady current measurements were obtained for 5 s after the emitter power supply reached its set point. Current measurements as a function of emitter voltage, or *IV* curves, are shown in Figure 5.4. The measured extractor current was below 0.5 % of the

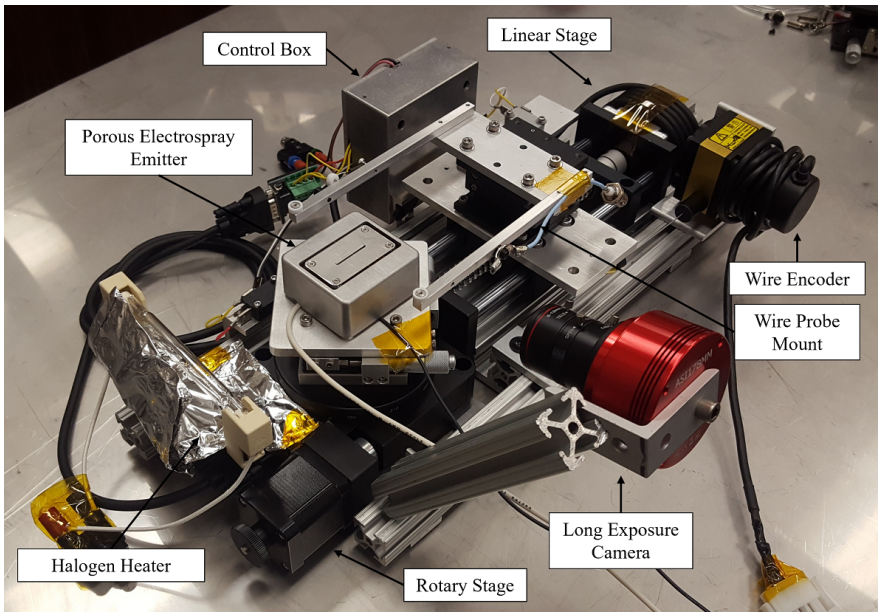

Figure 5.3: Wire probe test stand for far upstream plume characterization. A wire can be swept linearly just downstream from the emission surface while the emitter can be rotated for 2D plume mapping.

emitter current over the operational envelope of the device. Extractor current was initially low, i.e. less than 5 nA below 3300 V emitter voltage, but increased at higher emitter voltages.

A beam target bias of 30 V was implemented after investigating its effect on emitter illumination and extractor current. A potential of 30 V was chosen by varying the target potential during operation at 3500 V emitter potential until extractor current reached a minumum. Increasing the target potential further had a negligible effect on extractor current. As shown in Figure 5.5, beam target biasing reduced the extractor current fraction by 93 % at the given setpoint. Figure 5.6 shows that beam target bias had a negligible effect on most of the illumination in the facility, but drastically reduced the illumination produced at the emission surface.

Plume characterization was performed using orthogonal sweeps of the wire probe. Results from translating the wire probe along ridge of the wedge are shown in Figure 5.19a. The plumes of individual emission sites are distinguishable at low voltages and overlap at higher voltages. At low voltage, approximately 7 emission sites are present on the emitter, while 50 or more emission sites are present at higher voltages. Isolated individual plumes have a width of about 0.25 mm

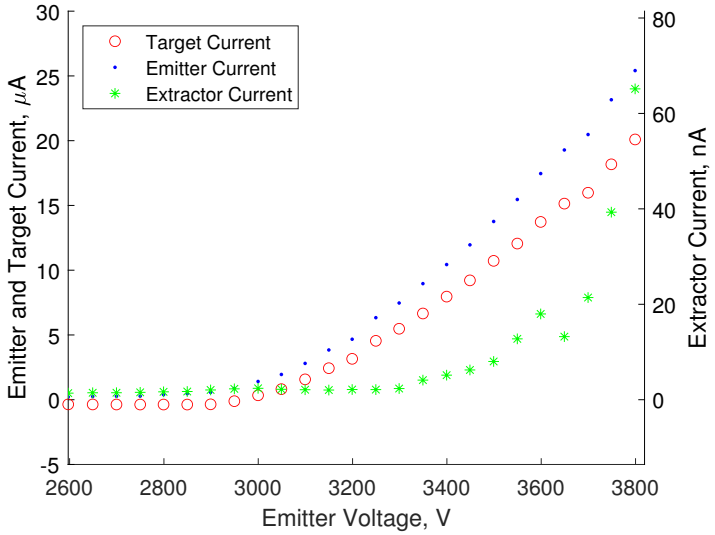

Figure 5.4: Current response from PoWEE with voltage. Current measured by the beam target and emitter current amplifier corroborate each other, while extractor current is much lower.

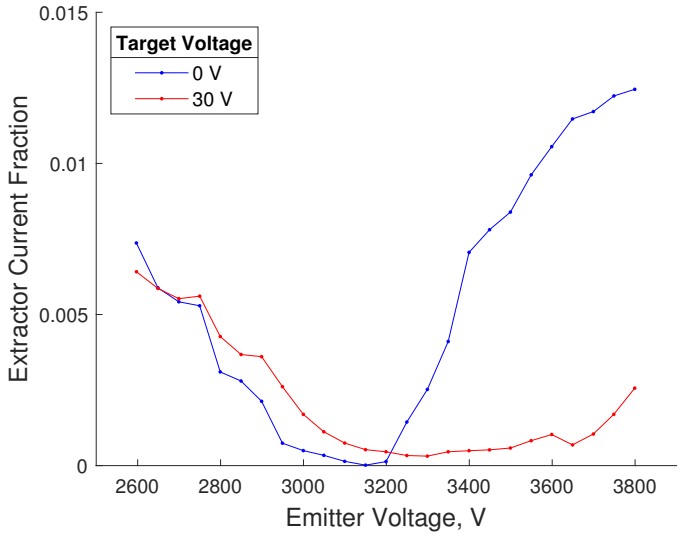

Figure 5.5: The ratio of extractor current to emitter current as a function of voltage. Below 3200 V, beam target bias does not have a significant effect. At higher voltages however, a beam target bias of 30 V significantly decreases extractor current.

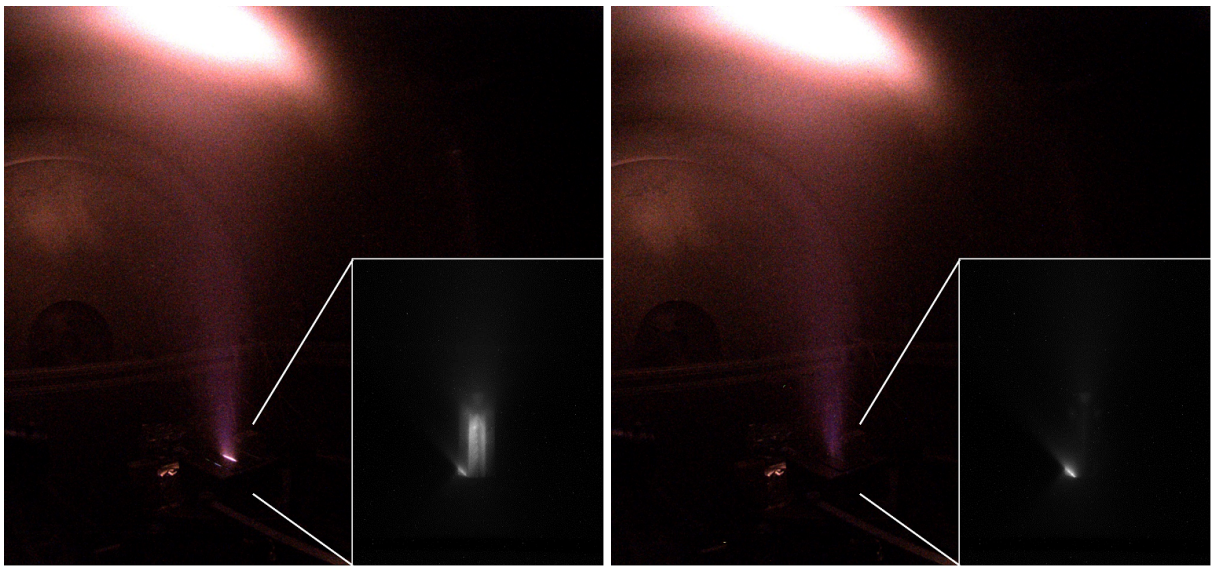

(a) Beam Target at 0 V.

(b) Beam Target at 30 V.

Figure 5.6: Illumination from PoWEE at an emitter voltage of 3500 V captured with wide-angle and close-up (inset) cameras with exposure times of 300 s and 60 s, respectively. The wide-angle images were brightened by a factor of 5. Inset view is with the emitter in the same orientation as Figure 5.8b. Beam target biasing eliminates illumination at the emitter but does not affect illumination in the plume or due to emitted particles incident on solid surfaces.

as measured by the wire probe, corresponding to a plume full-width of 8° along the direction of the wedge. The vertical striations shown in the plume in Figure 5.8a support this estimation of narrow plumes along the wedge direction. The width of isolated plumes does not appear to change with emitter voltage. Emission is recorded from 7 regions with multiple emission sites, separated by regions 0.5 mm or wider without recorded emission. Non emitting regions may be due to insufficient electric field or inadequate cleaning of the emission surface.

Results from translating the wire probe through the plume while oriented parallel to the ridge of the wedge are shown in Figure 5.19b. At low voltages, the plume is largely off-center. With increasing emitter voltage, emission becomes wider while the plume peak becomes more on-axis. At 3900 V emitter voltage, the measured plume extends to ± 1.2 mm from the center plane of the emitter, indicating a plume half angle of 35° perpendicular to the ridge of the wedge emitter.

Visualization of the emitter in operation was performed in the two previously mentioned orientations for wire probe sweeps. The photographs presented in this study were all obtained at an emitter voltage of 3500 V for uniformity, although the beam target bias was varied between 0 and 30 V. These photographs can be seen in Figures 5.6 and 5.8. Optical emission was observed from the emitter surface, beam target, extractor surface, and plume.

The 2D current density through the plane of the wire probe was computed using tomographic techniques. Multiple wire probe sweeps were performed from $-90°$ to 90° with respect to the orientation used to acquire the data shown in Figure 5.7a, in 5° increments. After acquiring data, the 2D current density map was produced by an inverse Radon transform. The details and challenges of this technique are described in detail in recent studies [54, 109]. Current density maps for three setpoints are shown in Figure 5.9. The thruster was operated for several hours between when the data was obtained for 1D and 2D plume mapping, which may explain some differences between the two sets of results. Specifically, the plumes at ± 8 mm are absent from the 2D map at 3200 V while present at lower voltages in 1D plume sweeps, as shown in Figure 5.7. These locations likely were dulled by emission while operating in a single polarity without a distal electrode [111]. The plumes of approximately 17 individual emission sites are visible when operating at 3200 V and approximately 50 or more are present as voltage increases to 3600 V. Although emission sites

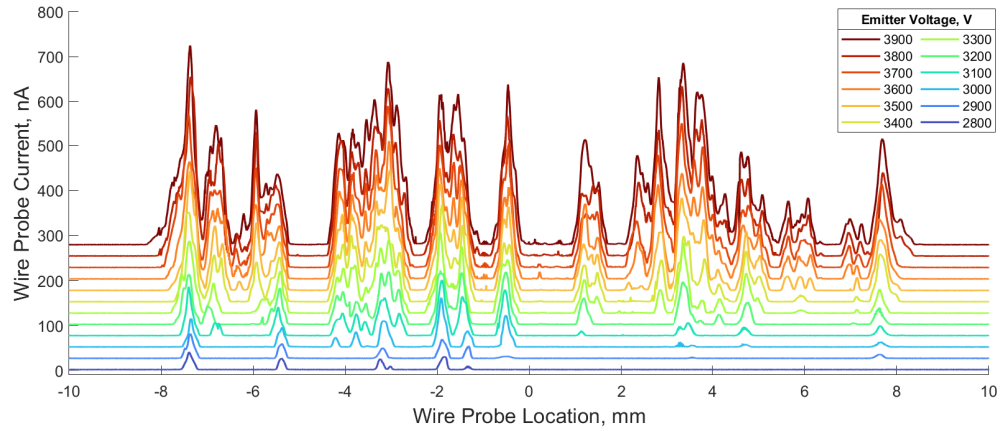

(a) Wire probe oriented perpendicular to the ridge of the wedge emitter.

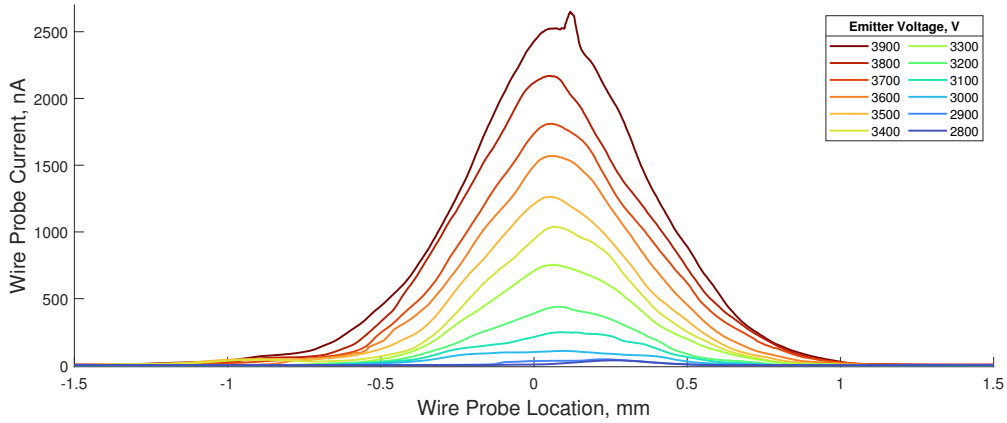

(b) Wire probe oriented parallel to the ridge of the wedge emitter.

Figure 5.7: Current collected by the wire probe as a function of position and emitter voltage for two orientations. Subsequent current traces are plotted with 25 nA offsets to distinguish traces in the top plot.

(a) View parallel to wedge.

(b) View parallel to wedge.

Figure 5.8: Illumination from PoWEE in operation at 3500 V emitter potential with the beam target at 30 V, captured with 600 s exposure.

notionally form in a straight line, each of the current maps show that many of the sites are tilted from the centerline of the emitter. Additionally, the plumes appear elongated perpendicular to the ridge of the wedge.

Perpendicular wire probe sweeps were analyzed further to understand the stability of emission sites along the emitter. Spectrograms of the signal measured by the wire probe was constructed from binned Fourier transforms of the signal. The spectrogram for PoWEE operating at 3700 V is shown in Figure 5.10a. Most emission sites operate steadily, however a minority of emission sites were observed to pulsate at frequencies between 10 Hz and 1 kHz. The pulsation frequency for a few unsteady emission sites were examined at each voltage set point. Pulsation frequency for each emission site generally increases with voltage, as shown in Figure 5.10b. While the pulsation frequency is much lower than the kHz order of pulsation recorded for capillary electrosprays [112, 20, 113], the trend of pulsation frequency increasing with voltage and eventually leading to stable emission is shared between these devices [92, 60].

The transient response was characterized by rapidly actuating the emitter from ground to a nonzero potential. A high speed, high voltage switching circuit was included on the supply side of the emitter current amp, controlled by the DAQ and a secondary Arduino. After the previously described steady characterization, the emitter was held at 0 V for at least 10 s before increasing

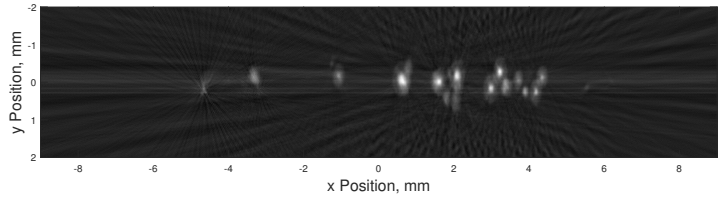

(a) Map for 3200 V emitter voltage, 2.1 µA.

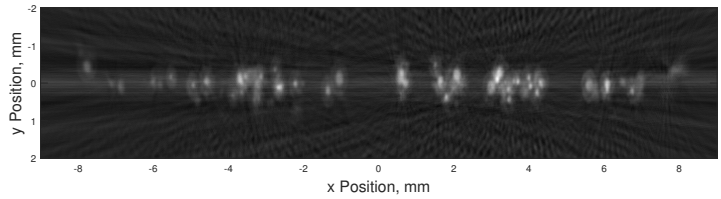

(b) Map for 3600 V emitter voltage, 11.2 µA.

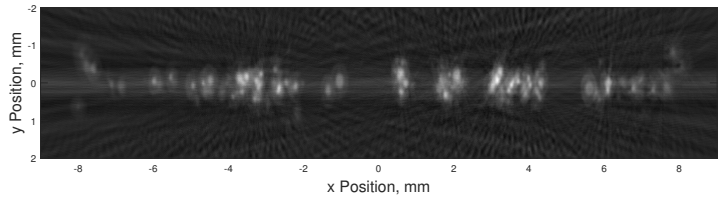

(c) Map for 3800 V emitter voltage, 17.2 µA.

Figure 5.9: 2D tomographical map of current density in the wire probe plane, developed from wire probe sweeps at 5° offsets.

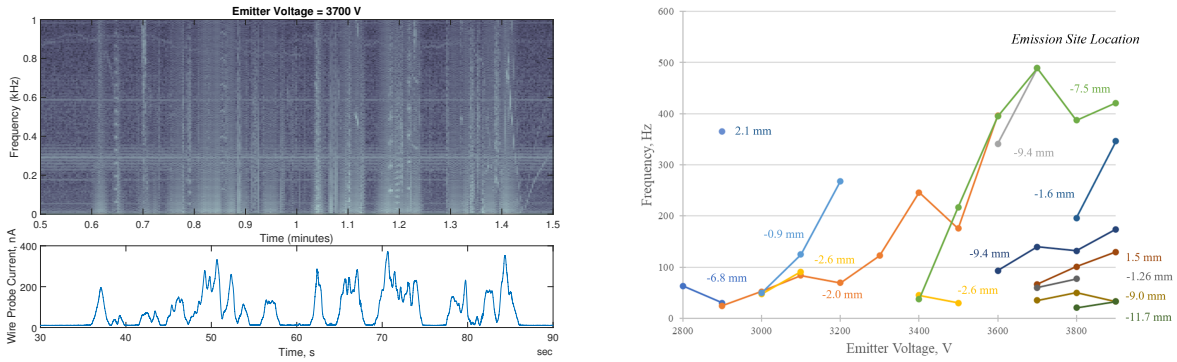

(a) Spectrogram of perpendicularly-oriented wire probe sweep.

(b) Frequency of pulsating emission sites with voltage.

Figure 5.10: A small number of emission sites pulsate at each operational voltage. Generally, pulsation frequency increases with voltage for individual emission sites.

to a nonzero potential for 10 s. The transient current response measured to the emitter and beam target are shown in Figure 5.11. Current measured by the beam target and emitter current amplifier generally agree with the exception of the inrush current to the emitter. Emitted current increases to a steady value over 10 to 40 ms after actuation, although some current decay was observed at higher voltages over a scale of several seconds. Some step changes in the emitted current were observed as shown in Figure 5.11b, which I attribute to intermittent emission sites.

5.6 Discussion

The number of emission sites can be estimated from the plume characterization curves. At low emitter voltages, individual emission site plumes are mostly separated and roughly less than 10 emission sites exist on the emitter. As emitter voltage increases, the number of emission sites increases and individual plumes overlap, making determining the number of emission sites difficult. However, counting the number of peaks and inflection points suggests that up to 80 emission sites exist on the emitter at higher operational voltages (i.e. 3900 V emitter voltage). From 2900 V to 3900 V, the number of emission sites increases roughly 10× while emitter current increases 45×, showing that the increase in emitter current cannot be solely due to emission site proliferation.

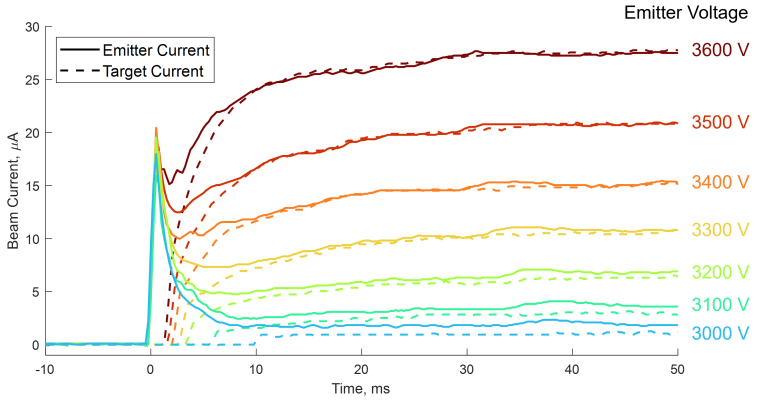

(a) Short-term response.

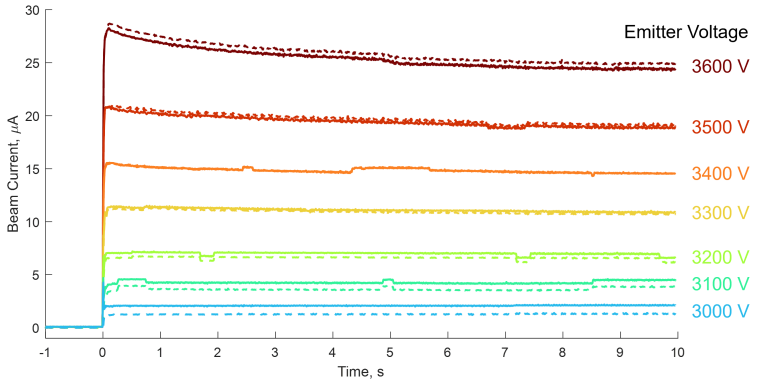

(b) Long-term response.

Figure 5.11: Transient current response of PoWEE, captured by the emitter and beam target current amplifiers, with the beam target at 0 V.

Increasing emitter voltage results in both an increase in the number of active emission sites and an increase in throughput from each emission site. The dramatic increase in emission sites shown in the 2D current maps of Figure 5.9 at low currents compared to the minor increase in emission sites at higher currents supports this conclusion as well.

During operation in vacuum, illumination has been frequently observed from the emission surface of electrospray thrusters [114, 55, 115], from within the plume [116], and from downstream surfaces [117] during operation. It has been claimed to be a natural phenomenon associated with the ionization process [52, 55], but a recent study by Uchizono et al. places the responsibility for illumination upon secondary species production and interactions within the plume [118]. The underlying factors responsible for optical emission during operation, and its implications for device lifetime and performance, are still poorly understood. The results from this study, namely Figures 5.5 and 5.6, help to clarify the causes of illumination from electrospray thrusters. The beam target reduces the luminance of the emitter not by affecting the emission process, but by preventing secondary electrons or anions from the beam target from reaching the thruster [107]. Secondary electrons emitted from a positively biased beam target are more likely to be reabsorbed by the beam target after emission. Because the emitter luminance can be mitigated through beam target biasing, it is a facility effect that is not likely to occur during operation in space as long as backstreaming electrons are adequately screened by an accelerator electrode [119]. The remaining source of emitter glow is direct impingement to the extractor, which is most evident at the plumes originating from the ends of the wedge, as shown in Figure 5.6. The presence of diffuse light production at the half-cylindrical beam target seen in Figure 5.6, and intense luminance of the probe during wire sweeps (not shown) further supports the notion that optical emission is directly related to plume interception. Plausible causes of photoemission include sputtering of target materials [120, 121], and/or dissociation of incident primary molecules [122].

Experimental measurements from other wedge-shaped emitters far downstream show that the emitted plumes are wide in the direction perpendicular to the wedge and narrow along the wedge [50, 89]. The presented experimental measurements match with these conclusions about plume shape. Photography and current density measurements show that the plume of the emitter is com-

prised of many individual plumes that are very narrow in the direction along the wedge. Experimental measurements of current density just downstream of the emission surface, shown in Figure 5.19b show that the characteristic plume shape from wedge electrospray emitters measured far downstream [50, 89] forms very near to the emitter. 2D current density maps inform the results for downstream plume shape by revealing both that emission sites form off center on the wedge emitter and that the individual plumes are elongated perpendicular to the wedge. Due to the geometry of the extraction field, there is an electric field pushing emitted particles perpendicular to the wedge direction but none along the wedge; a deeper look into the physics of plumes in these unique conditions may reveal more about the extraction conditions of wedge electrosprays [123].

A model developed by Wright and Wirz [1] described how the flow to each emission site could be coupled with the charge concentration at each emission site to understand site spacing as a function of operational parameters. Applying the model to PoWEE predicts that emission sites should be spaced by 60 to 200 µm over the operational range. The number of emission sites determined through experimentation is generally an order of magnitude lower than the analytically predictions would suggest. As evidenced by the plume characterization curves presented in Figure 5.19a, emission occurs somewhat sparsely over the length of the emitter, especially at low emitter voltages. Increasing voltage causes emission over more of the length of the emitter, indicating that the dominant effect responsible for emission site multiplexing is electric field variation on the emission surface. It is anticipated that improving the uniformity of the emission surface should allow for more emission sites to form over the operational envelope of the device. Additionally, 2D plume maps reveal that emission sites do not lie in a straight line on the emitter surface. Further refinement may be necessary to apply this model to the results from physical devices, where emission sites have an additional degree of freedom not accounted for in the analytical model.

Measuring the transient response showed that PoWEE responds quickly to voltage actuation. Current response generally matches with the high-speed transient response of the BET-300-P thruster [100] despite differences in actuation. Because the current mostly increases to its steady value, my interpretation is that the onset delays of individual emission sites are large compared to the diffusion of pressure in the porous medium.

Observing pulsating emission sites was surprising due to how stable ionic liquid electrospray sources are [124]. Pulsation frequencies on the order of 10 Hz were much lower than kHz-level pulsations recorded for a capillary emitter using EMI-Im [113]. Although pulsating emission from porous emitters is a relatively unexplored research topic, pulsating emission from capillary electrospray emitters is well understood [92, 125, 126, 127, 128, 20]. For capillary electrosprays, pulsating emission on the order of 1 kHz is associated with cone oscillation while lower frequency pulsating emission is due to insufficient flow to the emitter [129, 92]. Although pulsation frequency is independent of voltage for capillary electrosprays [112], flow rate is a result of local electric field for passively-fed porous electrospray emitters. The contribution of voltage to pulsating emission on a porous electrospray cannot be ignored, even at low pulsation frequencies. Because the pulsation frequency is proportional to flow rate in the 'choked flow' regime [60, 112], pulsation may provide insight into the flow rate to individual emission sites at voltages near their startup condition. If cone-jet scaling laws are applicable, then the pulsating emission sites may be supplied by flow rates much smaller than the minimum flow rate of 2.9 pL/s for EMI-Im [130].

5.7 PoWEE Wedge Redevelopment and Improvements

Encouraged by the preliminary success of the PoWEE-wedge thruster in producing experimental data to support analytical models for electrospray behavior, another revision of the thruster was developed in order to improve the design. The goals of these modifications were to improve the spatial uniformity of the plume of the emitter and to increase the maximum emitted current.

5.7.1 Experimental Setup

The PoWEE thruster was redeveloped with multiple lessons learned from the previous development effort.

A platinum distal electrode has been incorporated to increase device lifetime and demonstrate feasibility. Distal electrodes have been shown to increase the lifetime of tungsten electrospray emitters operating in a single polarity through reducing electrochemical interaction at the emitter

surface. Reducing electrochemical interaction at the tungsten surface prevents emitter erosion and propellant decomposition, both of which can lead to premature thruster failure [111].

The emitter was submerged in EMI-Im under vacuum prior to assembly to ensure that the entire emission surface would be fully wetted. After assembly, an amount of propellant was added to the emitter that would fill the porous reservoir to approximately 70% capacity. The amount of propellant added to the reservoir slightly exceeds the total propellant added to the emitter, interface, and reservoir in the previous revision.

A copper extractor was used for optical emission spectroscopy. Copper, being a monatomic metal, has simpler and more distinct spectral emission than stainless steel, the original extractor material. Furthermore, its optical signature is distinct from that of the beam target. Furthermore, if trace elements can be detected on the extractor and emitter after testing, then possible material transport between these three electrodes can be detected.

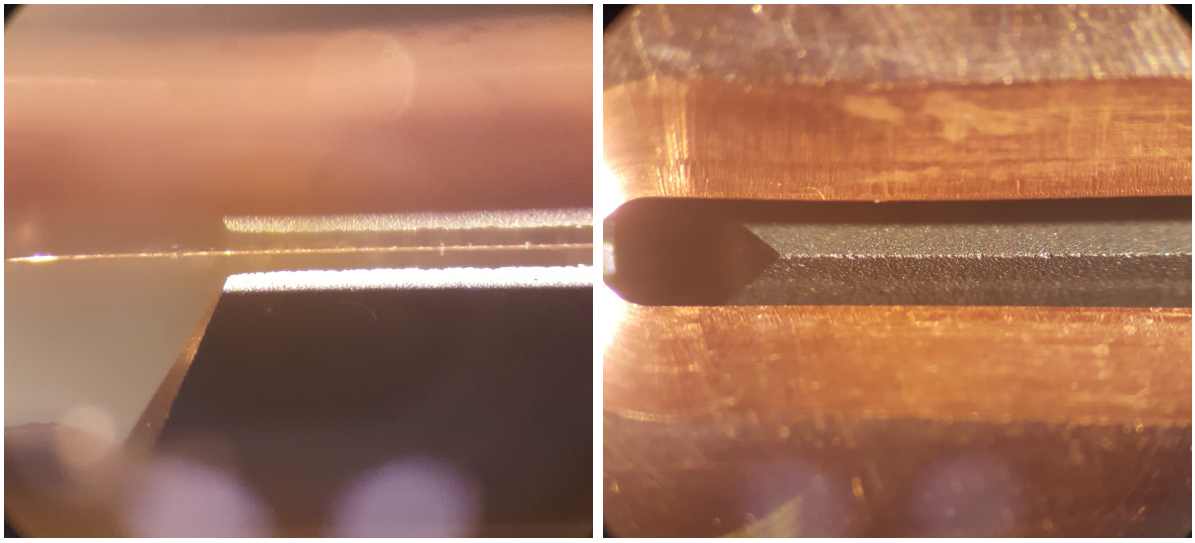

(a) Side view (b) Top view

Figure 5.12: Images of the emitter and extractor after alignment. Both images were taken at the same magnification.

A second emitter was added to the experimental setup in order to understand thruster facility effects. In contrast to the main thruster, the second thruster did not have any propellant. The two thrusters had the same notional geometry. The porous reservoir was replaced with a porous alu-

minum disc and the interface material was removed. With two nearly identical thrusters that only differ functionally by the inclusion of propellant, ideally the current associated with backstreaming secondary species and emitted primary species can be deconvolved. The experimental setup for this experiment is shown in Figure 5.13. One of the benefits of using a tungsten emitter instead of porous glass is that the emitter is conductive, so it can be adapted for this context without modifying the emitter in order to make it conductive.

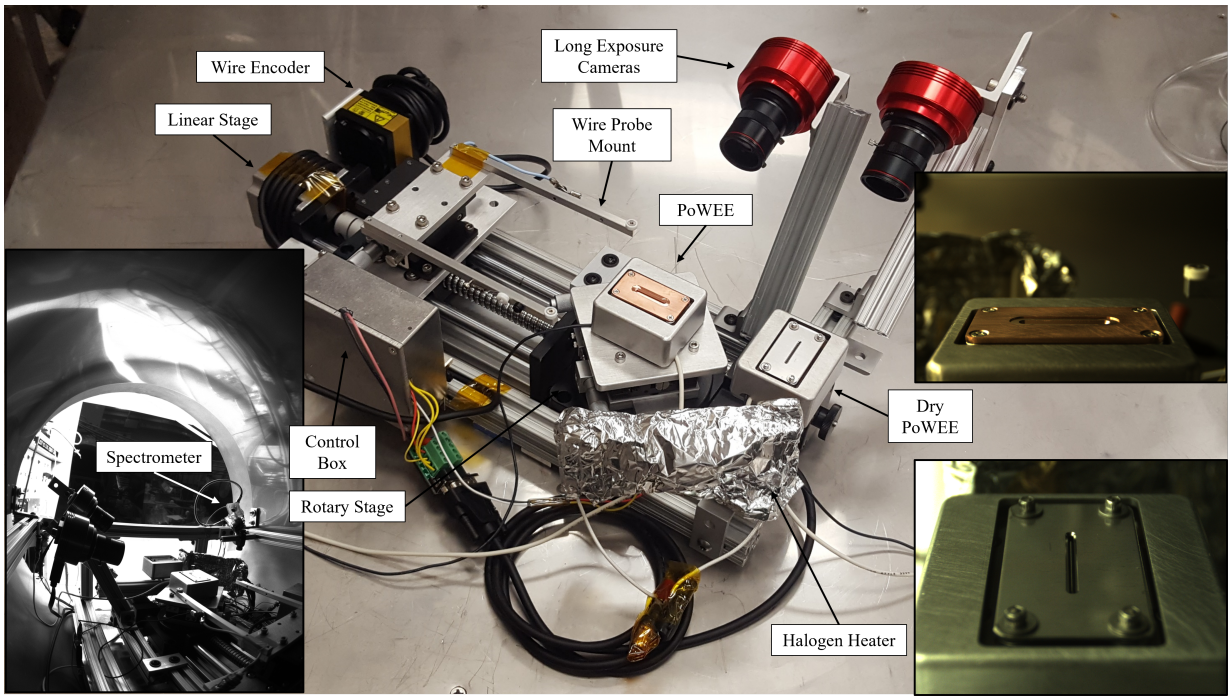

Figure 5.13: Experimental setup for testing the second PoWEE-wedge thruster. Two thrusters are included for facility effects investigation.

Inspired by the great variety of cuisine available in West LA, we have been referring to this experiment as our *Mazemen* test, which is style of ramen that retains the essence of the dish while removing liquid broth [131, 132]. Similar to the adaptation from ramen to mazemen, removing propellant from PoWEE may allow for understanding facility effects with "unadulterated access ... that would otherwise be veiled in liquid" [133]. In the context of propulsion system testing, operating a thruster without propellant allows for access to the current due to collection of secondary species which would otherwise be overwhelmed by primary emission in the case of the emitter or direct impingement in the case of extractor. Understanding facility effects is currently one of

the biggest challenges in electrospray propulsion [118] and requires flexibility in order to develop experiments to tackle these challenges.

Both the wet and dry thrusters are operated at the same voltage but with separate current amplifiers. A single high voltage power supply is used to charge both, although the high voltage connection to each can be removed and either can be grounded. Both extractors were operated at ground potential and current was measured with individual current amplifiers.

5.7.2 Results

The current response of PoWEE was measured over a range of beam target potentials in order to understand the effect that the facility has on operation. Positive target biases were found to be useful for eliminating the glow at the emission surface. An example of this can be seen in Figure 5.14, introducing a target voltage of 60 V eliminated emitter glow. Increasing the target voltage from 0 V to 60 V eliminated the glow from the emitter while the glow at the target remained. Modifying the target voltage both affects the energy of secondary species emission (SSE) from the target and causes species of the opposite polarity to be recollected by the target. An increase in target voltage prevents negatively charged secondary particles from reaching the emitter, which causes the glow at the emission surface [118]. Target voltage did not have a significant effect on glow at the target at low emitter voltages. The results shown in Figure 5.18 match with the results shown in Figure 5.6, but with increased clarity due to the higher light sensitivity of the sensor and larger aperture. Both of these sets of images (Figures 5.18 and 5.6) show that beam target biasing eliminates illumination at the emitter. Light emission can also be seen faintly in the plume. The glow at the emitter was accompanied by a steep increase in current collected by the extractor electrode. For fear of premature thruster failure, operational set points where there was significant light emission from the emitter surface were generally avoided.

At higher emitter voltages, the glow behavior of the emitter has a strong dependence on target bias. Images taken of the emitter at voltage high in the operating range are shown in Figure 5.15. Without the target bias, a strong glow forms at around the emission surface, while this glow is eliminated with target voltage. Diffuse lighting is observed in the background at high target voltage,

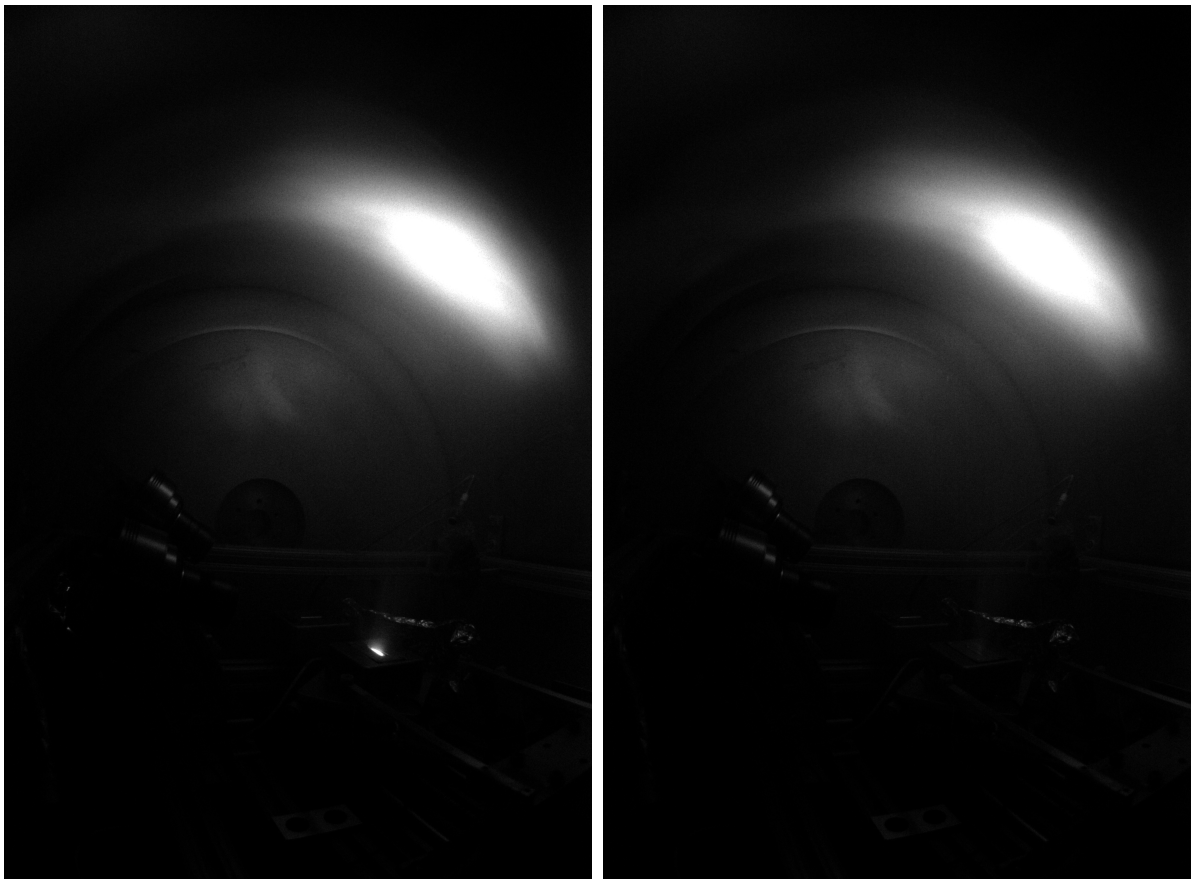

(a) 0V beam target potential

(b) 60V beam target potential

Figure 5.14: Glow in the chamber during operation at 3600V emitter potential. Both images had a 35s exposure time.

indicating the the glow at the target may vary significantly between biased and unbiased setpoints while operating the emitter at higher current. The impingement site at the near end of the extractor shows that the light produced by direct impingement has little dependence on target voltage.

When operating at a negative beam target polarity, the energy of negatively-charged secondary species from the target is increased while positively-charged species are suppressed through recollection. Negative target voltages were seen to produce a greenish glow from below the extractor, while positive target voltages eliminated this glow. The effect of beam target on the green glow between the emitter and extractor is shown in Figure 5.16. the direct cause of this glow is unknown but is expected to be associated with positively-charged secondary species originating from

(a) 0V beam target potential (b) 80V beam target potential

Figure 5.15: Glow at the emitter during operation at 4700V emitter potential. Both images had a 7s exposure time.

the beam target and reaching the emitter.

The effect of beam target biasing was investigated in greater detail by measuring the emitter, target, and extractor currents over a range of emitter and target voltages. Results from this investigation are shown in Figure 5.17. Over the range of parameters tested, the emitter current was observed to be largely independent of target voltage. Increasing emitter voltage significantly past the point at which the extractor current began to increase may have resulted in a significant increase in emitter current if increasing voltage further was not avoided. The ratio of target current to emitter current shows that positive target bias reduces target current below that of the emitter, and vice versa. The explanation for this behavior is that target bias enhances secondary emission of the same polarity while suppressing secondary emission of the opposite polarity [118]. Unfortunately, charge is not conserved when only considering the emitter and target currents; the missing current margin represents species which are attracted to grounded electrodes such as the facility, which were not measured. Current to extractor is high when there is a current deficit to the beam target, and vice versa, which supports the hypothesis of the missing margin passing into other grounded conductors such as the facility walls.

Glow was observed during operation and shown in Figure 5.18, with a smaller field of view than shown in Figure 5.14. Images were taken with a long exposure at 4000 V emitter voltage and

60 V target voltage. A faint purple glow is seen in the emitter plume up to the emitter surface, and a few bright spots are visible on the extractor due to direct interception from a few off-plane emission sites. Based on the images shown in Figures 5.14 and 5.18, and investigation by Uchizono et al. [118], we conclude that the glow at the emitter is due to facility effects and direct interception, rather than a direct result of the emission process as has been previously stated. It is yet to be seen whether facility effects can be mitigated to the point where glow in the plume can be eliminated or attributed to primary emission processes.

The plume current distribution is shown in Figure 5.19. The plumes of numerous emission sites are visible in the data for when the wire was oriented perpendicular to the wedge ridgeline, while individual plumes are indistinguishable when the wire is oriented parallel to the ridgeline. The plume becomes increasingly oriented towards one side of the extractor with voltage; the peak in wire probe signal translates from 1.0 to 1.2 mm as voltage increases. These offsets correspond to 20 to 24° off of the centerplane of the emitter. An oscillatory variation in the data is observed in the parallel-oriented wire probe data, with a period of roughly 0.25 mm. The cause of this variation is unknown but may be mechanical, related to the wire probe position or wire encoder accuracy.

As compared to previous PoWEE revision, the plume is much more uniform. Non-emitting locations are seemingly removed from the device, which is attributed to submerging the emitter in propellant prior to assembly. Vacuum submersion ensured that the emission surface was fully wetted during operation, which was the fault attributed to non emitting location. Because the tungsten emitter is conductive, it prevents electric field from penetrating into porous medium; in porous electrosprays with glass emitters, electric field penetration into the porous medium may ensure that propellant is pulled to the emission surface over its entire area.

The transient response of PoWEE was measured through the emitter and beam target current amplifiers during rapid voltage actuation with a high voltage relay circuit. Signals measured by the emitter and beam target current amplifiers are shown in Figure 5.20. The monotonic increase in current in the short term over tens of ms is consistent with previous results from the PoWEE thruster [39] and other porous wedge electrosprays [100]. The nonmonotonic settling response observed in the long term response over several seconds is roughly consistent with the typical

response of porous electrosprays [106, 38]. A transient response consisting of an initial overshoot and decay is as expected for systems which can be described by transient diffusion equations. The inconsistency of the short term transient response with the expectations for diffusion limited transient processes prompted further investigation into the behavior of individual emission sites rather than the total system response.

The localized transient response was measured by positioning the wire probe at a few locations over the emitter and measuring the transient current to the wire. The transient current measured by the wire probe is shown in Figure 5.19. The emitter and beam target currents were consistent with the previous signals shown in Figure 5.20. Depending on the voltage applied to the emitter, roughly 4 to 6 discrete increasing steps in wire probe current were observed at each of the probe locations. The steps correspond to individual emission sites beginning to emit shortly after voltage actuation. Each emission site behavior exhibits a response that matches the onset delay to transient decay response that is typical for the total emission behavior for porous electrospray emitters with a low number of emission sites. With increasing voltage, the onset delay decreases to the point where emission is nearly immediate. Additionally, pulsating emission is observed with the the wire probe that is masked by the cumulative behavior of the numerous emission present on the emitter.

Further investigation of these emission sites reveals that individual emission sites exhibit nearly exponential decay after an initial onset delay. The transient response of emission sites, with exponential fits, are shown in Figure 5.22. The response of an early emission site is slower than that of the intermittent emission site seen later in the data, with a time constant of 80 ms compared to 3.5 ms. In Figure 5.22b, the signals from each time the emission site pulses are superposed to show that the transient decay is consistent. The difference in time constant between the two response is particularly interesting. Once the intermittent emission site begins, there is already flow within the emitter. On the other hand, the long transient decay observed earlier occurs while the flow is initially stagnant. The key difference between these two behaviors is the state of the flow within the porous medium at the beginning of emission. In other words, the long term transient response is due to development of the net flow in the bulk, while the shorter, intermittent response

is due to development of the concentration flow to each emission site. Recalling the different transient flow solutions presented in Chapter 3, the bulk flow and flow concentration to each emission site correspond to the primary and secondary flow solutions respectively. Additionally, the long term response correlates well with the time constant of the first mode for the primary flow after accounting for accumulation in channels as described in the appendix.

The transient current response measured by the wire probe represents an important connection between the transient response of wedge electrosprays and more traditional porous electrosprays. Despite the atypical transient response of porous edge electrosprays, the individual emission sites exhibit a typical porous electrospray response, from cone-shaped emitters for example. The onset delays of individual emission sites were observed to be in the hundreds of ms, which corresponds well with the increase in current after voltage actuation. For this reason, the short term increase in current after voltage actuation is attributed to the range in onset delays of individual emission sites on the emitter, mirroring the explanation proposed by Courtney et al. [100]. The cause of the discrepancy between cone-shaped and wedge shaped emitters is due to the high number of emission sites compared to the number of exposed pores on the emitter. The dominant effect of the transient response for a porous electrospray emitter can be determined by comparing the volume of fluid needed to form Taylor cones at emission sites with the change in volume of stored fluid at the exposed pores on the surface. If the volume of fluid required for forming Taylor cones is low compared to the change in volume due to receding menisci in exposed pores, then the emission sites while emit before the pressure diffuses from the emission surface to the reservoir, so diffusion will be the dominant cause of the transient response. For the case where the magnitudes of these two volumes are the opposite, diffusion of pressure to the reservoir will complete before a sufficient propellant has passed through to the emission surface, so onset delay will be the dominant effect for transient response. For porous wedge electrosprays, the number of emission sites is typically much larger than that of porous one emitters, which the increase in exposed pores is not as great, so it is expected that onset delay would be the dominant effect for the transient response.

Inspection of the porous surface after testing revealed the structure of the meniscus on none-mitting surfaces of the emitter. The purpose of inspection was to interrogate the validity of the

transient flow model, which assumed that a spherical meniscus would form in exposed pores. A picture of the emitter surface is shown in Figure 5.23. Rather than spherical menisci forming in exposed pores, it appears that channels of propellant form in between sintered tungsten particles that sit proud on the nonemitting surfaces. The analytical prediction of surface propellant storage as a function of pressure has been redeveloped to reflect the accumulation of propellant in channels rather than pores. If the meniscus is assumed to form in quasi-cylindrical channels, then a new estimation of the meniscus can be formed using the area of a circular segment, extruded along the nonemitting surface. The diffusion coefficient has been rederived as shown in the Appendix. On the other hand, the picture shown in Figure 5.23 was taken of an emitter that did not have a porous reservoir in place. Because of this, the propellant may have had an artificially increased restorative pressure, which may have decreased the width of the channels on the emitter surface. If the restorative pressure decreasing would allow the channels to expand, then a meniscus shape will have to be assumed that leads to violating the linearity that is a key part of the analytical diffusion equation originally produced. Either way, although the transient flow analysis has produced reasonable predictions of transient flow behavior, the transient flow predictions may need to be modified based on the formation of menisci that may be specific to porous materials and/or surface geometry.

Due to the off-center plume, impingement upon the extractor is observed more often on one side of the extractor than the other. An image of PoWEE operating with multiple observed impingement locations is shown in Figure 5.24. Locations where impingement occurs are associated with a strong emission of purple visible light. As determined from wire probe signals, plumes are narrow in the direction along the wedge; narrow sources of light in the downstream direction are consistent with observations of plumelet width.

The previously described *mazemen* tests were performed over a range of emitter and target voltages. Results are shown in Figure 5.25. Current was recorded to both emitters and extractors as a function of emitter and target voltage. The order of testing various target voltages was semi-randomized in order to account for possible hysteresis.

A camera pointed at the dry emitter captured the illumination of the dry emitter during testing.

Images of the dry emitter at 4 setpoints are shown in Figure 5.26. Much of the light at the dry emitter is due to reflection of light produced at the beam target; the variations between images due to target and dry emitter potentials are minimal. When the dry emitter was at emitter voltage and the beam target was at ground potential, the dry emitter was noticeably brightened. The additional illumination at the emitter indicates that optical emission is produced at the dry emitter when energized to high voltage and at 0 V target potential. To highlight this observation, the difference in illumination between the dry emitter being energized and being grounded was calculated, and is shown in Figure 5.27. This image highlights that there is a purple glow at the dry emitter with isolated points of green glow, and a orange diffuse light behind the extractor that roughly matches the color of the ultem isolator. For clarity, images from Figures 5.26 and 5.27 cropped to the extractor aperture and reshown in Figure 5.28.

Results show that the emitter current is largely independent of target voltage, which is consistent with previous results. A small decrease in emitter current with increasing target voltage indicates that positive target voltages may suppress negatively charged secondary species, produced at the beam target, from reaching the emitter. Analyzing current to other electrodes more complicated and thus requires more nuance in order to analyze.

As with the previously described results, both positive and negative target biases reduce the extractor current. Highly negative biases lead to a change in the extractor current polarity, indicating that the extractor has begun to collect negatively charged secondary species born from the target. Extractor current is a complicated combination of incident, secondary emission, secondary collection, and possible tertiary collection and emission currents. As a result of its complexity, further analysis of the extractor currents has been avoided apart from recognizing that reducing extractor current is beneficial.

At target biases near ground potential, the dry emitter has a positive current, indicating that negatively charged species are backstreaming to the dry emitter. Due to the high potential of the emitter and resulting electric field, negatively charged particles are attracted to the emitter and positive charges are repelled. Increasing the target potential prevents backstreaming of positively charged secondary species from reaching the emitter, reducing the dry emitter current. This effect

is seen with both emitters, although at different magnitudes; at 4400 V emitter potential, increasing beam target bias from 0 to 80 V reduced the wet emitter current by 5 µA while reducing the dry emitter current by 150 nA. Illumination was measured at the dry emitter under certain conditions, showing that glow is not necessarily associated with electrospray emission. The requisit conditions for illumination from the dry emitter are the same as that for backstreaming current to the dry emitter: high emitter bias and a grounded target. The increase in dry emitter glow with dry emitter backstreaming current shows that the glow at the dry emitter is caused by facility effects, specifically backstreaming secondary particles to the dry emitter.

The glow images, beam target biasing experiment, and dry thruster (*mazemen*) experiment have yielded important information about how to conduct electrospray experiments in order to best prevent facility effects from harming the emitter or resulting in poor measurements. Measuring current to the dry emitter shows that both positive and negative target biases reduce backstreaming current to the emitter. Glow images however show that negative target biases produce an unsettling glow near the emitter, which may be due to the enhanced emission of negatively charged secondary species which are able to reach the emitter. Secondary species reaching the emitter can result in emitter heating, leading to anomalous mass loss and propellant decomposition [118]. Significant positive biases were identified as the best way to mitigate harmful facility effects per the variety of experimental measurements of this study and supported by the recently developed facility effects modeling by Uchizono et al. [118, 134].

5.8 Conclusion

This study has shown that using a porous wedge emitter is a noteworthy way of producing a multiplexed electrospray thruster. The experimental investigation has produced useful data relevant for the design and operation of porous electrospray devices in vacuum. Operating at up to 4.8 kV emitter potential lead to 130 µA of emitted current from the device, with emission sites numbering in the hundreds. Investigating the nearfield plume has shown that the number of emission sites increases with voltage, up to about 80 sites at 3900 V shown through 2D plume characterization.

2D plume characterization also showed that emission sites form both on and off of the center plane of the wedge emitter. Individual sites were recorded pulsating over the entire operating range of PoWEE at various locations. Further development has shown that emission site uniformity can be increased through emitter preparation. Additionally, despite the unique transient response of porous wedge electrospray emitters, localized plume measurements show that individual emission sites exhibit the typical response for porous emission sites from more universally adopted emitter geometries. Finally, in situ photography, system-wide current measurement and biasing, and a novel experimental setup with notionally identical thrusters have provided insight into the facility effects associated with operating an electrospray in a vacuum chamber. Long exposure photography showed that the two sources of illumination at the emitter are direct impingement and secondary species backstreaming; eliminating secondary species collection at the emitter through beam target biasing eliminated glow at the emitter.

(a) 10 V

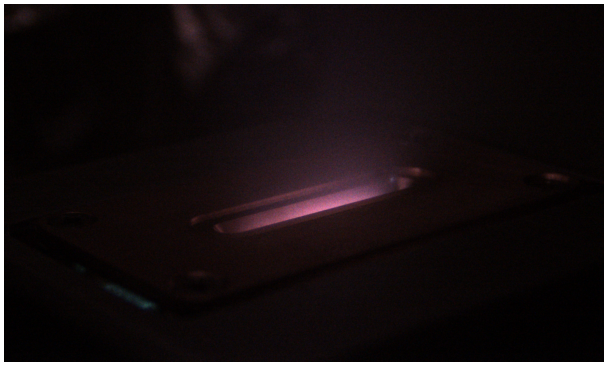

(b) 0 V

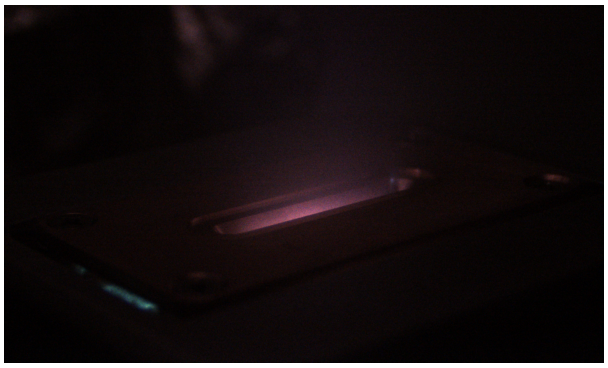

(c) -5 V

Figure 5.16: Glow at the emitter when operated at 4400 V. Images were captured with 5 s exposure times and beam target voltages of 10 V, 0 V, and -5 V, from top to bottom. A greenish glow from below the extractor appears at negative beam target voltages.

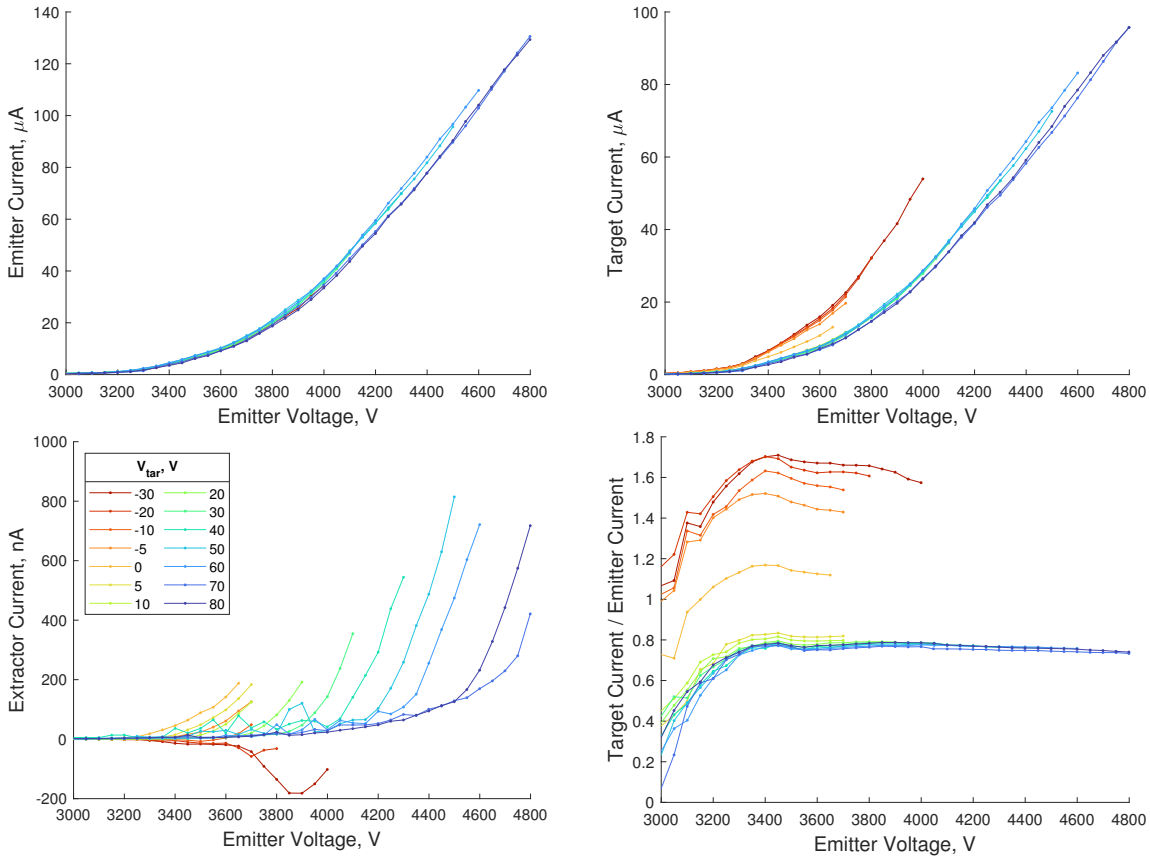

Figure 5.17: IV characteristics. Clockwise from top left: emitter current, target current, target current ratio, and extractor current as functions of emitter voltage. All plots share a common legend, indicating target voltage.

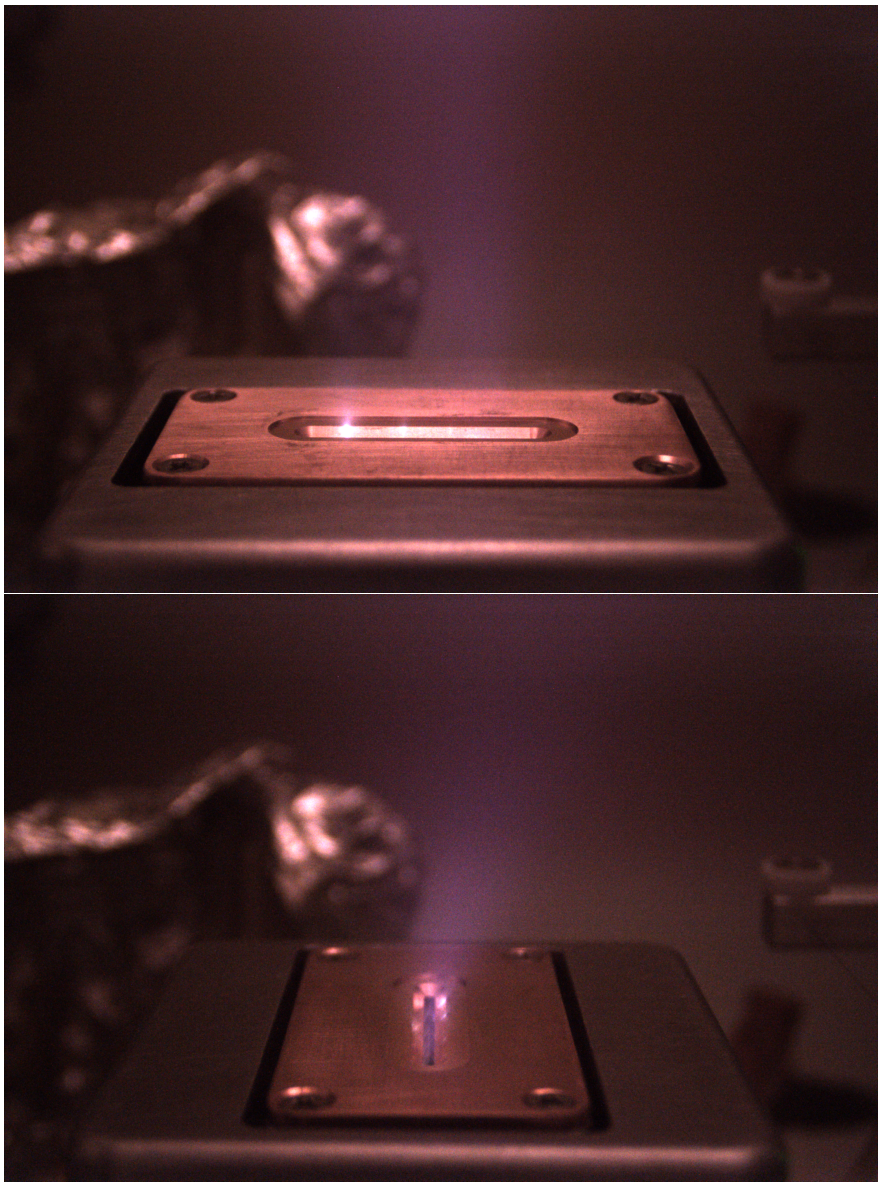

Figure 5.18: Glow at the emitter at 4000 V, observed with a 35 s exposure, in two orientations.

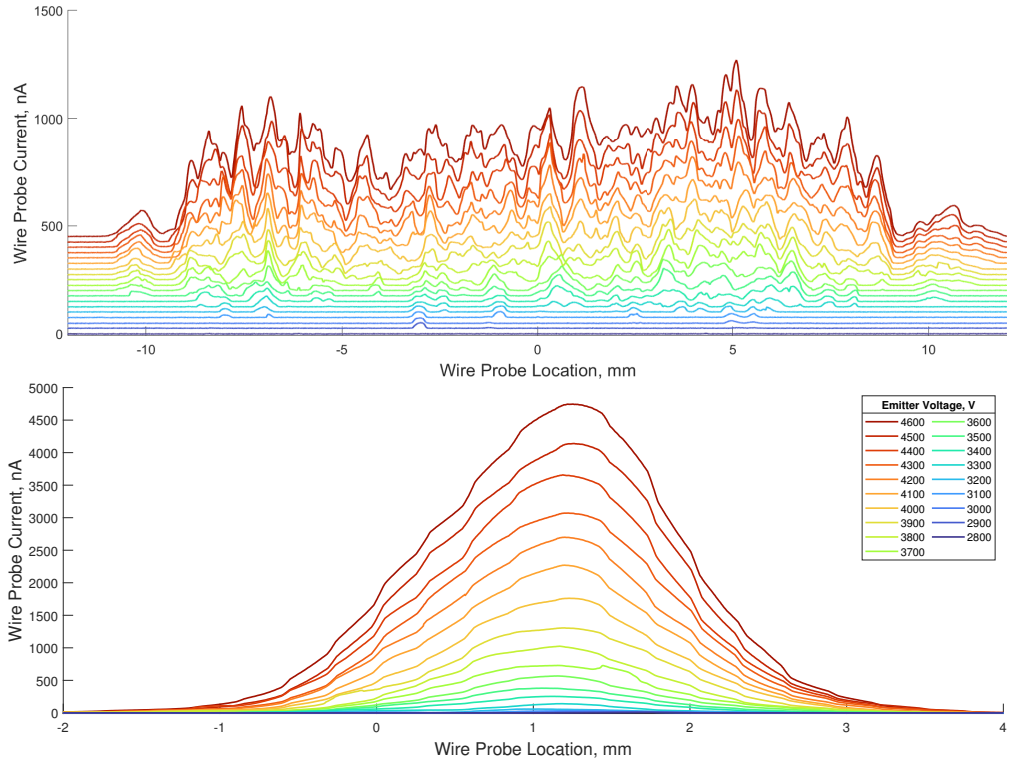

Figure 5.19: Wire probe sweeps, in the perpendicular (above) and parallel (below) orientations. Plots share a common legend.

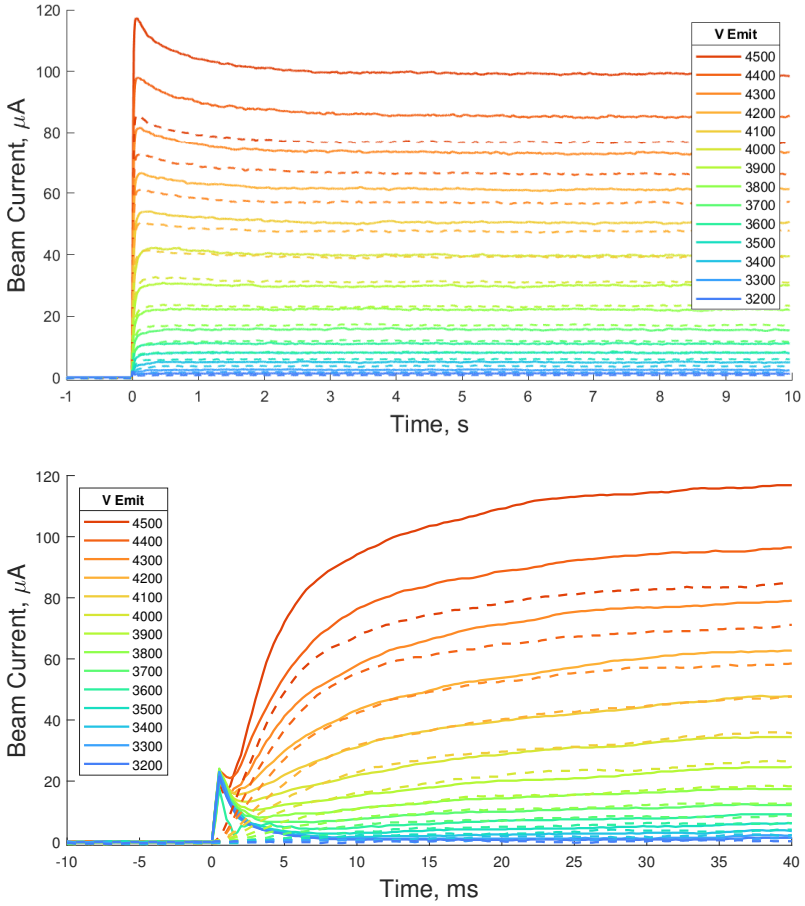

Figure 5.20: Transient onset of emission at a range of operating voltages, with the beam target at 60 V. Above, long term response, and below, the short term response.

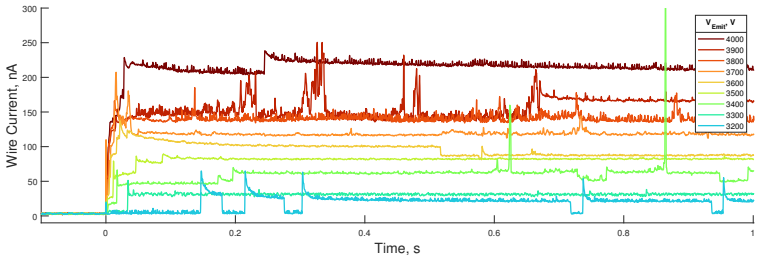

(a) 6.17 mm

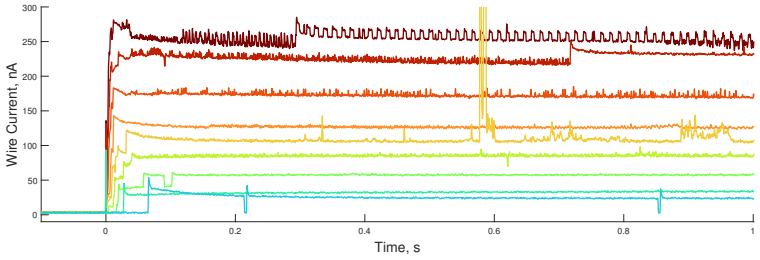

(b) 3.59 mm

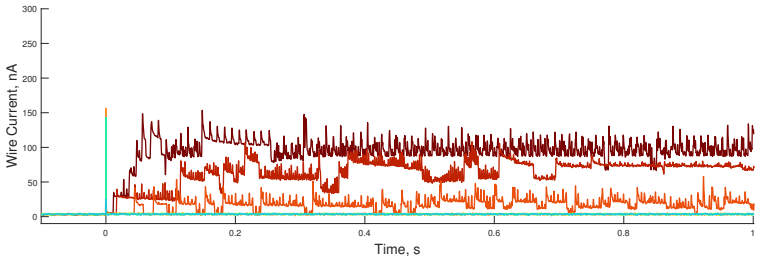

(c) -3.98 mm

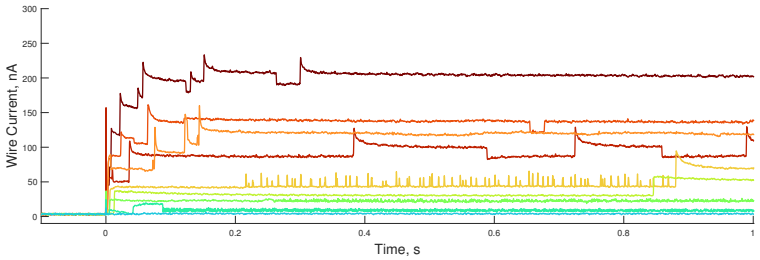

(d) -6.60 mm

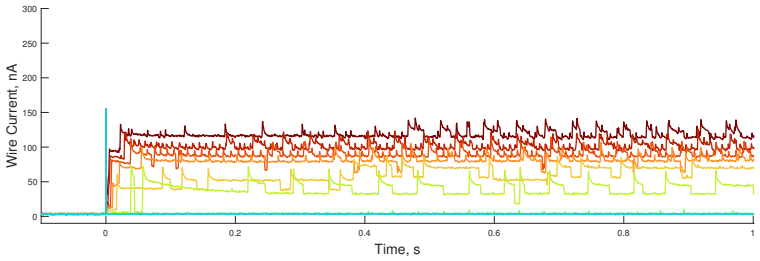

(e) -8.91 mm

Figure 5.21: Transient current, at a range of emitter voltages, measured in the plume by the wire probe at 5 locations as indicated.

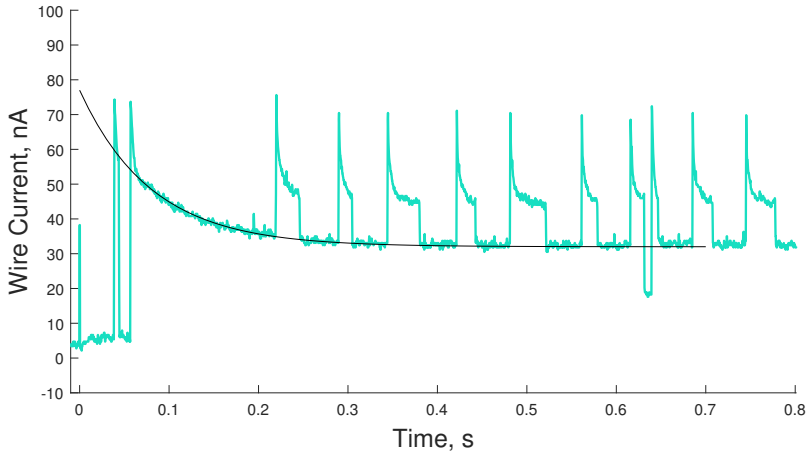

(a) Fit to long term response, τ_c =80 ms

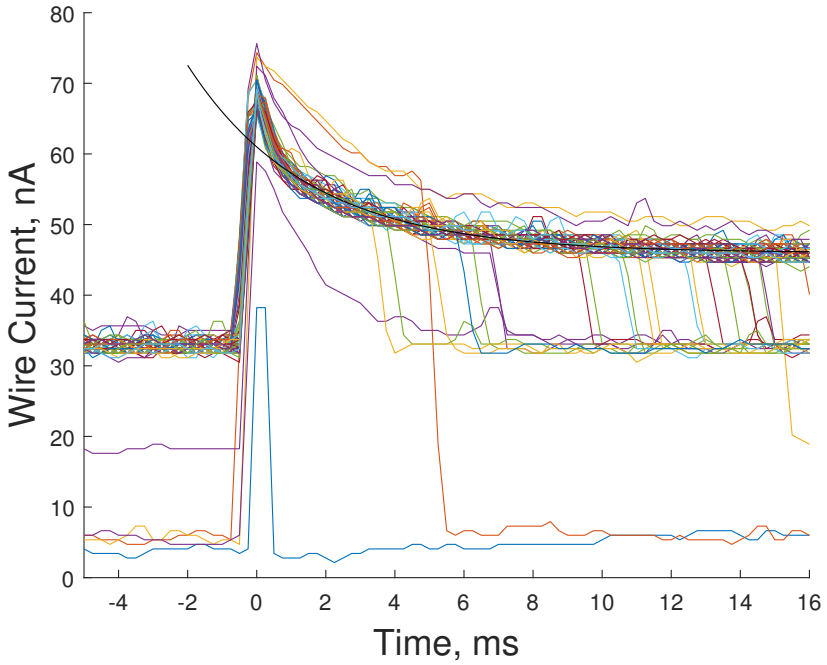

(b) Fit to intermittent response, τ_c =3.5 ms

Figure 5.22: Response of individual emission sites at -8.91 mm, 3400 V. The long term and intermittent responses exhibit exponential decay that is initially slightly steeper. Exponential fits are shown with indicated time constants τ_c.

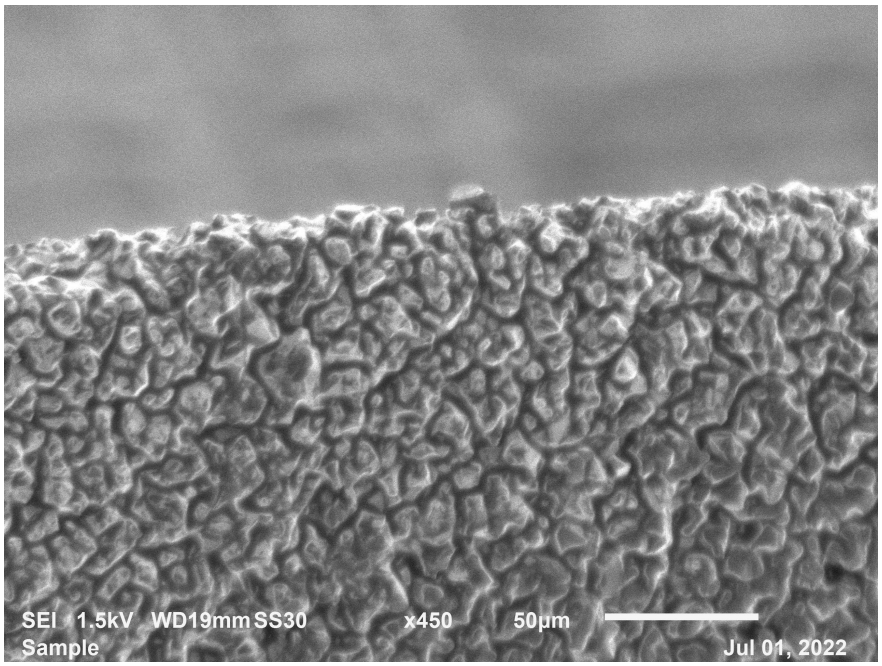

Figure 5.23: The menisci formed by propellant on nonemitting surfaces of the emitter, taken by an SEM.

Figure 5.24: The PoWEE emitter, viewed at an oblique angle, at 4700V emitter voltage and 4s exposure time. Multiple locations where plumelets impinge upon the extractor are visible.

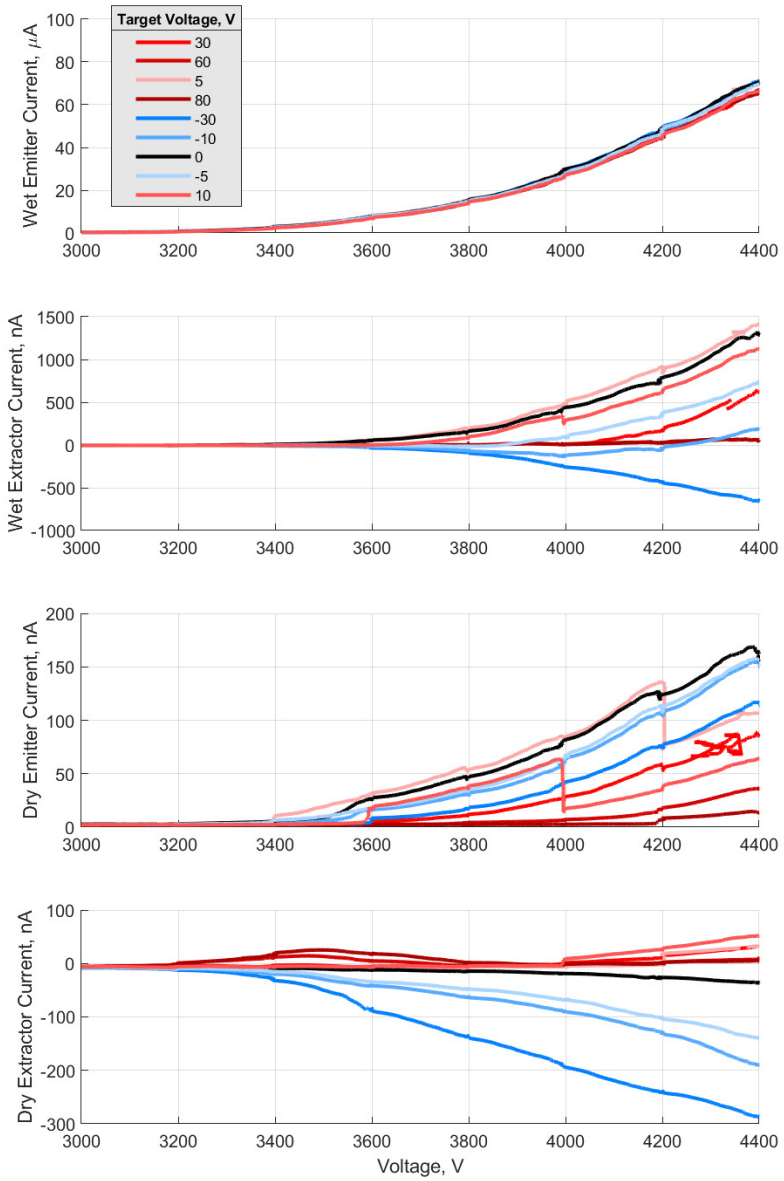

Figure 5.25: Current measurements from the emitters and extractors from the wet and dry thrusters, as a function of emitter and target voltages. Both emitters were operated at the same voltage for this test. The target voltages are listed in the order they were tested from top to bottom. Blue and red curves indicate negative and positive target voltages respectively.

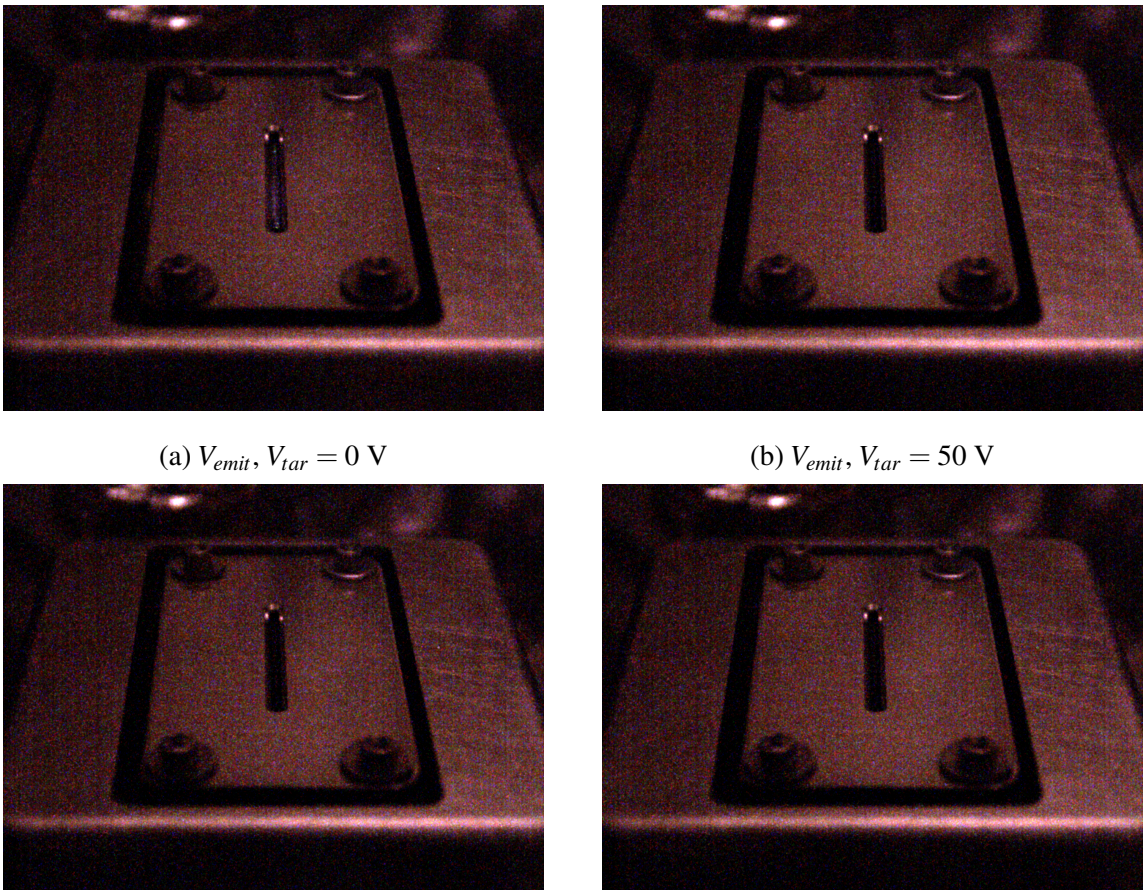

(a) V_{emit}, $V_{tar} = 0$ V

(b) V_{emit}, $V_{tar} = 50$ V

(c) 0 V, $V_{tar} = 0$ V

(d) 0 V, $V_{tar} = 50$ V

Figure 5.26: In situ observation of the dry emitter while emitting from the wet emitter, as a function of dry emitter voltage and target potential (indicated in the subfigure captions respectively). Glow from the dry emitter was observed when the dry emitter was energized and the target was at ground potential. Images were captured with an 80 s exposure time and brightened by a factor of 5.

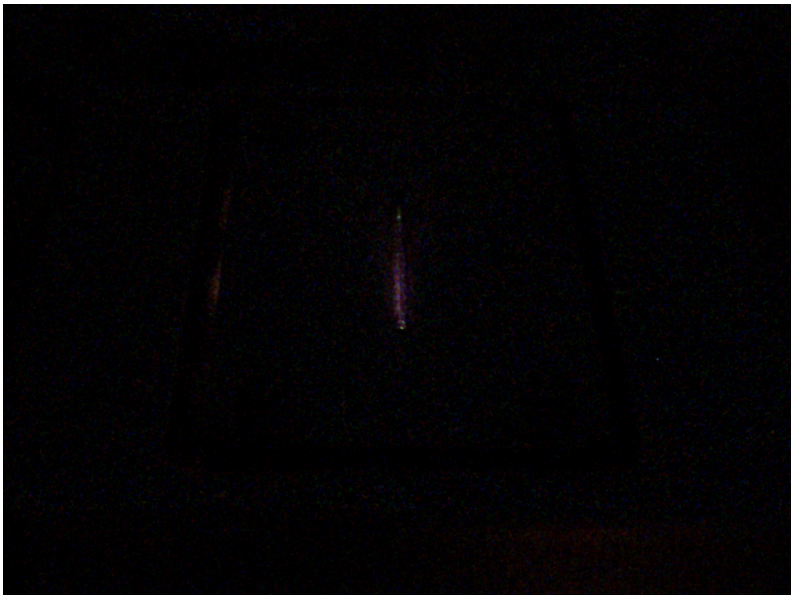

(a) Illumination difference

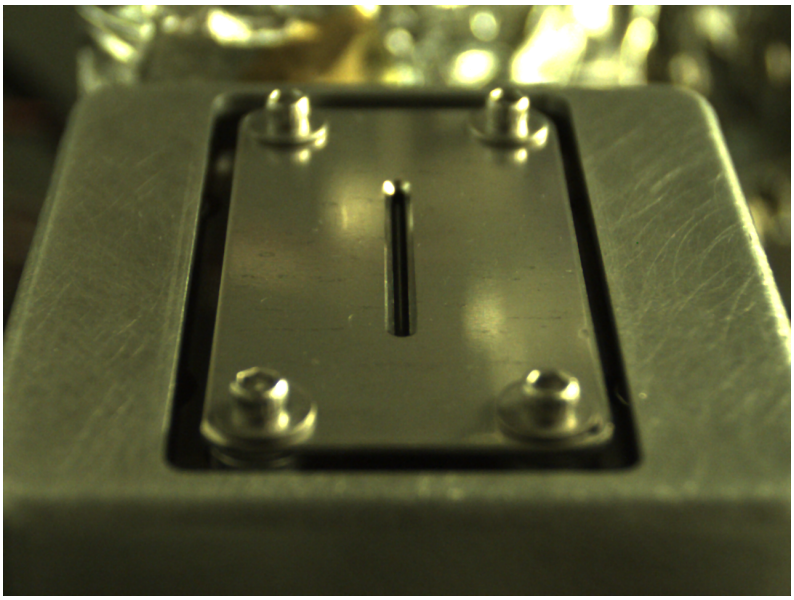

(b) Bright image for reference

Figure 5.27: The difference between illumination recorded with the dry emitter energized and unenergized, at 0 V beam target potential. This image isolates the additional illumination observed due to energizing the dry emitter.

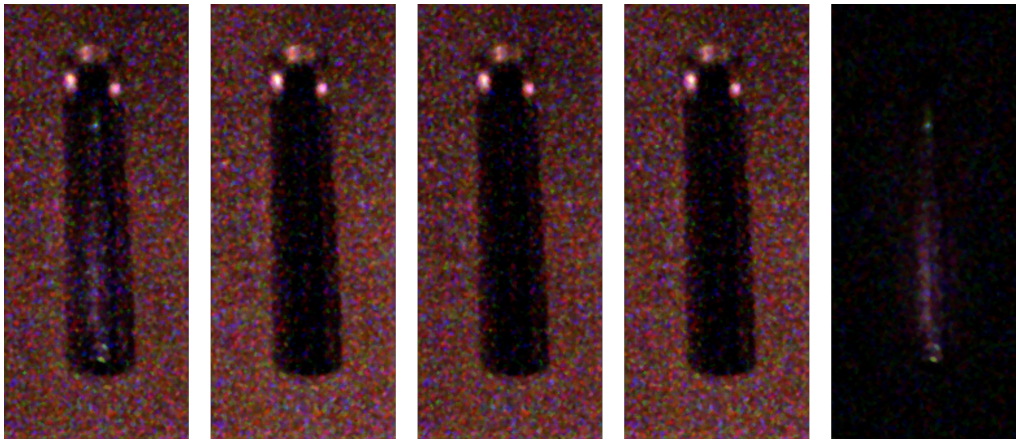

Figure 5.28: From left to right, the views of the dry emitter shown in Figures 5.26a-d and Figure 5.27, cropped to the extractor aperture for clarity.

CHAPTER 6

Porous Electrospray Operational Model

6.1 Introduction

To understand the fluid effects responsible for emergent behavior from porous electrospray emitters, we have developed multiple complementary models from first principles of porous flow, electrostatics, and hydrodynamics. The steady state flow through a porous electrospray device has been described by Darcy's law in the porous medium and the applied pressure difference across the device. A model to describe emission site multiplexing on a porous wedge has been developed. Additionally, the transient response of a porous emitter is affected by the volume required for onset of emission and diffusion of pressure through the porous medium. To capture transient device behavior, an analytical model has been developed to describe the role of fluid storage in transverse exposed pores on flow settling.

The objective of this effort is to utilize recently developed porous flow models to understand the fluid mechanics responsible for the behavior of the Porous Tungsten Electrospray Emitter (PoWEE). Additionally, this effort serves as an example for how to combine models for transient flow (as described in Chapter 4), onset volume, and multiplexing (as described in Chapter 3) in order to understand the fluid mechanics of porous electrospray devices.

6.2 Emitter Configuration

The emitter is formed from a porous material with an experimentally measured porous permeability of $7.83 \times 10^{-15}\,\mathrm{m}^2$ and a mean pore size of $2.0\,\mu\mathrm{m}$. The emitter has a total length of $17.8\,\mathrm{mm}$, a full-angle of $60°$, and a height of $2.54\,\mathrm{mm}$. The etching process produced an emission surface

radius of roughly 30 µm.

The emitter assembly utilizes a fluid stack that is comparable to porous electrospray thrusters using emitters manufactured from porous glass [2, 34, 35, 36]. A P3-grade porous glass reservoir was used to provide a controlled backpressure in the emitter. The small piece of filter paper placed between the emitter and reservoir helps to ensure hydraulic coupling of the emitter and reservoir.

In the context of the present porous flow model, the filter paper and porous reservoir are assumed to have very high porous permeability such that there is no pressure gradient in these media. The pore size of the porous reservoir is 10 to 40 µm, which is much larger than that of the emitter (2 to 3 µm). The reservoir pressure is assumed to be produced by the largest pores in the medium.

6.3 Electrostatics

The electric field at the surface of the emitter was evaluated in COMSOL parametrically, as a function of emitter-extractor distance and extractor gap. The extractor aperture had a 1 mm width. The emitter to extractor distance varies between 0.15 mm and 0.19 mm over the length of the emitter. A coefficient f^{-1} is introduced to describe the electric field at the emission surface:

$$E = f^{-1}V \tag{6.1}$$

With these geometric constraints, simulation of the extraction field suggests that $f^{-1} = 7.5 \times 10^3\ \mathrm{m}^{-1}$. The results from electrostatic simulation over a wide range of geometries are shown in Figure 6.1b. The potential near the emitter and extractor are shown in Figure 6.1a, with pathlines shown for stationary charged particles released at the emission surface. The low interception current measured in operation is likely due to how particles released from the radius of the emitter do not intercept the extractor.

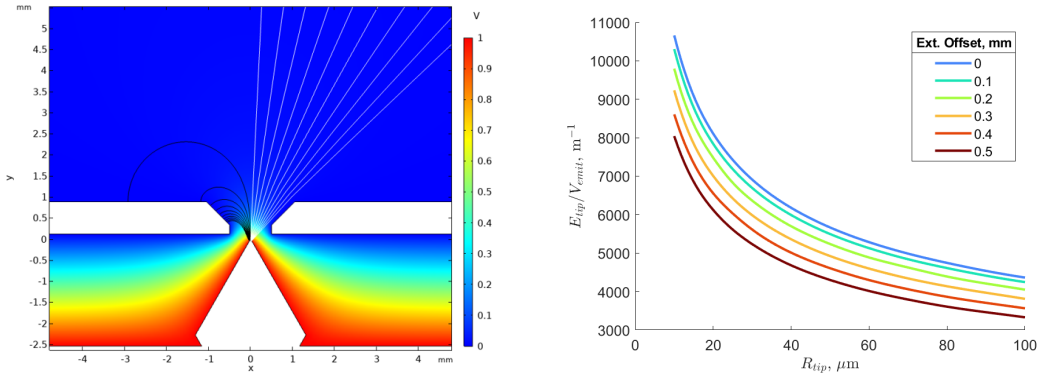

Figure 6.1: Left, electric potential for the PoWEE extraction geometry. Particle pathlines are shown in white and electric field streamlines are shown in black, originating from the right and left halves of the emitter radius respectively. Right, the electric field produced at the emission surface as a function of emitter tip sharpness and extractor-emitter offset.

6.4 Steady Fluid Mechanics

6.4.1 Low Site Density

When the number of emission sites is low, the porous flow supporting each emission site most resembles a radially-uniform flow to the emission site. Flow can reach the emission site through an orange-slice shaped porous domain with spherical symmetry, as constrained by the angle of the wedge. Insert diagram of the flow domain here. Along the ridgeline, flow is confined by the ridge and reaches $-\pi$ to π. Perpendicular to the ridgeline, flow extends from $-\theta_w/2$ to $\theta_w/2$. The pressure within the domain is:

$$P_{cone} = \left(\frac{R_2}{R_1 - R_2}\right)\left(\frac{R_1}{r} - 1\right). \tag{6.2}$$

The flow rate through the emission site is found by integrating the fluid velocity, from Darcy's law, over the solid angle of the wedge:

$$Q = \frac{2\theta_w k \Delta P R_1 R_2}{\mu(R_1 - R_2)}. \tag{6.3}$$

The hydraulic resistance of the site is the ratio of pressure difference and flow rate:

$$R_{hyd,1} = \frac{\mu(R_1 - R_2)}{2\theta_w k R_1 R_2}. \tag{6.4}$$

Equation 6.4 is expected to produce a reasonable estimation of site hydraulic resistance when the site spacing is much larger than the height of the emitter.

6.4.2 Moderate Site Density

Supposing that the emission site spacing may not be small compared to the radius of the wedge base, a more general solution for the pressure in the wedge is sought. For this case, we consider a secondary flow which satisfies the following boundary conditions in r:

$$P_s(R_1, z) = 0, \quad P_s(R_2, z) = \hat{P} e^{i\alpha z}, \tag{6.5}$$

where $\hat{P}$ is a constant to represent the magnitude of pressure variation at the emission surface, $r = R_2$. The solution to Laplace's equation in this case is similar to Eq. 2.5:

$$P_s(r, z) = \hat{P}\left[\hat{C}_2 K_0(\alpha r) + \hat{C}_3 I_0(\alpha r)\right] e^{i\alpha z}, \tag{6.6}$$

where $\hat{C}_2$ and $\hat{C}_3$ are constant coefficients. Solving for the given boundary conditions yields:

$$\hat{C}_2 = -\frac{\frac{I_0(\alpha R_1)}{K_0(\alpha R_1)}}{I_0(\alpha R_2) - \frac{I_0(\alpha R_1)}{K_0(\alpha R_1)} K_0(\alpha R_2)}, \tag{6.7}$$

$$\hat{C}_3 = \frac{1}{I_0(\alpha R_2) - \frac{I_0(\alpha R_1)}{K_0(\alpha R_1)} K_0(\alpha R_2)}. \tag{6.8}$$

The radial flow due to the secondary flow, $u_{r,s}$, at the emission surface is given by Darcy's law:

$$u_{r,s}(R_2, z) = -\frac{k}{\mu}\frac{\mathrm{d}P_s}{\mathrm{d}r} = -\frac{k}{\mu}\hat{P}\alpha\left[-\hat{C}_2 K_1(\alpha R_2) + \hat{C}_3 I_1(\alpha R_2)\right] e^{i\alpha z}. \tag{6.9}$$

The net flow through the emission surface is driven by the primary flow. The radial flow due to the primary flow, $u_{r,p}$, is:

$$u_{r,p}(R_2) = \frac{k P_0}{\mu R_2 \ln(R_2/R_1)}. \tag{6.10}$$

The individual site flow rate is determined by integrating the primary flow over the emission surface in the cell of one emission site:

$$Q_{site}(\lambda) = \frac{\lambda k \theta_w P_0}{\mu \ln(R_1/R_2)}. \tag{6.11}$$

The relationship between P_0 and $\hat{P}$ is determined through enforcing the no flow condition at stagnation points:

$$\hat{P} = \frac{P_0}{\alpha R_2 \ln\left(\frac{R_2}{R_1}\right)} \left[-\hat{C}_2 K_1(\alpha R_2) + \hat{C}_3 I_1(\alpha R_2)\right]^{-1}. \tag{6.12}$$

The pressure difference between the porous reservoir and the emission surface is:

$$\Delta P = \hat{P} + P_0, \tag{6.13}$$

$$P_0 = \Delta P f(\alpha), \tag{6.14}$$

where

$$f(\alpha) = \left(1 + \left(\alpha R_2 \ln\left(\frac{R_1}{R_2}\right)\left[-\hat{C}_2 K_1(\alpha R_2) + \hat{C}_3 I_1(\alpha R_2)\right]\right)^{-1}\right)^{-1}. \tag{6.15}$$

The hydraulic resistance of an emission site is the ratio of pressure difference and flow rate, which is determined by substituting Equation 6.13 into Equation 6.11:

$$R_{hyd,2} = \frac{\mu \ln(R_1/R_2)}{\lambda \theta_w k f(\alpha)}. \tag{6.16}$$

6.4.3 High Site Density

When site spacing is very low, the flow concentration to the emission sites is no longer a dominant factor in determining the hydraulic resistance. For this case, the increase in flow concentration is neglected and the hydraulic resistance is determined solely from the primary flow. Interestingly, the hydraulic resistance associated with the primary flow is equivalent to Equation 6.16 if $P_0 = \Delta P$

and $f(\alpha) = 1$. This hydraulic resistance is analogous to the approach adopted by Dressler et al. for cone-shaped emitters, where the emission site hydraulic resistance was found by multiplying the total resistance by the number of emission sites. Ignoring the hydraulic resistance associated with emission site flow concentration is reasonable for cone-shaped emitters due to the close proximity of emission sites.

$$R_{hyd,approx} = \frac{\mu \ln(R_1/R_2)}{\lambda \theta_w k}. \tag{6.17}$$

6.4.4 Comparing Hydraulic Resistances

The hydraulic resistance of individual emission sites as determined through Equations 6.4 and 6.16 are plotted in Figure 6.2. Additionally, two analytical hydraulic resistance estimations are included, per Wright and Wirz [1]. First is the hydraulic resistance calculated for flow concentration to emission sites on a wedge, neglecting the contribution of modified Bessel function of the first kind, i.e. the I_0 term, in Equation 6.6.

Figure 6.2 shows that for densely packed emission sites, the three $\lambda-$ dependent hydraulic resistance estimations converge. As emission site spacing increases, hydraulic resistance increases with the number of Bessel terms considered in Equation 6.6. Spherical flow, as used to determine the low site density hydraulic resistance estimation, produces a higher emission site hydraulic resistance than any of the other three due to restricting emission surface fluid flow to only very close to the emission site. Of these four hydraulic resistance estimations, Equations 6.4 and 6.16 are considered to be the most accurate and are used depending on which estimation is higher.

6.5 Transient Fluid Mechanics

Diffusion of pressure through a porous electrospray can be described through how the meniscus recedes at the emitter surfaces where emission does not occur. Surface tension causes the surface curvature to change with the local pressure, which is enforced through Darcy's law. Even though the flow through porous electrospray emitters is generally low Reynolds number, which is

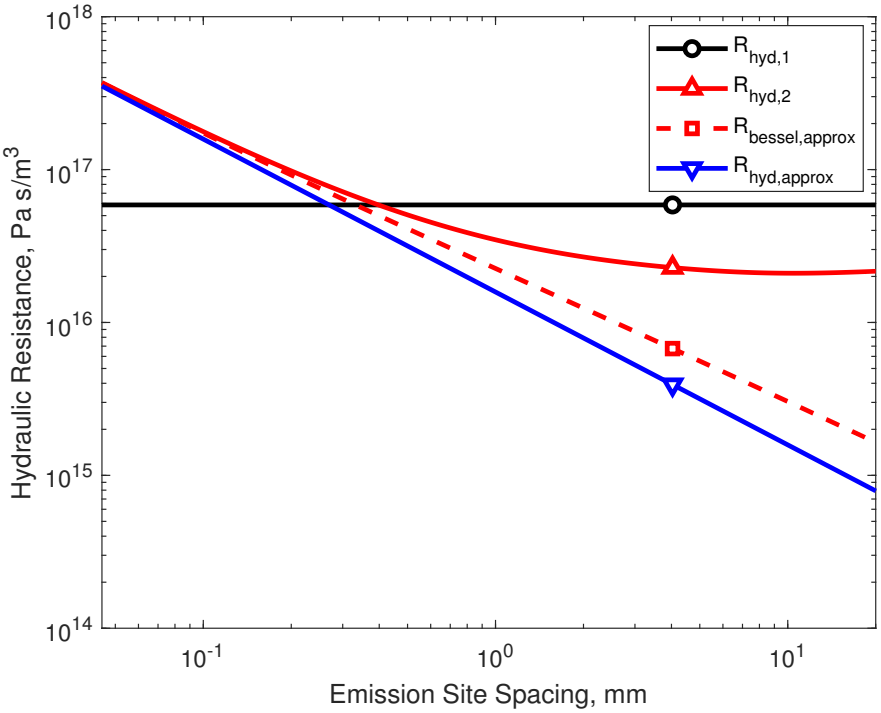

Figure 6.2: Hydraulic resistance of an emission site as a function of site spacing, depending on the flow model used.

typically associated with instantaneous reaction to pressure changes, the pressure-dependent accumulation of propellant at the surface of the emitter can cause transient flow conditions. Evaluating the change in storable propellant at exposed pores due to the Young-Laplace equation yields a diffusion equation for pressure in a porous medium with an exposed surface, where D is the diffusion coefficient for this flow:

$$\frac{\partial}{\partial t}P = D\nabla^2 P; \quad D = \frac{16\gamma k}{\alpha\mu R_{pore}^2}\frac{\mathrm{d}V}{\mathrm{d}A}. \tag{6.18}$$

The diffusion equation has been solved for the wedge primary flow as:

$$P_t(r,t) = \sum_{n=1}^{N} 2C_n \left[Y_0\left(2\sqrt{\frac{\lambda_n r}{D_0}}\right) - \frac{Y_0\left(2\sqrt{\frac{\lambda_n R_2}{D_0}}\right)}{J_0\left(2\sqrt{\frac{\lambda_n R_2}{D_0}}\right)} J_0\left(2\sqrt{\frac{\lambda_n r}{D_0}}\right) \right] e^{-\lambda_n t}. \tag{6.19}$$

The flow rate due to the settling of the primary flow, into a single emission site is solved using Darcy's Law:

$$\begin{aligned} Q_t(t) = &\frac{kR_2\theta_w\lambda\Delta P}{\mu} \sum_{n=1}^{N} 2C_n \sqrt{\frac{\lambda_n}{D_0 R_2}} e^{-\lambda_n t} \\ &\times \left[Y_1\left(2\sqrt{\frac{\lambda_n R_2}{D_0}}\right) - \frac{Y_0\left(2\sqrt{\frac{\lambda_n R_2}{D_0}}\right)}{J_0\left(2\sqrt{\frac{\lambda_n R_2}{D_0}}\right)} J_1\left(2\sqrt{\frac{\lambda_n R_2}{D_0}}\right) \right]. \end{aligned} \tag{6.20}$$

The eigenvalues and coefficients required for evaluating Equation 6.20 are shown in Table 6.1.

This diffusion equation has provided useful predictions for the transient response of a porous pillar style electrospray emitter [38]. In a wedge electrospray emitter, two time constants are expected to emerge based on the relevant length scales for the base flow (emitter size) and flow separation to each emission site (site spacing). A more detailed description of porous diffusion in electrospray emitters and analytical predictions for diffusion in cone, pillar, and wedge emitters is planned for an upcoming manuscript

n	λ_n, 1/s	C_n
1	316	0.2743
2	1339	0.2043
3	3056	0.1398
4	5463	0.0722
5	8560	0.0077
6	12347	-0.0455
7	16821	0.0883

Table 6.1: Eigenvalues and projection coefficients for the first 7 modes of the transient primary flow.

6.6 Emitted Specific Charge

This approach has been adopted from ESPET [98]; a condensed version of their analysis is included for clarity.

At high flow rates, electrospray emitters operate in cone-jet mode, where the emitted current is determined through investigation of the transition between Taylor cone and jet. Current is proportional to the square root of flow rate:

$$I_{droplet} = C_1 Q^{0.5}, \tag{6.21}$$

where C_1 is an analytically informed, experimentally determined constant. Experimental investigation of cone jet emission has yielded values of C_1 of 0.3 to 0.5 $\mathrm{As}^{0.5}/\mathrm{m}^{1.5}$ for EMI-Im [135, 136, 137]. Variation in the coefficient can be explained by temperature variation to a large extent. We expect that cone jet relations may hold for porous electrospray emission at high flow rates because the restorative pressure provided by the reservoir becomes negligible in comparison to the surface tension and electric pressures near the tip of the Taylor cone.

As flow rate decreases, more current may be emitted as ions rather than droplets. The emitted ion current, I_{ion} is predicted through the area from which ions are emitted, A, and the electric field

internal to the ionic liquid, E^I_{max}.

$$I_{ion} = AKE^I_{max}, \tag{6.22}$$

$$A = \pi \left(\frac{4\gamma}{\varepsilon_0 E^2_{max}} \right)^2, \tag{6.23}$$

$$E^I_{max} = \frac{E_{max}/\varepsilon}{1 + \frac{hK}{\varepsilon_0 \varepsilon k_b T} \exp\left[\frac{\Delta G - G(E_{max})}{k_b T} \right]}, \tag{6.24}$$

$$E_{max} = \left(\frac{\gamma^3 K}{\varepsilon_0^4 Q} \right)^{\frac{1}{6}}, \tag{6.25}$$

For more details, see Coffman and Lozano [62, 138, 64], and Peter et al. [98].

The current as a function of flow rate is shown in Figure 6.3a, with droplet and ion components indicated. Ion emission contributes a negligible increase in mass flux, so its contribution to mass flux is neglected. Above 0.1 pL/s, mass from ion emission is less than 5 % of the droplet current. These results are implemented in the model as specific charge as a function of flow rate, as shown in Figure 6.3b. A mathematical fit for specific charge as a function of flow rate is developed using the following form:

$$\frac{q}{m} = \frac{C_1}{\rho Q^{1/2}} \left(1 + \frac{a-1}{1 + \left(\frac{Q}{Q_c} \right)^b} \right), \tag{6.26}$$

where a is the ratio of total specific charge to droplet specific charge for $Q \ll Q_c$, b is a steepness coefficient, and Q_c is the transitional flow rate between ion emitting and non ion emitting modes; these parameters were determined by least squares optimization. The value of ΔG was set to 1.48 eV in agreement with literature and to set Q_c to Q_{min}, 2.93 pL/s. The values of a and b were 2.71 and 4.25 for this study.

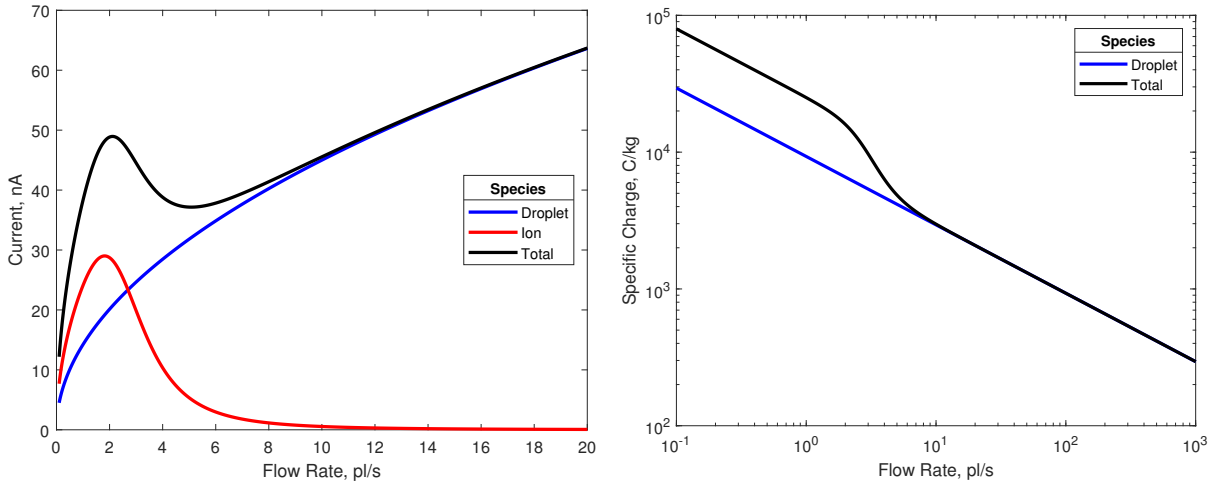

(a) Current

(b) Averaged specific charge

Figure 6.3: Behavior of a single emission site as a function of flow rate, showing the contributions of ion and droplet emission.

6.7 Onset Volume

The high electric field required for electrospray emission is a result of the natural sharpening of the meniscus in response to an external electric field [18]. A certain volume of liquid is required to pass through the emitter substrate before this meniscus sharpening can occur. An understanding of the liquid volume required for emission as well as the viscous dissipative forces restricting flow to the emission surface are combined to form common onset delay models. Flow through the emitter has already been investigated in previous sections, now it is time to consider the volume required for emission.

Multiple descriptions of emission from a porous surface have been presented, as shown in Figure 6.4. Each model results in a different estimate for the volume required for onset of emission. From left to right in Figure 6.4, modes of emission generally require a larger volume of liquid to accumulate on the surface of the emitter.

The least propellant is required to accumulate on the emission surface for emission from the sharp points of sintered particles. The porous medium of interest was constructed through sintering of particles with a diameter of roughly 5 to 10 μm.

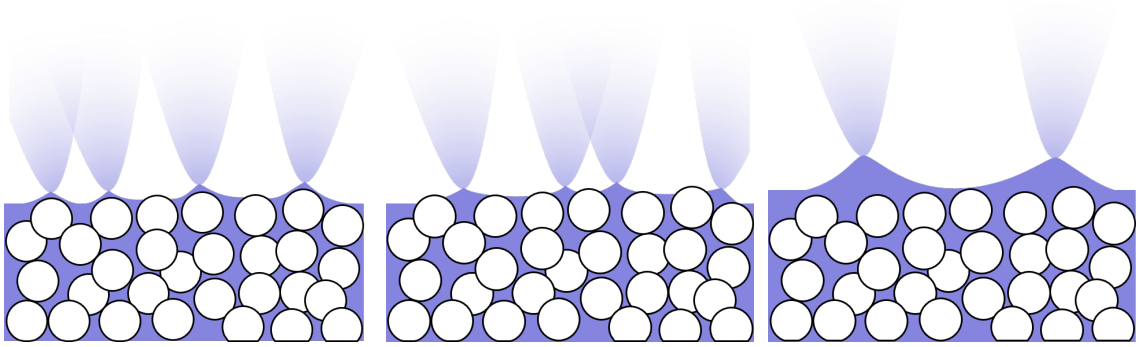

(a) (b) (c)

Figure 6.4: Three proposed schemes for emission from porous electrosprays. From left to right, emission from sharp points on sintered particles of the porous medium, emission from the pores of the porous medium, and emission due to pooling on the porous medium. Adapted from Ober [3].

The radius of a Taylor cone on a the porous medium, emitting in an externally-wetted mode, should have a base radius, $r_{TC,E}$, as follows:

$$r_{TC,E} = r_p \cos(\theta_{TC}), \tag{6.27}$$

where r_p is the radius of sintered particles in the medium.

Based on the particle size of the medium used for the emitter, the base radius of Taylor cones in an externally-wetted mode should be 3 to 5 µm.

For emission resembling capillary emission, the Taylor cone is confined to a surface pore. The base of the Taylor cone should match the pore size of the medium. For the porous medium used in this study, the pore diameter was measured to be 2 to 3 µm.

For emission where the Taylor cone is unconfined by the geometry of porous medium, the radius of the cone may be much larger than the sintered particles or pores. Analytical models predict that the cone base radius scales with γ/P [63] for emission from a porous medium with restorative pressure. At onset, the pressure in the porous medium is provided by the porous reservoir and not yet reduced by the viscous dissipation. In this case, the unconfined Taylor cone base radius, $r_{TC,\gamma}$, scales with the reservoir pore size:

$$r_{TC,\gamma} \sim \frac{\gamma}{P} = \frac{D_{res}}{4}. \tag{6.28}$$

Per manufacturer specifications, the pore size for the P3-grade porous reservoir used in the emitter assembly is as large as 40 µm, so unconstrained Taylor cones may have a radius of roughly 10 µm. This brief analytical approach misses some of the nuance of cones formed on a porous emitter; for example, the electric field is assumed not to have an effect on the size of the cone despite experimental evidence that voltage has a strong effect on emission properties. Porous emission cone shape and size has been investigated in more detail but is outside of the scope of this dissertation.

Depending on the mode of operation, it is reasonable to expect that Taylor cones with a base radius of 1 to 10 µm. The volume of the Taylor cone, V_{TC}, is calculated using the equation for the volume of a cone and Taylor's angle, θ_{TC}:

$$V_{TC} = \frac{\pi r_{TC}^3 \cos^4(\theta_{TC})}{3\sin(\theta_{TC})}, \tag{6.29}$$

6.8 Model Construction

6.8.1 Steady emission

First, we assume that there exists a number of sites on the emitter where emission may occur. A few models have been proposed for where emission occurs on the emitter. Emission sites may resemble externally-wetted emitters by forming on sintered particles in the porous medium [139], and/or at the pores in the porous medium resembling capillary emission [139, 140]. With a particle size of 10 µm, emitter length of 17.8 µm, and an emission surface roughly 1 to 3 pores across, up to about 5000 emission locations may exist. Due to the roughness of the emission surface produced by the medium and emitter manufacturing process, a fraction of these candidate sites serve as electric field concentration points where emission is more likely to occur. The number of emission sites is informed by experimental results at high voltage, where around 200 plumelets were measured.

Next, a distribution of electric fields are assumed among the candidate emission sites. A nomi-

nal electric field of 7.5×10^3 V/m per V extraction was determined computationally. Sharp points on the emitter are assumed to have up to double this nominal electric field due to the additional radius of curvature. Uniform and normal distributions were assumed, but its unclear which is more reasonable.

Next, the pressure difference at each emission site was determined. The reservoir pressure was determined though the Young-Laplace equation and the Maxwell pressure was used at the emission sites:

$$\Delta P_i = -\frac{1}{2}\varepsilon_0 (f_i^{-1} V)^2 + \frac{4\gamma}{D_{res}}. \tag{6.30}$$

Only sites with a emission site pressure lower than the reservoir pressure, i.e. $\Delta P < 0$, emit at the given voltage set point.

Third, the hydraulic resistance of each emission site is determined from the number of emitting sites. We assume that emission sites are equally spaced, independent, and with equal hydraulic resistance. The hydraulic resistance model used depends on the number of emitting sites and N_{cutoff} is the number of emission sites for which the two hydraulic resistance models produce equal estimates.

$$N < N_{cutoff} \quad \rightarrow \quad R_i = R_{hyd,1}. \tag{6.31}$$

$$N > N_{cutoff} \quad \rightarrow \quad R_i = R_{hyd,2}. \tag{6.32}$$

This method may overestimate the hydraulic resistance of highly-emitting sites and underestimate those with little flow rate. In the physical device, sites with high flow rates will deform streamlines in the porous medium towards nearby emission sites, and this is not captured by the present model. The flow rate to each site is calculated from the hydraulic resistance and pressure difference, where $Q_i > 0$ indicates flow out of the emitter.

$$Q_i = -\frac{\Delta P_i}{R_i}. \tag{6.33}$$

For each emission site, emitted current is determined from the mass flow rate and specific charge as a function of flow rate, from Equation 6.26.

$$I_i = \rho Q_i \left(\frac{q}{m}\right)_i \tag{6.34}$$

Finally, the total current from the emitter is determined by summing the current from each emission site:

$$I_{tot} = \sum_{i=1}^{N} I_i. \tag{6.35}$$

6.8.2 Transient Response

After determining the steady response, the transient response can be calculated. The emission site spacing, λ, emission site flow rate, Q_i, and pressure difference, ΔP_i, are included from the steady response.

First, the transient flow rate, $Q_{t,i}$, is determined using Equation 6.20. For emission with a low number of emission sites, L/N_{cutoff} is used instead of the emission site spacing. The transient flow rate (determined from the transient homogeneous pressure solution) adds to the steady flow rate:

$$Q_i(t) = Q_{s,i} + Q_{t,i}. \tag{6.36}$$

Next, the onset cone volume is determined. In this model, we have proposed a semi analytical model for emission from a meniscus covering multiple pores and from a meniscus of predetermined size.

Third, the flow rate to each emission site is numerically integrated as a function of time to determine the volumetric fluence:

$$F_i(t) = \int_0^t Q_i(t)\mathrm{d}t. \tag{6.37}$$

Sites begin to emit once the fluence exceeds the onset cone volume for the emission site. Emitted current is determined from the mass flow rate and specific charge as a function of flow rate, from Equation 6.26.

$$F_i(t) < V_{onset} \quad \rightarrow \quad I_i(t) = 0; \tag{6.38}$$

$$F_i(t) > V_{onset} \quad \rightarrow \quad I_i(t) = \rho Q_i(t) \left(\frac{q}{m}\right)_i. \tag{6.39}$$

As with the steady current response, the total current from the emitter is the sum of the emitted current from each emission site:

$$I_{tot}(t) = \sum_{i=1}^{N} I_i(t). \tag{6.40}$$

The total emitted flow rate can be found through a similar time-dependent summation of flow through each emission site.

6.9 Results and Discussion

Thruster parameters where chosen based on the properties of the components in the assembly. Based on the sharp feature spacing of roughly 50 to 100 µm and a total emitter length of 17.8 mm, 200 emission site locations are assumed to exist on the surface of the emitter. While the nominal electric field on the surface was determined to be 7.5×10^3 V/m per extraction volt, the electric field at each emission site was assumed to be normally distributed with a 10 % standard distribution about 1.25 times the nominal electric field. Sharp points increase the electric field above its nominal value, so the elecrtic field at emission sites is generally above the nominal electric field. The downstream emitter radius was 30 µm and the upstream emitter radius was selected to match the emitter height of 2.54 mm. The porous reservoir is assumed to have a uniform collection of pores at 25 µm diameter, the average of the extents of pore size per the manufacturer. Onset delay was accounted for by assuming that Taylor cones have a base radius of 5.5 µm.

The distribution of electric field coefficients are shown in Figure 6.5. These coefficients are independent of emitter potential. The electric field at emission sites are determined through Equation 6.1 and shown in Figure 6.6. The electric field is used to determine the pressure difference driving flow through each emission site through Equation 6.30, the results from which are shown in Figure 6.7. A positive pressure difference in this figure indicates that the pressure is lower at the emission site than in the reservoir. Negative pressure differences, per the convention of Figure 6.7, are assumed to produce no flow. Flow rate supplying each site is calculated using Equation 6.33 and shown in Figure 6.8. Finally, the current from each emission site is calculated from the mass

flow rate and corresponding specific charge. Emission site current distributions are shown in Figure 6.9.

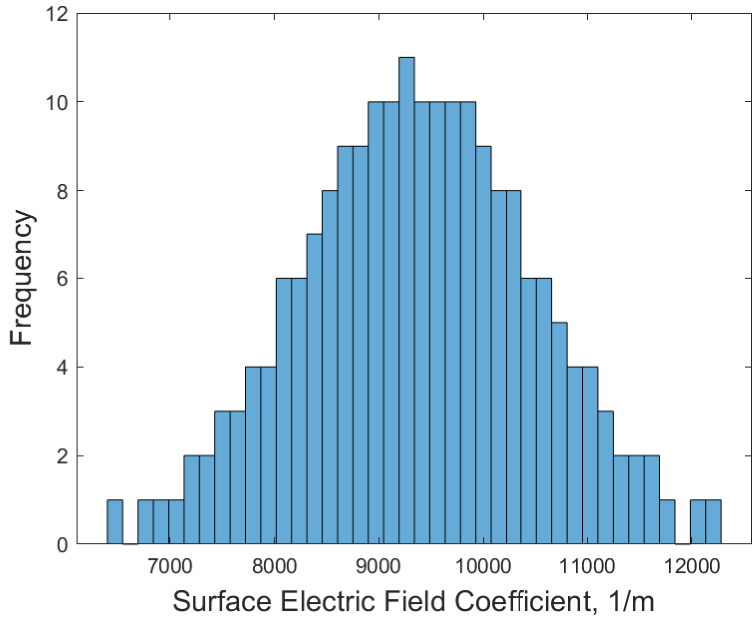

Figure 6.5: Distribution of electric field coefficients at emission locations on the surface of the emitter.

After determining the behavior of each emission site, the collective behavior is determined by summing the output from each emission site. The total current and number of emitting sites can be seen in Figure 6.10. While the magnitude of current predicted by the model is much lower than the that of the physical device, the shape of the IV-curve produced by the model matches quite well with experimental results.

Experimental investigation of electrospray emitters using a porous reservoir for controlled backpressure [2] showed that implementing a P3-grade porous reservoir decreased the contribution of low specific charge species to about 10 % of the total current, while the ion and droplet emission models used in this study produce plumes from individual emission sites that are at least 40 % droplets by current contribution. The underestimation of the current from the device may be due to the underestimation of the current contribution from ions. Increasing the ion emission area at least 30-fold is required to produce a good agreement between the model with experimental results. Due

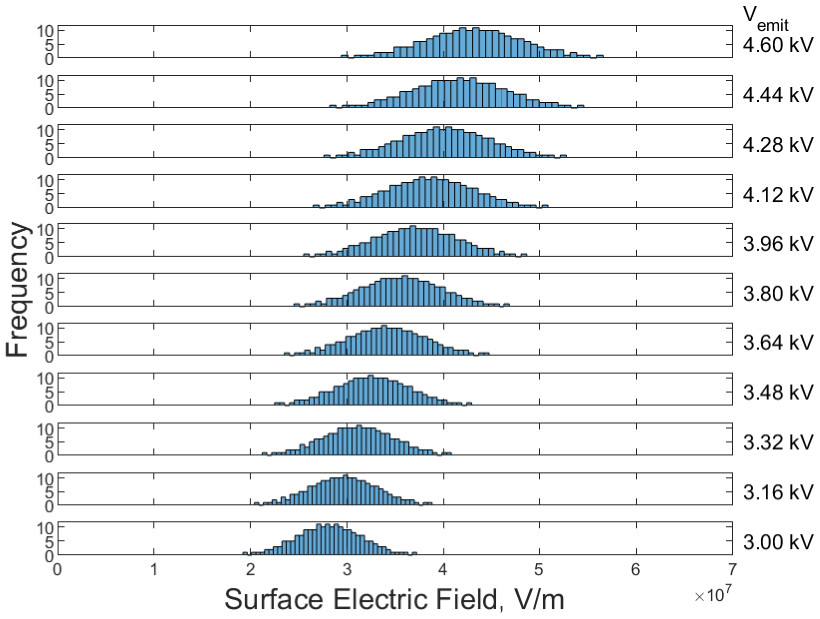

Figure 6.6: Distribution of electric field at emission sites as a function of emitter voltage.

to the disparity between experimental data and modeling predictions, the predicted mass flow rate will be used to show qualitative agreement between transient experimental data and predictions.

Individual site behavior, specifically the average current and spacing between sites, are determined from the total device behavior and number of emitting sites. The emission site spacing rapidly decays near to a steady value as more sites emit at high voltage. Emission site current shows a somewhat chaotic, nonmonotonic response with emitter voltage. A strong kink in the curve is shown at roughly 3700 V where the model switches between using the two separate methods of estimating hydraulic resistance.

The transient response predicted by the model is shown in Figure 6.12 alongside experimental results for reference. The two show good qualitative agreement given the previously mentioned discrepancy between experimental and modeling results for total emitted current. Onset delay is the dominant effect in causing the transient response of the porous wedge electrospray per the model; accounting for transient flow in the emitter has a negligible effect on the transient emission response per the given model operating parameters.

The typical transient of a porous electrospray involves an onset delay, followed by a sharp

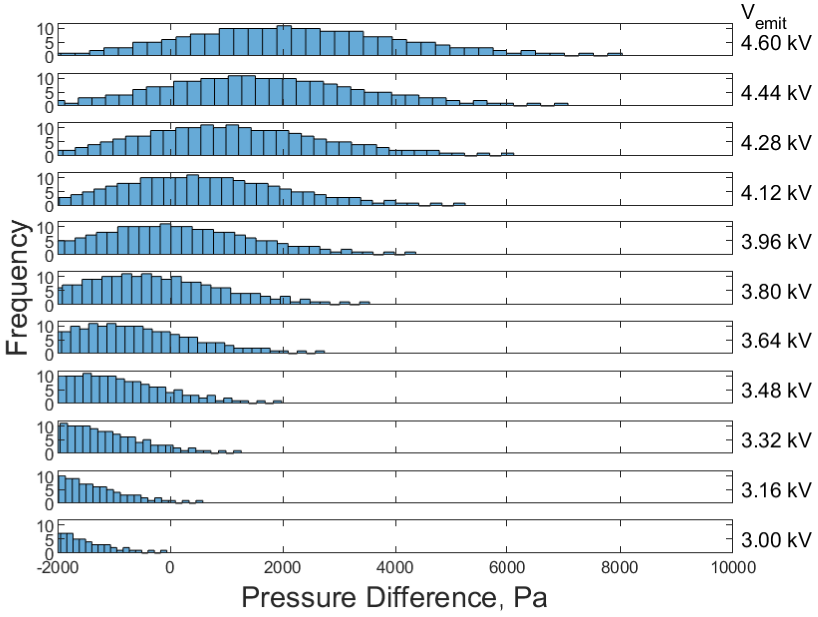

Figure 6.7: Distribution of driving pressure difference at emission sites as a function of emitter voltage. Sites with a pressure difference below 0 are nonemitting.

overshoot and transient decay to the steady emission current. Porous wedge electrosprays differ from this response by having a low onset delay followed by a transient ramp to the steady emission current. The modeling effort has focused on replicating this behavior with physical descriptions of the transient flow in the porous medium and volume required to form Taylor cones on the emission surface. Results show good agreement with experimental results, suggesting that the characteristic response of the porous wedge electrosprays is due to the combined effects of many emission sites, each with transient overshoot events and differing onset delay times. The summation of these many events leads to a decaying increase in emitted current, as these onset events become less common and less prominent as the flow settles. Experimental investigation of the localized transient response, measured in the plume using a wire probe, confirm that individual emission sites have differing onset delays, with shorter onset delays being more common. Both the model and experimental results are in agreement that emission onset events become less common and less prominent with increasing time.

The success of the model presented in this manuscript in replicating experimental results in

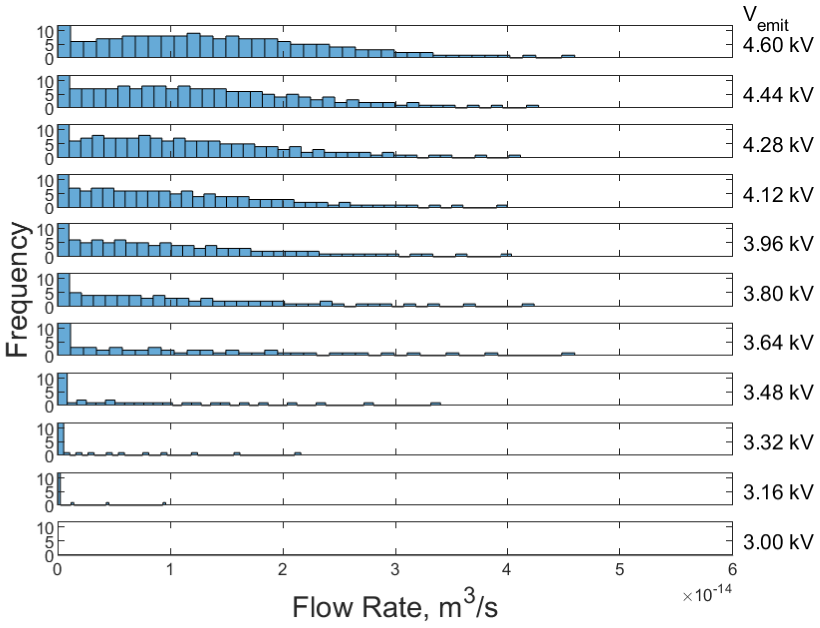

Figure 6.8: Distribution of flow rates to emission sites as a function of emitter voltage.

turn supports the validity of the assumptions used to develop the model. In particular, the observed surface roughness of the emitter was used to justify the assumption that electric field varies at the many emission sites on the tip of the wedge. In the presented flow model, the varying electric field allows for a varying pressure condition on the surface, which leads to the range of onset delays contributing to the transient response of the emitter. To summarize, the surface roughness of the emission surface is incredibly important for understanding the transient response of porous wedge electrosprays. Surface roughness is a result of both the porous material and emission surface fabrication processes.

The presented flow model bears a strong resemblance to the Electrospray Propulsion Engineering ToolKit (ESPET), which is an established toolkit for understanding capillary, externally-wetted, and porous electrospray device behavior [98]. The most clear influence is our adoption of the specific charge determination scheme as a function of flow rate from ESPET. However, the presented model differentiates itself from ESPET in its emphasis on understanding porous fluid mechanics. For porous emitters, ESPET uses a planar flow assumption which inaccurately estimates the hydraulic resistance of cone and wedge electrospray emitters, where flow is radial. Our

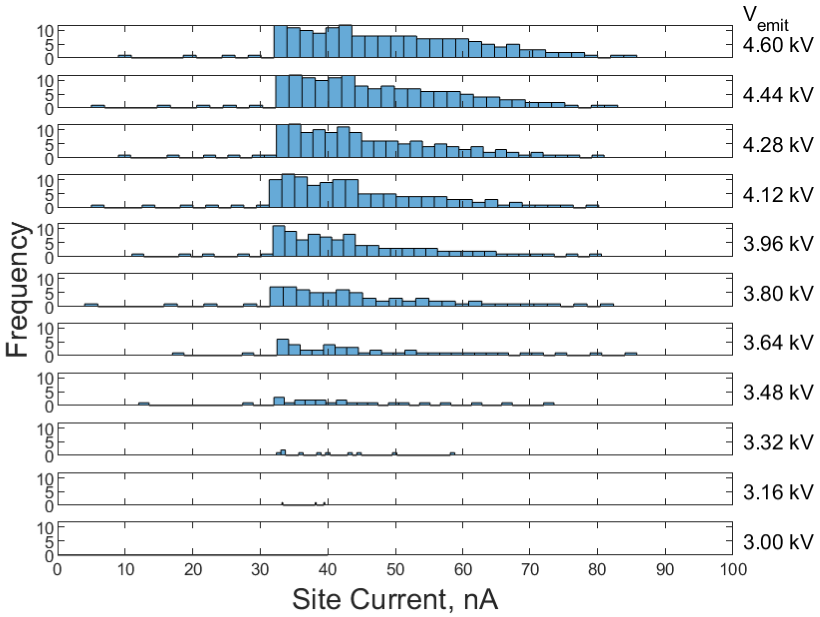

Figure 6.9: Distribution of current from emission sites as a function of emitter voltage.

model improves on the even-sharing assumption made in ESPET to understand hydraulic resistance of individual emission sites. Additionally, ESPET does not incorporate transient flow in the emitter due to desaturation of surface pores [37] to understand transient device behavior. We suggest these as aspects where ESPET could improve its fidelity in future revisions.

In the future, it will be important to interrogate further the quantitative assumptions used to produce this model, such as the number of emission sites and electric field strengths. Bayesian inference techniques, such as those used by Parmar et al. [141] and Whittaker et al. [140], have shown a promising ability to investigate the ability of electrospray models to replicate experimental behavior. The Quantification of Margins and Uncertainty (QMU) framework [142] has been used to allow for experimental results and analytical models to inform lifetime predictions [143]. Each of these techniques would allow for a more detailed investigation of the tolerances that allow for the modeling parameters to replicate experimental results.

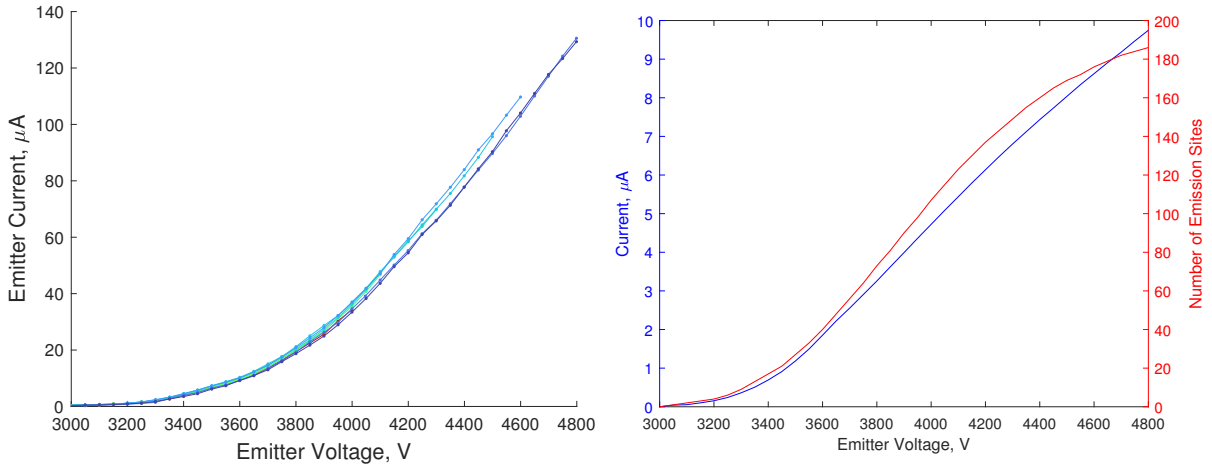

(a) Experimental data

(b) Model results

Figure 6.10: Total current and number of emitting sites as a function of emitter voltage. Experimental results are shown for reference.

6.10 Conclusion

In conclusion, a modeling framework has been explored which allows for the estimating steady and transient response curves from first principles of electrospray emission and porous flow. The agreement between the model and experimental data suggests that emission occurs from sharp features on the surface of the electrospray emitter, which exhibit a range of electric field concentration magnitudes. At each of these emission site locations, a certain amount of propellant is required to develop the electric field concentration required for emission. For the porous wedge electrospray, onset delay is the dominant mechanism for causing the transient response of the porous wedge electrospray considered in this study. The range of onset delays observed in both experiments and the modeling results are caused by the variation in electric field along the emission surface. Broadly speaking, these results inform the considerations engineers and scientists must take into account when developing a porous electrospray thruster.

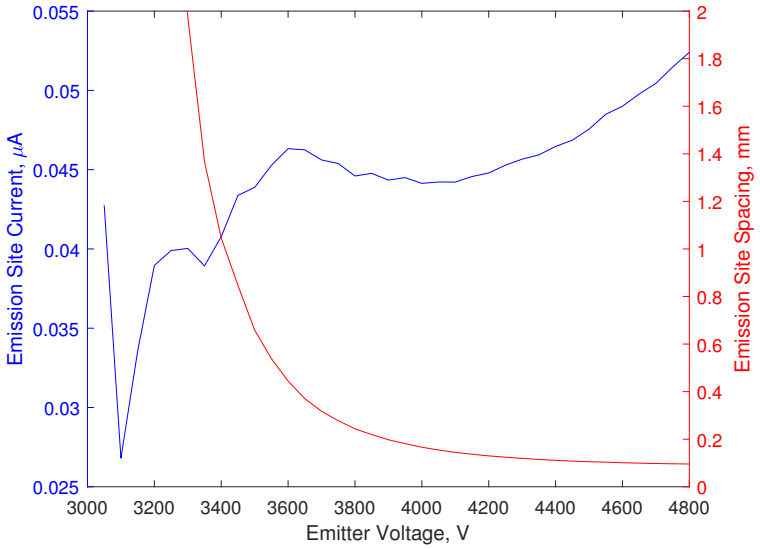

Figure 6.11: Site current and spacing as a function of emitter voltage. Experimental results are shown for reference.

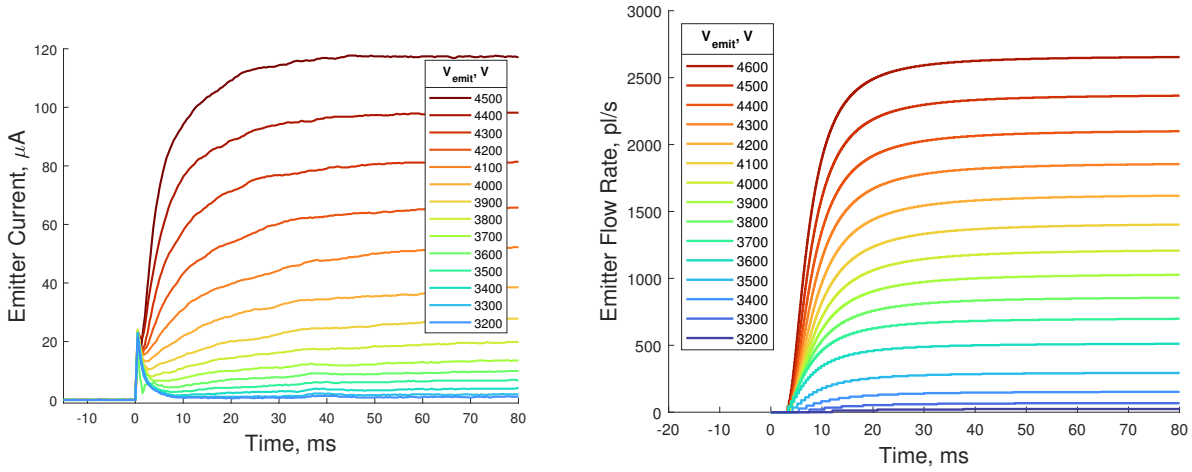

(a) Experimental data

(b) Modeling results

Figure 6.12: Transient emission behavior as a function of voltage.

CHAPTER 7

Conclusion

7.1 Conclusions

The focus of this effort has been to understand the fluid mechanics responsible for electrospray thruster behavior. In particular, the porous wedge electrospray device emerged as an interesting application for this study due to open questions related to their operation. For example, does emission from wedge electrosprays occur at discrete locations? What are the factors responsible for site multiplexing on porous emitters? Why does the transient response of wedge electrospray devices vary from more traditional porous electrospray emitters? The models produced as part of this study have yielded physical answers to all of these questions.

The analytical model for steady, multiplexed emission from the porous wedge assumed that the emission sites naturally space on the porous wedge through a balance of Coulomb repulsion and the hydrostatic pressure variation as a result of the flow concentration to each emission site. These effects were combined to predict that both emission site density and current increased with voltage, which has been confirmed experimentally. Later experimental investigation of the electrospray emission surface showed that the emission surface may not be uniform enough to allow for implementing this model to understand device behavior without modification. Despite this, the steady emission portion and hydrostatic analysis have been valuable to implement in later analytical models for electrospray emission.

A model for understanding the diffusion of pressure through a porous medium with exposed boundaries was developed to understand transient flow in porous electrosprays was developed. The model was derived from first principles of porous flow and interfacial fluid mechanics to

ensure its validity. From the derived diffusion coefficient, surface tension adn porous permeability decrease the settling time, while porosity, viscosity, pore size, and exposed surface area increase settling time. To accommodate the three commonly porous emitter geometries (pillar, cone, and wedge), the diffusion equation was applied to derive the flow solution in each geometry. Analytical solutions show that the flow through emission surface responds immediately and overshoots the steady flow rate before decaying to the steady response. These solutions should be valuable for engineers and scientists who are interested in analyzing the transient response of their thrusters, and to designers who want to reduce the transient settling time of their thrusters. When combined with the existing onset delay model for electrospray transient response, the two models provide a nearly complete view of the fluid mechanics responsible for electrospray transient response. For a truly complete model of transient electrospray emission, a model of transient Taylor cone behavior on a porous medium with a restorative pressure would be necessary, but has been outside the scope of this investigation.

The experimental investigation of porous electrosprays has been incredibly useful for gaining insight into the design and operation of these devices. A simple proof of concept test was valuable for showing the viability of the porous tungsten stock for fabricating electrospray emitters. A pillar style electrospray was developed, showing preliminary data in support of steady and transient emission models. Partly due to manufacturing challenges, the wedge geometry of porous electrosprays was adopted and a more refined experimental setup was developed. The PoWEE wedge emitter is capable of emitting up to 130 µA at 4.8 kV emitter potential, with emission sites in the hundreds along the wedge. Experimental results from the porous wedge electrospray have revealed key insights into facility effects, impingement, thruster glow, emission site uniformity, and thruster transient response. More specifically, the experiments showed that thruster glow can be eliminated through careful design of the extraction geometry and beam target biasing. A detailed investigation of the transient response showed that individual emission sites on porous wedges operate similarly to the thruster response of cone and pillar electrospray emitters despite the total thruster response differing from more traditional cone and pillar electrosprays. Emission sites on the wedge have varying onset delays, which cause the transient ramp observed from porous wedge electrosprays.

Improvements to the preparation of the thruster showed that nearly uniform emission is capable and previously observed nonemitting regions can be eliminated.

A control volume model for porous electrosprays was developed which allowed for predicting the steady and transient response of these devices. The model was partly motivated to understand the device behavior, while also developed to show that multiplexed emission, transient flow, and onset delay models can be combined to make meaningful predictions. The model showed that transient and steady device behavior can be replicated by utilizing the varying electric field along the emission surface, caused by the roughness created as a result of the material and emitter fabrication processes. The success of the model in replicating experimental results supports its assumptions: firstly that onset delay is the dominant mechanism for causing the transient response of porous wedge electrosprays, and second that the range of onset delays among emission sites is due to the variation in electric field as a result of a rough emission surface.

A key feature of the model is its modularity; as new understandings of the flow and emission processes are developed, they can be implemented within the framework to improve the validity of its predictions. The model can be further evaluated using Bayesian techniques for example, to understand the validity of assumptions made to replicate results as well as to understand the sensitivity of device behavior to emitter properties.

7.2 Future Work

Based on the experiments and analyses presented in this dissertation, there are a number of possible future works avenues for further investigation of porous electrospray devices.

The porous flow modeling makes the assumption that fluid accumulates on the emission surface in exposed pores, although investigation of the porous emitter surface when wet shows that the fluid accumulates in channels, which may be associated with a higher volume of fluid accumulation. This change could be accounted for with the development of a different diffusion equation for transient flow, or simply a separate diffusion coefficient. It will be necessary to understand why the porous menisci form channels. Is this feature specific to the subject porous material or

manufacturing process? In other words, is the fluid behavior universal to all emitter materials and manufacturing processes? Additionally, it has not been tested whether these channel-like features remain when a porous reservoir is introduced. Further investigation of the porous menisci may be beneficial.

The porous emission model presented as part of this research has taken a simplified perspective of the emission process. To summarize, the electric field is assumed to impart a negative pressure on the emission surface that does not change with time. Transient emission measurements indicate that emission decays after an initial spike and does so consistently, which suggests that there is a change the pressure at the emission site before and after emission begins. This type of effect was ignored throughout the effort due to the assumption that the pressure contributions from electric field and surface tension are much larger than the contribution from the backpressure provided by the porous reservoir, and are equal and opposite on the meniscus when approaching the cone tip. The extension of this is that a change in electric field due to emission will be counteracted by a change in the effect of surface tension through the curvature of the meniscus. One aspect of the emission process that this perspective neglects is the contribution of momentum on the emission process. Through further investigation of the fluid mechanics of emission from a porous medium, perhaps a more accurate estimation of the hydrostatic pressure at the base of the cone (compared to the Maxwell pressure) can be formed to aid porous flow models.

Experimental measurements of the porous electrospray emitter have focused on facility effects and characterizing the near-field plume spatial and temporal response. For understanding facility effects, the controlled variables have been target bias, emitter bias, and dry emitter bias, while target current and wet and dry emitter and extractor currents have been measured. Although implemented in other electrospray experimental setups, the effect of secondary screening grids, extractor bias, or accelerator electrodes on facility effects have not been considered for this study. These additional components should be implemented and their efficacy evaluated for a more complete understanding of facility effects and how to mitigate them. Additionally, the current deficit or surplus to the beam target implies that a significant portion of current in the system is redirected to the chamber walls; implementing a proxy electrode to substitute for the facility walls will provide

insight into the this missing current component.

The purpose of the beam target is to collect all emitted current from the thruster. Due to the charge and high velocity of incident particles from the emitter, a distribution of negatively- and positively-charged particles are emitted from the target as secondary particles, as discussed previously. Further experimental investigation is required in order to understand the effect that the secondary population has on backstreaming current to the emitter and extractor. Having emitters capable of operation with and without propellant allows for flexibility that can make interesting experiments possible. For example, the beam target can be replaced with a known electron source (cathode) at a variable potential, emitting a known population of electrons at a dry emitter. Control over the cathode temperature and voltage may allow for replicating the effects of the negatively-charged secondaries produced by the beam target. If possible, the replicating experimental results with a characterized electron source may provide greater insight into the secondary species produced by the beam target. The UCLA PSPL is in a good position to perform tests such as these due to recent development of tungsten filament cathodes, for example.

Emission sites are assumed to form on individual sharp points on the emitter surface, and these points are assumed to have a Gaussian distribution in the resulting electric field during emission. A linear distribution has also been considered; both distributions give reasonable results for the emitter response. Further characterization of the emitter surface, through tomographical mapping or confocal microscopy, may give more insight into the variation in sharpness on the emission surface which results in the electric field variation. Characteristics of the emission surface will be particularly sensitive to material fabrication, emitter machining, and surface preparation procedures, so it is difficult to say how universal any conclusion about resulting surface morphology would be. A beginning-to-end model of the surface features, correlated to emission site locations, would be incredibly useful for informing porous electrospray emission models such as the one presented in this dissertation.

7.3 Closing Words

A number of published research efforts that were performed as a part of the research process unfortunately did not find a place in this dissertation. An early experimental investigation of capillary electrospray emitter behavior in atmosphere showed the impact of the many electrospray operating modes on device lifetime [20]. This experience led directly into the development of a hybrid emitter geometry, utilizing a capillary and a concentrically-located externally-wetted needle to achieve both high specific impulse and high thrust to power operating modes with a single device [21]. The challenge of experimental development during the COVID-19 pandemic unfortunately made further development of this design infeasible. The analytical model for capillary electrospray lifetime, developed in collaboration with Dr. Anirudh Thuppul, has been valued by the community for our distillation and simplification of the challenges associated with long device lifetime [56]. These efforts helped to build a broad perspective related to electrospray propulsion, but were not directly related to the porous flow theme of this dissertation. On the other hand, applying the perspectives of each of these efforts to emission from porous electrosprays may be valuable future work related to this effort. In particular, the hybrid electrospray emitter geometry has incredible potential to be further developed with porous emitters as a replacement for the externally-wetted needle. By combining the versatility of porous electrosprays with the operation of capillary emitters, a powerful dual mode electrospray emitter could be developed in the future.

If you have made it this far into this manuscript, thank you for your dedication to my humble effort and writing. This project started as a career and morphed into an extreme passion project over the last few years. I hope that this project and manuscript helps you to understand porous electrospray emitters or allows you to improve upon the body of knowledge in or outside of the electrospray and space propulsion fields. This project would not have been possible without the support and guidance of my peers and mentors, and I am incredibly grateful to you for spending time understanding my work.

ELECTROSPRAY GLOSSARY

- *Bipolar Configuration*: the use of two thrusters with opposite current for the purpose of spacecraft charge neutralization.
- *Alternating polarity operation*: Switching a single thruster between negative and positive emission current to maintain propellant supply neutrality, which prevents propellant degradation and allows for full propellant supply utilization.
- *Multi-mode Propulsion*: The use of 2 or more thrusters, using different thruster architectures (i.e. a chemical rocket and Hall-effect thruster) on a single spacecraft using the same propellant supply.
- *Dual Mode propulsion*: the use of a single thruster to achieve variable performance operation (i.e. a high specific impulse, low thrust-to-power mode and a low specific impulse, high thrust-to-power mode).
- *Extractor Electrode*: The first electrode to the emitter, with an aperture for transmission of the plume. This electrode is used to produce the extraction electric field for electrospraying.
- *Extraction Voltage*: The voltage difference between the emitter and extractor. Typically, this is held constant at a value that promotes stable emission.
- *Accelerator Electrode*: The space-facing electrode (downstream). This electrode is used to maintain a space-facing voltage even when the emitter or extractor voltages are altered. An accelerator electrode is used to prevent electron backstreaming from the space plasma.
- *Electrode vs. grid*: An electrode is a conductor at a controlled voltage, used to produce an electric field. In the context of an electrospray thruster, a grid is an electrode with an array of apertures in it.
- *Ionic Liquid*: a liquid used for electrospraying, in either droplet mode or ion mode. They are beneficial due to their high conductivity and negligible vapor pressure.

- *Colloid*: A colloid is a liquid with a suspension of solid particles in it. It is probably a holdover from when propellants were made from solvents (e.g. glycerol) and solutes (e.g. sodium iodide). Sometimes the term 'colloid thruster' is used to describe droplet mode electrospray thrusters (i.e. Colloid Micro Newton Thruster and Colloid Microthruster Technology).

- *Ion mode*: operation where the plume is predominantly composed of monomers and dimers of the ionic liquid.

- *Droplet mode*: operation where the plume is predominantly composed of ionic liquid droplets.

- *Mixed mode*: operation where the plume consists of both ions and droplets. This is typically such that the polydispersive efficiency is greatly reduced.

- *Capillary Emitter*: An internally-wetted tube is used as the emitter, with the emission site being formed at the tip.

- *Porous Emitter*: Emission sites are formed on a porous structure with flow through the porous medium. The emitter can be formed into a variety of shapes, such as pyramids, wedges, cones, or flat surfaces.

- *Externally-Wetted Emitter*: A needle is used as an emitter, with flow reaching the tip via wicking up the outside of the needle. The needle may be roughened to increase the wicking ability to the emission surface.

- *Polydispersive efficiency*: The reduction in effective thrust produced due to the charge-to-mass ratio disparity between high q/m ions and low q/m droplets.

- *Emission modes*: A quantitative and qualitative description of the electrospray behavior spatially and temporally

- *Pulsating emission mode*: at low voltages, intermittent (less than 50% duty cycle) formation of a jet at the tip of an ellipsoidal meniscus. At higher voltages, intermittent jet formation at roughly 50% duty cycle from a pulsating ellipsoidal meniscus.

- *Pulsating transition emission mode*: a jet is constantly present, but emission properties, such as jet width, change with time. This differs from the pulsating emission mode, where the duty cycle of emission approaches roughly 50% with increasing voltage, and the steady cone-jet mode where the jet and current are constant.

- *Cone-jet emission mode*: a single emission site with 100% duty cycle of emission and a distinct cone and jet structure.

- *Whipping emission mode*: a jet of steady diameter forms at the apex of the cone and oscillates in the radial direction. (Note: this should be differentiated from whipping jet breakup better)

- *Whipping + Multijet emission mode*: emission is reminiscent of whipping mode but with intermittent splitting of the jet into multiple jets.

- *Multijet emission mode*: multiple emission sites form along the edge of an emission site. Each of these sites is representative of individual cone-jet emission sites.

- *Active Feed*: flow to the emission site is driven by an upstream static pressure condition. The flow to the emission site is defined by a flow rate boundary condition.

- *Passive Feed*: flow to the emission site is not driven by an upstream pressure. The flow is caused by a pressure difference between the restorative capillary pressure (or lack thereof) at the reservoir and the electric (Maxwell) pressure at the emission site. Therefore, the flow to the emission site is defined by a pressure boundary condition.

- *Ion fragmentation*: Dissociation of emitted clusters of propellant. Typically this fragmentation results in a neutral cluster and a cluster of the original charge but smaller mass.

- *Monomer, dimer, trimer, ... N-mer*: An ion cluster that contains N ions of the indicated polarity and $N-1$ of the opposite polarity. For example, a positive trimer emitted from EMI-Im will be $(EMI^+)_3$-$(Im^-)_2$, or $EMI^+(EMI\text{-}Im)_2$.

Supposing that the emission site spacing may not be small compared to the radius of the wedge base, a more general solution for the pressure in the wedge is sought. For this case, we consider a secondary flow which satisfies the following boundary conditions in r:

$$P_s(R_1,z)=0, \quad P_s(R_2,z)=\hat{P}e^{i\alpha z}. \tag{.1}$$

where $\hat{P}$ is a constant to represent the magnitude of pressure variation at the emission surface, $r=R_2$. The solution to Laplace's equation in this case is similar to Eq. 2.5:

$$P_s(r,z)=\hat{P}\left[\hat{C}_2K_0(\alpha r)+\hat{C}_3I_0(\alpha r)\right]e^{i\alpha z} \tag{.2}$$

where $\hat{C}_2$ and $\hat{C}_3$ are constant coefficients. Solving for the given boundary conditions yields:

$$\hat{C}_2=-\frac{\frac{I_0(\alpha R_1)}{K_0(\alpha R_1)}}{I_0(\alpha R_2)-\frac{I_0(\alpha R_1)}{K_0(\alpha R_1)}K_0(\alpha R_2)}, \tag{.3}$$

$$\hat{C}_3=\frac{1}{I_0(\alpha R_2)-\frac{I_0(\alpha R_1)}{K_0(\alpha R_1)}K_0(\alpha R_2)} \tag{.4}$$

The pressure within the wedge is given by the superposition of the primary and secondary flows:

$$P(r,z)=\frac{P_0\ln\left(\frac{r}{R_2}\right)}{\ln\left(\frac{R_1}{R_2}\right)}+\hat{P}\left[\hat{C}_2K_0(\alpha r)+\hat{C}_3I_0(\alpha r)\right]e^{i\alpha z}, \tag{.5}$$

where P_0 is the pressure at R_1 relative to the mean pressure at R_2. The flow field is then solved through Darcy's law, where $\vec{u}=-\frac{k}{\mu}\nabla P$:

$$u_r=-\frac{kP_0}{\mu r\ln\left(\frac{R_1}{R_2}\right)}-\frac{2\pi k\hat{P}}{\mu\lambda}\left[-\hat{C}_2K_1(\alpha r)+\hat{C}_3I_1(\alpha r)\right]e^{i\alpha z}, \tag{.6}$$

$$u_z=i\frac{2\pi k\hat{P}}{\mu\lambda}\left[\hat{C}_2K_0(\alpha r)+\hat{C}_3I_0(\alpha r)\right]e^{i\alpha z}. \tag{.7}$$

Integrating u_r over the base of the base of the wedge at R_1 yields the total flow rate, Q:

$$Q=\frac{kP_0\theta_wL}{\mu\ln\left(\frac{R_1}{R_2}\right)}+\frac{ik\hat{P}}{\mu}\left[-\hat{C}_2K_1(\alpha R_1)+\hat{C}_3I_1(\alpha R_2)\right]\left(1-e^{i\alpha L}\right). \tag{.8}$$

To solve for $\hat{P}$, the radial flow is solved at stagnation points on the emission surface, R_2. Stagnation points exist at the maxima of the secondary flow pressure on the emission surface, $(r,z) = (R_2, n\lambda)$ where n is an integer. Solving Eq. .6 for these conditions yields:

$$-\frac{P_0}{R_2 \ln\left(\frac{R_1}{R_2}\right)} - \frac{2\pi\hat{P}}{\lambda}\left[-\hat{C}_2 K_1(\alpha R_2) + \hat{C}_3 I_1(\alpha R_2)\right] = 0, \tag{.9}$$

Rearranging terms yields an equation for $\hat{P}$:

$$\hat{P} = -\frac{\lambda P_0}{2\pi R_2 \ln\left(\frac{R_1}{R_2}\right)}\left[-\hat{C}_2 K_1(\alpha R_2) + \hat{C}_3 I_1(\alpha R_2)\right]^{-1}. \tag{.10}$$

P_0 is then solved for by applying the Maxwell pressure and the reservoir Laplace pressure conditions to the flow.

Inspection of emitter after testing reveals that propellant wets nonemitting surfaces in channels between sintered particles rather than just in pores, as informed by porous indium emitters [144]. Propellant wetting the emitter is shown in Figure .1; analyzing the pixel brightness histograms from this image (shown in Figure .2) shows that roughly 39 % of the surface is wetted by propellant. Compared to the 23 % porosity of the medium, this surface wetting ratio is higher than expected. From 10 manually-measured channel widths, the mean channel width is 1.73 µm with a standard deviation of 0.52 µm, which roughly matches with the pore diameter of the emitter porous medium.

The difference between the expected and observed surface wetting behaviors prompts reinvestigating the effect of surface propellant storage on transient flow in the porous medium. Equation 3.7 described the propellant storage in a circular pore; it is necessary to investigate the propellant storage in a channel. The channel is assumed to be straight, long, and with a defined width D_{chan}. A diagram of the cross-section of the channel is shown in Figure .3. A circular section of height h and width D_{chan} describes the receding of propellant into the porous medium. The area of this segment, A, is approximated as [145]:

$$A \approx \frac{2}{3} D_{chan} h + \frac{h^3}{2 D_{chan}}. \tag{.11}$$

Evaluating this expression to replicate the experimental conditions (i.e. $R_{men} \gg D_{chan}$), shows that the first term in Equation .11 is sufficient to predict meniscus behavior. If the radius of the of the meniscus, R_{men}, is known, the half angle of the meniscus within a pore, θ_{chan}, is:

$$\theta_{chan} = \arcsin\left(\frac{D_{chan}}{2 R_{men}}\right). \tag{.12}$$

The depth that the meniscus recedes into the porous medium is the height of the circular segment h, which is determined through geometry:

$$h = R_{men}(1 - \cos\theta_{chan}). \tag{.13}$$

Through Taylor expansions at $h = \theta_{chan} = 0$, h is simplified as:

$$h \approx R_{men}\frac{\theta^2}{2} \approx \frac{D_{chan}^2}{4R_{men}}. \tag{.14}$$

Equation .11 can then be evaluated as:

$$A = \frac{D_{chan}^3}{12R_{men}}. \tag{.15}$$

The cross-sectional area A is equivalent to the volume associated with the channel of propellant receeding into the porous medium, evaluated on a per unit length basis, ΔV_{chan}. The change in volume as a function of pressure is shown in Figure .4. Two parameters are introduced for nondimensionalization: a characteristic pressure and volume. The characteristic volume, V_C, is reached when the meniscus has a radius of half the channel diameter; the characteristic pressure, P_C, is the pressure difference across such a meniscus:

$$V_C = \frac{\pi D_{chan}^2}{8}, \quad P_C = \frac{2\gamma}{D_{chan}}. \tag{.16}$$

Nondimensionalization is possible with a characteristic pressure and volume:

$$\hat{V} = \frac{A}{V_C}, \quad \hat{P} = \frac{P}{P_C}. \tag{.17}$$

Through the Young-Laplace Equation, the pressure difference across the meniscus is evaluated:

$$\Delta P = \frac{\gamma}{R_{men}}. \tag{.18}$$

The linear channel density on the surface of the emitter, α_{chan}, is evaluated through the surface wetting characteristics and channel width:

$$\alpha_{chan} = \frac{\varepsilon_{surf}}{D_{chan}}, \tag{.19}$$

where ε_{surf} is the surface wetting ratio. The change in liquid capacity in a differential element, $\Delta V / \mathrm{d}V$, is evaluated as:

$$\frac{\Delta V}{\mathrm{d}V} = \Delta V_{chan} \alpha_{chan} \frac{\mathrm{d}A}{\mathrm{d}V} = \left(\frac{D_{chan}^3}{12 R_{men}} \right) \left(\frac{\varepsilon_{surf}}{D_{chan}} \right) \frac{\mathrm{d}A}{\mathrm{d}V}. \tag{.20}$$

where $\frac{\mathrm{d}A}{\mathrm{d}V}$ describes the characteristics of differential elements of the flow domain. Equation .20 can be substituted into Equation 3.9 in lieu of Equation 3.10 to develop an equation for diffusion of pressure. The diffusion coefficient can then be evaluated as:

$$D = \frac{12 \gamma k}{\mu \alpha_{chan} D_{chan}^2} \frac{\mathrm{d}V}{\mathrm{d}A}. \tag{.21}$$

Because the channel width is approximately twice the pore radius and increased surface wetting fraction above the porosity, Equation .21 produces a diffusion coefficient that is roughly $1/8$ of that which was estimated through the wetting of circular pores. As a result, the flow settling times may be 8 times longer than previously expected, while accounting for the same fluid phenomena.

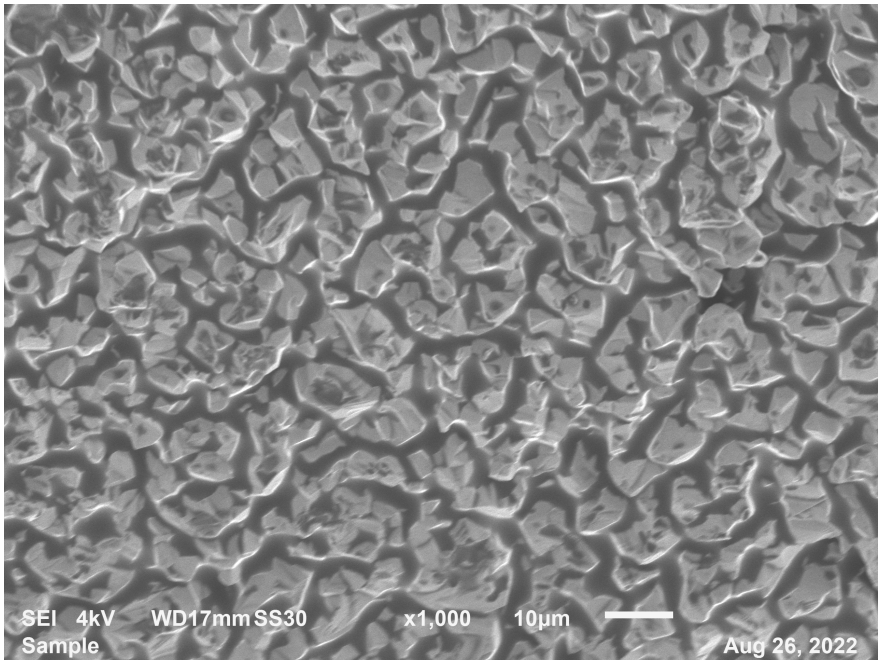

(a) Original

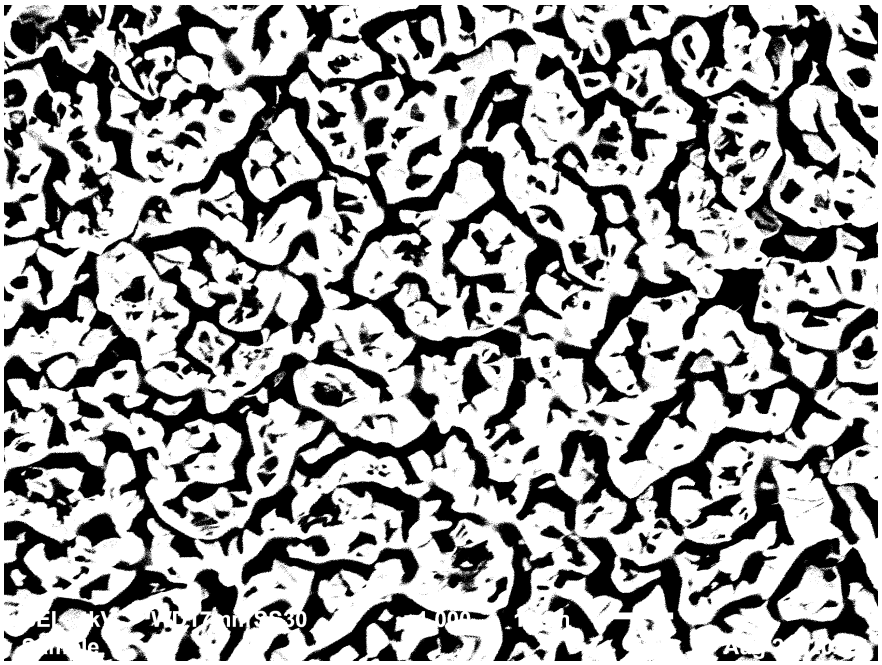

(b) Black and white image

Figure .1: Images of a nonemitting surface. The bottom image has been adjusted to distinguish wet surfaces from dry surfaces.

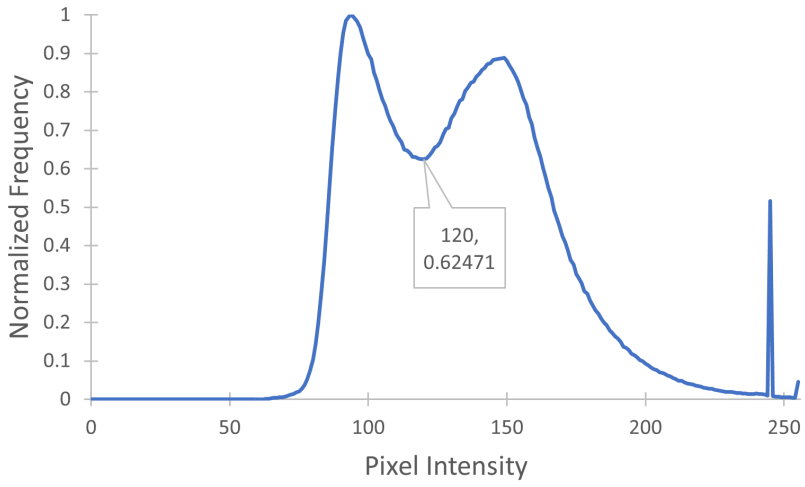

(a) Normalized PDF

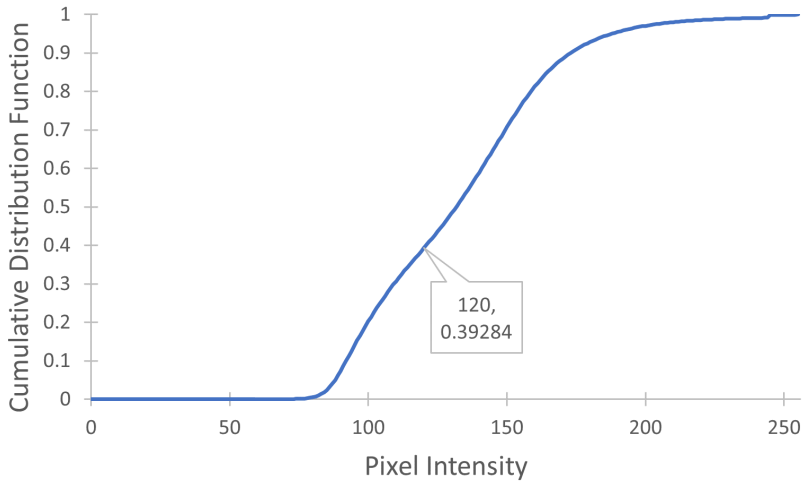

(b) Normalized CDF

Figure .2: Normalized probability and cumulative distribution functions (PDF and CDF) for pixel brightness over the image shown in Figure .1a. The local minimum indicated is used to distinguish wet from dry locations.

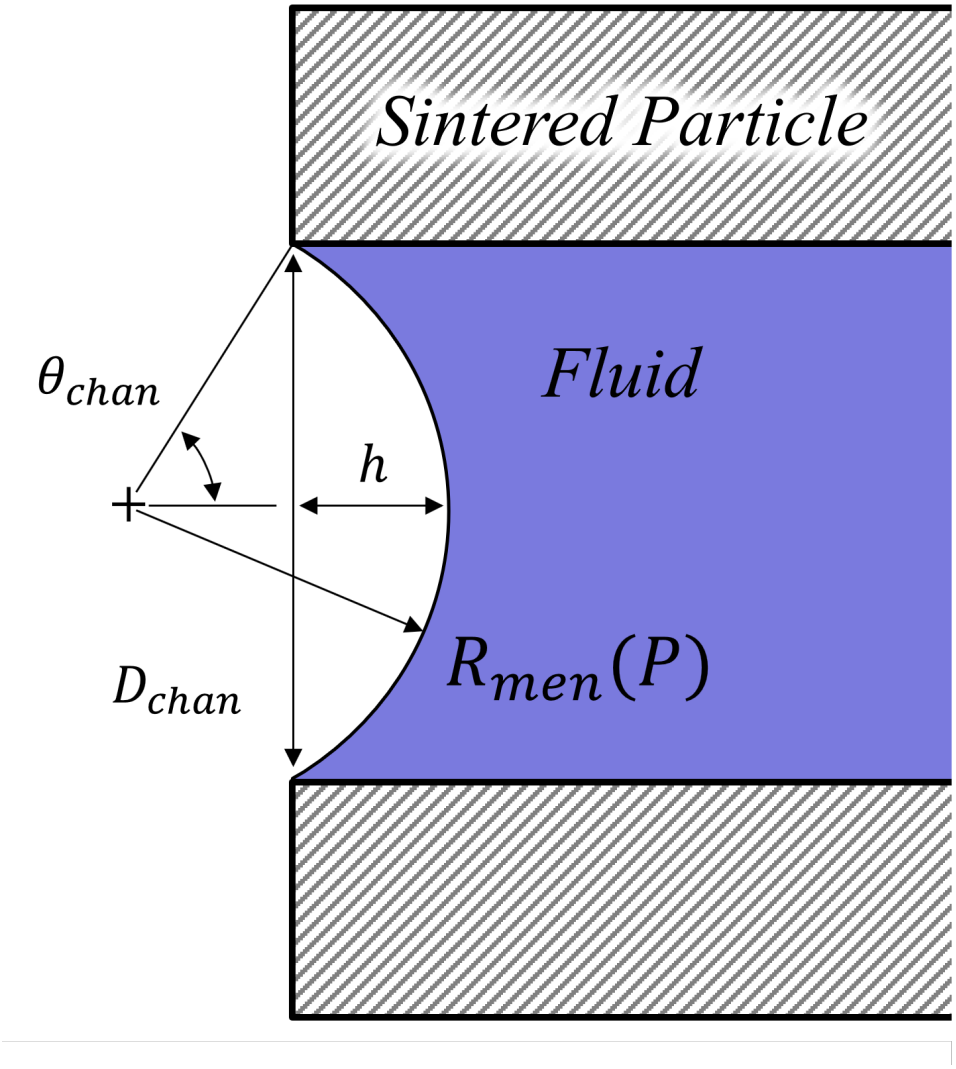

Figure .3: Diagram showing the geometry used to analyze the effect of fluid accumulation in channels on the porous surface.

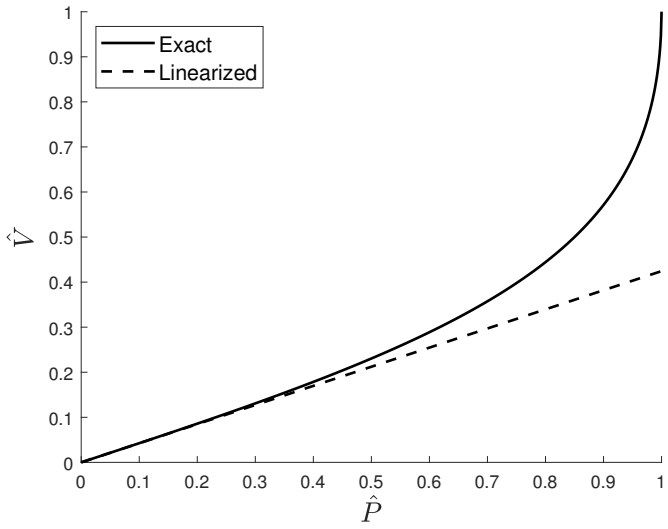

Figure .4: Exact and linearized forms of the volume of fluid stored in a channel. The linearized form matches the exact form as long as the pressure in the medium is much less than the characteristic pressure.

ELECTROSPRAY MURAL FOR UCLA MAE

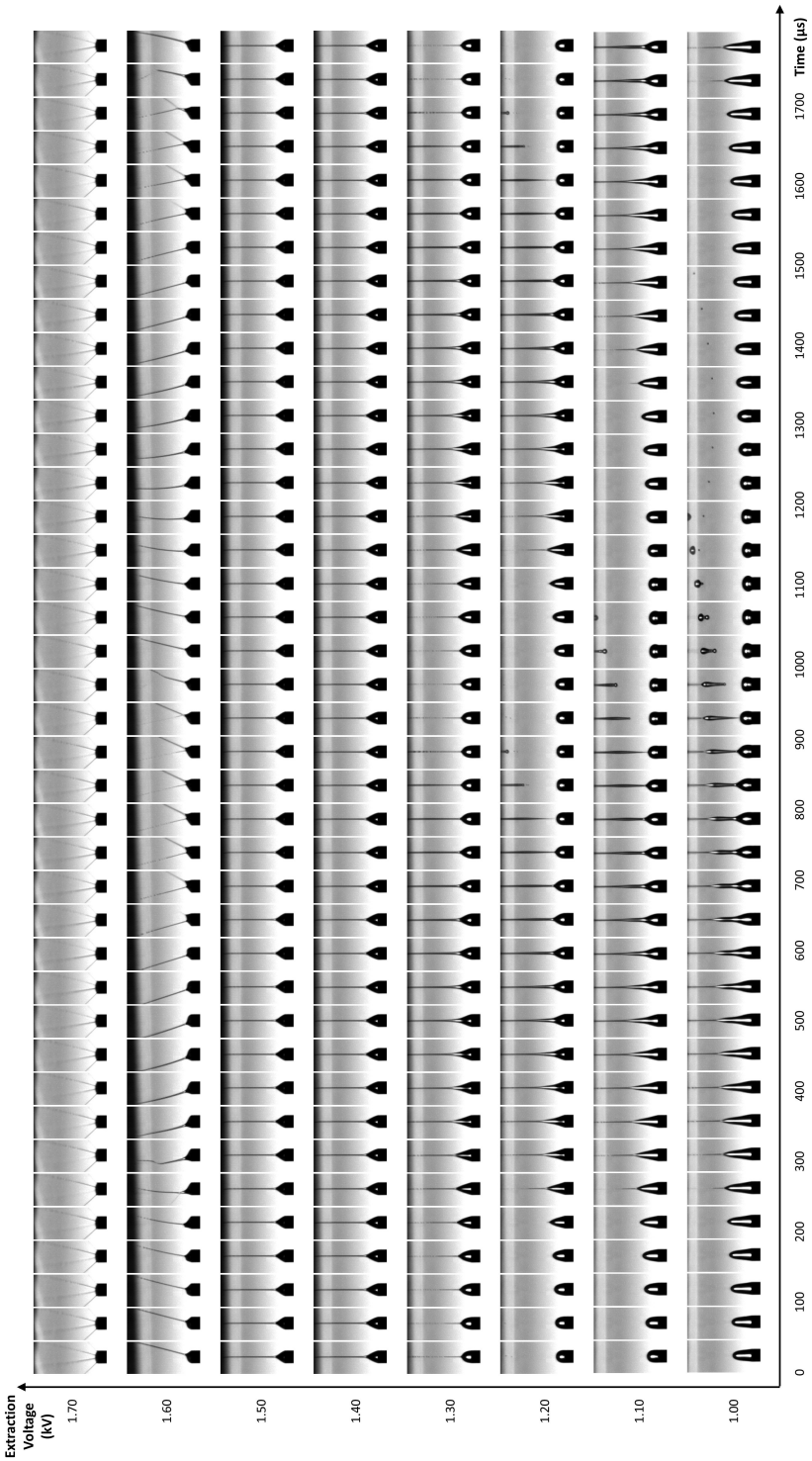

BIBLIOGRAPHY

[1] Wright, P. L. and Wirz, R. E., "Multiplexed electrospray emission on a porous wedge," *Physics of Fluids*, Vol. 33, No. 1, 2021, pp. 012003.

[2] Courtney, D. G. and Shea, H., "Influences of Porous Reservoir Laplace Pressure on Emissions from Passively Fed Ionic Liquid Electrospray Sources," *Applied Physics Letters*, Vol. 107, No. 10, 2015, pp. 103504.

[3] Ober, S., Branam, R., Huffman, R., Demmons, N., and Martin, R., "Electrospray thruster for CubeSat," *49th AIAA Aerospace Sciences Meeting including the New Horizons Forum and Aerospace Exposition*, 2010, p. 522.

[4] Courtney, D. G., Alvarez, N., and Demmons, N. R., "Electrospray Thrusters for Small Spacecraft Control: Pulsed and Steady State Operation," *Joint Propulsion Conference*, AIAA, 2018, p. 4654.

[5] Rudolph, A., "LISA Pathfinder Launch and Early Operations Phase-In-Orbit Experience," *14th International Conference on Space Operations*, 2016, p. 2412.

[6] Baker, A. M., da Silva Curiel, A., Schaffner, J., and Sweeting, M., ""You can get there from here": Advanced low cost propulsion concepts for small satellites beyond LEO," *Acta Astronautica*, Vol. 57, No. 2-8, 2005, pp. 288–301.

[7] Drinkwater, M., Floberghagen, R., Haagmans, R., Muzi, D., and Popescu, A., "VII: Closing session: GOCE: ESA's first earth explorer core mission," *Space science reviews*, Vol. 108, No. 1, 2003, pp. 419–432.

[8] Burkhardt, H., Sippel, M., Krülle, G., Janovsky, R., Kassebom, M., Lübberstedt, H., Romberg, O., and Fritsche, B., "Evaluation of propulsion systems for satellite end-of-life de-orbiting," *38th AIAA/ASME/SAE/ASEE Joint Propulsion Conference & Exhibit*, 2002, p. 4208.

[9] Russell, C. and Raymond, C., "The dawn mission to Vesta and Ceres," *The Dawn Mission to Minor Planets 4 Vesta and 1 Ceres*, 2011, pp. 3–23.

[10] Tsiolkovsky, K. E., "Exploration of the universe with reaction machines," *The Science Review*, Vol. 5, 1903.

[11] Goebel, D. M. and Katz, I., *Fundamentals of electric propulsion: ion and Hall thrusters*, Vol. 1, John Wiley & Sons, 2008.

[12] Jones, H., "The recent large reduction in space launch cost," 48th International Conference on Environmental Systems, 2018.

[13] Smith, A., "Economic Prerequisites for Space Solar Power," *Solar Power from Space-SPS'04*, Vol. 567, 2004, p. 75.

[14] "Electric Power Monthly - U.S. Energy Information Administration (EIA)," .

[15] Gilbert, W. and Thompson, S. P., *On the Magnet, Magnetick Bodies Also, and on the Great Magnet the Earth: A New Physiology, Demonstrated by Many Arguments & Experiments*, Imprinted at the Chiswick Press, 1900.

[16] Rayleigh, L., "XX. On the equilibrium of liquid conducting masses charged with electricity," *The London, Edinburgh, and Dublin Philosophical Magazine and Journal of Science*, Vol. 14, No. 87, 1882, pp. 184–186.

[17] Zeleny, J., "The electrical discharge from liquid points, and a hydrostatic method of measuring the electric intensity at their surfaces," *Physical Review*, Vol. 3, No. 2, 1914, pp. 69.

[18] Taylor, G. I., "Disintegration of water drops in an electric field," *Proceedings of the Royal Society of London. Series A. Mathematical and Physical Sciences*, Vol. 280, No. 1382, 1964, pp. 383–397.

[19] Jackson, J. D., "Electrodynamics," *The Optics Encyclopedia: Basic Foundations and Practical Applications*, 2007.

[20] Wright, P., Thuppul, A., and Wirz, R. E., "Life-Limiting Emission Modes for Electrospray Thrusters," *2018 Joint Propulsion Conference*, 2018, p. 4726.

[21] Wright, P. L., Huh, H., Uchizono, N. M., Thuppul, A., and Wirz, R. E., "A novel variable mode emitter for electrospray thrusters," *The 36th International Electric Propulsion Conference, IEPC-2019*, Vol. 650, 2019.

[22] Kidd, P. W., "Parametric studies with a single-needle colloid thruster." *Journal of Spacecraft and Rockets*, Vol. 5, No. 9, 1968, pp. 1034–1039.

[23] Burton, W. and Stark, K., "Annular slit colloid thruster research and development," 1970.

[24] Zafran, S., Beynon, J. C., Kidd, P. W., Shelton, H., and Jackson, F. A., "One-mlb colloid thruster system development," *Journal of Spacecraft and Rockets*, Vol. 10, No. 8, 1973, pp. 531–533.

[25] Bailey, A. G., "Investigation of a single spraying site of a colloid thruster," *Journal of Physics D: Applied Physics*, Vol. 6, No. 2, 1973, pp. 276.

[26] Kidd, P. and Shelton, H., "Life test/4350 hours/of an advanced colloid thruster module," *10th Electric Propulsion Conference*, 1973, p. 1078.

[27] Lorenz, R., "Electric Propulsion for Small Spacecraft," 1989.

[28] Welton, T., "Ionic liquids: a brief history," *Biophysical reviews*, Vol. 10, No. 3, 2018, pp. 691–706.

[29] Wilkes, J. S. and Zaworotko, M. J., "Air and water stable 1-ethyl-3-methylimidazolium based ionic liquids," *Journal of the Chemical Society, Chemical Communications*, , No. 13, 1992, pp. 965–967.

[30] Gamero-Castano, M. and Hruby, V., "Electrospray as a source of nanoparticles for efficient colloid thrusters," *Journal of Propulsion and Power*, Vol. 17, No. 5, 2001, pp. 977–987.

[31] Lozano, P. and Martínez-Sánchez, M., "Ionic liquid ion sources: suppression of electrochemical reactions using voltage alternation," *Journal of colloid and interface science*, Vol. 280, No. 1, 2004, pp. 149–154.

[32] Lozano, P. and Martinez-Sanchez, M., "Ionic liquid ion sources: characterization of externally wetted emitters," *Journal of colloid and interface science*, Vol. 282, No. 2, 2005, pp. 415–421.

[33] Courtney, D., Demmons, N., and Wright, P., "Colloid thruster and method," May 2 2017, US Patent 9,638,178.

[34] Antypas, R. J. and Wang, J. J., "Pure ionic electrospray extractor design optimization," *International Electric Propulsion Conference*, 2019, p. 372.

[35] Ma, C. and Ryan, C., "Plume characterization of a porous electrospray thruster," *36th International Electric Propulsion Conference*, ERPS, 2019, p. A223.

[36] Natisin, M., Zamora, H., McGehee, W., Arnold, N., Holley, Z., Holmes, M., and Eckhardt, D., "Fabrication and characterization of a fully conventionally machined, high-performance porous-media electrospray thruster," *Journal of Micromechanics and Microengineering*, Vol. 30, No. 11, 2020, pp. 115021.

[37] Wright, P. and Wirz, R. E., "Transient Flow in Porous Electrosprays," *Manuscript Submitted to Transport in Porous Media*, 2022.

[38] Wright, P. and Wirz, R. E., "Transient Flow in Porous Electrospray Emitters," *AIAA Propulsion and Energy 2021 Forum*, 2021, p. 3437.

[39] Wright, P. L., Uchizono, N. M., Collins, A. L., and Wirz, R. E., "Characterization of a Porous Tungsten Electrospray Emitter," *37th International Electric Propulsion Conference*, ERPS, 2022, p. 232.

[40] Byon, C., Ku, S., Lee, W., Jung, J. H., and Kim, W., "Electrospray characterization based on an emitter of cone-shaped porous medium for the high-throughput microliter aerosol generation," *Applied Physics Letters*, Vol. 111, No. 12, 2017, pp. 123504.

[41] Koerner, T., Turck, K., Brown, L., and Oleschuk, R. D., "Porous polymer monolith assisted electrospray," *Analytical chemistry*, Vol. 76, No. 21, 2004, pp. 6456–6460.

[42] Legge, R., Lozano, P., and Martinez-Sanchez, M., "Fabrication and characterization of porous metal emitters for electrospray thrusters," *International Electric Propulsion Conference*, Electric Rocket Propulsion Soc. Fairview Park, OH, 2007, pp. 2007–145.

[43] Natisin, M. R. and Zamora, H. L., "Performance of a Fully Conventionally Machined Liquid-Ion Electrospray Thruster Operated in PIR," *International Electric Propulsion Conference*, ERPS, 2019, p. 522.

[44] Courtney, D. G., Li, H. Q., and Lozano, P., "Emission measurements from planar arrays of porous ionic liquid ion sources," *Journal of Physics D: Applied Physics*, Vol. 45, No. 48, 2012, pp. 485203.

[45] Guo, Y., Li, S., Wu, Z., Hen, Y., and Sun, Z., "Study on Performance of Ionic Liquid Electrospray Thruster in Atmospheric and Vacuum Environment," *International Electric Propulsion Conference*, ERPS, 2019, p. 559.

[46] Ma, C., Bull, T., and Ryan, C., "Feasibility Study of a Micro-Electrospray Thruster Based on a Porous Glass Emitter Substrate," 2017.

[47] Liu, X., He, W., Kang, X., and Xu, M., "Fabrication of porous emitters for ionic liquid ion source by wire electrical discharge machining combined with electrochemical etching," *Review of Scientific Instruments*, Vol. 90, No. 12, 2019, pp. 123304.

[48] Demmons, N. R., Wood, Z., and Alvarez, N., "Characterization of a High Thrust, Pressure-Fed Electrospray Thruster for Precision Attitude Control Applications," *AIAA Propulsion and Energy 2019 Forum*, 2019, p. 3817.

[49] Spence, D., Ehrbar, E., Rosenblad, N., Demmons, N., Roy, T., Hoffman, S., Williams, W. D., Tsay, M., Zwahlen, J., Hohman, K., et al., "Electrospray Propulsion Systems for Small Satellites and Satlets," *AIAA SPACE 2013 Conference and Exposition*, 2013, p. 5329.

[50] Courtney, D. G., Dandavino, S., and Shea, H., "Comparing direct and indirect thrust measurements from passively fed ionic electrospray thrusters," *Journal of Propulsion and Power*, Vol. 32, No. 2, 2015, pp. 392–407.

[51] Little, B. and Jugroot, M., "Bimodal Propulsion System for Small Spacecraft: Design, Fabrication, and Performance Characterization," *Journal of Spacecraft and Rockets*, 2020, pp. 1–13.

[52] Chen, C., Chen, M., and Zhou, H., "Characterization of an ionic liquid electrospray thruster with a porous ceramic emitter," *Plasma Science and Technology*, 2020.

[53] Guerra-Garcia, C., Krejci, D., and Lozano, P., "Spatial uniformity of the current emitted by an array of passively fed electrospray porous emitters," *Journal of Physics D: Applied Physics*, Vol. 49, No. 11, 2016, pp. 115503.

[54] Courtney, D. G., Wood, Z., and Fedkiw, T., "Reconstructing Electrospray Plume Current Spatial Distributions using Computed Tomography," *International Electric Propulsion Conference*, ERPS, 2019, p. 787.

[55] Chen, C., Chen, M., Fan, W., and Zhou, H., "Effects of non-uniform operation of emission sites on characteristics of a porous electrospray thruster," *Acta Astronautica*, Vol. 178, 2021, pp. 192 – 202.

[56] Thuppul, A., Wright, P. L., Collins, A. L., Ziemer, J. K., and Wirz, R. E., "Lifetime Considerations and Estimation for Electrospray Thrusters," *Aerospace*, Vol. 7, No. 8, 2020, pp. 108.

[57] Bear, J., *Dynamics of fluids in porous media*, Courier Corporation, 2013.

[58] Hassanizadeh, S. M. and Gray, W. G., "Thermodynamic basis of capillary pressure in porous media," *Water resources research*, Vol. 29, No. 10, 1993, pp. 3389–3405.

[59] Smith, D. P., "The Electrohydrodynamic Atomization of Liquids," *IEEE Transactions on Industry Applications*, , No. 3, 1986, pp. 527–535.

[60] Chen, C.-H., Saville, D., and Aksay, I. A., "Scaling laws for pulsed electrohydrodynamic drop formation," *Applied Physics Letters*, Vol. 89, No. 12, 2006, pp. 124103.

[61] Jackson, J. D., *Classical electrodynamics*, John Wiley & Sons, 2007.

[62] Coffman, C., Martínez-Sánchez, M., Higuera, F., and Lozano, P. C., "Structure of the menisci of leaky dielectric liquids during electrically-assisted evaporation of ions," *Applied Physics Letters*, Vol. 109, No. 23, 2016, pp. 231602.

[63] Fernández de La Mora, J., "The fluid dynamics of Taylor cones," *Annu. Rev. Fluid Mech.*, Vol. 39, 2007, pp. 217–243.

[64] Coffman, C. S., Martínez-Sánchez, M., and Lozano, P. C., "Electrohydrodynamics of an ionic liquid meniscus during evaporation of ions in a regime of high electric field," *Physical Review E*, Vol. 99, No. 6, 2019, pp. 063108.

[65] De La Mora, J. F., "On the outcome of the coulombic fission of a charged isolated drop," *Journal of colloid and interface science*, Vol. 178, No. 1, 1996, pp. 209–218.

[66] Peters, J., "Rayleigh's electrified water drops," *European Journal of Physics*, Vol. 1, No. 3, 1980, pp. 143.

[67] Gomez, A. and Tang, K., "Charge and fission of droplets in electrostatic sprays," *Physics of Fluids*, Vol. 6, No. 1, 1994, pp. 404–414.

[68] Davis, E. and Bridges, M., "The Rayleigh limit of charge revisited: light scattering from exploding droplets," *Journal of aerosol science*, Vol. 25, No. 6, 1994, pp. 1179–1199.

[69] Marginean, I., Nemes, P., Parvin, L., and Vertes, A., "How much charge is there on a pulsating Taylor cone?" *Applied Physics Letters*, Vol. 89, No. 6, 2006, pp. 064104.

[70] Tang, K. and Smith, R. D., "Theoretical prediction of charged droplet evaporation and fission in electrospray ionization," *International journal of mass spectrometry*, Vol. 185, 1999, pp. 97–105.

[71] "Flowrate / Pressure Calculation VitraPOR® - Filterdiscs," http://www.adamschittenden.com/Robu%20flowrate%20graphs.pdf, Accessed: 2019-09-01.

[72] Zhou, Z.-B., Matsumoto, H., and Tatsumi, K., "Structure and properties of new ionic liquids based on alkyl-and alkenyltrifluoroborates," *ChemPhysChem*, Vol. 6, No. 7, 2005, pp. 1324–1332.

[73] Wang, H., Liu, J., Cooks, R. G., and Ouyang, Z., "Paper spray for direct analysis of complex mixtures using mass spectrometry," *Angewandte Chemie International Edition*, Vol. 49, No. 5, 2010, pp. 877–880.

[74] Tepper, G. and Kessick, R., "Nanoelectrospray aerosols from microporous polymer wick sources," *Applied Physics Letters*, Vol. 94, No. 8, 2009, pp. 084106.

[75] Thuppul, A., Collins, A. L., Wright, P. L., Uchizono, N. M., and Wirz, R. E., "Spatially-Resolved Mass Flux and Current Measurements of Electrospray Plumes," *Proceedings of the 36th International Electric Propulsion Conference, Vienna, Austria*, 2019, pp. 15–20.

[76] Karadag, B., Cho, S., and Funaki, I., "Note: Precision balance for sub-miliNewton resolution direct thrust measurement," *Review of Scientific Instruments*, Vol. 89, No. 8, 2018, pp. 086108.

[77] Krejci, D., Hugonnaud, V., Schönherr, T., Little, B., Reissner, A., Seifert, B., Koch, Q., Bosch-Borràs, E., and González del Amo, J., "Full performance mapping of the IFM Nano Thruster, including direct thrust measurements," *JoSS*, Vol. 8, 2019, pp. 881–93.

[78] Krpoun, R. and Shea, H. R., "A method to determine the onset voltage of single and arrays of electrospray emitters," *Journal of Applied Physics*, Vol. 104, No. 6, 2008, pp. 064511.

[79] Martinez-Sanchez, M. and Lozano, P., "16.522 space propulsion," *MIT OpenCourseWare*, 2015.

[80] Lozano, P. and Martínez-Sánchez, M., "On the dynamic response of externally wetted ionic liquid ion sources," *Journal of Physics D: Applied Physics*, Vol. 38, No. 14, 2005, pp. 2371.

[81] Ma, C., Bull, T., and Ryan, C. N., "Plume Composition Measurements of a High-Emission-Density Electrospray Thruster," *Journal of Propulsion and Power*, Vol. 37, No. 6, 2021, pp. 816–831.

[82] Vasiljevich, I., Tajmar, M., Grienauer, W., Plesescu, F., Buldrini, N., Gonzalez del Amo, J., Carnicero Domunguez, B., and Betto, M., "Development of an indium mN-FEEP thruster," *44th AIAA/ASME/SAE/ASEE Joint Propulsion Conference & Exhibit*, 2008, p. 4534.

[83] Rojas-Herrera, J., Jivanescu, I., Freeman, D., Krejci, D., Fucetola, C., and Lozano, P., "Porous materials for ion-electrospray spacecraft microengines," *Journal of Nanomechanics and Micromechanics*, Vol. 7, No. 3, 2017, pp. 04017006.

[84] Panton, R. L., *Incompressible flow*, John Wiley & Sons, 2013.

[85] Petro, E., Bruno, A., Lozano, P., Perna, L. E., and Freeman, D., "Characterization of the TILE electrospray emitters," *AIAA Propulsion and Energy 2020 Forum*, 2020, p. 3612.

[86] Huang, C., Li, J., and Li, M., "Performance measurement and evaluation of an ionic liquid electrospray thruster," *Chinese Journal of Aeronautics*, 2021.

[87] Haberman, R., *Elementary applied partial differential equations*, Vol. 987, Prentice Hall Englewood Cliffs, NJ, 1983.

[88] Bretti, M., "AIS-ILIS1 Ionic Liquid Ion Source Electrospray Thruster," *Applied Ion Systems LLC*, 2020.

[89] Liu, X., Kang, X., Deng, H., and Sun, Y., "Energy properties and spatial plume profile of ionic liquid ion sources based on an array of porous metal strips," *Plasma Science and Technology*, 2021.

[90] Weisstein, E. W., "Confluent Hypergeometric Function of the Second Kind," 2003.

[91] Weisstein, E. W., "Laguerre Polynomial," 2003.

[92] Juraschek, R. and Röllgen, F., "Pulsation phenomena during electrospray ionization," *International journal of mass spectrometry*, Vol. 177, No. 1, 1998, pp. 1–15.

[93] Choi, H. K., Park, J.-U., Park, O. O., Ferreira, P. M., Georgiadis, J. G., and Rogers, J. A., "Scaling laws for jet pulsations associated with high-resolution electrohydrodynamic printing," *Applied Physics Letters*, Vol. 92, No. 12, 2008, pp. 123109.

[94] Kajishima, T. and Taira, K., *Computational fluid dynamics: incompressible turbulent flows*, Springer, 2016.

[95] Thompson, S. and Prewett, P., "The dynamics of liquid metal ion sources," *Journal of Physics D: Applied Physics*, Vol. 17, No. 11, 1984, pp. 2305.

[96] Huang, C., Li, J., Li, M., Si, T., Xiong, C., and Fan, W., "Experimental investigation on current modes of ionic liquid electrospray from a coned porous emitter," *Acta Astronautica*, Vol. 183, 2021, pp. 286–299.

[97] Mair, G., "The effects of flow impedance on the current-voltage characteristics of liquid-metal ion sources," *Journal of Physics D: Applied Physics*, Vol. 30, No. 13, 1997, pp. 1945.

[98] Peter, B. S., Dressler, R. A., Chiu, Y.-h., and Fedkiw, T., "Electrospray propulsion engineering toolkit (ESPET)," *Aerospace*, Vol. 7, No. 7, 2020, pp. 91.

[99] Krejci, D., Mier-Hicks, F., Thomas, R., Haag, T., and Lozano, P., "Emission characteristics of passively fed electrospray microthrusters with propellant reservoirs," *Journal of Spacecraft and Rockets*, Vol. 54, No. 2, 2017, pp. 447–458.

[100] Courtney, D. G., Wood, Z., Gray, S., and Model, J., "High-speed transient characterization of the busek BET-300-P electrospray thruster," *36th International Electric Propulsion Conference*, ERPS, 2019, p. 788.

[101] "VitraPOR Sinterfilter, Flowrate / Pressure Calculation," https://adamschittenden.com/files/frit-flowrate-graphs.pdf, Accessed: 2021-06-01.

[102] "Standard Test Methods for Pore Size Characteristics of Membrane Filters by Bubble Point and Mean Flow Pore Test," Standard, ASTM, 2019.

[103] Brady, J., "A simple technique for making very fine, durable dissecting needles by sharpening tungsten wire electrolytically," *Bulletin of the World Health Organization*, Vol. 32, No. 1, 1965, pp. 143.

[104] Beigi, A. A. M., Abdouss, M., Yousefi, M., Pourmortazavi, S. M., and Vahid, A., "Investigation on physical and electrochemical properties of three imidazolium based ionic liquids (1-hexyl-3-methylimidazolium tetrafluoroborate, 1-ethyl-3-methylimidazolium bis (trifluoromethylsulfonyl) imide and 1-butyl-3-methylimidazolium methylsulfate)," *Journal of Molecular Liquids*, Vol. 177, 2013, pp. 361–368.

[105] Carvalho, P. J., Freire, M. G., Marrucho, I. M., Queimada, A. J., and Coutinho, J. A., "Surface tensions for the 1-alkyl-3-methylimidazolium bis (trifluoromethylsulfonyl) imide ionic liquids," 2008.

[106] Legge Jr, R. S. and Lozano, P. C., "Electrospray propulsion based on emitters microfabricated in porous metals," *Journal of Propulsion and Power*, Vol. 27, No. 2, 2011, pp. 485–495.

[107] Magnusson, J. M., Collins, A. L., and Wirz, R. E., "Polyatomic Ion-Induced Electron Emission (IIEE) in Electrospray Thrusters," *Aerospace*, Vol. 7, No. 11, 2020, pp. 153.

[108] Conroy, D. and Ziemer, J., "Water Contaminant Mitigation in Ionic Liquid Propellant," *International Electric Propulsion Conference*, ERPS, Sept 2009, p. 172, https://trs.jpl.nasa.gov/handle/2014/44687.

[109] Fedkiw, T., Wood, Z. D., and Demmons, N. R., "Improved Computed Tomography Current Mapping of Electrospray Thrusters," *AIAA Propulsion and Energy 2021 Forum*, 2021, p. 3389.

[110] Wirz, R. E., Thuppul, A., Wright, P. L., Uchizono, N. M., Huh, H., Davis, M. J., Ziemer, J. K., and Demmons, N. R., "Electrospray Thruster Performance and Lifetime Investigation for the LISA Mission," *AIAA Propulsion and Energy 2019 Forum*, 2019, p. 3816.

[111] Brikner, N. and Lozano, P. C., "The role of upstream distal electrodes in mitigating electrochemical degradation of ionic liquid ion sources," *Applied Physics Letters*, Vol. 101, No. 19, 2012, pp. 193504.

[112] Bober, D. B. and Chen, C.-H., "Pulsating electrohydrodynamic cone-jets: from choked jet to oscillating cone," *Journal of fluid mechanics*, Vol. 689, 2011, pp. 552–563.

[113] Zhang, K., Kuang, S., Suo, X., Huang, X., Li, Z., Wang, D., Jia, H., Tu, L., and Song, P., "Analysis of beam currents under an oscillating cone-jet mode for developing high-precision electrospray thrusters," *Journal of Applied Physics*, Vol. 131, No. 9, 2022, pp. 094501.

[114] Hanwu, J., Maolin, C., Xuhui, L., Chong, C., Haohao, Z., Hao, Z., and Zhicong, H., "Experimental study of a porous electrospray thruster with different number of emitter-strips," *Plasma Science and Technology*, Vol. 23, No. 10, 2021, pp. 104003.

[115] Liu, X., Kang, X., Guo, D., He, W., and Hang, G., "Electrospray emission using porous emitters with flat ends," *IEPC*, 2017, pp. 173.

[116] Chong, C., Maolin, C., and Haohao, Z., "Characterization of an ionic liquid electrospray thruster with a porous ceramic emitter," *Plasma Science and Technology*, Vol. 22, No. 9, 2020, pp. 094009.

[117] Máximo, D. V. M. and Velásquez-García, L. F., "Additively manufactured electrohydrodynamic ionic liquid pure-ion sources for nanosatellite propulsion," *Additive Manufacturing*, Vol. 36, 2020, pp. 101719.

[118] Uchizono, N., Collins, A., Marrese-Reading, C., Arestie, S., Ziemer, J., and Wirz, R., "The role of secondary species emission in vacuum facility effects for electrospray thrusters," *Journal of Applied Physics*, Vol. 130, No. 14, 2021, pp. 143301.

[119] Williams, J., Goebel, D., and Wilbur, P., "Analytical model of electron backstreaming for ion thrusters," *39th AIAA/ASME/SAE/ASEE Joint Propulsion Conference and Exhibit*, 2003, p. 4560.

[120] Thomas, E. W., "Ion bombardment induced photon and Auger emission for surface analysis," *Vacuum*, Vol. 34, No. 12, Dec 1984, pp. 1031–1044.

[121] Suchańska, M., "Ion-induced photon emission of metals," *Progress in Surface Science*, Vol. 54, No. 2, Feb 1997, pp. 165–209.

[122] Xu, Q. M., Zhang, C. H., Yang, Z. H., Guo, Y. P., Song, Y., and Chen, Y. H., "The research on optical radiation in the collisions of low energy, highly charged Xeq+ ions with MgOAl2O3 surfaces," *Nuclear Instruments and Methods in Physics Research Section B: Beam Interactions with Materials and Atoms*, Vol. 494-495, May 2021, pp. 16–22.

[123] Davis, M., Collins, A. L., and Wirz, R. E., "Electrospray plume evolution via discrete simulations," *36th International Electric Propulsion Conference*, ERPS, 2019, p. 590.

[124] Uchizono, N. M., Collins, A. L., Thuppul, A., Wright, P. L., Eckhardt, D. Q., Ziemer, J., and Wirz, R. E., "Emission modes in electrospray thrusters operating with high conductivity ionic liquids," *Aerospace*, Vol. 7, No. 10, 2020, pp. 141.

[125] Wei, J., Shui, W., Zhou, F., Lu, Y., Chen, K., Xu, G., and Yang, P., "Naturally and externally pulsed electrospray," *Mass Spectrometry Reviews*, Vol. 21, No. 3, 2002, pp. 148–162.

[126] Paine, M., Alexander, M., Smith, K., Wang, M., and Stark, J., "Controlled electrospray pulsation for deposition of femtoliter fluid droplets onto surfaces," *Journal of Aerosol Science*, Vol. 38, No. 3, 2007, pp. 315–324.

[127] Marginean, I., Kelly, R. T., Prior, D. C., LaMarche, B. L., Tang, K., and Smith, R. D., "Analytical characterization of the electrospray ion source in the nanoflow regime," *Analytical Chemistry*, Vol. 80, No. 17, 2008, pp. 6573–6579.

[128] Paine, M. D., "Transient electrospray behaviour following high voltage switching," *Microfluidics and Nanofluidics*, Vol. 6, No. 6, 2009, pp. 775–783.

[129] Rosell-Llompart, J., Grifoll, J., and Loscertales, I. G., "Electrosprays in the Cone-jet Mode: from Taylor Cone Formation to Spray Development," *Journal of Aerosol Science*, Vol. 125, 2018, pp. 2–31.

[130] De La Mora, J. F. and Loscertales, I. G., "The Current Emitted by Highly Conducting Taylor Cones," *Journal of Fluid Mechanics*, Vol. 260, 1994, pp. 155–184.

[131] Vianna, C., "Inside a ramen master's pursuit of perfecting ramen 2.0," Feb 2019.

[132] Mishan, L., "Nothing Sacred and An Assault on the Tongue and Interlopers," *The Best American Magazine Writing 2020*, Columbia University Press, 2020, pp. 339–358.

[133] Goldfield, H., "Niche's mazemen ramen cuts to the Chase," Mar 2019.

[134] Uchizono, N. M., Wright, P. L., Collins, A. L., and Wirz, R. E., "Facility Effects for Electrospray Thrusters," *AIAA SCITECH 2022 Forum*, 2022, p. 1361.

[135] Gamero-Castaño, M., "Characterization of the electrosprays of 1-ethyl-3-methylimidazolium bis (trifluoromethylsulfonyl) imide in vacuum," *Physics of Fluids*, Vol. 20, No. 3, 2008, pp. 032103.

[136] Ziemer, J. K., "Performance of electrospray thrusters," *International Electric Propulsion Conference*, ERPS, 2009, pp. 1–13.

[137] Thuppul, A., Collins, A., Wright, P., Uchizono, N., and Wirz, R., "Mass flux and current density distributions of electrospray plumes," *Journal of Applied Physics*, Vol. 130, No. 10, 2021, pp. 103301.

[138] Coffman, C. S., *Electrically-assisted evaporation of charged fluids: Fundamental modeling and studies on ionic liquids*, Ph.D. thesis, Massachusetts Institute of Technology, 2016.

[139] Ober, S. T., "CubeSat packaged electrospray thruster evaluation for enhanced operationally responsive space capabilities," 2011.

[140] Whittaker, C. B., Eckels, J., Gorodetsky, A. A., and Jorns, B. A., "A Moment-Based Model of Multi-Site Emission for Porous Electrosprays," *International Electric Propulsion Conference*, ERPS, 2022, p. 205.

[141] Parmar, S. M., Collins, A. L., and Wirz, R. E., "A Bayesian Data-driven Model for Quantifying Electrospray Lifetime," *International Electric Propulsion Conference*, ERPS, 2022, p. 230.

[142] Peterson, L. D., "Quantification of Margins and Uncertainties (QMU): Turning Models Uncertainties (QMU): Turning Models and Test Data into Mission Confidence," *Keck Institute for Space Studies*, 2011.

[143] Marrese-Reading, C., Arestie, S., Ziemer, J. K., Wirz, R., Collins, A., Uchizono, N., Gamero-Castano, M., and Demmons, N., "Electrospray Thruster Lifetime Modeling with Uncertainty Quantification and Experimental Test Validation," *International Electric Propulsion Conference*, ERPS, 2022, p. 234.

[144] Tajmar, M., Vasiljevich, I., and Grienauer, W., "High current liquid metal ion source using porous tungsten multiemitters," *Ultramicroscopy*, Vol. 111, No. 1, 2010, pp. 1–4.

[145] Harris, J. and Stocker, H., "Segment of a circle," *Handbook of Mathematics and Computational Science*, 1998, pp. 92–93.